Methods for the transfer matrix evaluation of thermoacoustic cores with application to the design of thermoacoustic engines

Flavio de Campos Bannwart

Thèse de Doctorat

Flávio de Campos BANNWART

Mémoire présenté en vue de l'obtention du
grade de Docteur de l'Université du Maine
sous le label de L'Université Nantes Angers Le Mans

École doctorale : SPIGA

Discipline : 60
Spécialité : Acoustique
Unité de recherche : Laboratoire d'Acoustique de l'Université du Maine — UMR CNRS 6613

Soutenue le 24 février 2014

Méthodes d'évaluation de la matrice de transfert des noyaux thermoacoustiques avec application à la conception de moteurs thermoacoustiques

JURY

Rapporteurs :	**David Lee GARDNER**, Senior Research Fellow, MS K764 - Los Alamos National Laboratory/USA **Arcanjo LENZI**, Professeur, Universidade Federal de Santa Catarina/BRÉSIL
Examinateur :	**José Maria Campos dos SANTOS**, Professeur, Unversidade Estadual de Campinas/BRÉSIL
Invité :	**Jean-Pierre DALMONT**, Professeur, LAUM, Université du Maine
Directeurs de Thèse :	**Pierrick LOTTON**, Directeur de Recherche, LAUM, Université du Maine **José Roberto de França ARRUDA**, Professeur, Universidade Estadual de Campinas/BRÉSIL
Co-directeur de Thèse :	**Guillaume PENELET**, Maître de Conférences, LAUM, Université du Maine

Thèse de Doctorat

Flávio de Campos BANNWART

Méthodes d'évaluation de la matrice de transfert des noyaux thermoacoustiques avec application à la conception de moteurs thermoacoustiques

Methods for the transfer matrix evaluation of thermoacoustic cores with application to the design of thermoacoustic engines

Résumé

La conception d'un moteur thermoacoustique dépend de façon critique de la fiabilité des outils de prédiction théorique de ses performances. Une tentative pour réussir cette prédiction consiste à exploiter les coefficients de la matrice de transfert du noyau thermoacoustique (NTA) dans les modèles analytiques du moteur considéré. La matrice de transfert peut être obtenue soit par modélisation analytique, soit par des mesures acoustiques. Ce dernier cas, cependant, se présente comme une option intéressante pour éviter d'avoir à considérer la complexité des éléments constitutifs du NTA. La méthode analytique est tout d'abord présentée ; elle ne vise que les cas de matériaux à géométrie simple. En ce qui concerne l'approche expérimentale, une méthode classique à deux charges est appliquée dans deux configurations différentes et, en outre, une méthode alternative basée sur des mesures d'impédance est développée ici et appliquée également. Une comparaison entre ces deux approches est évaluée au moyen d'une analyse de sensibilité. Différents matériaux sont testés, chacun jouant le rôle de l'élément poreux à l'intérieur d'un NTA soumis à plusieurs gradients de température. Seulement la méthode alternative s'avère performante pour tous les matériaux. Les matrices de transfert mesurées sont utilisées dans des modèles dédiés à prédire la fréquence de fonctionnement et le gain d'amplification thermoacoustique intrinsèque d'une machine équipée du NTA caractérisé au préalable. Une analyse comparative montre dans quelles conditions le seuil de déclenchement thermoacoustique est prévu ou non pour chaque matériau ; elle révèle aussi les limites dimensionnelles de l'appareil expérimental pour mieux répondre aux estimations de performances.

Mots clés

Thermoacoustique, acoustique, impédance acoustique, matériaux poreux, résonance

Abstract

The design of a thermoacoustic (TA) engine is improved towards the reliability of its performance prediction. An attempt to succeed in this prediction comes from the knowledge of the TA core (TAC) transfer matrix, which can be exploited in analytical models for the given engine. The transfer (T) matrix itself may be obtained either by analytical modeling or acoustic measurements. The latter consist in an interesting option to avoid thermo-physical or geometrical considerations of complex structures, as the TAC is treated as a *black box*. However, before proceeding with the experimental approach, an analytical solution is presented for comparison purposes, but it contemplates only cases of materials of simple geometry. Concerning the experimental approach, a classical two-load method is applied in two different configurations and an alternative method based on impedance measurements is here developed and applied. A comparison between these approaches is evaluated by means of a sensitivity analysis. Different materials are tested, each one playing the porous element allotted inside the TAC, which is in its turn submitted to several different regimes of steady state temperature gradient. The alternative method is the only one successful for all materials. In this manner, the measured transfer matrices are applied into a proper modeling devoted to predict both the operating frequency and the intrinsic TA amplification gain. A comparative analysis shows in what conditions the TA threshold is expected or not for each material ; it also reveals the limitations of the experimental apparatus in what concerns the appropriate dimensions to better fit the performance investigations.

Key Words

Thermoacoustics, acoustics, acoustic impedance, porous materials, resonance

Dedico esta tese à minha filha que logo vai nascer.

Je dédie cette thèse à ma fille qui naîtra bientôt.

I dedicate this thesis to my daughter who will be born soon.

Acknowledgments

This doctoral thesis has been accomplished at the Departamento de Mecânica Computacional (DMC) of the Faculdade de Engenharia Mecânica (FEM) of the Universidade Estadual de Campinas (UNICAMP), Brazil, and at the Laboratoire d'Acoustique de l'Université du Maine (LAUM), France, under the frame of a co-tutelage agreement between these universities, and with the financial and infra-structural support from the Brazilian funding agency CAPES, from LAUM, and from UNICAMP, to which I am deeply grateful. I would like to thank M. Yves Aurégan, Research Director CNRS, and M. Joël Gilbert, Director of LAUM, for being welcome during the two years period that I lived in Le Mans as a Ph.D. Student.

Writing this "Acknowledgments"essay is not a simple task. To accomplish this doctorate I depended on so many people, in so particularly different ways, that I can be sure that I will be unfair in my following words. But what I am indeed sure of is that I will do my best. What those forgotten or insufficiently acknowledged people can be sure of is that, even though not fairly mentioned here, they are imprinted in my heart.

First of all, I would like to express my deepest gratitude to my supervisors Pierrick Lotton, Research Director at LAUM, José Roberto de França Arruda, Professor at DMC/UNICAMP, and Guillaume Penelet, Maître de Conférence at LAUM, for their supervision, support, and guidance along these years either in Brazil or in France - the whole period, from both countries. They have taught me how to pursuit a scientific investigation, how to deal with the risks of failure in this process, and how to publish its results. With and because of them, I could live a discovery experience - which is always priceless no matter how modest it is. That I will carry for life. I am also grateful for their interest, efforts, and full commitment to carry on the non-trivial administrative tasks involved in the co-tutelage agreement, besides the arrangements for my moving to and staying in France. And we still had time to have some beers.

I would like to thank Jean-Pierre Dalmont, Professor at LAUM, for his strong support in dealing with the acoustic impedance sensor. I used to just appear at his office and knock at his door - no appointments at all - and he was always available for discussion. We had a number of meetings, for months, and his technical advices were crucial to properly operate the sensor and to understand important aspects concerning impedance measurements.

I would like to give special thanks to David Lee Gardner, Senior Research Fellow at Los Alamos National Laboratory/USA, for coming to my defense in Brazil as member of both Brazilian and French juries (*rapporteur*). He spent his own money to rush his VISA permit specifically to come to my defense. It was a great pleasure welcoming him, and also a privilege. Hopefully I can make good use of his scientific and life experience advices.

I would also like to thank all members of the Thermoacoustic Group of LAUM, Pierrick Lotton, Guillaume Penelet, Gaëlle Poignand (Research Engineer), and Matthieu Guedra (Ph.D. Student). Our weekly meetings were very productive, as we could regularly share our work and discuss solutions to advance in our research. Those meetings were inestimable opportunities to learn from each other.

Technical support was by all means crucial for my acoustic measurements, which consisted in a very important feature of my thesis work at LAUM. I express my sincere gratitude to all technicians with whom I had contact, because all of them were absolutely precise and efficient - and kind. Without them, I could not have done nothing.

Documents, bureaucracy and paperwork in general are not simple for all doctorates. However, in my particular case, the co-tutelage context added some issues, and they were not just a few. So I depended on many secretaries, either in Brazil or in France. As the French period of two years was in the middle of my doctorate, two changes of university/country had to be dealt with. Lucky me, all services were effective. I thank them all, in particular Carlos Della Betta.

Still in the beginning of my doctorate, in Brazil, I had the opportunity to learn from hard disciplines, from exigent professors. Their exigence, nevertheless, was balanced with their strong enthusiasm to teach. So my gratitude is extended to those professors, who taught me that these two features favor one another as part of an effective learning.

I am grateful to all my friends, among them many climbers with whom I had the opportunity to share trust on belay. And when I think about them, I always remember of my rock-climbing group GEEU - Grupo de Escalada Esportiva e Montanhismo da Unicamp.

I wish to give special thanks to my close friends Arthur de Miranda Neto, Matthew Alban Boucher, Frederico Theotonio, and Véronique Bour.

I owe my family much more than I can imagine. I owe my parents much more than my own existence. They gave me everything they could since I was born. Along these doctorate years, my father spared no effort to help me whenever I needed. For two years he was my support from the other side of the Atlantic Ocean.

At last, my other half.
My wife.
She was there all the time for me. She always is.
I thank my wife for her unconditional support, for her unconditional love.

Os dias que estes homens passam nas montanhas são os dias em que realmente vivem. Quando a mente se limpa das teias de aranha e o sangue corre com força pelas veias. Quando os cinco sentidos recobram a vitalidade e o homem completo se torna mais sensível, e então já pode ouvir as vozes da natureza, e ver as belezas que só estão ao alcance dos mais ousados.

Reinhold Messner

Les jours que ces hommes passent dans les montagnes sont des jours durant lesquels ils vivent réellement. Quand l'esprit se lave des toiles d'araignées et que le sang coule avec force dans les veines. Quand les cinq sens retrouvent leur vitalité et que l'homme entier devient plus sensible, il peut alors écouter les voix de la nature et voir les beautés à portée des plus audacieux.

Reinhold Messner

The days that these men are in the mountains are the days when they actually live. When the mind is clean of cobwebs and blood runs strongly through the veins. When the five senses regain vitality and the complete man becomes more sensitive, so he can listen to the voices of nature, and see the beauties that are only within the reach of the boldest.

Reinhold Messner

List of Figures

1.1 Schematic view of a thermoacoustic engine. In this example, the acoustic load is a linear alternator. . . . 3
1.2 Scheme of a standing-wave thermoacoustic engine with closed extremities and a representative example of a non-uniform temperature profile along its longitudinal axis. . . . 5
1.3 Engine cycle followed by a fluid particle under the influence of an acoustic standing wave in the vicinity of a solid wall which is subjected to a temperature gradient ∇T. (a) Particle initially at rest. (b) Adiabatic compression. (c) Isobaric expansion. (d) Adiabatic expansion. (e) Isobaric contraction. . . . 7
1.4 **(a)** Sinusoidal and "articulated" time evolution, respectively represented by solid lines and dotted lines, of the acoustic variables of pressure (p), temperature (τ) and displacement (ξ) for an acoustic standing wave. Points O, A, B, C and D correspond to the states (a), (b), (c), (d) and (e) of Fig. 1.3. **(b)** Clapeyron diagram of an "articulated" acoustic cycle. **(c)** "Real" Clapeyron diagram. . . . 8
1.5 The ideal Brayton cycle with the corresponding states of Fig. 1.4. . . . 8
1.6 **(a)** Engine cycle followed by a fluid particle under the influence of an acoustic traveling wave in the vicinity of a solid wall which is subjected to a temperature gradient ∇T. **(b)** Sinusoidal and "articulated" time evolution, respectively represented by solid lines and dotted lines, of the acoustic variables of pressure (p), temperature (τ) and displacement (ξ) for an acoustic standing wave. **(c)** The ideal Stirling cycle with the corresponding states. . . . 10
2.1 Coordinate system used for the problem modeling. . . . 13
2.2 Adopted *pressure-volume velocity* convention for the quadripole description; anti-symmetric orientation. . . . 18
2.3 (a) Sketch of a standing-wave thermoacoustic engine. (b) Open end. (c) Closed end. (d) Coupling with a electrodynamic alternator. . . . 25
2.4 Schematic representations of traveling-wave thermoacoustic engines. (a) Annular resonator. (b) Annular resonator coupled to a secondary acoustic load (secondary resonator, electrodynamic alternator, or any other load). (c) Co-axial resonator. . . . 28
3.1 Approximate scale plan of the ThermoAcoustic Core. . . . 32
3.2 ThermoAcoustic Core. . . . 32
3.3 The four-microphone apparatus with the thermoacoustic core. . . . 36
3.4 Experimental setup - Two-Load Method. . . . 42
3.5 Ceramic Catalyst in detail and partially inserted in the open TAC. . . . 44
3.6 Stainless Steel Grids, ceramic washers and stack/regenerator holder. . . . 45
3.7 Ceramic Catalyst 1: amplitude (solid line) and phase (dotted line) of the $\mathbf{T}_{\mathrm{TAC}}$ coefficients in the frequency domain for $Q_H = 0\,W(circle)$, $Q_H = 36\,W(square)$ and $Q_H = 72\,W(diamond)$ - Two-Load Method. . . . 46

3.8 Amplitude and phase of the $\mathbf{T}_{\mathrm{TAC}}$ reciprocity in the frequency domain for $Q_H = 0\,W$ for the Ceramic Catalyst 600 cpsi (bold lines) and the Stainless Steel Grids (thin lines)- Two-Load Method. 47
3.9 Stainless Steel Grids: amplitude (solid line) and phase (dotted line) of the $\mathbf{T}_{\mathrm{TAC}}$ coefficients in the frequency domain for $Q_H = 0\,W(circle)$, $Q_H = 36\,W(square)$ and $Q_H = 72\,W(diamond)$ - Two-Load Method. 48
3.10 Sketch of the inverted ThermoAcoustic Core. 49
3.11 Stainless Steel Grids: amplitude of the $\mathbf{T}_{\mathrm{TAC}}$ coefficients in the frequency domain for $Q_H = 0\,W$ - Two-Load Method with TAC Inversion (bold lines), Two-Load Method (thin lines) and Theory (dashed lines). 52
3.12 Stainless Steel Grids: zoomed amplitude in linear scale of the $\mathbf{T}_{\mathrm{TAC}}$ coefficients in the frequency domain for $Q_H = 0\,W$ - Two-Load Method with TAC Inversion (bold lines), Two-Load Method (thin lines) and Theory (dashed lines). 53
3.13 Stainless Steel Grids: amplitude of the $\mathbf{T}_{\mathrm{TAC}}$ coefficients in the frequency domain for $Q_H = 0\,W$ - Two-Load Method with TAC Inversion (bold lines), Two-Load Method (thin lines) and Theory (dashed lines). 54
3.14 Stainless Steel Grids: amplitude and phase of the $\mathbf{T}_{\mathrm{TAC}}$ reciprocity in the frequency domain for $Q_H = 0\,W$ - Two-Load Method with TAC Inversion (bold lines) and Two-Load Method (thin lines). 55
3.15 Ceramic Catalyst: amplitude of the four $\mathcal{T}$ coefficients in the frequency domain for $Q_H = 0\,W$ in bold lines for the measurements (solid) and theory (dashed) with the respective theoretical *bias* (four thin solid lines per graph) and *noise* (five dotted lines per graph). - Two-Load Method. 57
3.16 Ceramic Catalyst: phase of the four $\mathcal{T}$ coefficients in the frequency domain for $Q_H = 0\,W$ in bold lines for the measurements (solid) and theory (dashed) with the respective theoretical *bias* (four thin solid lines per graph) and *noise* (five dotted lines per graph). - Two-Load Method. 58
3.17 Ceramic Catalyst: amplitude of the four $\mathcal{T}$ coefficients in the frequency domain for $Q_H = 0\,W$ in bold lines for the theory (dashed) with the respective theoretical *bias* (four thin solid lines per graph) and *noise* (five dotted lines per graph). - Two-Load Method with TAC Inversion. 59
3.18 Ceramic Catalyst: phase of the four $\mathcal{T}$ coefficients in the frequency domain for $Q_H = 0\,W$ in bold lines for the theory (dashed) with the respective theoretical *bias* (four thin solid lines per graph) and *noise* (five dotted lines per graph). - Two-Load Method with TAC Inversion. 60
3.19 Stainless Steel Grids: amplitude of the four $\mathcal{T}$ coefficients in the frequency domain for $Q_H = 0\,W$ in bold lines for the measurements (solid) and theory (dashed), with the respective theoretical *bias* (four thin solid lines per graph) and *noise* (five dotted lines per graph). - Two-Load Method. 61
3.20 Stainless Steel Grids: phase of the four $\mathcal{T}$ coefficients in the frequency domain for $Q_H = 0\,W$ in bold lines for the measurements (solid) and theory (dashed), with the respective theoretical *bias* (four thin solid lines per graph) and *noise* (five dotted lines per graph). - Two-Load Method. 62

3.21 Stainless Steel Grids: amplitude of the four $\mathcal{T}$ coefficients in the frequency domain for $Q_H = 0\,W$ in bold lines for the measurements (solid) and theory (dashed), with the respective theoretical *bias* (four thin solid lines per graph) and *noise* (five dotted lines per graph). - Two-Load Method with TAC Inversion. 63
3.22 Stainless Steel Grids: phase of the four $\mathcal{T}$ coefficients in the frequency domain for $Q_H = 0\,W$ in bold lines for the measurements (solid) and theory (dashed), with the respective theoretical *bias* (four thin solid lines per graph) and *noise* (five dotted lines per graph). - Two-Load Method with TAC Inversion. 64
3.23 Front and back views of the AIS, and the AIS with the Adaptive Part. 65
3.24 Sketch of the AIS attached to the TAC for both measurements. 66
3.25 AIS attached to the TAC for both measurements. 66
3.26 Sketch of the Acoustic Impedance Sensor and the Adaptive Part. 68
3.27 Stainless Steel Grids: amplitude of the four $\mathcal{T}$ coefficients in the frequency domain for $Q_H = 0\,W$ in bold lines for the measurements (solid) and theory (dashed), with the respective theoretical *bias* (four thin solid lines per graph) and *noise* (five dotted lines per graph). - Impedance Method. 74
3.28 Stainless Steel Grids: phase of the four $\mathcal{T}$ coefficients in the frequency domain for $Q_H = 0\,W$ in bold lines for the measurements (solid) and theory (dashed), with the respective theoretical *bias* (four thin solid lines per graph) and *noise* (five dotted lines per graph). - Impedance Method. 75
3.29 Ceramic Catalyst: amplitude of the four $\mathcal{T}$ coefficients in the frequency domain for $Q_H = 0\,W$ in bold lines for the measurements (solid) and theory (dashed), with the respective theoretical *bias* (four thin solid lines per graph) and *noise* (five dotted lines per graph). - Impedance Method. 76
3.30 Ceramic Catalyst: phase of the four $\mathcal{T}$ coefficients in the frequency domain for $Q_H = 0\,W$ in bold lines for the measurements (solid) and theory (dashed), with the respective theoretical *bias* (four thin solid lines per graph) and *noise* (five dotted lines per graph). - Impedance Method. 77
3.31 Nichrome Foam (six discs), a ceramic washer and the stack/regenerator holder. 79
3.32 Reticulated Vitreous Carbon (RVC) Foam and the open TAC. 79
3.33 Temperature measurements at the right side of the HHX by means of a $35\,cm$ long thermocouple accessing it from the TAC right side; the RVC Foam is within the TAC. 80
3.34 Stainless Steel Grids: amplitude (solid line) and phase (dotted line) of the $\mathbf{T}_{\mathrm{TAC}}$ coefficients in the frequency domain for $Q_H = 0\,W(circle)$, $Q_H = 36\,W(square)$ and $Q_H = 72\,W(diamond)$ - Impedance Method. 81
3.35 Ceramic Catalyst: amplitude (solid line) and phase (dotted line) of the $\mathbf{T}_{\mathrm{TAC}}$ coefficients in the frequency domain for $Q_H = 0\,W(circle)$, $Q_H = 36\,W(square)$ and $Q_H = 72\,W(diamond)$ - Impedance Method. 82
3.36 Nichrome Foam: amplitude (solid line) and phase (dotted line) of the $\mathbf{T}_{\mathrm{TAC}}$ coefficients in the frequency domain for $Q_H = 0\,W(circle)$, $Q_H = 36\,W(square)$ and $Q_H = 72\,W(diamond)$ - Impedance Method. 83
3.37 RVC Foam: amplitude (solid line) and phase (dotted line) of the $\mathbf{T}_{\mathrm{TAC}}$ coefficients in the frequency domain for $Q_H = 0\,W(circle)$, $Q_H = 9\,W(square)$ and $Q_H = 18\,W(diamond)$ - Impedance Method. 84

3.38 Amplitude and phase of the $\mathbf{T}_{\mathrm{TAC}}$ reciprocity in the frequency domain for $Q_H = 0\,W$ for the Stainless Steel Grids (relatively noisy lines), Ceramic Catalyst (continuous thin lines), Nichrome Foam (dotted lines) and RVC Foam (dashed lines) - Impedance Method. 86
3.39 Stainless Steel Grids: amplitude and phase of the $\mathbf{T}_{\mathrm{TAC}}$ reciprocity in the frequency domain for $Q_H = 0\,W$ for the Impedance Method and for the Two-Load Method (very noisy lines). 87
3.40 Ceramic Catalyst: amplitude and phase of the $\mathbf{T}_{\mathrm{TAC}}$ reciprocity in the frequency domain for $Q_H = 0\,W$ for the Impedance Method and for the Two-Load Method (lines of narrower frequency range). 88
4.1 Basic configurations for standing-wave and closed-loop engines. 92
4.2 Ceramic Catalyst: modulus and real part of the reflected acoustic impedance for $Q_H = 9W$ (dash-dotted line), $Q_H = 18\,W$ (dashed line), and $Q_H = 27\,W$ (solid line). 94
4.3 Theoretical $f_{op.}$ for standing-wave engines at $Q_H = 0\,W$ for the Ceramic Catalyst. 99
4.4 Theoretical $Gain$ for standing-wave engines at $Q_H = 0\,W$ for the Ceramic Catalyst. 100
4.5 $Gain$ for standing-wave engines at $Q_H = 0\,W$ from measured $\mathbf{T}_{\mathrm{TAC}}$ of the Ceramic Catalyst by the Impedance Method. 100
4.6 $Gain$ for standing-wave engines at $Q_H = 0\,W$ from measured $\mathbf{T}_{\mathrm{TAC}}$ of the Ceramic Catalyst using polynomial regression of fifth degree - Impedance Method. 100
4.7 $f_{op.}$ for standing-wave engines at $Q_H = 81\,W$ from measured $\mathbf{T}_{\mathrm{TAC}}$ of the Ceramic Catalyst using polynomial regression of fifth degree - Impedance Method. 102
4.8 $Gain$ for standing-wave engines at $Q_H = 81\,W$ from measured $\mathbf{T}_{\mathrm{TAC}}$ of the Ceramic Catalyst using polynomial regression of fifth degree - Impedance Method. 103
4.9 $f_{op.}$ for closed-loop engines at $Q_H = 81\,W$ from measured $\mathbf{T}_{\mathrm{TAC}}$ of the Nichrome Foam using polynomial regression of fifth degree - Impedance Method. 104
4.10 $Gain$ for closed-loop engines at $Q_H = 81\,W$ from measured $\mathbf{T}_{\mathrm{TAC}}$ of the Nichrome Foam using polynomial regression of fifth degree - Impedance Method. 105
4.11 $Gain$ for closed-loop engines at $Q_H = 81\,W$ from measured $\mathbf{T}_{\mathrm{TAC}}$ of the Nichrome Foam using polynomial regression of fifth degree - Impedance Method. 105
4.12 $Gain$ for closed-loop engines at $Q_H = 81\,W$ from measured $\mathbf{T}_{\mathrm{TAC}}$ of the Ceramic Catalyst using polynomial regression of fifth degree - Impedance Method. 106
4.13 $Gain$ for closed-loop engines at $Q_H = 81\,W$ from measured $\mathbf{T}_{\mathrm{TAC}}$ of the Ceramic Catalyst using polynomial regression of fifth degree - Impedance Method. 106
A.1 Amplitude proportions and phase differences between the transfer functions measured before and 12.5 min after turning in the ambient water cooling system for $\widetilde{H}_{21}$ (solid line), $\widetilde{H}_{31}$ (dashed line), and $\widetilde{H}_{43}$ (dotted line). 122
A.2 Amplitude proportions and phase differences between the transfer functions measured just before and $5min$ after the transition of heating input from $Q_H = 29.3W$ to $Q_H = 32.3W$ for $\widetilde{H}_{21}$ (solid line), $\widetilde{H}_{31}$ (dashed line), and $\widetilde{H}_{43}$ (dotted line). 124
A.3 Amplitude proportions and phase differences between the transfer functions measured 13 and $18min$ both after the transition of heating input from $Q_H = 29.3W$ to $Q_H = 32.3W$ for $\widetilde{H}_{21}$ (solid line), $\widetilde{H}_{31}$ (dashed line), and $\widetilde{H}_{43}$ (dotted line). 125

B.1 Detail of the calibration device showing the two micros and the small cavity as the coupling volume submitted to uniform acoustic pressures provided by the compression chamber. 128
B.2 Calibrating corrections expressed as the spectra of amplitude ratio and phase difference between acoustic pressures as stated in equations B.1. 129
C.1 Detail of the third microphone head and its attachment to the AIS for calibration. 131
D.1 Ceramic Catalyst 600 CPSI: amplitude of the four $\mathcal{T}$ coefficients in the frequency domain for Q_H ranging from $0W$ to $81W$, by a constant increment of $3W$. The bold graph line corresponds to $Q_H = 0W$. - Two-Load Method. . . . 133
D.2 Ceramic Catalyst 600 CPSI: phase of the four $\mathcal{T}$ coefficients in the frequency domain for Q_H ranging from $0W$ to $81W$, by a constant increment of $3W$. The bold graph line corresponds to $Q_H = 0W$. - Two-Load Method. 134
D.3 Stainless Steel Grids: amplitude of the four $\mathcal{T}$ coefficients in the frequency domain for Q_H ranging from $0W$ to $81W$, by a constant increment of $3W$. - Two-Load Method. 135
D.4 Stainless Steel Grids: phase of the four $\mathcal{T}$ coefficients in the frequency domain for Q_H ranging from $0W$ to $81W$, by a constant increment of $3W$. - Two-Load Method. 136
D.5 Stainless Steel Grids: amplitude of the four $\mathcal{T}$ coefficients in the frequency domain for Q_H ranging from $0W$ to $81W$, by a constant increment of $9W$. The bold graph line corresponds to $Q_H = 0W$. - Impedance Method. 137
D.6 Stainless Steel Grids: phase of the four $\mathcal{T}$ coefficients in the frequency domain for Q_H ranging from $0W$ to $81W$, by a constant increment of $9W$. The bold graph line corresponds to $Q_H = 0W$. - Impedance Method. 138
D.7 Ceramic Catalyst 600 CPSI: amplitude of the four $\mathcal{T}$ coefficients in the frequency domain for Q_H ranging from $0W$ to $81W$, by a constant increment of $9W$. The bold graph line corresponds to $Q_H = 0W$. - Impedance Method. . . . 139
D.8 Ceramic Catalyst 600 CPSI: phase of the four $\mathcal{T}$ coefficients in the frequency domain for Q_H ranging from $0W$ to $81W$, by a constant increment of $9W$. The bold graph line corresponds to $Q_H = 0W$. - Impedance Method. 140
D.9 NiCr Foam: amplitude of the four $\mathcal{T}$ coefficients in the frequency domain for Q_H ranging from $0W$ to $81W$, by a constant increment of $9W$. The bold graph line corresponds to $Q_H = 0W$. - Impedance Method. 141
D.10 NiCr Foam: phase of the four $\mathcal{T}$ coefficients in the frequency domain for Q_H ranging from $0W$ to $81W$, by a constant increment of $9W$. The bold graph line corresponds to $Q_H = 0W$. - Impedance Method. 142
D.11 RVC Foam: amplitude of the four $\mathcal{T}$ coefficients in the frequency domain for Q_H ranging from $0W$ to $18W$, by a constant increment of $3W$. The bold graph line corresponds to $Q_H = 0W$. - Impedance Method. 143
D.12 RVC Foam: phase of the four $\mathcal{T}$ coefficients in the frequency domain for Q_H ranging from $0W$ to $18W$, by a constant increment of $3W$. The bold graph line corresponds to $Q_H = 0W$. - Impedance Method. 144
E.1 NiCr Foam: amplitude and phase of the $\mathbf{T}_{\mathrm{TAC}}$ reciprocity in the frequency domain for $Q_H = 0\,W$ for the Impedance Method before (biased and noisy line) and after a better thermal stabilization. 145

List of Tables

3.1 Geometrical properties of the sample materials. 33
3.2 Average reciprocities and standard deviations in the frequency range from 50 to $200\,Hz$ for all three approaches and also from 30 to $500\,Hz$ for the Impedance Method. 78
4.1 Performances for a standing-wave engine equipped with a stack (Ceramic Catalyst) ($L_1 = 160\,cm$ and $L_2 = 10\,cm$). 95
4.2 Maximal performances and respective configurations for standing-wave engines at $Q_H = 0\,W$ calculated from theoretical and experimental data, fitted or not with polynomial regression of fifth degree, with their corresponding average reciprocities and average standard deviations in the frequency range from 30 to $500\,Hz$. 101
4.3 Maximal performances and respective configurations for standing-wave engines at $Q_H = 81\,W$. 103
4.4 Maximal performances and respective configurations for closed-loop engines at $Q_H = 81\,W$. 107

SUMMARY

List of Figures vii

List of Tables xiii

SUMMARY xv

1 INTRODUCTION 1
1.1 Literature review and historical context . . . 3
1.2 Thermoacoustic principle . . . 5

2 THERMOACOUSTIC PROCESSES: THE FUNDAMENTAL MODELING 11
2.1 Fundamental equations of thermoacoustics . . . 11
2.1.1 Primary equations of dissipative fluids . . . 11
2.1.2 Simplifying hypotheses . . . 12
2.1.3 Propagation equation governing the acoustic pressure . . . 14
2.2 Transfer matrices of acoustic two-port . . . 17
2.2.1 Conventions . . . 17
2.2.2 Case of a straight waveguide . . . 18
2.2.3 Case of a porous element . . . 20
2.2.4 Case of a tapered waveguide . . . 21
2.3 Analytical expression for the transfer matrix of an acoustic two-port submitted to a non-uniform temperature distribution . . . 22
2.4 Characteristic equation of a thermoacoustic device . . . 24
2.4.1 Case of a standing-wave thermoacoustic engine . . . 24
2.4.2 Case of a traveling-wave thermoacoustic engine . . . 26

3 EXPERIMENTAL CHARACTERIZATION OF THE THERMOACOUSTIC CORE 31
3.1 Description of the TAC under study . . . 31
3.2 Common features . . . 34
Framework solution for the two-port system . . . 35
3.3 First approach: the Two-Load Method - about its failure . . . 36
3.3.1 Principle of the method . . . 36
3.3.2 Experimental setup and procedures . . . 41
3.3.3 Results . . . 44
Case of the Ceramic Catalyst . . . 44
Case of the Stainless Steel Grids . . . 45
3.3.4 Comparison with theory and analysis . . . 46
3.3.5 Discussion . . . 48
3.4 Second approach: the Two-Load Method with TAC Inversion - about its failure 49
3.4.1 Principle of the method . . . 49
3.4.2 Experimental procedures . . . 51

3.4.3 Results for the Stainless Steel Grids . . . 52
3.5 Sensitivity analysis for both Two-Load Methods (with and without TAC inversion) 54
3.6 Third approach: the Impedance Method . . . 60
3.6.1 Principle of the method . . . 62
The Acoustic Impedance Sensor - AIS . . . 67
Consideration of the waveguide discontinuity . . . 70
Consideration of the Adaptive Part . . . 72
Final equations for the $\mathbf{Z}_{\mathrm{TAC}}$ and the $\mathbf{T}_{\mathrm{TAC}}$ coefficients . . . 72
3.6.2 Sensitivity analysis for the Impedance Method . . . 73
3.6.3 Experimental setup and procedures . . . 76
3.6.4 Results . . . 78
Case of the pile of Stainless Steel Grids . . . 81
Case of the Ceramic Catalyst . . . 82
Case of the NiCr Foam . . . 83
Case of the RVC Foam . . . 84
3.6.5 Discussion and comparative analysis with the previous approaches . . . 85
3.7 Conclusion . . . 89

4 APLICATION TO THE DESIGN OF THERMOACOUSTIC ENGINES 91
4.1 Introduction . . . 91
4.2 Theory . . . 91
4.2.1 Standing-wave engine . . . 92
4.2.2 Closed-loop engine . . . 96
4.3 Calculation of G and $f_{op.}$ from experimental data . . . 97
4.3.1 Comparison between results from theoretical and experimental data . . . 98
4.3.2 Standing-wave engines for $Q_H > 0$ . . . 101
4.3.3 Closed-loop engines for $Q_H > 0$ . . . 103

5 GENERAL CONCLUSIONS 109

REFERENCES 113

APPENDICES 120

A Transient regime investigation 121

B Calibration for the Two-Load Method 127

C Calibration for the Impedance Method 131

D Results for all heating conditions 133

E Thermal effects on reciprocity 145

1 INTRODUCTION

Thermoacoustic machines belong to the family of cyclic thermodynamic machines that exchange heat and work with their environment. Like any thermodynamic machine, they have two operating modes depending on the direction of energy exchange: the engine mode for which the system uses the heat transfer from a hot source to a cold source to produce acoustic work and the heat-pump mode for which the system uses the acoustic energy produced by an external source to extract heat from a cold reservoir. The thermoacoustic effect on which the operation of these engines is based comes from the interaction between acoustic oscillations in a fluid and a temperature gradient imposed along the walls of a porous material (usually called "stack" or "regenerator", depending on whether the heat contact is quasi-adiabatic or quasi-isothermal).

The development of efficient thermoacoustic engines is largely due to the work carried out at Los Alamos National Laboratory (USA), including the development of the software *Delta*-E (Ward, 1994) (then *Delta*-EC (Ward *et al.*, 2008)). *Delta*-EC is a robust tool dedicated to the design of thermoacoustic systems and remains the most widely used tool to date. However, although it is suitable for calculating the performance of thermoacoustic machines, *Delta*-EC has some shortcomings implicitly related to the theory on which it is based. First, *Delta*-EC is based on a one-dimensional approach of the thermoacoustic effects and therefore does not take into account any variation in transverse fields, which can play a significant role in the amplification process of the wave. Moreover the modeling of thermoacoustic instability is described in steady state and ignores the transient regime which may contain important information about the non-linear processes responsible for saturation (Swift, 1992; Yu *et al.*, 2003; Penelet *et al.*, 2002). Finally, *Delta*-EC is based on the linear theory of thermoacoustics (Rott, 1980; Swift, 1988) and the only saturating processes taken into account are the acoustically induced heat flux and singular head losses at the edges of the stack. These limitations require the development of tools to describe what *Delta*-EC can not predict and lead to the following questions: what theoretical approach can be adopted for the description of the thermoacoustic amplification from the onset until the saturation amplitude? What methods can be used to avoid uni-dimensional considerations and simplifying assumptions regarding the distribution of temperature, the presence of heat exchangers or the thermophysical properties of regenerators?

In response to the last question, the Laboratoire d'Acoustique de l'Université du Maine (LAUM) has recently launched work on the theoretical description and the design of thermoacoustic engines, using the formalism of transfer matrices. In this context, the thermoacoustic core (TAC) is considered as a black box and its transfer matrix is obtained experimentally (Guedra *et al.*, 2011). The TAC is the element of a thermoacoustic engine in which the temperature

field is heterogeneous. It is divided into an “active” and a “passive” part (Fig 1.1). The “active” part consists of an open cell porous material (stack or regenerator) equipped with a hot (HHX) and an ambient (AHX) heat exchangers at its ends. These heat exchangers are used to maintain a steep temperature gradient, which is responsible for the onset of large amplitude acoustic waves oscillating at the frequency of the most unstable acoustic mode of the complete device. The “passive” part is the so-called thermal buffer tube (TBT), which refers to the waveguide region between the HHX and a secondary AHX. The TAC is generally surrounded by an acoustical network to compose a resonant device in which a mechanical (acoustic) power is produced by thermoacoustic energy conversion. This acoustic power can then be supplied to an acoustic load, e.g. an electrodynamic alternator, as illustrated in Fig. 1.1.

Even below the threshold of thermoacoustic instability, the theoretical description of acoustic propagation and heat transfer through the thermoacoustic core (TAC) is anything but simple. This is essentially due to the fact that thermoacoustic engines make use of geometrically complicated materials (piles of stainless meshes, metallic foams) whose thermophysical parameters are unknown. Moreover, the accuracy of the description of acoustic propagation through the TAC also depends critically on the shape of the temperature field within the TAC, the latter being very difficult to describe theoretically. Therefore, alternative methods allowing the description of the TAC shall be developed. In a previous study carried out in LAUM, a stack-based TAC has been characterized experimentally. Guedra *et al.* (2011) performed the measurement of the transfer matrices of a heated TAC by means of a classical "two load - four microphone" method (Boden, 1986). These transfer matrices were then introduced into an analytical model which predicts the onset of self-sustained oscillations in a thermoacoustic device. Experimental data obtained from a stack made up of a 600 cells per square inch (cpsi) ceramic catalyst have been introduced in the model and theoretical predictions of the onset conditions were consistent with those actually observed in different engines equipped with this TAC. However, in the frame of this previous work, the method developed by Guedra et al. has not been tested to describe the behaviour of a heated regenerator-based TAC.

Therefore, the aim of this thesis is twofold. First, in the continuation of the works by Guedra *et al.*, it is to investigate alternative methods for the experimental characterization of a TAC, allowing accurate description of both stack-based and regenerator-based TAC made of different materials besides the Ceramic Catalyst 600 cpsi, such as a Reticulated Vitreous Carbon Foam, a Nichrome Foam, and a Pile of Stainless Steel Grids. Second, it is to introduce the experimental data obtained from these alternative methods into an analytical modeling for the optimal design of different kinds of thermoacoustic engines, and the estimation of the onset of self-sustained oscillations.

After a brief history of thermoacoustics given in Chapter 1, the theoretical basis of thermoacoustics are recalled in Chapter 2. In particular, characteristic equations of thermoacoustic devices are derived using the formalism of the transfer matrices. The solution of such equation allows the description of the onset of self-sustained oscillations in a thermoacoustic engine (in terms of working frequency and amplification rate (Guedra *et al.*, 2011)). This theoretical method requires the knowledge of the transfer matrix of the TAC. Different experimental procedures to measure the coefficients of the transfer matrix (including the procedure developed by Guedra et al.) are presented and evaluated in Chapter 3. Finally, using the knowledge of the transfer matrices of different TAC tested in Chapter 3, the design of several thermoacoustic systems is discussed in Chapter 4.

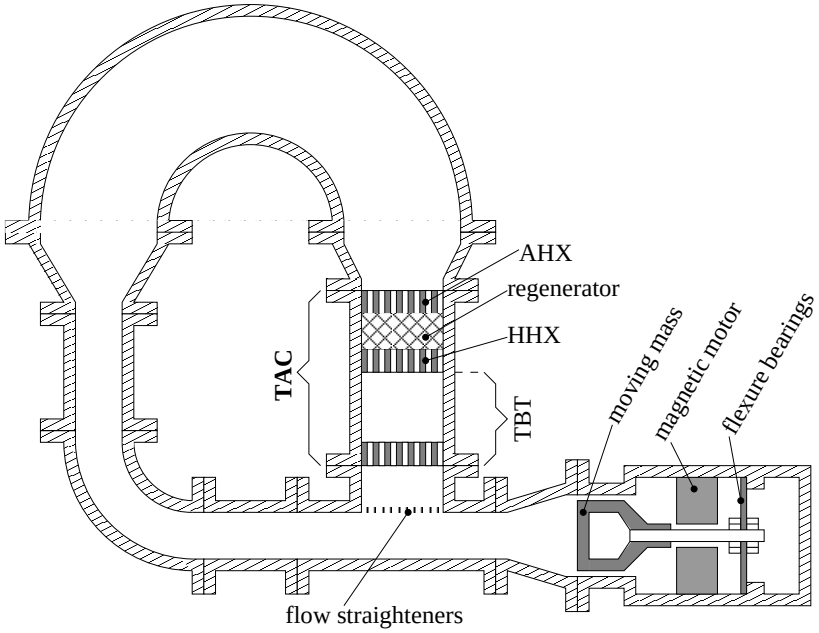

Figure 1.1: Schematic view of a thermoacoustic engine. In this example, the acoustic load is a linear alternator.

1.1 Literature review and historical context

Thermoacoustic wave generators (or engines) are made of acoustic resonators in which the interaction between acoustic and thermal oscillations in the vicinity of solid walls subjected to a high temperature gradient produces a conversion of thermal energy into acoustic energy. This thermoacoustic process aroused the interest of the scientific community of the late XVIIIth century when Byron Higgins succeeded in creating acoustic oscillations in a tube with a flame judiciously placed on the wall of a resonator (Higgins, 1802). Other types of this kind of devices have been realized in the late XIXth century since the Sondhauss tube (Sondhauss, 1850) or the

Rijke's tube (Rijke, 1859). A first theory of thermoacoustic interaction (between acoustic and thermal fields) was given in 1868 by Kirschhoff, who introduced the conduction of heat in the theory of sound propagation. Based on this work, a first qualitative interpretation of the Sondhauss tube was given by Lord Rayleigh in 1896 (Strutt, 1945). In this work, Rayleigh specially emphasizes that the acoustical temperature oscillations of a fluid particle located near a wall subjected to a high temperature gradient must necessarily be phase-shifted with respect to the particle displacement, so that the thermoacoustic amplification process occurs. In his original words:

"In almost all cases where heat is communicated to a body expansion ensues, and this expansion may be made to do mechanical work. If the phases of the forces thus operative be favorable, a vibration may be maintained ... . For the sake of simplicity, a tube, hot at the closed end and getting gradually cooler towards the open end, may be considered. At a quarter of period before the phase of greatest condensation ... the air is moving inwards, i.e. towards the closed end, and therefore is passing from colder to hotter parts of the tube; ... but in fact the adjustment of temperature takes time, and thus the temperature of the air deviates from that of the neighboring parts of the tube, inclining towards the temperature of that part of the tube from which the air has just come. From this it follows that at the phase of greatest condensation heat is received by the air, and at the phase of greatest rarefaction heat is given up from it, and thus there is a tendency to maintain the vibrations."

In the 1960s, an important step was taken by Carter *et al.* (1962), who devised an "optimized" Sondhauss tube by adding a stack of plates (stacks) in the resonator, thereby significantly increasing the machine efficacy and efficiency. This device, schematically represented in Fig. 1.2, belongs to the class of standing-wave thermoacoustic engine. In this system, when the temperature gradient along the stack of plates reaches the instability threshold, self-sustained acoustic oscillations of high amplitude (about 1 to 10 percent of the static pressure) take place in the resonator at the frequency of the most unstable mode, which usually is, in a first approximation, the longitudinal half-wave mode.

Based on Carter's work, many studies have been carried out ever since, and several prototypes of thermoacoustic engines have been realized. From 1970 to 1990, Rott (1969, 1973, 1980) established the theoretical foundations of thermoacoustics and provided an analytical model of the instability caused by the thermoacoustic interaction in the tubes of Taconis and Sondhauss. The experimental work of Yazaki *et al.* (1980a,b) qualitatively confirmed the validity of the theory of Rott. Since the early 1980s, research in thermoacoustic intensifies, notably through the work carried out at the Los Alamos National Laboratory (e.g. Swift (1988)). If the

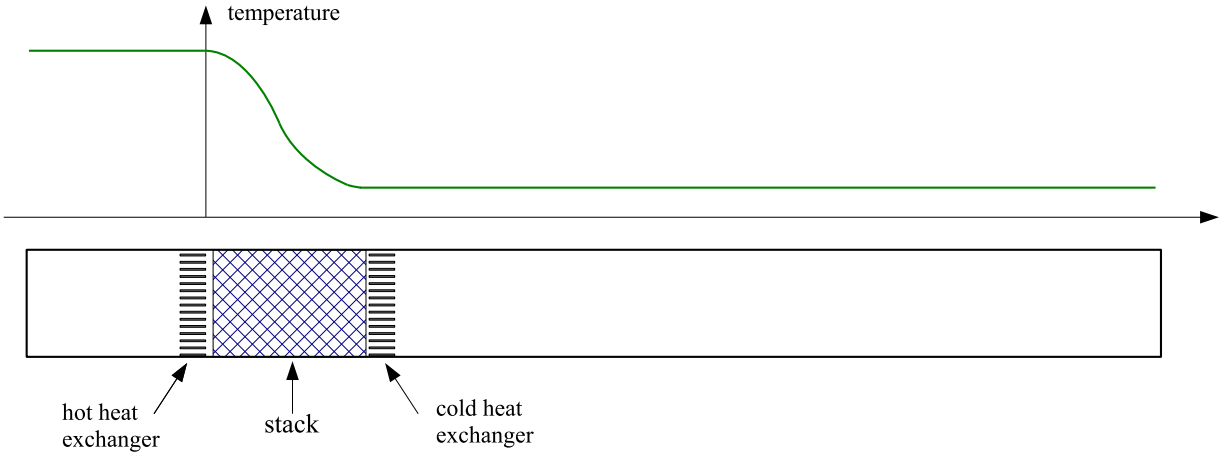

Figure 1.2: Scheme of a standing-wave thermoacoustic engine with closed extremities and a representative example of a non-uniform temperature profile along its longitudinal axis.

thermoacoustic processes could have been considered at first as a simple scientific curiosity, its use as a converter of thermal energy into mechanical energy constitutes a real challenge itself. Indeed, there are many potential applications of this kind of machines combining simplicity, robustness and reasonable efficiency (Garrett, 2004). Since then, efforts have been made to improve the performance of either thermoacoustic devices. That led, for example, to the development of a cascade thermocoustic engine (Gardner, 2003), where the overall engine efficiency is enhanced by means of combining several elementary engines, to better use the available energy. In this sense, de Blok (2010) developed a power generator where only a low temperature difference is required to make it work; such a system has a strong environmental impact since it allows the harvesting of waste heat. Simultaneously, important efforts have been made towards the thermoacoustic efficiency by improving the comprehension of the nonlinear processes involved when the acoustic wave saturation occurs in thermoacoustic engines (Penelet, 2004; Penelet *et al.*, 2002), and also by developing models for the temperature distribution along their heated sections (Penelet *et al.*, 2005b,a).

1.2 Thermoacoustic principle

The process of interaction between a fluid and a solid wall resulting in the conversion of thermal energy into acoustic energy involves complex processes and requires accurate modeling (Bailliet, 1998; Job, 2001; Rott, 1980). However, a simplified approach allows to understanding the main mechanisms involved in the apparatus of Fig. 1.2. For that, it is considered a fluid

particle in the vicinity of a solid wall of the stack, along which a strong temperature gradient ∇T is set (Fig. 1.3 (a)). The temperature of the particle at rest, under a given static pressure P_0, is imposed by the presence of the wall (whose thermal inertia is assumed to be very large compared with that of the fluid). Supposing that the thermodynamic state of the particle fluctuates under the influence of a sinusoidal stationary sound field, thus this particle oscillates in a consequent sinusoidal motion, to which are associated small oscillations of sound pressure $p(t)$ ($p << P_0$) in phase with the acoustic particle displacement $\xi(t)$ (or in phase quadrature with the acoustic velocity). The acoustic pressure oscillations are associated with temperature oscillations; the latter which are assumed, in a first approximation, in phase with the first ones (Fig. 1.4 (a), solid line). This is a valid hypothesis when the particle motion is under quasi-adiabatic conditions, which means temperature oscillations small enough (and fast enough either) to render negligible the heat transport between adjacent particles. As an illustrative example of the orders of magnitude involved, a particle of air submitted to a sinusoidal free field at a frequency of $1kHz$, whose pressure level reaches the pain threshold of the human ear ($P_{max} = 20Pa$), has its amplitude of temperature oscillations reaching only $T_{max} \approx 10^{-2}K$, and its displacement amplitude ξ_{max} is of the order of $10^{-5}m$. That stated, each thermodynamical process follows a harmonic cycle. However, an additional simplification helps to understanding of fundamental physical phenomena involved. That would be the particle motion being represented no longer by a sinusoidal temporal profile, but actually by a square profile instead (Fig. 1.4 (a), dashed line). Four phases are then clearly distinguished in one cycle: adiabatic compression, isobaric expansion, adiabatic expansion, and isobaric compression. The adiabatic condition is approximated whether these processes are considered sufficiently fast, while the heat transfer occurs during the isobaric processes between the fluid particle and the wall solid surface. The cycle followed by the particle has its shape shown in Fig. 1.3 (b)-(e), when the temperature gradient ∇T applied to the wall is such that $\xi_{max}\nabla T > \tau_{max}$. Thus, the particle receives a quantity of heat Q during its compression phase and returns a quantity of heat Q' during its expansion phase. This same cycle in four phases can be represented schematically following a Clapeyron diagram (Fig. 1.4 (b) and (c)). It then becomes clear that during the motion of the particle, a quantity of heat $Q - Q'$ has been converted into mechanical work (i.e. acoustic energy), represented by the shaded area.

In reality, the heat exchange mechanism between fluid and wall is of course far more complex than suggested by the previous remarks. In fact, to fully understand the real thermoacoustic amplification process, special attention must be paid to the phase relations between oscillations of pressure, particle velocity and acoustic temperature. As indicated above, the temperature variations of a fluid particle are related to its compression-relaxation and the local wall temperature. The distance between fluid particle and wall is therefore an important

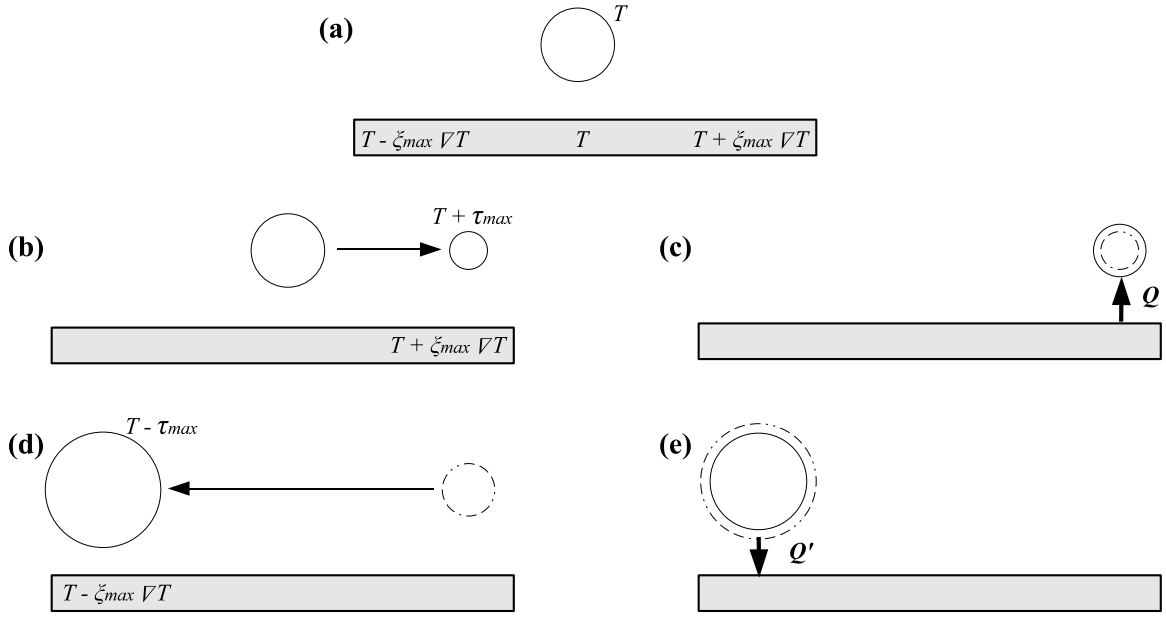

Figure 1.3: Engine cycle followed by a fluid particle under the influence of an acoustic standing wave in the vicinity of a solid wall which is subjected to a temperature gradient ∇T. (a) Particle initially at rest. (b) Adiabatic compression. (c) Isobaric expansion. (d) Adiabatic expansion. (e) Isobaric contraction.

parameter regarding the nature of heat exchange process: "far" from the wall, the process is adiabatic and the temperature oscillates over time and phase with the acoustic pressure; "close" by the wall, the process is isothermal and the fluid particle has its temperature imposed at each instant by the local temperature of the wall. But for a particle of fluid located at a distance of the order of a boundary layer thickness δ_κ of the wall, the thermal contact between particle and wall is "good enough" for the heat exchange to take place, but "bad enough" for this heat exchange to not result in an instantaneous change of temperature in the fluid particle; actually, at this intermediary region there is a delay in the heat exchange, or, more precisely, a phase shift between particle motion and heat transfer ($\delta_\kappa = \sqrt{2\kappa/\omega}$, where δ_κ is the thermal penetration depth, κ is the thermal diffusivity of the fluid, and ω is the angular frequency). This is indeed the phase shift between oscillations of temperature and acoustic pressure that is responsible for the energy conversion, and the cycle followed by the particle is analogous to the diagram in Fig. 1.4 (c). In summary , only fluid particles located at a distance of the order of a thermal boundary layer thickness effectively contribute to the thermoacoustic energy conversion. Therefore, a stack whose pores (i.e. inter-wall distance) are properly sized for the distance δ_κ is optimized for the thermoacoustic conversion, since the amount of "effective" fluid is maximized.

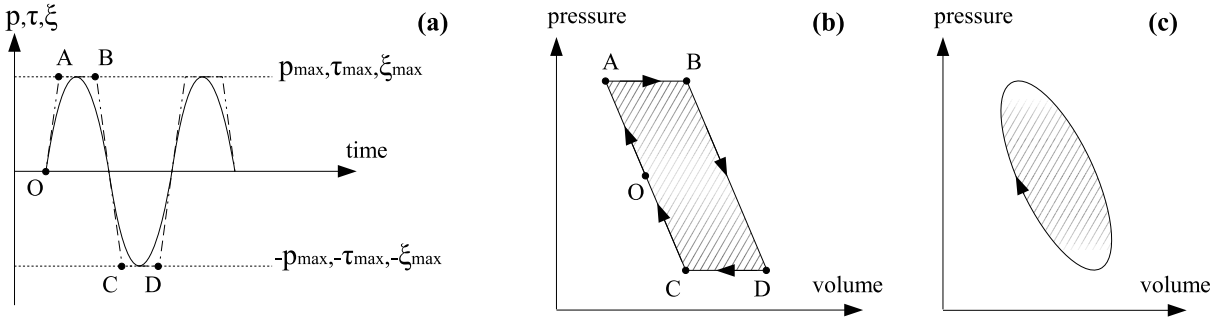

Figure 1.4: **(a)** Sinusoidal and "articulated" time evolution, respectively represented by solid lines and dotted lines, of the acoustic variables of pressure (p), temperature (τ) and displacement (ξ) for an acoustic standing wave. Points O, A, B, C and D correspond to the states (a), (b), (c), (d) and (e) of Fig. 1.3. **(b)** Clapeyron diagram of an "articulated" acoustic cycle. **(c)** "Real" Clapeyron diagram.

To resume, this cycle approaches to an ideal Brayton cycle, as illustrated in Fig. 1.5, and therefore it operates in an intrinsically irreversible cycle due to the finite temperature difference in the heat transfer processes. This cycle results in a positive acoustic work production, like a thermal engine. However, as well known from the laws of thermodynamics, an inversion in its processes leads the system to operate as a "heat pump". Indeed, it clearly appears on the schematic cycle of Fig. 1.3 that if the temperature gradient applied along the wall is such that $\xi_{max}\nabla T < \tau_{max}$, the orientation of thermoacoustic heat transfer from one end of the stack to another is inverted (here, from left to right), so that a temperature gradient is established and maintained along the stack.

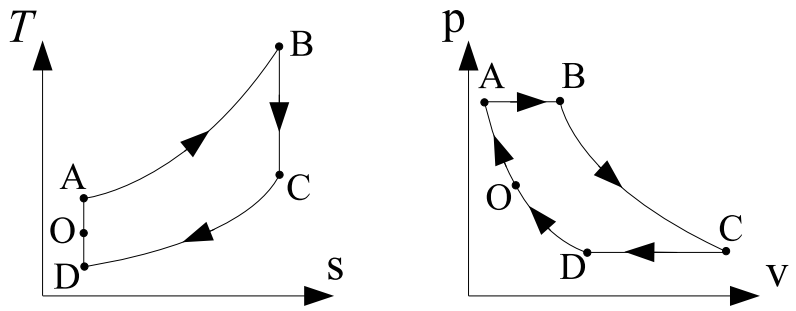

Figure 1.5: The ideal Brayton cycle with the corresponding states of Fig. 1.4.

In the case of traveling-wave systems, the thermoacoustic principle operates differently. The main difference relies in the fact that the acoustic pressure and the volume velocity are in phase (and the displacement is $\pi/2$ rad out of phase with the acoustic pressure, consequently),

what leads to approximate to an isothermal heat transfer between the fluid particle and the solid wall. This feature leads the cycle to approach to a Stirling cycle, which is ideally reversible. To enhance this approximation, the fluid particle must oscillate in very close thermal contact with the solid surfaces of the porous material, whose pores therefore result much thinner than in the case of standing-wave systems. Besides, the porous material shall possess a higher thermal conductivity, so as to allow an adequate oscillating heat transfer in such a condition; that promotes a regenerative cycle. As a consequence, the traveling-wave thermoacoustic systems tend to be, in principle, more efficient than the standing-wave ones. However, there are some disadvantages that may risk this preponderance and should be managed, such as the higher susceptibility to acoustic streaming and viscous losses due to the smaller pores, among others.

Analogously to Figs. 1.3, 1.4, and 1.5, the traveling-wave thermoacoustic cycle is displayed in Fig. 1.6. Figure 1.6 (a) shows the following six ideal processes: A-B: reversible adiabatic compression; B-C: isothermal and reversible heat transfer; C-D: reversible adiabatic expansion; D-E: reversible adiabatic expansion; E-F: isothermal and reversible heat transfer; F-A: reversible adiabatic compression. All these processes are in accordance with Figs. 1.6 (b) and 1.6 (c).

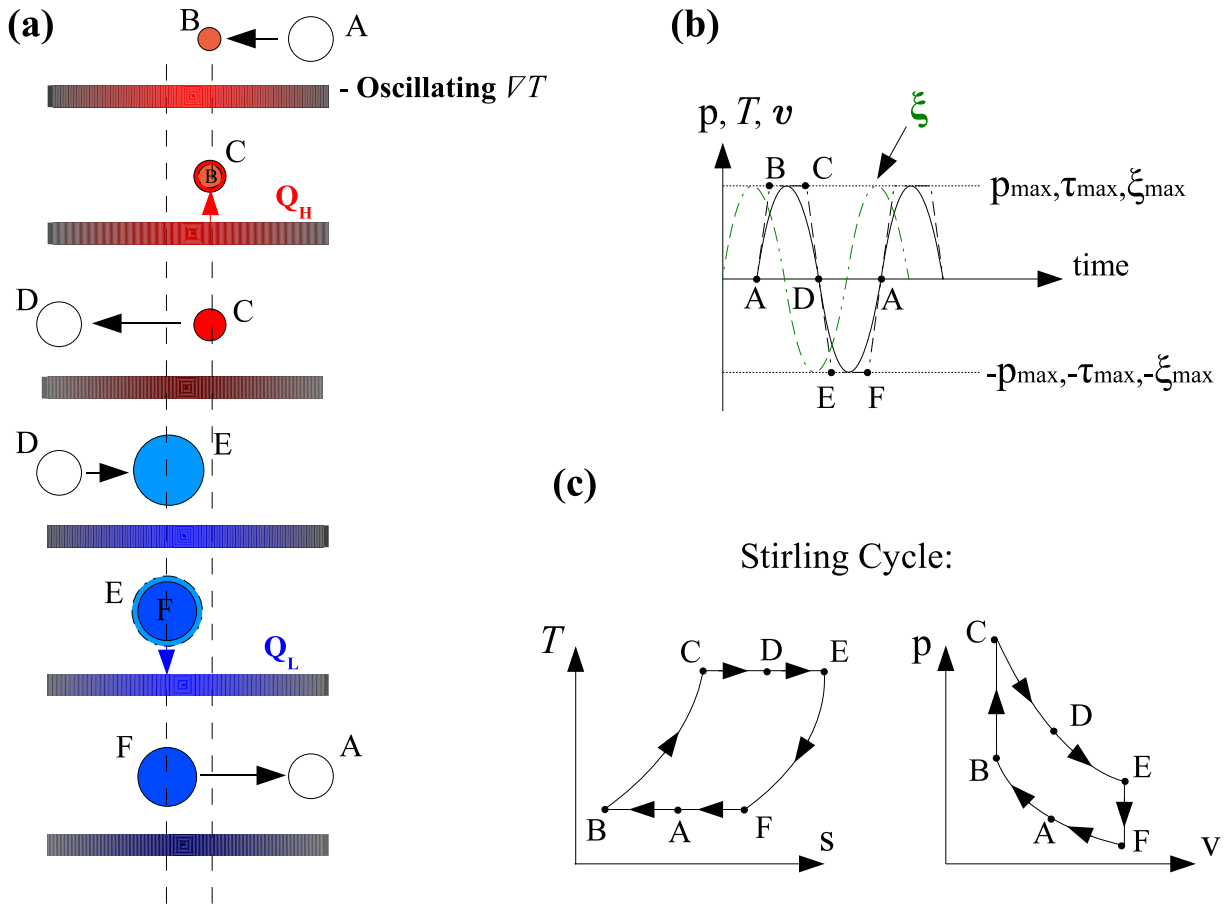

Figure 1.6: **(a)** Engine cycle followed by a fluid particle under the influence of an acoustic traveling wave in the vicinity of a solid wall which is subjected to a temperature gradient ∇T. **(b)** Sinusoidal and "articulated" time evolution, respectively represented by solid lines and dotted lines, of the acoustic variables of pressure (p), temperature (τ) and displacement (ξ) for an acoustic standing wave. **(c)** The ideal Stirling cycle with the corresponding states.

2 THERMOACOUSTIC PROCESSES: THE FUNDAMENTAL MODELING

This chapter deals with the analytical description of the thermoacoustic processes. Fundamental equations governing thermoacoustics are presented in Section 2.1. Then, analytical expressions are given for the transfer matrices of several acoustic two-ports submitted (Section 2.3) or not submitted (Section 2.2) to a temperature distribution. Lastly, Section 2.4 is devoted to the characteristic equation of a thermoacoustic device.

2.1 Fundamental equations of thermoacoustics

2.1.1 Primary equations of dissipative fluids

The movement of a fluid particle is described by the following set of equations:

- the conservation of mass equation,

$$\frac{\partial \rho}{\partial t} + \overrightarrow{\nabla} \cdot (\rho \vec{v}) = 0, \tag{2.1}$$

where ρ is the density of the fluid and $\vec{v}$ is the particle velocity,

- the Navier-Stokes vectorial equations expressing the conservation of momentum

$$\rho \frac{d\vec{v}}{dt} = -\overrightarrow{\nabla} p + \mu \overrightarrow{\nabla}^2 \vec{v} + \left(\mu_v + \frac{\mu}{3}\right) \overrightarrow{\nabla} (\overrightarrow{\nabla} \cdot \vec{v}), \tag{2.2}$$

where p is the acoustic pressure and where μ and μ_v are the dynamic shear and volume viscosities, respectively,

- and the equation of energy conservation

$$\rho T \frac{dS}{dt} = \overrightarrow{\bigtriangledown} \cdot (\lambda \overrightarrow{\bigtriangledown} T) + \overline{\overline{\sigma}} \cdot \bigtriangledown(\vec{v}) \tag{2.3}$$

where T is the temperature of the fluid, S is the entropy, λ represents the thermal conductivity of the fluid and $\overline{\overline{\sigma}}$ is the stress tensor.

These conservation equations (Eqs. (2.1) to (2.3)) are complemented by the following state relations considering the fluid as a perfect gas:

$$d\rho = -\frac{\rho}{T} dT + \frac{\gamma}{c_0^2} dp, \tag{2.4}$$

$$dS = \frac{C_p}{T} dT - \frac{1}{\rho T} dp, \tag{2.5}$$

where $\gamma = \frac{C_p}{C_v}$ is the polytropic coefficient of the fluid, where $c_0 = \sqrt{\frac{\gamma R_g T}{M_{mol}}}$ is the adiabatic speed of sound (M_{mol} being the molar mass of the fluid and $R_g = 8.314 J.mol^{-1}.K^{-1}$ red the perfect gas constant) and where C_p and C_v are the isobaric and the isochoric heat capacity of the fluid, respectively.

2.1.2 Simplifying hypotheses

It is considered that the acoustic propagation occurs in a cylindrical tube (corresponding, for example, to a stack pore). The diagram given in Fig. 2.1 shows the geometry of the problem considered. The coordinate x represents the direction of acoustic propagation in a volume of fluid located within a cylinder of radius R; y is the transversal coordinate, and r is the radial coordinate. In the following, the dimensionless transverse coordinate η is hereby introduced:

$$\eta = \frac{r}{R} \quad (0 \leq \eta \leq +1). \tag{2.6}$$

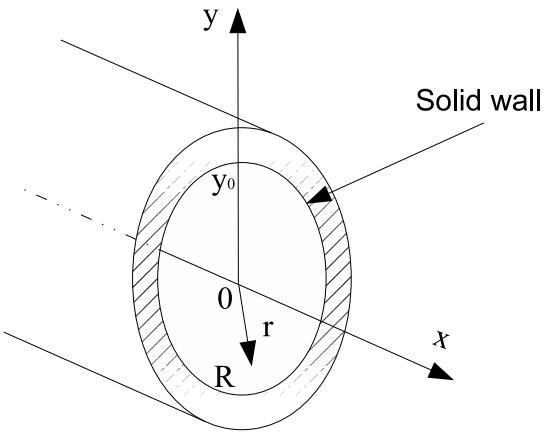

Figure 2.1: Coordinate system used for the problem modeling.

In order to obtain analytical expressions for the acoustic variables, a number of assumptions shall be formulated. In the framework of linear or weakly non-linear acoustics, the thermodynamic variables are expressed using a method of successive approximations in the form:

$$\xi = \xi_0 + \epsilon\xi_1 + \epsilon^2\xi_2 + O(\epsilon^3), \tag{2.7}$$

where ξ represents either the pressure p, the density ρ, the temperature T, the entropy S or the three components of the particle velocity $\vec{v}$, and where ϵ is a small parameter ($\epsilon \ll 1$) reflecting the magnitude of each term.

In Eq. (2.7), the zero-order terms are the static components of the thermodynamic variables. Among them, the static pressure p_0 is assumed to be constant and uniform, and the temperature $T_0(x)$ is assumed to be inhomogeneous in the x direction of wave propagation. The spatial temperature distribution also implies taking into account spatial variations of density $\rho_0(x)$ and entropy $S_0(x)$. Finally, the fluid is assumed initially at rest in the absence of acoustic disturbances so that $\vec{v_0} = \vec{0}$.

The first-order terms in Eq. (2.7) correspond to acoustic fluctuations, which are very low in comparison to the static components. Under the assumption of a harmonic plane wave propagating in the x direction and using the time convention $-i\omega t$, it is possible to write the acoustic variables as

$$p_1(x,t) = \Re\left\{\tilde{p}_1(x)e^{-i\omega t}\right\}, \tag{2.8}$$

for the acoustic pressure, and

$$\xi_1(x,\eta,t) = \Re\left\{\tilde{\xi}_1(x,\eta)e^{-i\omega t}\right\}, \tag{2.9}$$

where $\Re$ is "*the real part of*", and ξ_1 represents the acoustic part of either the density ρ_1, the temperature τ_1, the entropy s_1 or the three components of the particle velocity $\vec{v_1}$. In Eqs. (2.8) and (2.9), ω is the acoustic pulsation, and the symbol $\sim$ denotes for the complex amplitudes of the acoustic variables.

The second-order terms are not taken into account here, but must be considered to describe higher order effects, such as acoustic streaming (Bailliet *et al.*, 2001; Guedra, 2012b), for example.

At last, under the boundary layer approximation, the transverse component of the particle velocity is assumed to be very small compared to the longitudinal component ($|v_{1,\eta}| \ll |v_{1,x}|$), and longitudinal variations of variables $\xi_1(x,\eta)$ are assumed to be small compared to the transverse variations ($\partial_x \ll \partial_r$).

2.1.3 Propagation equation governing the acoustic pressure

According to the asumptions mentioned above, the Navier-Stokes equation, Eq. (2.2), applied to the x component of the particle velocity, $\tilde{v}_{1,x}$, reduces to

$$-i\omega\rho_0\tilde{v}_{1,x} = -\frac{\partial\tilde{p}_1}{\partial x} + \frac{\mu}{\eta}\frac{\partial}{\partial\eta}\left(\eta\frac{\partial\tilde{v}_{1,x}}{\partial\eta}\right). \tag{2.10}$$

Integrating Eq. (2.10) across the transverse variable, and taking into account a non-slip condition on the walls ($\tilde{v}_{1,x}(\eta=1)=0$), the solution of Eq. (2.10) for the longitudinal component of the acoustic velocity can be written as

$$\tilde{v}_{1,x}(x,\eta) = \frac{1}{i\omega\rho_0}\frac{\partial\tilde{p}_1}{\partial x}\left(1 - F_\nu(\eta)\right). \tag{2.11}$$

The function F_ν in Eq. (2.11) depends on the geometry under consideration and accounts for the viscous effects (Rott, 1980; Swift, 1988; Arnott *et al.*, 1991). In the particular case of a cylindrical guide of radius R, the function F_ν takes the form:

$$F_\nu(\eta) = \frac{J_0\left((1+i)\frac{\eta R}{\delta_\nu}\right)}{J_0\left((1+i)\frac{R}{\delta_\nu}\right)} \quad \text{pour} \quad 0 \leq \eta \leq 1, \tag{2.12}$$

where J_0 is the zero-order Bessel function of the first kind. Equivalent expressions for F_ν can be obtained for guides with other section geometries, like rectangular, triangular, or, specially, for stacked plates (Arnott *et al.*, 1991). Equation (2.12) introduces the critical parameter in thermoacoustics, namely the ratio between the hydraulic radius and the viscous penetration depth (the thermal penetration depth is analogous); in this case of the cylindrical pore, the hydraulic radius is taken into account by the transversal dimension R of the channel, and the viscous penetration depth $\delta_\nu = \sqrt{\frac{2\nu}{\omega}}$ depends on the frequency and on the kinematic viscosity of the fluid $\nu = \frac{\mu}{\rho_0}$.

The linearization of the equation of heat transfer, Eq. (2.3), and of the state equations, Eqs. (2.4) and (2.5), lead to expressions of the acoustic variables $\tilde{\tau}_1$, $\tilde{\rho}_1$ and $\tilde{s}_1$ as functions of the acoustic pressure and its spatial derivatives, as following:

$$\tilde{\tau}_1(x,\eta) = \frac{\tilde{p}_1}{\rho_0 C_p}\left[1 - F_\kappa(\eta)\right] - \frac{1}{\omega^2\rho_0}\frac{\partial\tilde{p}_1}{\partial x}\frac{\partial T_0}{\partial x}\left[1 - \frac{\sigma F_\nu(\eta) - F_\kappa(\eta)}{\sigma - 1}\right], \tag{2.13}$$

$$\tilde{\rho}_1(x,\eta) = \frac{\tilde{p}_1}{c_0^2}\left[1 + (\gamma-1)F_\kappa(\eta)\right] + \frac{1}{\omega^2}\frac{\partial\tilde{p}_1}{\partial x}T_0^{-1}\frac{\partial T_0}{\partial x}\left[1 - \frac{\sigma F_\nu(\eta) - F_\kappa(\eta)}{\sigma - 1}\right], \tag{2.14}$$

$$\tilde{s}_1(x,\eta) = -\frac{\tilde{p}_1}{\rho_0 T_0}F_\kappa(\eta) - \frac{C_p}{\omega^2\rho_0}\frac{\partial\tilde{p}_1}{\partial x}T_0^{-1}\frac{\partial T_0}{\partial x}\left[1 - \frac{\sigma F_\nu(\eta) - F_\kappa(\eta)}{\sigma - 1}\right], \tag{2.15}$$

where $\sigma = \frac{\nu}{\kappa}$ is the Prandtl number and where the function F_κ accounts for thermal effects. This function is defined analogously to F_ν [cf. Eq. (2.12) for a cylindrical guide], δ_ν being replaced by the thermal penetration depth $\delta_\kappa = \sqrt{\frac{2\kappa}{\omega}}$, where κ is the fluid thermal diffusivity.

At last, from Eqs. (2.11), (2.13), (2.14) and (2.15), and introducing thermo-viscous functions averaged over the guide transverse coordinate,

$$f_{\nu,\kappa} = 2\int_0^1 F_{\nu,\kappa}\eta d\eta, \tag{2.16}$$

the averaged acoustic variables are obtained in the following forms:

$$\langle\tilde{v}_{1,x}\rangle(x) = \frac{1}{i\omega\rho_0}\frac{\partial\tilde{p}_1}{\partial x}\left(1-f_\nu\right), \tag{2.17}$$

$$\langle\tilde{\tau}_1\rangle(x) = \frac{\tilde{p}_1}{\rho_0 C_p}\left[1-f_\kappa\right] - \frac{1}{\omega^2\rho_0}\frac{\partial\tilde{p}_1}{\partial x}\frac{\partial T_0}{\partial x}\left[1-\frac{\sigma f_\nu - f_\kappa}{\sigma-1}\right], \tag{2.18}$$

$$\langle\tilde{\rho}_1\rangle(x) = \frac{\tilde{p}_1}{c_0^2}\left[1+(\gamma-1)f_\kappa\right] + \frac{1}{\omega^2}\frac{\partial\tilde{p}_1}{\partial x}T_0^{-1}\frac{\partial T_0}{\partial x}\left[1-\frac{\sigma f_\nu - f_\kappa}{\sigma-1}\right], \tag{2.19}$$

$$\langle\tilde{s}_1\rangle(x) = -\frac{\tilde{p}_1}{\rho_0 T_0}f_\kappa - \frac{C_p}{\omega^2\rho_0}\frac{\partial\tilde{p}_1}{\partial x}T_0^{-1}\frac{\partial T_0}{\partial x}\left[1-\frac{\sigma f_\nu - f_\kappa}{\sigma-1}\right]. \tag{2.20}$$

In the case of a cylindrical guide, substituting F_ν (respectively F_κ) by its expression of Eq. (2.12) into Eq. (2.16) leads to the analytical expression for the thermo-viscous function f_ν (respectively f_κ):

$$f_{\nu,\kappa} = \frac{2\delta_{\nu,\kappa}}{(1+i)R}\frac{J_1\left((1+i)\frac{R}{\delta_{\nu,\kappa}}\right)}{J_0\left((1+i)\frac{R}{\delta_{\nu,\kappa}}\right)}, \tag{2.21}$$

where J_1 is the first-order Bessel function of first kind.

The substitution of Eqs. (2.17) and (2.19) into the equation of mass conservation of Eq. (2.1) linearized and averaged over the coordinate η leads to the propagation equation for sound pressure in a dissipative medium in the presence of a temperature gradient:

$$\frac{\partial^2\tilde{p}_1}{\partial x^2} + \left[\frac{\partial_x T_0}{T_0}\left(1+\frac{f_\kappa - f_\nu}{(\sigma-1)(1-f_\nu)}\right) - \frac{\partial_x f_\nu}{1-f_\nu}\right]\frac{\partial\tilde{p}_1}{\partial x} + k_0^2\left(\frac{1+(\gamma-1)f_\kappa}{1-f_\nu}\right)\tilde{p}_1 = 0, \tag{2.22}$$

where $k_0 = \frac{\omega}{c_0}$ represents the lossless wavenumber. This differential equation is equivalent to that given by Rott (1969) and Swift (1988, 2002) for an ideal gas and assuming that the fluid thermal effusivity is negligible compared with that of the solid. When the temperature distribution $T_0(x)$ is known, the solution of this differential equation can be obtained either numerically (Ward, 1994; Ward *et al.*, 2008) or analytically in an implicit form by transforming the equation (2.22) in a Volterra integral equation of the second kind (Gusev *et al.*, 2000; Job, 2001).

2.2 Analytical expressions for the transfer matrix of acoustic two-port

A thermoacoustic system can be seen as an assembly of several elements designated as *acoustic two-ports*. In its simplest arrangement, an engine is a combination of a thermoacoustic core (TAC) and a set of waveguides with various geometries (either cylindrical, rectangular, or another one). Each of these acoustic two-ports may be (or not) submitted to an inhomogeneous temperature distribution.

To describe the propagation of an acoustic wave in a thermoacoustic engine, each acoustic two-port may be characterized by its transfer matrix (Guedra, 2012a; Ueda, 2008; Tu *et al.*, 2003). In this section, the analytical expression of the transfer matrix is derived in the case of a straight duct, a porous material, and a tapered waveguide, as these are the classical two-ports generally used for the design of a themoacoustic engine. The temperature distribution along these elements is first considered homogeneous. The case of a non-uniform temperature distribution is treated in Sec. 2.3.

Surely, powerful thermoacoustic engines do not consist of only such basic elements. They also include parts of more complex geometries (Backhaus, 1999, 2000; Backhaus *et al.*, 2004), allowing either a diminution of nonlinear losses by means of semi-empirical design (jet pumps, tapered tubes) or the improvement of the efficiency the system. The experimental determination of the transfer matrix of such complex elements with a non-uniform temperature distribution is the subject of the next chapter.

2.2.1 Conventions

In the following, the longitudinal dimension of the two-port is denoted by d and the coordinate system is defined so that the entrance of the two-port is placed at the origin $x = 0$ and

its output at $x = d$, with the plane wave propagation following the $\vec{Ox}$ axis. As illustrated in Fig. 2.2, the volume velocity $\tilde{u}_{1,x}(0)$ at the entrance of the quadrupole is counted positive, while $\tilde{u}_{1,x}(d)$ is positive as well, but located at the exit (anti-symmetric orientation).

Figure 2.2: Adopted *pressure-volume velocity* convention for the quadripole description; anti-symmetric orientation.

The transfer matrix of the two-port corresponding to Fig. 2.2 is thus defined as following:

$$\begin{pmatrix} \tilde{p}_1(d) \\ \tilde{u}_{1,x}(d) \end{pmatrix} = \begin{pmatrix} a & b \\ c & d \end{pmatrix} \times \begin{pmatrix} \tilde{p}_1(0) \\ \tilde{u}_{1,x}(0) \end{pmatrix} = \mathbf{T} \times \begin{pmatrix} \tilde{p}_1(0) \\ \tilde{u}_{1,x}(0) \end{pmatrix}. \tag{2.23}$$

2.2.2 Case of a straight waveguide

The Equation (2.22) defined in Section 2.1 describes the propagation of a plane wave along the waveguide in the presence of a longitudinal temperature distribution. When the temperature profile is assumed to be constant and equal to the ambient temperature T_c ($\partial_x T_0 = 0$ and $\partial_x f_\nu = 0$ because the dynamic viscosity μ and the fluid density ρ_0 do not depend on x) this equation becomes

$$\frac{\partial^2 \tilde{p}_1}{\partial x^2} + k^2 \tilde{p}_1 = 0, \tag{2.24}$$

where the complex wavenumber

$$k = k_0 \sqrt{\frac{1 + (\gamma - 1) f_\kappa}{1 - f_\nu}} \tag{2.25}$$

takes into account the viscous-thermal coupling between the fluid and the waveguide walls by means of the f_ν and f_κ functions. The general solution of Eq. (2.24) is writing

$$\tilde{p}_1 = \tilde{A}e^{+ikx} + \tilde{B}e^{-ikx}. \tag{2.26}$$

Substituting this solution into Eq. (2.17) allows writing the axial component of the particle velocity averaged over the guide section in the form

$$\langle \tilde{v}_{1,x} \rangle = \frac{\sqrt{\frac{1+(\gamma-1)f_\kappa}{1-f_\nu}}}{\rho_0 c_0} (1 - f_\nu) \left(\tilde{A}e^{+ikx} - \tilde{B}e^{-ikx} \right). \tag{2.27}$$

Introducing the guide cross section S and knowing that $\tilde{u}_{1,x} = S\langle \tilde{v}_{1,x} \rangle$, the volume velocity is then given below

$$\tilde{u}_{1,x} = \frac{1}{Z_c} \left(\tilde{A}e^{+ikx} - \tilde{B}e^{-ikx} \right). \tag{2.28}$$

where Z_c is the characteristic complex impedance of the waveguide defined by

$$Z_c = \frac{\rho_0 c_0}{S\sqrt{(1 - f_\nu)(1 + (\gamma - 1)f_\kappa)}}. \tag{2.29}$$

Finally, Eqs. (2.26) and (2.28) expressed for $x = 0$ lead to the determination of the complex amplitudes $\tilde{A}$ and $\tilde{B}$:

$$\tilde{A} = \frac{\tilde{p}_1(0) + Z_c \tilde{u}_{1,x}(0)}{2}, \tag{2.30}$$

$$\tilde{B} = \frac{\tilde{p}_1(0) - Z_c \tilde{u}_{1,x}(0)}{2}. \tag{2.31}$$

Using these relations into Eqs. (2.26) and (2.28) expressed for $x = d$ allows to derive the analytical expression of the transfer matrix $\mathbf{T}$ of the guide below:

$$\mathbf{T} \equiv \begin{pmatrix} \cos(k_w d) & iZ_c \sin(k_w d) \\ iZ_c^{-1} \sin(k_w d) & \cos(k_w d) \end{pmatrix}. \tag{2.32}$$

2.2.3 Case of a porous element

To ensure a temperature gradient along the stack/regenerator, thermoacoustic engines often incorporate heat exchangers constituted of porous material which includes a heating or cooling system. Unlike the stack or the regenerator, the thermal gradient along the heat exchangers may be neglected in first approximation without implicating major errors in this modeling. Exchangers are generally modeled as porous elements at a constant hot or ambient temperature, which are respectively T_H or T_C.

The transfer matrix of such an element is deduced from the matrix of Eq. (2.32):

$$\mathbf{T} \equiv \begin{pmatrix} \cos(k_{eq} d) & iZ_{eq} \sin(k_{eq} d) \\ iZ_{eq}^{-1} \sin(k_{eq} d) & \cos(k_{eq} d) \end{pmatrix}. \tag{2.33}$$

Using the equivalent wavenumber

$$k_{eq} = k_0 \sqrt{\frac{1 + (\gamma - 1) f_\kappa^{(r_0)}}{1 - f_\nu^{(r_0)}}} \tag{2.34}$$

and the equivalent characteristic impedance

$$Z_{eq} = \frac{\rho_0 c_0}{\phi S \sqrt{(1 - f_\nu^{(r_0)})(1 + (\gamma - 1) f_\kappa^{(r_0)})}}, \tag{2.35}$$

where ϕ is the porosity and where the functions $f_\nu^{(r_0)}$ and $f_\kappa^{(r_0)}$ take into account the viscous-thermal coupling between the fluid and the pore walls of a characteristic transverse

dimension r_0. For example, in the case of a network of cylindrical pores, the analytical expressions of these functions are given by Eq. (2.21) replacing R by r_0.

2.2.4 Case of a tapered waveguide

Most studied thermoacoustic engines incorporate adaptive conical parts connecting waveguide sections (Chen, 1999; Backhaus, 2000; Biwa *et al.*, 2001; Yu *et al.*, 2003; Hao *et al.*, 2011). These conical parts affect the distribution of acoustic fields.

In accordance with the notations used so far, the cone is defined as a waveguide of radius R that varies linearly between $R_0 = R(0)$ and $R_d = R(d)$ (see Fig. 2.2). The analytical expression of the transfer matrix of a conical two-port can be found in the reference (Mechel, 2008) for different writing conventions than those adopted in this manuscript. For clarity, this analytical expression is rewritten from (Mechel, 2008) as:

$$\begin{pmatrix} a & b \\ c & d \end{pmatrix} \equiv \begin{pmatrix} \frac{z_1}{z_2}\cos(k_w d) + \dfrac{\sin(k_w d)}{k_w z_2} & iZ_c \frac{z_2}{z_1}\sin(k_w d) \\ iZ_c^{-1}\left[\frac{z_1}{z_2}\left(1+\frac{1}{k_w^2 z_1 z_2}\right)\sin(k_w d) - \left(1-\frac{z_1}{z_2}\right)\dfrac{\cos(k_w d)}{k_w z_2}\right] & \frac{z_2}{z_1}\cos(k_w d) - \dfrac{\sin(k_w d)}{k_w z_1} \end{pmatrix}, \tag{2.36}$$

with $z_1 = \frac{R_0}{R_0 - R_d} d$, $z_2 = z_1 + d$ and where the wave number k and the characteristic impedance Z_c are respectively given by equations Eq. (2.25) and Eq. (2.29) [with $S = \pi R_d^2$ in Eq. (2.29)]. However, it should be noted that Eq. (2.36), outcome from Mechel (2008) , is initially derived from the equation of Webster without loss. Taking into account the losses (which depend strictly on R) would imply to solve a wave equation similar to that of linear thermoacoustics [Eq. (2.22)], whose solution is more demanding than in Eq. (2.36). That means, in other words, that the analytical expression (2.36) is an approximation of acoustic propagation in a cone with parietal losses, with functions f_ν et f_κ performing in expressions (2.25) and (2.29) evaluated for $R = (R_0 + R_d)/2$.

2.3 Analytical expression for the transfer matrix of an acoustic two-port submitted to a non-uniform temperature distribution

To describe the propagation of harmonic plane waves in an acoustic two-port subject to an inhomogeneous distribution of temperature $T_0(x)$, the differential equation of second order, Eq. (2.22), with non-constant coefficients has to be solved. Gusev *et al.* proposed an exact analytical solution of this equation in the form of an infinite series of integral operators (Gusev *et al.*, 2000; Job, 2001; Penelet *et al.*, 2005b; Penelet, 2004). Them, Eq. (2.22) is rewritten as

$$\frac{\partial^2 \tilde{p}_1}{\partial x^2} + \frac{d\Phi_1}{dx}\frac{\partial \tilde{p}_1}{\partial x} + \left(\frac{\omega}{c_0}\right)^2 \Phi_0 \tilde{p}_1 = 0, \tag{2.37}$$

where $c_0 = c_0(T_c)$ is the adiabatic speed of sound at room temperature, and where the functions

$$\frac{d\Phi_1}{dx} = \frac{d_x T_0}{T_0}\left(1 + \frac{f_\kappa - f_\nu}{(\sigma - 1)(1 - f_\nu)}\right) - \frac{d_x f_\nu}{1 - f_\nu}, \tag{2.38}$$

$$\Phi_0 = \frac{T_c}{T_0}\left(\frac{1 + (\gamma - 1) f_\kappa}{1 - f_\nu}\right), \tag{2.39}$$

depend on x through the temperature T_0 (and thermophysical properties of the fluid).

Introducing the spatial variable ζ defined by

$$\frac{d\zeta}{dx} = \zeta_x = e^{(\Phi_1(0) - \Phi_1(x))}, \tag{2.40}$$

and the function

$$F(\zeta) = \Phi_0(x(\zeta))\zeta_x^{-2}, \tag{2.41}$$

the propagation Equation (2.37) becomes

$$\frac{d^2\tilde{p}_1}{d\zeta^2} + k_0^2 F(\zeta)\tilde{p}_1 = 0, \tag{2.42}$$

with $k_0 = \omega/c_0(T_c)$. By successive integrations of the coordinate ζ , Eq. (2.42) is rewritten in the form of a system of integral equations

$$\tilde{p}_1(\zeta) = \tilde{p}_1(0) + \int_0^\zeta \frac{d\tilde{p}_1}{d\zeta'} d\zeta', \tag{2.43}$$

$$\frac{d\tilde{p}_1}{d\zeta} = \left.\frac{d\tilde{p}_1}{d\zeta}\right|_0 - k_0^2 \int_0^\zeta F(\zeta')\tilde{p}_1(\zeta')d\zeta'. \tag{2.44}$$

In this system of equations the two integral operators can be noted

$$\Omega_1(y) \equiv ik_0 \int_0^\zeta F(\zeta')y(\zeta')d\zeta', \tag{2.45}$$

$$\Omega_2(y) \equiv ik_0 \int_0^\zeta y(\zeta')d\zeta'. \tag{2.46}$$

Finally, using successive approximations to calculate the terms on the left of Eqs. (2.43) and (2.44), the exact solution of this system can be written in matrix form showing infinite series of operators Ω_1 and Ω_2 (Penelet *et al.*, 2005b; Penelet, 2004):

$$\begin{pmatrix} \tilde{p}_1(\zeta) \\ \frac{d\tilde{p}_1}{d\zeta}(\zeta) \end{pmatrix} = \begin{pmatrix} \sum_{n=0}^{\infty} (\Omega_2\Omega_1)^n & \frac{\Omega_2}{ik_0}\sum_{n=0}^{\infty} (\Omega_1\Omega_2)^n \\ ik_0\Omega_1 \sum_{n=0}^{\infty} (\Omega_2\Omega_1)^n & \sum_{n=0}^{\infty} (\Omega_1\Omega_2)^n \end{pmatrix} \times \begin{pmatrix} \tilde{p}_1(0) \\ \frac{d\tilde{p}_1}{d\zeta}(0) \end{pmatrix}, \tag{2.47}$$

where the terms of the infinite series are defined in the following way [1]:

[1] It is important to note that, with a gradient of non-zero temperature, the integral operators Ω_1 and Ω_2 are not commutative and the diagonal elements of the matrix defined by (2.47) are not equal. However, this equality appears when $d_x T_0 = 0$, particular case where Ω_1 and Ω_2 are set to a multiplicative constant.

$$(\Omega_2\Omega_1)^n\, y = \underbrace{\Omega_2\Big(\Omega_1\Big(\ldots\Omega_2\big(\Omega_1(y)\big)\Big)\Big)}_{n \text{ times}}. \tag{2.48}$$

By using the relation of Eq. (2.17) from Chapter 1 for the average particle velocity and Eq. (2.40) equation, it results:

$$\frac{d\tilde{p}_1}{d\zeta} = ik_0 \frac{\rho_0 c_0}{S\,(1-f_\nu)} \zeta_x^{-1} \tilde{u}_{1,x}, \tag{2.49}$$

what allows to rewrite Eq. (2.47) in terms of acoustic pressure and volume velocity, and thus obtain the exact two-port analytical expression in the form

$$\begin{pmatrix} a & b \\ c & d \end{pmatrix} \equiv \begin{pmatrix} \sum_{n=0}^{\infty} (\Omega_2\Omega_1)^n & Z(0)\Omega_2 \sum_{n=0}^{\infty} (\Omega_1\Omega_2)^n \\ \frac{\Omega_1\zeta_x}{Z(x)} \sum_{n=0}^{\infty} (\Omega_2\Omega_1)^n & \frac{Z(0)\zeta_x}{Z(x)} \sum_{n=0}^{\infty} (\Omega_1\Omega_2)^n \end{pmatrix}, \tag{2.50}$$

wherein the amount $Z(x)$ is defined by

$$Z(x) = \frac{\rho_0(x) c_0}{S\,(1-f_\nu)}. \tag{2.51}$$

The Eq. (2.50) is valid either for a stack or the passive part of the core, simply evaluating the thermo-viscous functions for a narrow channel of radius r_1 or a wide channel of radius R, respectively (with $S \mapsto \phi S$ for a porous element). It should be noted that the Eq. (2.50) for a wide guide or a stack tends to asymptotically approach the expressions (2.32) and (2.33) when the temperature is constant along the two-port.

2.4 Characteristic equation of a thermoacoustic device

2.4.1 Case of a standing-wave thermoacoustic engine

Standing-wave thermoacoustic systems generally consist of a straight waveguide wherein the resonance of a fluid column occurs, and also of heat exchangers, as represented in the fol-

lowing (Fig. 2.3). These systems are simple and reliable, but not efficient. Although they are of little interest for industrial applications because of their low yield, the study of those systems is essential from an academic point of view, to better understand the complex phenomena involved in the thermoacoustic operating machines.

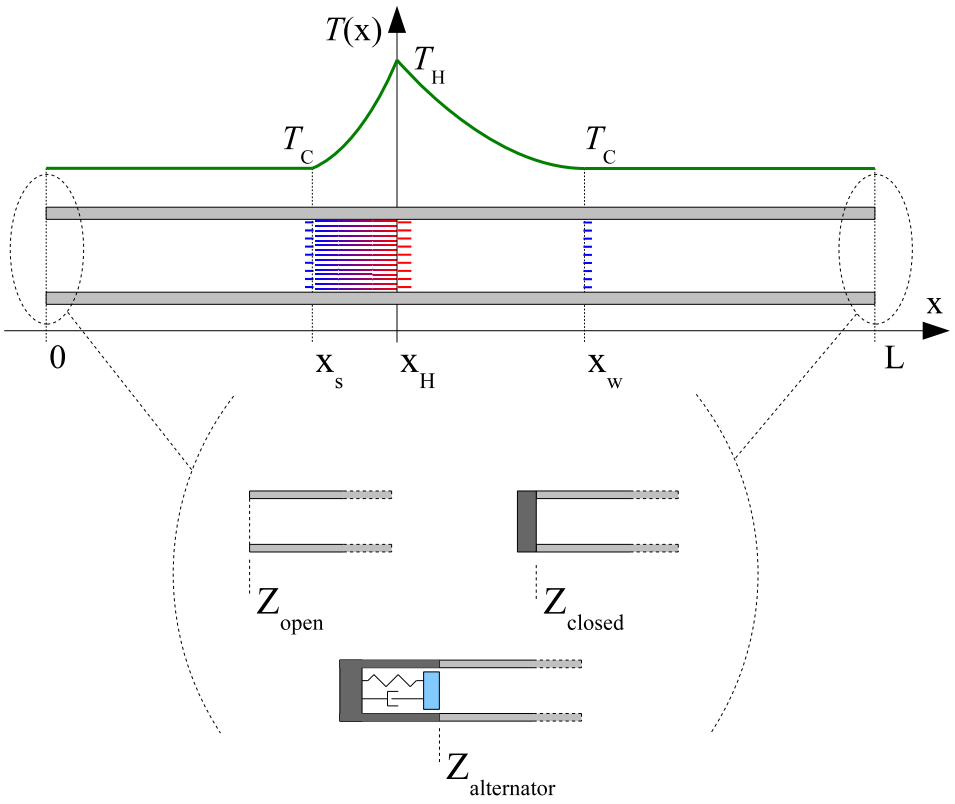

Figure 2.3: (a) Sketch of a standing-wave thermoacoustic engine. (b) Open end. (c) Closed end. (d) Coupling with a electrodynamic alternator.

The low performance of standing-wave engines is implicitly associated to the stationary nature of the fluid particle oscillation in the vicinity of the solid wall. Indeed, such acoustic cycle consists of thermodynamic processes similar to those of a Brayton cycle (adiabatic compression - isobaric expansion - adiabatic expansion/relaxation - isobaric contraction), whose performance is intrinsically lower than that of Carnot type. Therefore, to approach what would be considered adiabatic processes, an imperfect thermal contact between the fluid and solid walls is required. To optimize such imperfection in favor of cycle performance, a trade-off between the particle speed and its position in the thermal and viscous boundary layers shall be found, as they are inversely proportional. Employing a stack in these machines requires the pore radius to be of the order of magnitude of a thermal penetration depth ($r_s \sim \delta_\kappa$). This type of engine has been extensively studied in the literature (Swift, 2002, 1988, 1992; Atchley, 1992; Atchley *et al.*, 1992; Atchley, 1994b; Chen, 1999; Hao *et al.*, 2011) and, although being potentially less

attractive than the traveling-wave system, it still remains explorable even if the investigation involves complex acoustic phenomena of difficult theoretical prediction.

Using the formalism of transfer matrices, it is possible to write the equation relating the acoustic pressure and flow at $x = 0$ and $x = L$ in the form:

$$\begin{pmatrix} \tilde{p}_1(L) \\ \tilde{u}_{1,x}(L) \end{pmatrix} = \mathbf{T_r} \times \mathbf{T_{TAC}} \times \mathbf{T_l} \times \begin{pmatrix} \tilde{p}_1(0) \\ \tilde{u}_{1,x}(0) \end{pmatrix}, \tag{2.52}$$

where $\mathbf{T_l}$ and $\mathbf{T_r}$ are the transfer matrices of the tube portions at ambient temperature T_c, respectively at left and right side of the thermoacoustic core, and where $\mathbf{T_{TAC}}$ is the transfer matrix of the thermoacoustic core (i.e. the part of the system subjected to an inhomogeneous distribution temperature), which is defined as follows:

$$\mathbf{T_{TAC}} \equiv \begin{pmatrix} \mathcal{T}_{pp}(\omega, T_0(x)) & \mathcal{T}_{pu}(\omega, T_0(x)) \\ \mathcal{T}_{up}(\omega, T_0(x)) & \mathcal{T}_{uu}(\omega, T_0(x)) \end{pmatrix}. \tag{2.53}$$

The transfer matrix $\mathbf{T_{TAC}}$ depends on the geometric and thermophysical properties of the thermoacoustic core that are linked to its constitutive elements, namely stack, passive part, and heat exchangers. Nevertheless, it also depends on other factors such as temperature distribution $T_0(x)$ along both stack ($x \in [x_s, x_h]$) and passive part ($x \in [x_h, x_w]$), and on the acoustic pulsation ω. When the temperature distribution is known, $\mathbf{T_{TAC}}$ can be obtained theoretically (Job, 2001; Penelet *et al.*, 2005b; Penelet, 2004), as it has been presented in the last section. However, this matrix can also be measured under different heating conditions, as it will be shown and explored in Chapter 3.

2.4.2 Case of a traveling-wave thermoacoustic engine

The so-called *traveling-wave* thermoacoustic systems are characterized by the presence of a feedback loop favoring the amplification of traveling waves. These machines evoke the interest of the thermoacoustician community mostly by reason of their performances, often much higher than those which could be reached by an equivalent *standing-wave* system. This potentially high return is a result of the thermodynamic cycle to which the fluid particle is subjected. Its movement near a solid wall approximately follows the Stirling cycle, whose ideal efficiency

is that of Carnot's. Therefore, the thermodynamic processes involved in this cycle (isothermal compression - isochoric warming - isothermal expansion - isochoric cooling) are of interest to approximate the reversibility as much as possible. This is the key factor that distinguishes traveling-wave from standing-wave engines, as the latter relies instead on intrinsic irreversibility (Subsection 2.4.1). To enhance the heat transfer efficiency, the traveling wave systems require the porous material to have its average pore radius very small compared to the thermal penetration depth ($r_s \ll \delta_\kappa$), so that to approach the heat transfer process to an isothermal contact between the fluid particle and the pore internal wall. Besides, this porous material shall have an adequately higher thermal conductivity than that of a stack (applied in standing wave systems), to allow alternate heat storing and delivering during the acoustic cycle, perfoming hence as a regenerator.

Many engine configurations promoting the triggering of progressive wave are possible, and the more conventional one uses a annular resonator (Fig. 2.4-(a,b)). In 1979, P. Ceperley was the first to propose this idea to demonstrate the possibility of developing thermoacoustic Stirling engines (Ceperley, 1979); he did not appreciate the second-order flow (Gedeon) that would render his incarnations inoperable. Since then, this type of engine has been extensively studied (Ceperley, 1985; Yazaki *et al.*, 1985). In 1999, Backhaus *et al.* were successful in developing a prototype of thermoacoustic Stirling engine wherein the feedback loop is coupled to a straight resonator (Backhaus, 1999, 2000). A few years later, Backhaus *et al.* (2004) also developed a thermo-acoustic-electric transducer prototype, wherein the acoustic-electric conversion is performed by a linear electrodynamic alternator coupled to the annular resonator. Finally, Fig. 2.4-(c) shows a schematic version of a co-axial (Bastyr, 2003) system in which the feedback loop is formed by placing a core in the thermoacoustic tube of largest section.

Traveling-wave systems are here described analogously to the case of standing-wave, as previously in Subsection 2.4.1. Neglecting the effects on the wave propagation due the waveguide curvature, the annular thermoacoustic system shown in 2.4-(a) is also described by Eq. (2.52), except that the positions $x = 0$ and $x = L$ correspond in reality to the same location, as they meet each other in a loop (Fig. 2.4-(a)). Hence, taking into account this continuity conditions as below

$$\tilde{p}_1(0) = \tilde{p}_1(L), \tag{2.54}$$

$$\tilde{u}_{1,x}(0) = \tilde{u}_{1,x}(L), \tag{2.55}$$

and making the substitution into Eq. (2.52), it results in the following:

$$\begin{pmatrix} \tilde{p}_1(L) \\ \tilde{u}_{1,x}(L) \end{pmatrix} = \mathbf{T_r} \times \mathbf{T_{TAC}} \times \mathbf{T_l} \times \begin{pmatrix} \tilde{p}_1(L) \\ \tilde{u}_{1,x}(L) \end{pmatrix}. \tag{2.56}$$

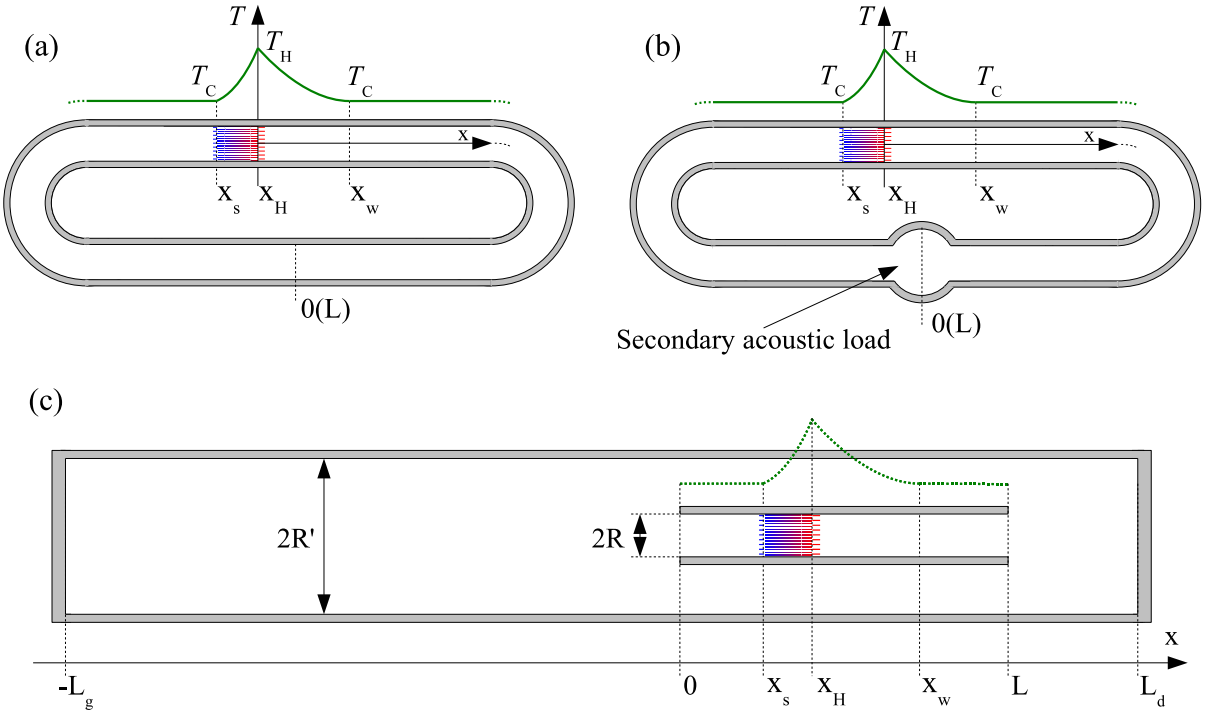

Figure 2.4: Schematic representations of traveling-wave thermoacoustic engines. (a) Annular resonator. (b) Annular resonator coupled to a secondary acoustic load (secondary resonator, electrodynamic alternator, or any other load). (c) Co-axial resonator.

When a secondary element is coupled to the loop [cf. Fig. 2.4-(b)], the conservation of acoustic pressures and volume velocity between $x = 0$ and $x = L$ leads in this case to:

$$\tilde{p}_1(0) = \tilde{p}_1(L), \tag{2.57}$$

$$\tilde{u}_{1,x}(0) = \tilde{u}_{1,x}(L) - Y_{ch}\tilde{p}_1(L), \tag{2.58}$$

where Y_{ch} is the acoustic admittance presented by the secondary load. This admittance can be that of a closed tube, an electrodynamic alternator, or a combination of any acoustic element characterized by its reduced admittance. Relations (2.57) and (2.58) introduced in Eq. (2.56) then lead to:

$$\begin{pmatrix} \tilde{p}_1(L) \\ \tilde{u}_{1,x}(L) \end{pmatrix} = \mathbf{T_r} \times \mathbf{T_{TAC}} \times \mathbf{T_l} \times \begin{pmatrix} 1 & 0 \\ -Y_{ch} & 1 \end{pmatrix} \times \begin{pmatrix} \tilde{p}_1(L) \\ \tilde{u}_{1,x}(L) \end{pmatrix}. \tag{2.59}$$

At last, in the case of a co-axial system [cf. Fig. 2.4-(c)], Eq. (2.52) establishes the relation between acoustic pressure and volume velocity at the extremities of the tube of small section S. The continuity relations expressed at $x = 0$, on the one hand,

$$\tilde{p}_1(0) = \tilde{p}_a(0), \tag{2.60}$$
$$\tilde{u}_{1,x}(0) = Y_g \tilde{p}_a(0) - \tilde{u}_{a,x}(0), \tag{2.61}$$

and at $x = L$, on the other hand,

$$\tilde{p}_1(L) = \tilde{p}_a(L), \tag{2.62}$$
$$\tilde{u}_{1,x}(L) = Y_d \tilde{p}_a(L) - \tilde{u}_{a,x}(L), \tag{2.63}$$

involve the acoustic pressure $\tilde{p}_a$ and the volume velocity $\tilde{u}_{a,x}$ in the peripheral ring of section $S_A = \pi(R'^2 - R^2)$ and the admittances Y_g and Y_d of the large section tubes $S_L = S_A + S$ and of respective lengths l_g and l_d:

$$Y_{g,l} = -iZ_c^{(L)} \cot(k^{(L)} l_{g,d}). \tag{2.64}$$

From Eqs. (2.60) to (2.63) and the transfer matrix of the peripheral ring denoted $\mathbf{T_A}$, a second matrix equation relating the acoustic pressure and speed in $x = 0$ and $x = L$ is then obtained as:

$$\begin{pmatrix} \tilde{p}_1(0) \\ \tilde{u}_{1,x}(0) \end{pmatrix} = \begin{pmatrix} 1 & 0 \\ Y_g & -1 \end{pmatrix} \times \mathbf{T_A}^{-1} \times \begin{pmatrix} 1 & 0 \\ Y_d & -1 \end{pmatrix} \times \begin{pmatrix} \tilde{p}_1(L) \\ \tilde{u}_{1,x}(L) \end{pmatrix}, \tag{2.65}$$

where the inverse matrix $\mathbf{T_A}$ is introduced here to meet the x-axis and the conventions defined in Subsection 2.2.1. It should be noted that the matrix $\mathbf{T_A}$, when symmetrical and reciprocal, has its inverse well defined. Substituting Eq. (2.65) into Eq. (2.52) leads to the following equation:

$$\begin{pmatrix} \tilde{p}_1(L) \\ \tilde{u}_{1,x}(L) \end{pmatrix} = \mathbf{T_r} \times \mathbf{T_{TAC}} \times \mathbf{T_l} \times \begin{pmatrix} 1 & 0 \\ Y_g & -1 \end{pmatrix} \times {\mathbf{T_A}}^{-1} \times \begin{pmatrix} 1 & 0 \\ Y_d & -1 \end{pmatrix} \times \begin{pmatrix} \tilde{p}_1(L) \\ \tilde{u}_{1,x}(L) \end{pmatrix}. \tag{2.66}$$

To conclude, regardless of the kind of system involved in the equations (2.56), (2.59) or (2.66), there can be identified an expression of a transfer matrix that embraces $\mathbf{T_{TAC}}$ and also connects the complex amplitudes of acoustic pressure and volume velocity to the same position $x = L$ by means of using the relation (2.52), thus completing a feedback loop. Equations (2.56), (2.59) and (2.66) may be written in the following general form:

$$\begin{pmatrix} \tilde{p}_1(L) \\ \tilde{u}_{1,x}(L) \end{pmatrix} = \begin{pmatrix} \mathcal{M}_{pp}(\omega, T_0(x)) & \mathcal{M}_{pu}(\omega, T_0(x)) \\ \mathcal{M}_{up}(\omega, T_0(x)) & \mathcal{M}_{uu}(\omega, T_0(x)) \end{pmatrix} \times \begin{pmatrix} \tilde{p}_1(L) \\ \tilde{u}_{1,x}(L) \end{pmatrix}, \tag{2.67}$$

equation admitting a non-trivial (non-zero) solution if and only if the determinant of the matrix

$$\begin{pmatrix} \mathcal{M}_{pp} & \mathcal{M}_{pu} \\ \mathcal{M}_{up} & \mathcal{M}_{uu} \end{pmatrix} - \mathbf{I_2} \tag{2.68}$$

is zero, where $\mathbf{I_2}$ is the identity matrix 2×2. That leads to the characteristic equation of the system:

$$1 + \mathcal{M}_{pp}\mathcal{M}_{uu} - \mathcal{M}_{pu}\mathcal{M}_{up} - (\mathcal{M}_{pp} + \mathcal{M}_{uu}) = 0. \tag{2.69}$$

3 EXPERIMENTAL CHARACTERIZATION OF THE THERMOACOUSTIC CORE

Even below the threshold of thermoacoustic instability, the theoretical description of acoustic propagation and heat transfer through the thermoacoustic core (TAC) is anything but simple. This is essentially due to the fact that thermoacoustic engines make use of geometrically complicated materials (piles of stainless steel meshes, metallic foams) whose thermophysical parameters are unknown. Moreover, the accuracy of the description of acoustic propagation through the TAC also depends critically on the shape of the temperature field within the TAC, the latter being very difficult to describe theoretically. Therefore, alternative methods allowing the description of the TAC are presented in this chapter. These methods consist of measuring the transfer matrix of the TAC, and the experimental data being used afterwards for the theoretical description of thermoacoustic engines. Three different methods are presented in this chapter. First, the so-called "two-load method" previously used by Guedra *et al.* (2011) is presented and it is shown that this method becomes inaccurate when the TAC is a regenerator-based one (Section 3.3). Then, two alternative experimental approaches are presented: a two-load method with TAC inversion (Section 3.4) and a new "impedance" method based on the measurement of the impedance matrix of the TAC by means of an acoustic impedance sensor (Section 3.6). In particular it is shown that the impedance method allows accurate descriptions of both stack-based TAC and regenerator-based TAC. Otherwise, it must be noted that, in essence, all three methods consist likewise in acoustic impedance measurements and require measurements under two different acoustic conditions. In spite of this, for simplicity of identification, these three methods are here called as stated above.

3.1 Description of the TAC under study

An approximate scale plan of the thermoacoustic core under study is presented in Fig. 3.1: its total length is $464\,mm$ with an inner radius of $16.9\,mm$. The active part is made of a roughly $70\,mm$ long stack/regenerator (sometiles combined with ceramic washers) bounded by a hot heat exchanger (HHX) and an ambient heat exchanger (AHX), on opposite sides. The passive part is the waveguide part set between the HHX and a secondary AHX. The geometrical properties of the sample materials used for the stack/regenerator in this study are reported in Tab. 3.1. With regards to the transversal dimensions, all are cylindrical and fit quite well the internal diameter of the stack holder, which is around $33.9\,mm$. The two AHX are made up of two copper pipes passing through a honeycombed aluminum disk, with flowing water inside the

pipes at room temperature. The HHX is made up of a sample of ceramic catalyst 900 cpsi (cells per square inch) in which a Nichrome resistance wire is coiled. The thickness of this sample is $10\,mm$ and the heat resistance wire is connected to an electrical DC power supply controlling the heat power Q_H dissipated by Joule effect throughout the wire. In order to avoid electric contact between the Nichrome resistance of the HHX and the stack/regenerator when made up of a conductive material, ceramic washers are placed between them. These washers are also sculpted from pieces of ceramic catalyst of 900 cpsi mesh size. Their lengths are adjusted to better fit all pieces together in the stack holder. In the case of the Stainless Steel Grids, two washers are necessary, one at each material side, to stabilize the grids assembling.

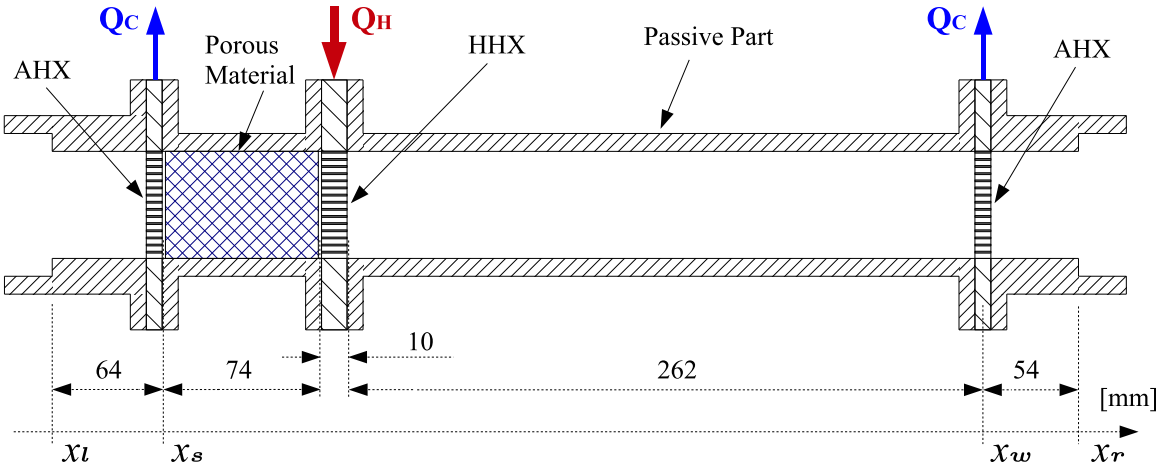

Figure 3.1: Approximate scale plan of the ThermoAcoustic Core.

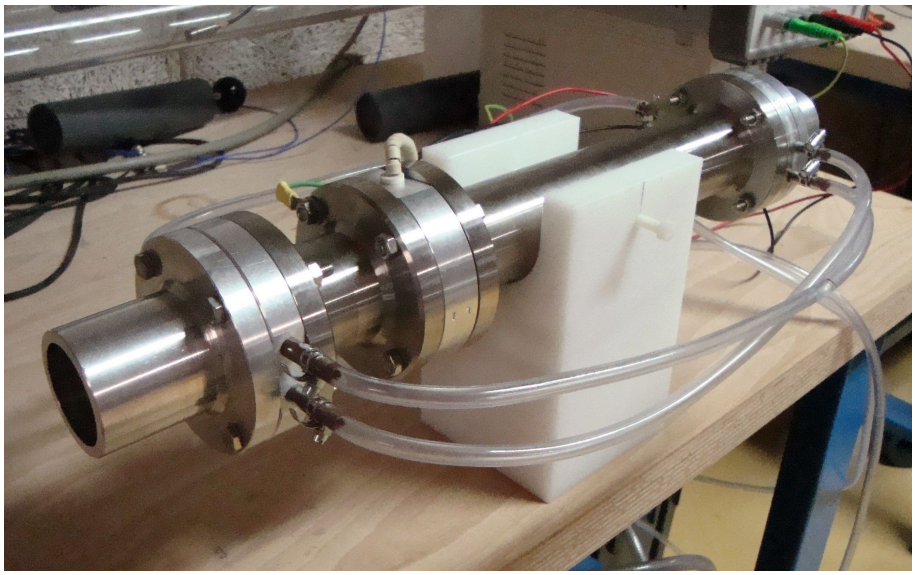

Figure 3.2: ThermoAcoustic Core.

Ceramic Catalyst	
Porosity	83 %
Number of cells per square inch	600 cpsi
Length	72.49 mm
Stainless Steel Grids[†]	
Porosity	50 %
Wire mesh diameter	0.08 mm
Number of meshes per inch	93.36
Length	60 mm + 2 ceramic washers (7 and 6mm)
Nichrome Foam[‡]	
Specific surface area	$2800\,\mathrm{m}^2/\mathrm{m}^3$
Average pore radius	0.6 mm
Length	63 mm + ceramic washer (4mm)
RVC Foam[♯]	
Porosity	96.5 %
Number of pores per inch	100 ppi
Length	68 mm + ceramic washer (3mm)

[†] http://www.gantois.fr, product ref. 104696

[‡] http://www.recemat.nl, product ref. RCM.NCAX.2733

[♯] http://www.goodfellow.com

Table 3.1: Geometrical properties of the sample materials.

In the following, the objective is to measure each coefficient of the transfer matrix of the thermoacoustic core as a function of both angular frequency ω and heat power supply Q_H. The transfer matrix $\mathbf{T}_{\mathrm{TAC}}\left(\omega, Q_H\right)$ is defined as

$$\begin{aligned}\begin{pmatrix} \widetilde{p}_r \\ \widetilde{u}_r \end{pmatrix} &= \begin{pmatrix} \mathcal{T}_{pp} & \mathcal{T}_{pu} \\ \mathcal{T}_{up} & \mathcal{T}_{uu} \end{pmatrix} \times \begin{pmatrix} \widetilde{p}_l \\ \widetilde{u}_l \end{pmatrix} \\ &= \mathbf{T}_{\mathrm{TAC}} \times \begin{pmatrix} \widetilde{p}_l \\ \widetilde{u}_l \end{pmatrix}, \end{aligned} \tag{3.1}$$

where $\widetilde{p}_{l,r} = \widetilde{p}(x_{l,r})$ and $\widetilde{u}_{l,r} = \widetilde{u}(x_{l,r})$ are the complex amplitudes of acoustic pressure p and acoustic volume velocity u at both ends $x = x_l$ (left) and $x = x_r$ (right) of the TAC (see Fig. 3.1). The positions x_l and x_r are considered attached to the TAC no mattering whether it is inverted or not with respect to its longitudinal axis.

3.2 Common features

The three approaches considered in this chapter allow the measurement of the $\mathbf{T}_{\mathrm{TAC}}$ coefficients as functions of both angular frequency ω and heat power supply Q_H: $Tpp(\omega, Q_H)$, $Tpu(\omega, Q_H)$, $Tup(\omega, Q_H)$ and $Tuu(\omega, Q_H)$. In the following, whatever the method considered, each set of coefficient measurements covers the whole range of frequencies of interest for each specific thermal condition Q_H, arbitrarily established. In the case of $Q_H = 0$, it is expected the TAC to be reciprocal, meaning that the determinant of its T-matrix equals 1. Therefore, the more $\det(\mathbf{T}_{\mathrm{TAC}})$ approaches the unity, the better the measurements quality is. The reciprocity can be evaluated for each frequency, leading to the average value $\mathbf{rc}$ of reciprocity defined as

$$\mathbf{rc} = \frac{\sum_{i=1,\ldots,N} \mathcal{T}_{pp}\left(\omega_i, 0\right) \mathcal{T}_{uu}\left(\omega_i, 0\right) - \mathcal{T}_{pu}\left(\omega_i, 0\right) \mathcal{T}_{up}\left(\omega_i, 0\right)}{N}, \tag{3.2}$$

where ω_i is the i^{th} value of the operating frequency, and N is the number of operating frequencies in the range of analysis. The standard deviation $\sigma_{\mathbf{rc}}$ of $\mathbf{rc}$ is also evaluated. These statistical values are the quality parameters to be accomplished in this experimental investigation, taking as references their ideal values: 1 for $\mathbf{rc}$, and 0 for $\sigma_{\mathbf{rc}}$. A discrepancy of $\mathbf{rc}$ from 1 means a deviation of *bias*, typically related to an inhomogeneous temperature profile and/or to the sensitivity to a significant propagation of numerical errors in the course of the data post-processing. On the other hand, a discrepancy of $\sigma_{\mathbf{rc}}$ from 0 is independent of the thermal profile and it is an indicator of *noise*, which may be caused by either an external interference or/and a significant numerical sensitivity, alike the *bias* case. By experience, an $\mathbf{rc}$ within 1 percent of the ideal unity and a $\sigma_{\mathbf{rc}}$ within 0.01 suggest the quality of measurement is acceptable.

However, when additional energy besides acoustical is inserted into the system, for example, thermal energy for, there is no longer unitary reciprocity. The more the temperature profile turns inhomogeneous with an increasing heat power input, the greater the gap between the resulted determinant and unity becomes. Hence, the reciprocity as a parameter of quality can only be usefully exploited if obtained from measurements with no heat supply, and, as much as possible, at a well established time-invariant and constant temperature profile along the TAC, so that the ideal unitary determinant can be pursued.

It is worth noting that the level of acoustic pressure in the TAC must be relatively small so as not to generate non-linear effects or thermoacoustically induced temperature gradient along the TAC.

In the following, it is assumed that the subsequent measurements with heating input can be performed at the same level of quality for their corresponding $\mathbf{T}_{\mathrm{TAC}}$ coefficients than the one achieved without heating, even though there is no longer a clear reference such as reciprocity. This assumption is grounded in the fact that, with or without heating supply, the whole setup and measurements are proceeded in the same way and standards for each approach. However, besides those common procedures, heated measurements also require the establishment of a steady-state regime along all measurements - at least to a satisfactory level - to maintain the quality concerns. Thus, the transitory thermal effects due to the imposed variations on Q_H, and also due to the cooling system interaction, are to be considered. They are investigated in Appendix A, and the resulting guidelines are followed in all measurements henceforth.

Framework solution for the two-port system

The experimental characterization of the TAC is based on the determination of the four coefficients of the transfer matrix, for given ω and Q_H, from the measurement of $\widetilde{p}_{l,r}$ and $\widetilde{u}_{l,r}$, according to Eq. (3.1). However, this measurement leads to a set of two equations with four unknown coefficients, what compels another set of two to fulfill the deterministic system requirements. Such algebraic constraints work either way for the other possible connecting matrices, namely diffusion, admittance and impedance, as stated in the two-port theory. Therefore, those connecting matrices are different ways to describe the same system, and they are interchangeable, thus allowing searches for the transfer matrix from different approaches. Another theoretical aspect to be illuminated is that the need for two measurements vanishes if the system is symmetrical. However, this is not the case for the TAC under investigation, as the porous material is located in a non-symmetrical position with respect to the TAC axis (see Fig. 3.1); moreover, the HHX is another element also asymmetrically placed, what enhances this resolution.

Essentially, one must proceed with two set of measurements to characterize a non-symmetrical system, no matter what kind of connecting matrix is sought. Such conceptual statements suggest that this need depends on the method or strategy to achieve $\mathbf{T}_{\mathrm{TAC}}$. Consequently, all three experimental approaches treated here end up within this frame.

3.3 First approach: the Two-Load Method - about its failure

The "Two-Load Method" is the method previously used by Guedra *et al.* (2011) to evaluate the experimental transfer matrix of a stack-based TAC. It consists of a classical experimental procedure for the acoustic characterization where a four-microphone method is used to obtain the four coefficients of the transfer matrix $\mathbf{T}_{\mathrm{TAC}}(\omega, Q_H)$ on a given frequency range and for various heating conditions (Boden, 1986; Munjal, 1987). The same experimental apparatus and most of the setup procedures used by Guedra *et al.* (2011) are implemented in the frame of the present work. The aim of this first approach is twofold: First, it is to check the repeatability of this measurement technique for a stack-based TAC. Second, it is to test the applicability of the Two-Load Method for a regenerator-based TAC, exhibiting high acoustic reflectivity and low transmissibility.

3.3.1 Principle of the method

A schematic view of the measurement system is given in Fig. 3.3. Two straight ducts are connected on either side of the TAC. The left tube is connected to an electrodynamic loudspeaker. Four microphones are set along the two waveguides at positions x_i with $i = 1, 2, 3, 4$. The $\mathbf{T}_{\mathrm{TAC}}$ coefficients are obtained using Eq. (3.1). Thus, the principle of the method consists of calculating the complex amplitudes of $\widetilde{p}_{l,r}$ and $\widetilde{u}_{l,r}$, from the pressure measurements at positions x_i. However, it is clear that the relation of Eq. (3.1) is a system of two equations with four unknowns. Two measurements are required to get the four transfer coefficients $\mathcal{T}_{pp}$, $\mathcal{T}_{pu}$, $\mathcal{T}_{up}$ and $\mathcal{T}_{uu}$. A "two-load" method is then performed which consists of two measurements for two different terminal acoustic loads, corresponding to two linearly independent states of the system: a first measurement is performed with an *open* waveguide, then a second measurement is performed when the waveguide is *closed* by a rigid plug.

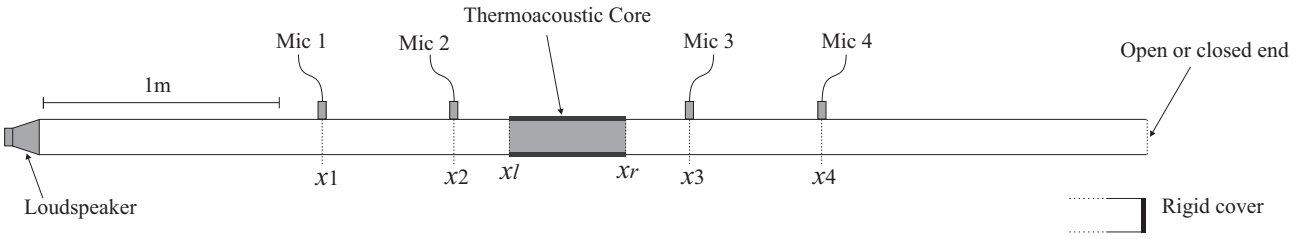

Figure 3.3: The four-microphone apparatus with the thermoacoustic core.

Under the assumption of an harmonic plane wave, the acoustic pressure in the waveguide can be expressed in terms of the linear combination of two counterpropagating plane waves dependent on the coordinate x,

$$\widetilde{p}(x) = \widetilde{p}^{+}(x) + \widetilde{p}^{-}(x). \tag{3.3}$$

The acoustic pressure can be written for two waveguide portions located at the left hand side of the TAC ($x \in (0, x_l)$) and at the right hand side of the TAC ($x \in (x_r, l)$),

$$\widetilde{p}(x) = \widetilde{p}_l^{+} e^{jk_w(x-x_l)} + \widetilde{p}_l^{-} e^{-jk_w(x-x_l)}, \forall x \in [0, x_l] \tag{3.4}$$

and

$$\widetilde{p}(x) = \widetilde{p}_r^{+} e^{jk_w(x-x_r)} + \widetilde{p}_r^{-} e^{-jk_w(x-x_r)}, \forall x \in [x_r, L], \tag{3.5}$$

where the complex wavenumber k_w takes into account the viscous and thermal losses on the waveguide internal walls, as explained in Subsection 2.2.2.

The four counterpropagating acoustic pressure components stated in Eqs. (3.4) and (3.5) can be expressed in terms of the measured acoustic pressures $\widetilde{p}_i = \widetilde{p}(x_i)$ taken at the four microphone locations:

$$\widetilde{p}_l^{+} = \frac{\widetilde{p}_2 e^{jk_w(x_l-x_1)} - \tilde{p}_1 e^{jk_w(x_l-x_2)}}{2jsin[k_w(x_2-x_1)]}, \widetilde{p}_l^{-} = \frac{\widetilde{p}_1 e^{-jk_w(x_l-x_2)} - \tilde{p}_2 e^{-jk_w(x_l-x_1)}}{2jsin[k_w(x_2-x_1)]}, \tag{3.6}$$

$$\widetilde{p}_r^{+} = \frac{\widetilde{p}_4 e^{-jk_w(x_3-x_r)} - \tilde{p}_3 e^{-jk_w(x_4-x_r)}}{2jsin[k_w(x_4-x_3)]}, \widetilde{p}_r^{-} = \frac{\widetilde{p}_3 e^{jk_w(x_4-x_r)} - \tilde{p}_4 e^{jk_w(x_3-x_r)}}{2jsin[k_w(x_4-x_3)]}, \tag{3.7}$$

from which the coefficients of the scattering matrix can be directly obtained when applying Eq. (3.8):

$$\begin{pmatrix} \widetilde{p}_r^{+} \\ \widetilde{p}_l^{-} \end{pmatrix} = \begin{pmatrix} T^{+} & R^{-} \\ R^{+} & T^{-} \end{pmatrix} \times \begin{pmatrix} \widetilde{p}_l^{+} \\ \widetilde{p}_r^{-} \end{pmatrix}. \tag{3.8}$$

However, the scattering matrix itself does not directly achieve the interests of this work, which rely instead in the transfer matrix $\mathbf{T}_{\mathrm{TAC}}$. Besides, even though the desired $\mathbf{T}_{\mathrm{TAC}}$ coefficients could be obtained from the scattering matrix simply by applying the proper two-port transforming relations, there is a more straightforward way to solve the problem, which is to apply Eq. (3.1).

The $\mathbf{T}_{\mathrm{TAC}}$ coefficients can be obtained from the determination of $\widetilde{p}_{l,r}$ and $\widetilde{u}_{l,r}$ by substituting the four counterpropagating components obtained from Eqs. (3.6) and (3.7), respectively, into the definition of Eq. (3.3) and into the Euler's equation (Eq. (3.9)) stated below:

$$\widetilde{u}(x) = \frac{S_w(1-f_\nu)}{j\omega\rho_0}\frac{\partial\widetilde{p}(x)}{\partial x} = \frac{1}{Z_c}[\widetilde{p}^{+}(x) - \widetilde{p}^{-}(x)], \tag{3.9}$$

where Z_c is the characteristic complex impedance of the guide, defined by

$$Z_c = \frac{\rho_0 c_0}{S\sqrt{(1-f_\nu)(1+(\gamma-1)f_\kappa)}}. \tag{3.10}$$

That finally gives

$$\widetilde{p}_{l,r} = \widetilde{p}_{l,r}^{+} + \widetilde{p}_{l,r}^{-}, \tag{3.11}$$

$$\widetilde{u}_{l,r} = \frac{1}{Z_c}[\widetilde{p}_{l,r}^{+} - \widetilde{p}_{l,r}^{-}]. \tag{3.12}$$

The terms $\widetilde{p}_{l,r}$ and $\widetilde{u}_{l,r}$ are developed below by substituting the four expressions (3.6) and (3.7) into the definitions (3.11) and (3.12):

$$\widetilde{p}_l = \frac{\widetilde{p}_2 sin[k_w(x_l - x_1)] - \widetilde{p}_1 sin[k_w(x_l - x_2)]}{sin[k_w(x_2 - x_1)]}, \tag{3.13}$$

$$\widetilde{p}_r = \frac{\widetilde{p}_4 sin[k_w(x_r - x_3)] - \widetilde{p}_3 sin[k_w(x_r - x_4)]}{sin[k_w(x_4 - x_3)]}, \tag{3.14}$$

$$\widetilde{u}_l = \frac{1}{jZ_c} \frac{\widetilde{p}_2 cos[k_w(x_l - x_1)] - \widetilde{p}_1 cos[k_w(x_l - x_2)]}{sin[k_w(x_2 - x_1)]}, \tag{3.15}$$

$$\widetilde{u}_r = \frac{1}{jZ_c} \frac{\widetilde{p}_4 cos[k_w(x_3 - x_r)] - \widetilde{p}_3 cos[k_w(x_4 - x_r)]}{sin[k_w(x_4 - x_3)]}. \tag{3.16}$$

When writing the transfer function $\widetilde{H}_{ij}$ between microphones i and j as

$$\widetilde{H}_{ij} = \frac{\widetilde{p}_i}{\widetilde{p}_j}, \tag{3.17}$$

Eqs. (3.13), (3.14), (3.15) and (3.16) result in the following expressions:

$$\widetilde{p}_l = \widetilde{p}_1 \frac{\widetilde{H}_{21} sin[k_w(x_l - x_1)] - sin[k_w(x_l - x_2)]}{sin[k_w(x_2 - x_1)]}, \tag{3.18}$$

$$\widetilde{p}_r = \widetilde{p}_3 \frac{\widetilde{H}_{43} sin[k_w(x_r - x_3)] - sin[k_w(x_r - x_4)]}{sin[k_w(x_4 - x_3)]}, \tag{3.19}$$

$$\widetilde{u}_l = \widetilde{p}_1 \frac{\widetilde{H}_{21} cos[k_w(x_l - x_1)] - cos[k_w(x_l - x_2)]}{jZ_c sin[k_w(x_2 - x_1)]}, \tag{3.20}$$

$$\widetilde{u}_r = \widetilde{p}_3 \frac{\widetilde{H}_{43} cos[k_w(x_3 - x_r)] - cos[k_w(x_4 - x_r)]}{jZ_c sin[k_w(x_4 - x_3)]}, \tag{3.21}$$

These expressions fulfill the requirements to determine the four unknowns of the definition of Eq. (3.1) as long as $\widetilde{p}_l$, $\widetilde{p}_r$, $\widetilde{u}_l$ and $\widetilde{u}_r$ are measured twice, under two different acoustic loads ($1st$ and $2nd$), as explained above. That results in a deterministic system of four equations:

$$\widetilde{p}_r^{1st} = \mathcal{T}_{pp}.\widetilde{p}_l^{1st} + \mathcal{T}_{pu}.\widetilde{u}_l^{1st}, \tag{3.22}$$

$$\widetilde{u}_r^{1st} = \mathcal{T}_{up}.\widetilde{p}_l^{1st} + \mathcal{T}_{uu}.\widetilde{u}_l^{1st}, \tag{3.23}$$

$$\widetilde{p}_r^{2nd} = \mathcal{T}_{pp}.\widetilde{p}_l^{2nd} + \mathcal{T}_{pu}.\widetilde{u}_l^{2nd}, \tag{3.24}$$

$$\widetilde{u}_r^{2nd} = \mathcal{T}_{up}.\widetilde{p}_l^{2nd} + \mathcal{T}_{uu}.\widetilde{u}_l^{2nd}. \tag{3.25}$$

Solving the system of equations above by substituting expressions from Eq. (3.18) to Eq. (3.21), the $\mathbf{T}_{\mathrm{TAC}}$ coefficients are found in terms of the measured transfer functions $\widetilde{H}_{ij}$ itemized in Eq. (3.17), which includes all measured acoustic pressures. The remaining terms related to the wavenumber k_w and to the axial positions x_i and x_j are obtained independently from those measurements. The resulting equations are shown in the following:

$$\mathcal{T}_{pp} = \frac{\widetilde{H}_{31}^{2nd}(\widetilde{H}_{43}^{2nd}.s_{3r} - s_{4r})(\widetilde{H}_{21}^{1st}.c_{l1} - c_{l2}) - \widetilde{H}_{31}^{1st}(\widetilde{H}_{43}^{1st}.s_{3r} - s_{4r})(\widetilde{H}_{21}^{2nd}.c_{l1} - c_{l2})}{s_{43}(\widetilde{H}_{21}^{2nd} - \widetilde{H}_{21}^{1st})}, \tag{3.26}$$

$$\mathcal{T}_{pu} = jZ_c\frac{\widetilde{H}_{31}^{1st}(\widetilde{H}_{43}^{1st}.s_{3r} - s_{4r})(\widetilde{H}_{21}^{2nd}.s_{l1} - s_{l2}) - \widetilde{H}_{31}^{2nd}(\widetilde{H}_{43}^{2nd}.s_{3r} - s_{4r})(\widetilde{H}_{21}^{1st}.s_{l1} - s_{l2})}{s_{43}(\widetilde{H}_{21}^{2nd} - \widetilde{H}_{21}^{1st})}, \tag{3.27}$$

$$\mathcal{T}_{up} = \frac{1}{jZ_c}\frac{\widetilde{H}_{31}^{1st}(\widetilde{H}_{43}^{1st}.c_{3r} - c_{4r})(\widetilde{H}_{21}^{2nd}.c_{l1} - c_{l2}) - \widetilde{H}_{31}^{2nd}(\widetilde{H}_{43}^{2nd}.c_{3r} - c_{4r})(\widetilde{H}_{21}^{1st}.c_{l1} - c_{l2})}{s_{43}(\widetilde{H}_{21}^{2nd} - \widetilde{H}_{21}^{1st})}, \tag{3.28}$$

$$\mathcal{T}_{uu} = \frac{\widetilde{H}_{31}^{2nd}(\widetilde{H}_{43}^{2nd}.c_{3r} - c_{4r})(\widetilde{H}_{21}^{1st}.s_{l1} - s_{l2}) - \widetilde{H}_{31}^{1st}(\widetilde{H}_{43}^{1st}.c_{3r} - c_{4r})(\widetilde{H}_{21}^{2nd}.s_{l1} - s_{l2})}{s_{43}(\widetilde{H}_{21}^{2nd} - \widetilde{H}_{21}^{1st})}, \tag{3.29}$$

where $s_{ij} = sin[k_w(x_i - x_j)]$ and $c_{ij} = cos[k_w(x_i - x_j)]$.

It is worth noting that the $\mathbf{T}_{\mathrm{TAC}}$ coefficients are acoustical properties that depend on frequency and temperature, and not on an imposed acoustic load. Hence, that allows such impositions to be arbitrarily defined to maximize the equations inter-independence, which increases the precision of the $\mathbf{T}_{\mathrm{TAC}}$ coefficients determination. The acoustic loads are therefore chosen

to differ each other as much as possible. Indeed, such independent conditions are evident in the denominators of all four coefficients, where the inequality $\widetilde{H}_{21}^{2nd} \neq \widetilde{H}_{21}^{1st}$ is to be ensured.

The complex notation in the frequency domain for the transfer functions is convenient, as has been shown in this section so far. However, the original signal input, which are the actual measurements captured by the four microphones, are necessarily taken in the time domain and in real values. Hence, a transformation takes place in this sense, in which these original signals have their amplitude amp_i and phase phi_i of the i^{th} microphone estimated by a numerical approach applied for each frequency ω, enabling the calculation of the complex transfer functions in the whole frequency domain. Explicitly, that gives:

$$\widetilde{H}_{21} = \frac{amp_2}{amp_1} e^{-j(phi_2 - phi_1)}, \widetilde{H}_{31} = \frac{amp_3}{amp_1} e^{-j(phi_3 - phi_1)}, \widetilde{H}_{43} = \frac{amp_4}{amp_3} e^{-j(phi_4 - phi_3)}. \quad (3.30)$$

Nevertheless, these original acoustic signals are too noisy to be put forward in the subsequent calculations, and thus shall be conditioned for a proper refinement to avoid significant error propagation. This treatment is made by applying a least square method in a process of estimating averages amp_i and phi_i, turning those signals closer to harmonic and less noisy.

3.3.2 Experimental setup and procedures

A photograph of the experimental setup is given in Fig. 3.4. The two tubes connected on either side of the TAC are made of PVC. They are two meters long and their inner radius $R = 16.47\,mm$ is slightly different than the TAC's one ($R_w = 16.93\,mm$). The acoustic field is generated by an electrodynamic loudspeaker attached to left extremity of the left duct, as shown in Fig. 3.3. It generates a stepped sine corresponding to a frequency range from 50 to $200\,Hz$ with increments of $1\,Hz$. Hence, the measurements are carried out for 151 frequencies. An optimum acoustic pressure is achieved at its maximum linear behavior, which is at a pressure level around $0.4Pa$, provided by a voltage of approximately $87mV$ delivered to the loudspeaker. Four microphones (model B&K 4138) are flush mounted along the pipes. They are placed in such locations that intrinsic measurement errors are minimized, in conformity with the criteria established by Boden (1986):

$$0.1\pi < k_0 \Delta x < 0.8\pi. \quad (3.31)$$

That resulted in the interval $\Delta x = 60\,cm$, what led the frequency range to fit within the proper interval between 50 and $200\,Hz$.

Figure 3.4: Experimental setup - Two-Load Method.

To ensure that no geometric discontinuity affects the sound field, the microphones are placed in suitable parts, machined so as to match the radius of curvature of the tubes, the junction between the waveguides and the microphone membrane being made by a capillary tube. The measurement signals are provided to the computer through the data acquisition card with a sampling frequency of $10\,kHz$, and their amplitude and phase are obtained using a least squares estimator from 500 samples taken for each frequency and at each microphone.

A relative calibration of microphones is done in order to take into account their respective sensitivities. The microphones are placed face-to-face in a cavity of very small size relative to the wavelength, so that the pressure field can be considered spatially uniform in the working frequency range (Fig. B.1). The transfer functions measured by this method are shown in Fig. B.2. These transfer functions, denoted $\widetilde{C}_{ij}$, defined as the ratios of sensitivities S of each microphone in the assumption of uniformity of pressure field,

$$\widetilde{C}_{ij} = \frac{S_i}{S_j}, \tag{3.32}$$

are used as a correction for the transfer function measured *in situ*. More information concerning the calibration procces is given in Appendix B.

To favor the stabilization of the temperature profile along the TAC axis, natural convection is minimized. That requires to keep the TAC always in the horizontal position, like in Fig. 3.1.

The cooling system is totally prevented from air bubbles in the cooper pipes and water hoses with the goal of improving the heat transfer efficiency, and also of avoiding the related noise - proved to be important. Within the same concern, vibration from the water pump and reservoir are minimized by means of keeping them apart from the TAC's workbench.

Close temperature monitoring is recorded for every thermal condition, for all measurements. These data are obtained by means of two thermocouples, one immersed in the water reservoir and the other attached to hottest external surface of the TAC. Moreover, a domestic thermometer/hygrometer/barometer register the laboratory ambient conditions, which are recorded as well. The average values are implemented in all post-processing to obtain the $\mathbf{T}_{\mathrm{TAC}}$ coefficients.

All setups are prepared the night before. The water circulation is turned on, and it is kept operating till the end of the experimentation for each material, according to the *transient regime investigation*. The TAC orientation is maintained in just one way, just like in Fig. 3.1. The transfer functions $\widetilde{H}_{21}$, $\widetilde{H}_{31}$ and $\widetilde{H}_{43}$ are obtained for each one of the two acoustic loads, before changing the heating supply; that means to obtain the needed six transfer functions per Q_H condition. To define the maximal Q_H, it is taken as reference the operational limit of the electrical resistance of the HHX here used, which is around $84\,W$. For this power, the temperature inside the TAC rises over 400ºC - as explored later in Section 3.33 - which covers most of typical values for the threshold condition for standard thermoacoustic engines. Therefore, such levels for Q_H are representative in what concerns real engine circumstances. That said, the increment on the Q_H variation is defined constant, and its number is calculated so that all measurements can be done within one day (non-interrupted 13 hours) for each material. This avoids major effects of ambient oscillations in temperature, humidity and pressure (less important). The interest is to have the number of power increments maximized as much as possible, to improve resolution with respect to performance predictions, to be explored later on in Chapter 4. As a result, there are 28 different values for Q_H, ranging from $0\,W$ to $81\,W$ by a constant increment of $3\,W$.

The measurement procedures follow the logical sequence presented in Subsection 3.3.1. It begins with $Q_H = 0W$, and then Q_H progresses by adjusting the power supply until Q_H reaches

$81W$, always in the increasing direction for both acoustic loads. For each Q_H the time-delay of $13\,min$ is respected.

3.3.3 Results

Two materials are investigated with the Two-Load Method: the Ceramic Catalyst (Fig. 3.5) and the pile of Stainless Steel Grids (Fig. 3.6).

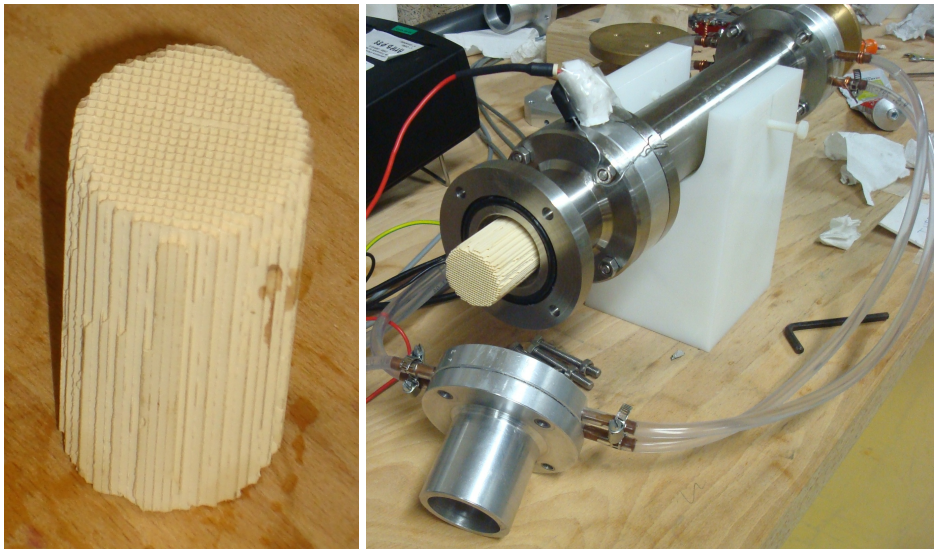

Figure 3.5: Ceramic Catalyst in detail and partially inserted in the open TAC.

Despite of both cases having been done for 28 values of Q_H as mentioned in paragraph 3.3.2, results are only shown for 3 heating conditions ($Q_H = 0$, $Q_H = 36\,W$ and $Q = 72\,W$) for the sake of clarity. This allows a visual evaluation of the curve progression with heating, if the noise level is not excessively high. The choice of these two materials allows testing the Two-Load Method with both stack-based and regenerator-based TAC.

Case of the Ceramic Catalyst

Figure 3.7 shows the four transfer coefficients (amplitude and phase) for the three selected heating conditions in the case of the Ceramic Catalyst. All curves are smooth and coherent with respect to the Q_H variation.

Figure 3.6: Stainless Steel Grids, ceramic washers and stack/regenerator holder.

To summarize the quality of this measurement, the Fig. 3.8 reveals the reciprocity behavior with frequency (for $Q_H = 0\,W$). Its average value is around $\mathbf{rc} = 1.010 + 0.002i$ - hence very close to 1 - which indicates a low *bias* level. The reciprocity standard deviation, in its turn, is $\sigma_{\mathbf{rc}} = 0.002 + 0.002i$. This is an indicator of low *noise* level, as it approaches 0.

Case of the Stainless Steel Grids

Figure 3.9 shows the four transfer coefficients (amplitude and phase) for the three heating conditions in the case of the Stainless Steel Grids. For this material, contrarily to the Ceramic Catalyst, all curves are very rough and do not allow a clear distinction of the Q_H progression. The reciprocity behavior in Fig. 3.8 shows that the problem comes from a very high *noise* level, since $\sigma_{\mathbf{rc}} = 0.134 + 0.123i$. *Bias*, on the other hand, is not an issue in this case: $\mathbf{rc} = 0.996 + 0.005i$. Therefore, as the method is the same one applied for the Ceramic Catalyst, under the same well-controlled experimental procedures, this high level of *noise* appears to be inherent in materials with low porosity - which means high reflectivity. The average level of acoustic pressure is much higher in the duct placed upstream from the sample than in the duct at the downstream side; that causes the microphones placed downstream to capture signals proportionally much more affected by *noise* than the ones placed upstream, what ends up affecting the transfer coefficients as well.

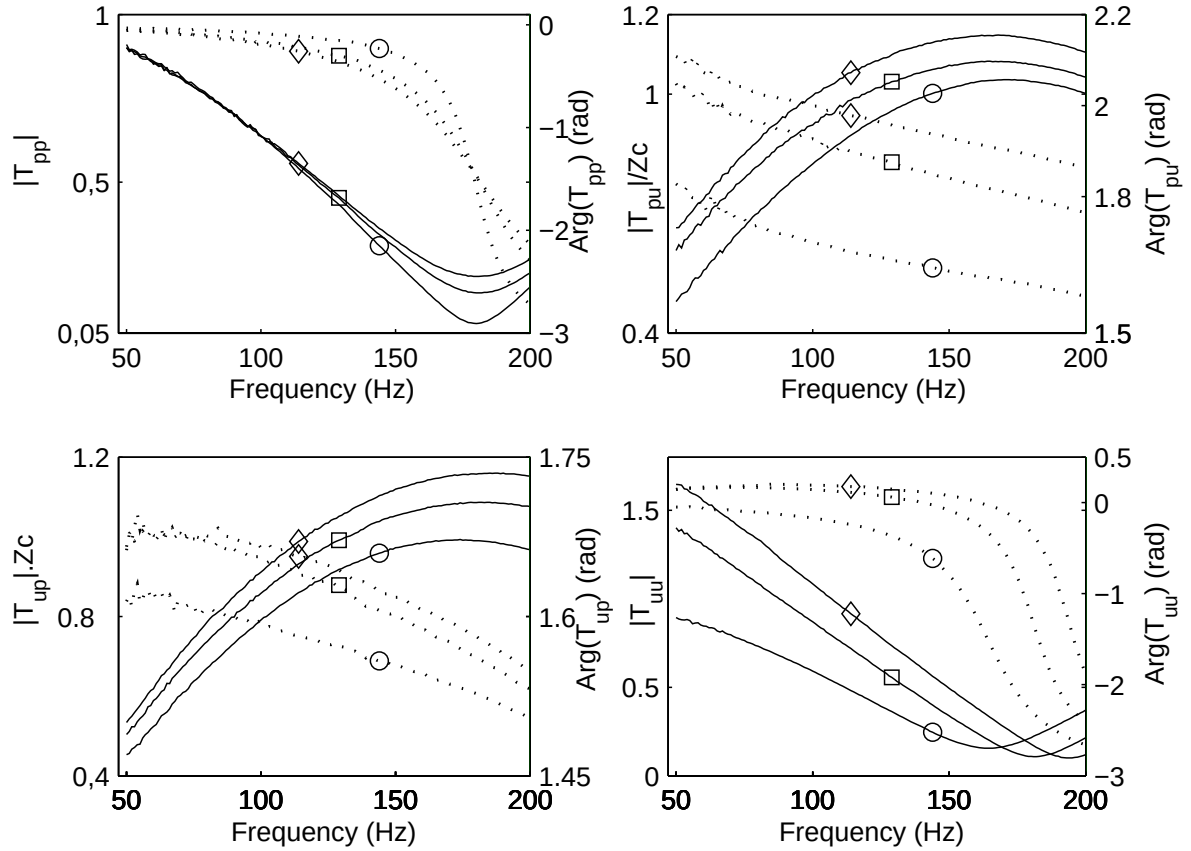

Figure 3.7: Ceramic Catalyst 1: amplitude (solid line) and phase (dotted line) of the $\mathbf{T}_{\mathrm{TAC}}$ coefficients in the frequency domain for $Q_H = 0\,W(circle)$, $Q_H = 36\,W(square)$ and $Q_H = 72\,W(diamond)$ - Two-Load Method.

3.3.4 Comparison with theory and analysis

Making use of the theory presented in Chapter 2, it is possible to derive the theoretical variation of $\mathbf{T}_{\mathrm{TAC}}$ coefficients with frequency for $Q_H = 0\,W$. A comparison between *theory* and *experiment* for the Ceramic Catalyst is given in Figs. 3.15 and 3.16. It shows a good agreement with respect to all $\mathbf{T}_{\mathrm{TAC}}$ coefficients, despite the fact that the values of parameters given in Tab.3.1 are not known with extreme accuracy. Those comparative results validate the experimental results, although restricted to the non-heated condition. In the case of heated conditions, the Two-Load Method should be valid as well, since the same procedure has been followed along all measurements, just as for $Q_H = 0$.

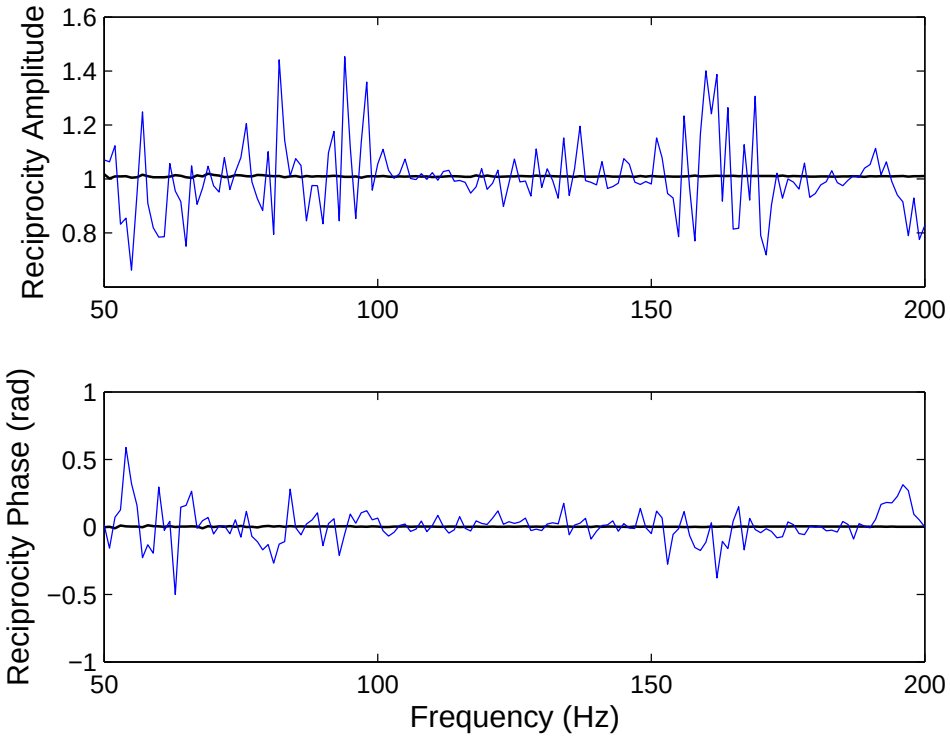

Figure 3.8: Amplitude and phase of the $\mathbf{T}_{\mathrm{TAC}}$ reciprocity in the frequency domain for $Q_H = 0\,W$ for the Ceramic Catalyst 600 cpsi (bold lines) and the Stainless Steel Grids (thin lines)- Two-Load Method.

For the $60\,mm$ pile of Stainless Steel Grids, however, there are no geometrical parameters accurate enough to obtain ϕ and equivalent cylindrical r_s because of its high tortuosity and complex geometry, and hence there are no theoretical $\mathbf{T}_{\mathrm{TAC}}$ coefficients available from the mentioned modeling. In spite of that, ϕ and r_s may estimated from the proper $\mathbf{T}_{\mathrm{TAC}}$ coefficients by applying an inverse method developed by Guedra (2012b) - as long as those coefficients are already obtained by other means, evidently. Then, using the measured $\mathbf{T}_{\mathrm{TAC}}$ by the Two-Load Method just presented, although noisy and imprecise (see Fig. 3.9), the estimation of ϕ and r_s for the Stainless Steel Grids are still convergent, leading to $\phi = 63.3\%$ and $r_s \approx 0.04\,mm$. From then on, the theoretical modeling can be applied to this material alike in the Ceramic Catalyst case, but the resulting $\mathbf{T}_{\mathrm{TAC}}$ coefficients are no longer purely theoretical nor precise since its origins are unsatisfying experimental results. On the other hand, such experimental limitation concerns only *noise* level ($\sigma_{\mathbf{rc}}$), and not so much *bias* level ($\mathbf{rc}$) - as shown in the previous subsection; that allows considering those experimental results to be valid for the estimation of average parameters such as ϕ and r_s, if there is a convergence, as shown just above. This assumption gives a near reliability on the semi-theoretical $\mathbf{T}_{\mathrm{TAC}}$ coefficients, at least when using them as approximative reference for further experimental investigations.

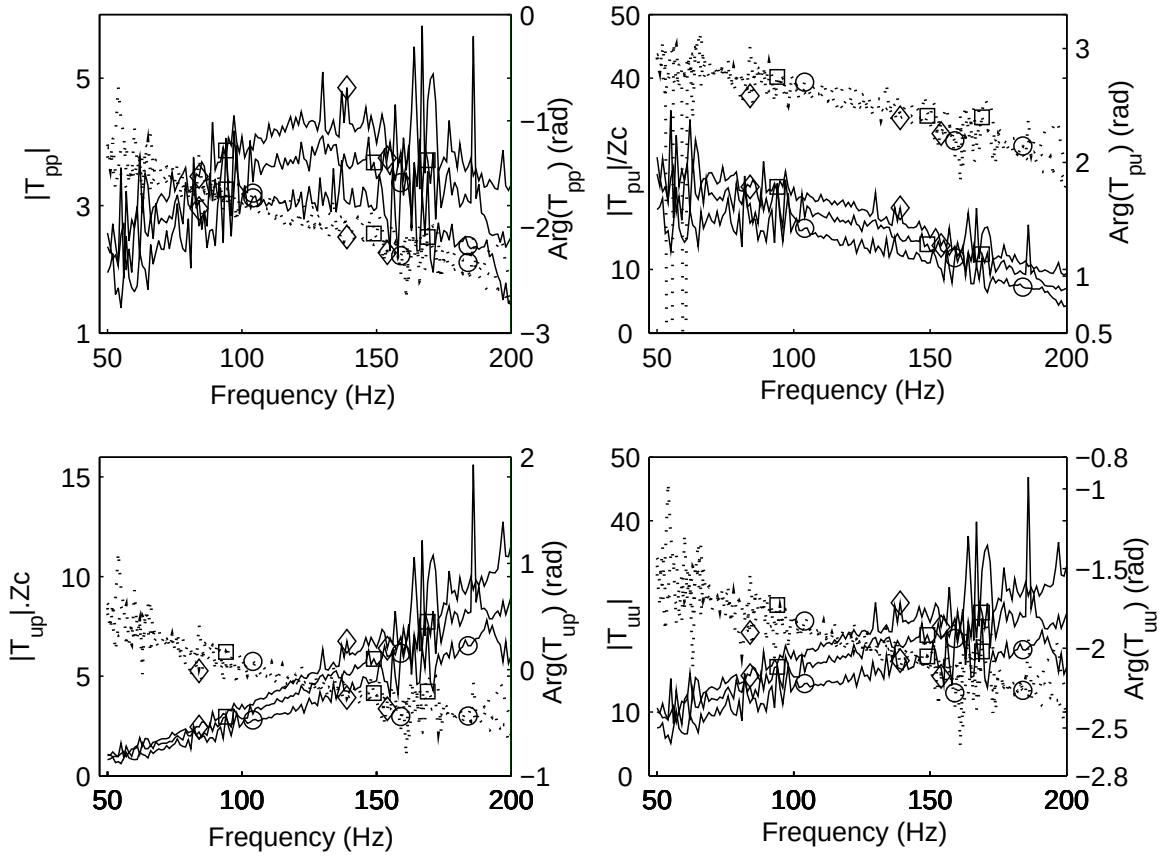

Figure 3.9: Stainless Steel Grids: amplitude (solid line) and phase (dotted line) of the $\mathbf{T}_{\mathrm{TAC}}$ coefficients in the frequency domain for $Q_H = 0\,W(circle)$, $Q_H = 36\,W(square)$ and $Q_H = 72\,W(diamond)$ - Two-Load Method.

3.3.5 Discussion

The Two-Load Method is revalidated for a *stack* application taking a Ceramic Catalyst as the tested sample. However, it fails to accurately measure the $\mathbf{T}_{\mathrm{TAC}}$ coefficients for materials with low porosity, like a *regenerator* as the pile of Stainless Steel Grids. In principle, this kind of problem could be accommodated by increasing the acoustic pressure level and the number of microphones. But higher levels of acoustic pressure have been tested which did not lead to significant improvements. Moreover, increasing the acoustic level magnitude leads to weakly nonlinear propagation, as well as to significant thermoacoustic heat transport by sound along the material that might increase the complexity of the experimental process. Then, another experimental approach is compelled to be found. The following attempt is a variation of the Two-Load Method.

3.4 Second approach: the Two-Load Method with TAC Inversion - about its failure

The Two-Load Method with TAC Inversion differs from the previous approach in just a single aspect: the TAC orientation is inverted for one of the acoustic loads. The idea behind this attempt is to increase the independence between the two systems of two equations, as an additional contrast is imposed between the two set of measurements besides the difference on the two acoustic loads. The higher such contrast is, the lower the expected sensitivities to transfer function variations are.

3.4.1 Principle of the method

In essence, the same method as previous is once again applied, contextualized in the same *black box* concept, just like in Section 3.3. That means that two sets of measurements involving two different acoustic loads are acquired. Nevertheless, the difference is that the TAC orientation is inverted for the first set of measurements (see Fig. 3.10), while the second set is kept as described in Subsection 3.3.2, referred to as the direct orientation. Order-of-inversion or opening/closing the TAC extremity is arbitrary.

Figure 3.10: Sketch of the inverted ThermoAcoustic Core.

This inversion procedure must be accompanied by a proper adjustment in the corresponding analytical expressions. The sole alteration in the equations is the inter-exchange of the positions x_l and x_r, since they are fixed to their original positions. Such exchange is therefore no longer coherent to the *in situ* meaning of *left* and *right* orientation, from the experimentalist viewpoint.

For the inverted TAC, the $\mathbf{T}_{\mathrm{TAC}}$ must be also inverted to maintain the same coefficients as in the direct orientation:

$$\begin{pmatrix} \widetilde{p}_r \\ \widetilde{u}_r \end{pmatrix} = \begin{pmatrix} \mathcal{T}_{pp} & \mathcal{T}_{pu} \\ \mathcal{T}_{up} & \mathcal{T}_{uu} \end{pmatrix}^{-1} \times \begin{pmatrix} \widetilde{p}_l \\ \widetilde{u}_l \end{pmatrix}. \tag{3.33}$$

Arranging the definitions (3.1) and (3.33) for the two set of measurements, it results:

$$\widetilde{p}_r^{1st} = \frac{\mathcal{T}_{uu}}{\mathcal{T}_{pp}\mathcal{T}_{uu} - \mathcal{T}_{pu}\mathcal{T}_{up}}.\widetilde{p}_l^{1st} + \frac{\mathcal{T}_{pu}}{\mathcal{T}_{pu}\mathcal{T}_{up} - \mathcal{T}_{pp}\mathcal{T}_{uu}}.\widetilde{u}_l^{1st}, \tag{3.34}$$

$$\widetilde{u}_r^{1st} = \frac{\mathcal{T}_{up}}{\mathcal{T}_{pu}\mathcal{T}_{up} - \mathcal{T}_{pp}\mathcal{T}_{uu}}.\widetilde{p}_l^{1st} + \frac{\mathcal{T}_{pp}}{\mathcal{T}_{pp}\mathcal{T}_{uu} - \mathcal{T}_{pu}\mathcal{T}_{up}}.\widetilde{u}_l^{1st}, \tag{3.35}$$

$$\widetilde{p}_r^{2nd} = \mathcal{T}_{pp}.\widetilde{p}_l^{2nd} + \mathcal{T}_{pu}.\widetilde{u}_l^{2nd}, \tag{3.36}$$

$$\widetilde{u}_r^{2nd} = \mathcal{T}_{up}.\widetilde{p}_l^{2nd} + \mathcal{T}_{uu}.\widetilde{u}_l^{2nd}, \tag{3.37}$$

with $\widetilde{p}_{l,r}$ and $\widetilde{u}_{l,r}$ being expressed analogously to the previous Eqs. (3.13) to (3.16), shown in the first approach (Section 3.3). In this set of equations, Eq. (3.34) and (3.35) differ from Eq. (3.22) and (3.23) due to the TAC inversion of the first measurement. As a consequence, a proper adjustment concerning such difference results in eight specific equations to be taken into account:

$$\widetilde{p}_l^{1st} = \frac{\widetilde{p}_4^{1st} sin[k_w(x_l - x_3)] - \widetilde{p}_3^{1st} sin[k_w(x_l - x_4)]}{sin[k_w(x_4 - x_3)]}, \tag{3.38}$$

$$\widetilde{p}_l^{2nd} = \frac{\widetilde{p}_2^{2nd} sin[k_w(x_l - x_1)] - \widetilde{p}_1^{2nd} sin[k_w(x_l - x_2)]}{sin[k_w(x_2 - x_1)]}, \tag{3.39}$$

$$\widetilde{p}_r^{1st} = \frac{\widetilde{p}_2^{1st} sin[k_w(x_r - x_1)] - \widetilde{p}_1^{1st} sin[k_w(x_r - x_2)]}{sin[k_w(x_2 - x_1)]}, \tag{3.40}$$

$$\widetilde{p}_r^{2nd} = \frac{\widetilde{p}_4^{2nd} sin[k_w(x_r - x_3)] - \widetilde{p}_3^{2nd} sin[k_w(x_r - x_4)]}{sin[k_w(x_4 - x_3)]}, \tag{3.41}$$

$$\widetilde{u}_l^{1st} = \frac{1}{jZ_c}\frac{\widetilde{p}_4^{1st}cos[k_w(x_3 - x_l)] - \widetilde{p}_3^{1st}cos[k_w(x_4 - x_l)]}{sin[k_w(x_4 - x_3)]}, \tag{3.42}$$

$$\widetilde{u}_l^{2nd} = \frac{1}{jZ_c}\frac{\widetilde{p}_2^{2nd}cos[k_w(x_l - x_1)] - \widetilde{p}_1^{2nd}cos[k_w(x_l - x_2)]}{sin[k_w(x_2 - x_1)]}, \tag{3.43}$$

$$\widetilde{u}_r^{1st} = \frac{1}{jZ_c}\frac{\widetilde{p}_2^{1st}cos[k_w(x_r - x_1)] - \widetilde{p}_1^{1st}cos[k_w(x_r - x_2)]}{sin[k_w(x_2 - x_1)]}. \tag{3.44}$$

$$\widetilde{u}_r^{2nd} = \frac{1}{jZ_c}\frac{\widetilde{p}_4^{2nd}cos[k_w(x_3 - x_r)] - \widetilde{p}_3^{2nd}cos[k_w(x_4 - x_r)]}{sin[k_w(x_4 - x_3)]}. \tag{3.45}$$

After some development, all acoustic pressure are reported in terms of the transfer functions $\widetilde{H}_{ij}$, so that the $\mathbf{T}_{\mathrm{TAC}}$ coefficients are calculated likewise.

$$\mathcal{T}_{pp} = \frac{s_{21}}{s_{43}}\frac{\widetilde{H}_{31}^{1st}(\widetilde{H}_{43}^{1st}.s_{l3} - s_{l4})(\widetilde{H}_{21}^{2nd}.c_{l1} - c_{l2}) - \widetilde{H}_{31}^{2nd}(\widetilde{H}_{43}^{2nd}.s_{r3} - s_{r4})(\widetilde{H}_{21}^{1st}.c_{r1} - c_{r2})}{\widetilde{H}_{21}^{2nd}s_{2l1r} - \widetilde{H}_{21}^{1st}s_{2r1l}}, \tag{3.46}$$

$$\mathcal{T}_{pu} = \frac{s_{21}}{s_{43}}\frac{\widetilde{H}_{31}^{2nd}(\widetilde{H}_{43}^{2nd}.s_{r3} - s_{r4})(\widetilde{H}_{21}^{1st}.s_{r1} - s_{r2}) - \widetilde{H}_{31}^{1st}(\widetilde{H}_{43}^{1st}.s_{l3} - s_{l4})(\widetilde{H}_{21}^{2nd}.s_{l1} - s_{l2})}{(1/jZ_c)(\widetilde{H}_{21}^{2nd}s_{2l1r} - \widetilde{H}_{21}^{1st}s_{2r1l})}, \tag{3.47}$$

$$\mathcal{T}_{up} = \frac{s_{21}}{s_{43}}\frac{\widetilde{H}_{31}^{1st}(\widetilde{H}_{43}^{1st}.c_{3l} - c_{4l})(\widetilde{H}_{21}^{2nd}.c_{c1} - c_{l2}) - \widetilde{H}_{31}^{2nd}(\widetilde{H}_{43}^{2nd}.c_{3r} - c_{4r})(\widetilde{H}_{21}^{1st}.c_{r1} - c_{r2})}{jZ_c(\widetilde{H}_{21}^{2nd}s_{2l1r} - \widetilde{H}_{21}^{1st}s_{2r1l})}, \tag{3.48}$$

$$\mathcal{T}_{uu} = \frac{s_{21}}{s_{43}}\frac{\widetilde{H}_{31}^{2nd}(\widetilde{H}_{43}^{2nd}.c_{3r} - c_{4r})(\widetilde{H}_{21}^{1st}.s_{r1} - s_{r2}) - \widetilde{H}_{31}^{1st}(\widetilde{H}_{43}^{1st}.c_{3l} - c_{4l})(\widetilde{H}_{21}^{2nd}.s_{l1} - s_{l2})}{\widetilde{H}_{21}^{2nd}s_{2l1r} - \widetilde{H}_{21}^{1st}s_{2r1l}}, \tag{3.49}$$

where $s_{ij} = sin[k_w(x_i - x_j)]$, $c_{ij} = cos[k_w(x_i - x_j)]$, $s_{2l1r} = sin[k_w(x_2 + x_l - x_1 - x_r)]$ and $s_{2r1l} = sin[k_w(x_2 + x_r - x_1 - x_l)]$.

3.4.2 Experimental procedures

Experiments are conducted for the Stainless Steel Grids configuration, as the Two-load Method fails with this material. For these experiments, no heating power is supplied to the HHX ($Q_H = 0\,W$). This simple configuration allows the estimation of the reciprocity. It is then possible to evaluate if this method is suitable using further measurements for various heat power levels.

The Two-Load Method with TAC Inversion requires special care relying on the successive connection and disconnection between the TAC and the waveguides, to proceed with the change on the TAC orientation before every new set of measurements. All joints are cleaned, re-greased, and well adjusted to avoid as much as possible length variations caused by clearances.

3.4.3 Results for the Stainless Steel Grids

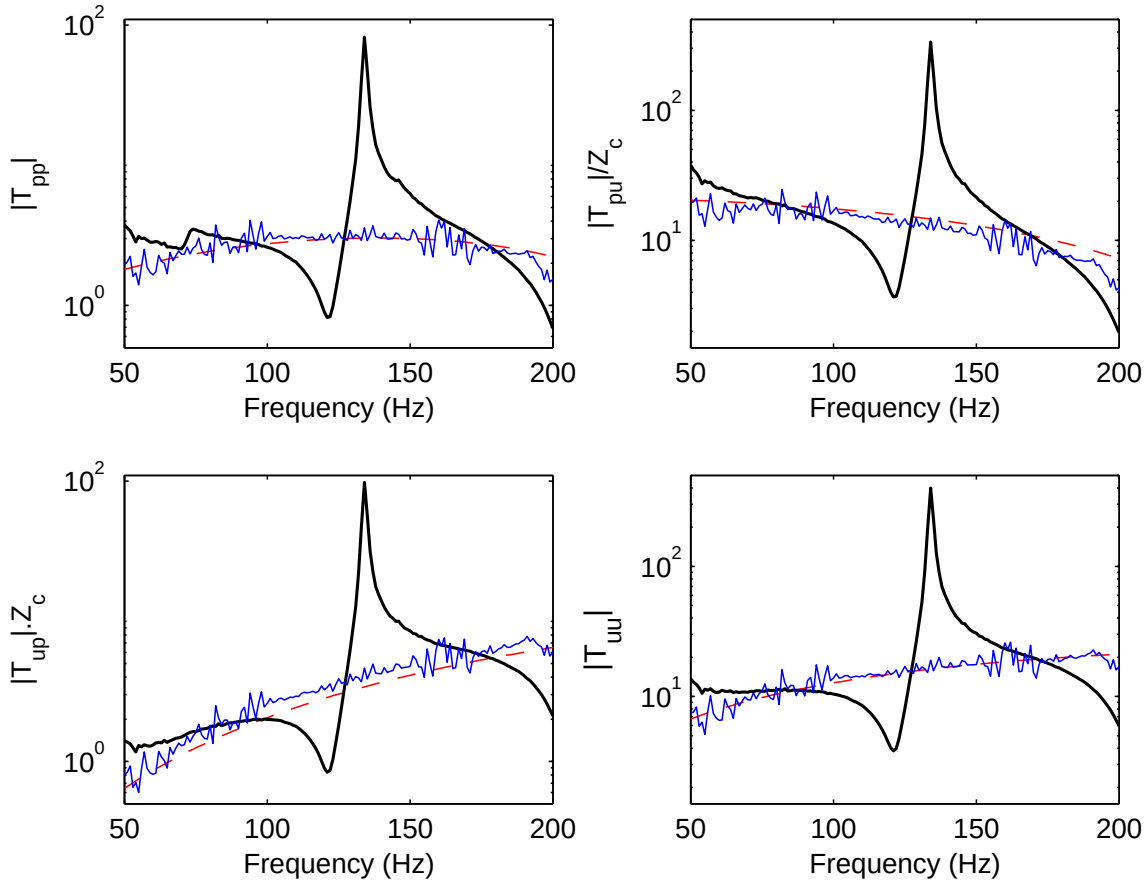

Figure 3.11: Stainless Steel Grids: amplitude of the $\mathbf{T}_{\mathrm{TAC}}$ coefficients in the frequency domain for $Q_H = 0\,W$ - Two-Load Method with TAC Inversion (bold lines), Two-Load Method (thin lines) and Theory (dashed lines).

The experimental $\mathbf{T}_{\mathrm{TAC}}$ coefficients of the Stainless Steel Grids are presented in Figs. 3.11 and 3.13, while the reciprocity spectrum is shown in both amplitude and phase in Fig. 3.14. In all of these figures the corresponding curves of the first approach are included, for comparison. The results of this second method vastly differ from those obtained with the Two-Load Method. Both amplitudes and phases are far more biased, but are less noisy - as can be verified in both

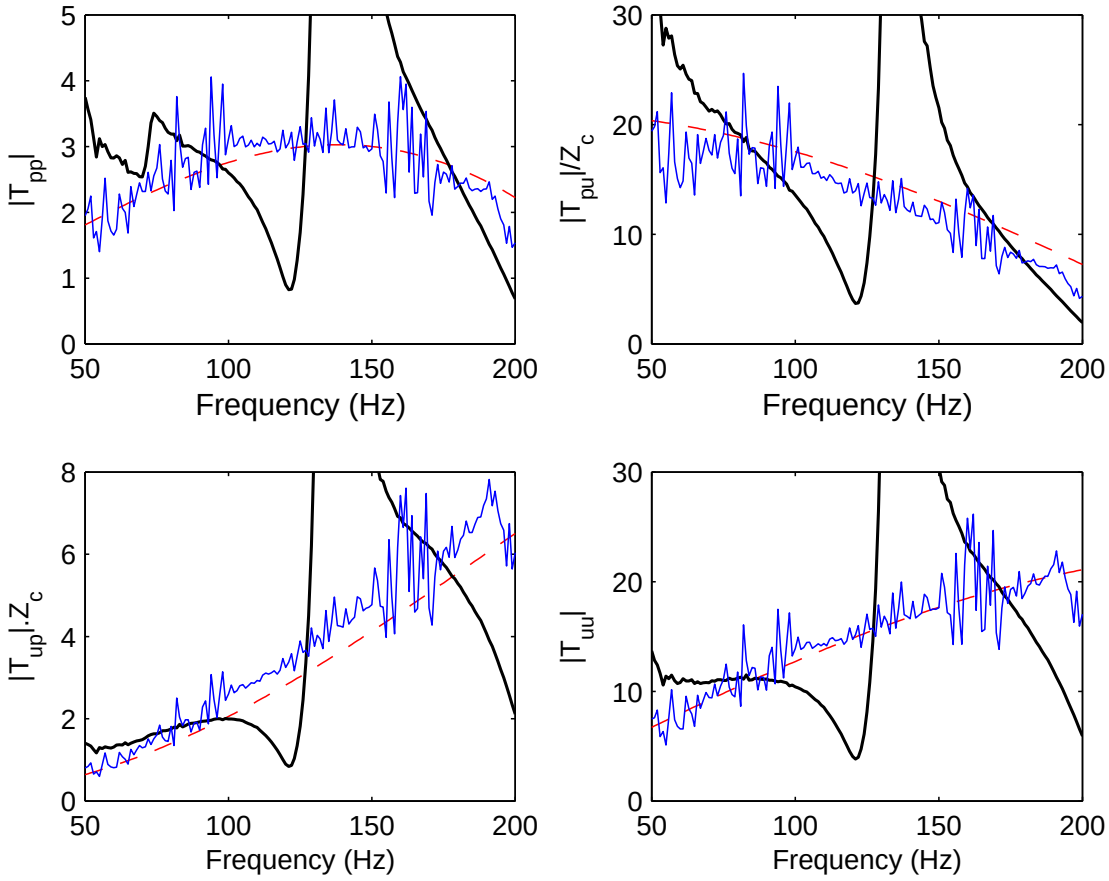

Figure 3.12: Stainless Steel Grids: zoomed amplitude in linear scale of the $\mathbf{T}_{\mathrm{TAC}}$ coefficients in the frequency domain for $Q_H = 0\,W$ - Two-Load Method with TAC Inversion (bold lines), Two-Load Method (thin lines) and Theory (dashed lines).

logarithmic and linear scales (Fig. 3.12). Moreover, a particular resonance frequency is clearly revealed at $134\,Hz$ either on the amplitudes or phases, which is not obtained with the previous method. Concerning the reciprocity statistical parameters, on the other hand, the Two-Load Method with TAC Inversion leads to an average value $\mathbf{rc} = 0.243 - 1.727i$ with a standard deviation $\sigma_{\mathbf{rc}} = 3.787 + 4.238i$, which indicates very poor performance not only for *bias* level but also for *noise* level, as $\sigma_{\mathbf{rc}}$ is so far from 0. This is an apparent contradiction that calls for further investigation. It is worth noting that this issue is not found in the first approach since its resulting $\mathbf{T}_{\mathrm{TAC}}$ coefficients behave accordingly to their corresponding $\mathbf{rc} = 0.996 + 0.005i$ and $\sigma_{\mathbf{rc}} = 0.134 + 0.123i$.

Finally, the high magnitude of such discrepancy between the two methods requires putting forward a sensitivity analysis, to investigate its origins, as shown in the following.

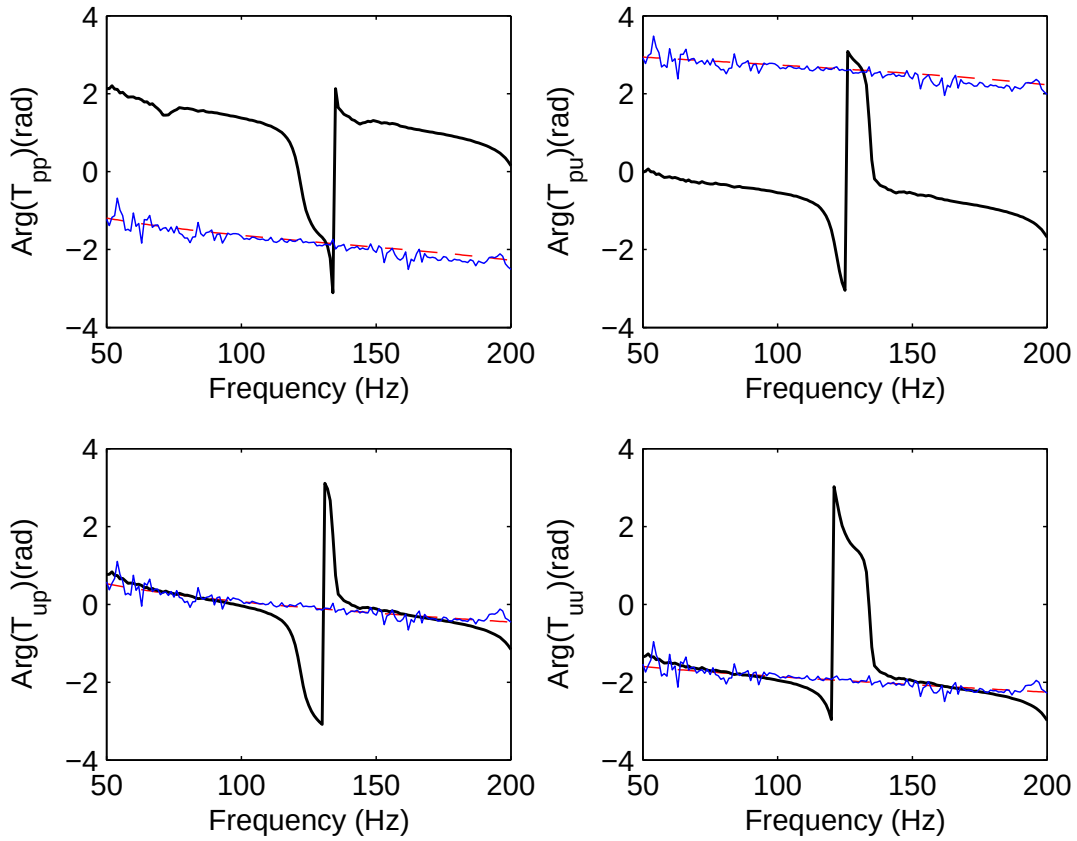

Figure 3.13: Stainless Steel Grids: amplitude of the $\mathbf{T}_{\mathrm{TAC}}$ coefficients in the frequency domain for $Q_H = 0\,W$ - Two-Load Method with TAC Inversion (bold lines), Two-Load Method (thin lines) and Theory (dashed lines).

3.5 Sensitivity analysis for both Two-Load Methods (with and without TAC inversion)

The discrepancies observed in results obtained with the different two-load methods require a sensitivity analysis for a more profound comprehension of such a behavior. Arbitrary *noise* and *bias* are then inserted into the theoretical transfer functions $\widetilde{H}$ obtained from the modeling given in Chapter 2. Two kinds of material are tested: the Ceramic Catalyst and the Stainless Steel Grids. These materials are described by their respective geometrical parameters which are the average pore radius r_s, the porosity ϕ and the length ℓ (see Table 3.1). In the case of the Stainless Steel Grids, the estimated porosity (ϕ) and the estimated representative average cylindrical pore radius (r_s) are obtained from the very noisy $\mathbf{T}_{\mathrm{TAC}}$ coefficients previously measured with the Two-Load Method without TAC inversion, using a specific method developed by Guedra (2012b).

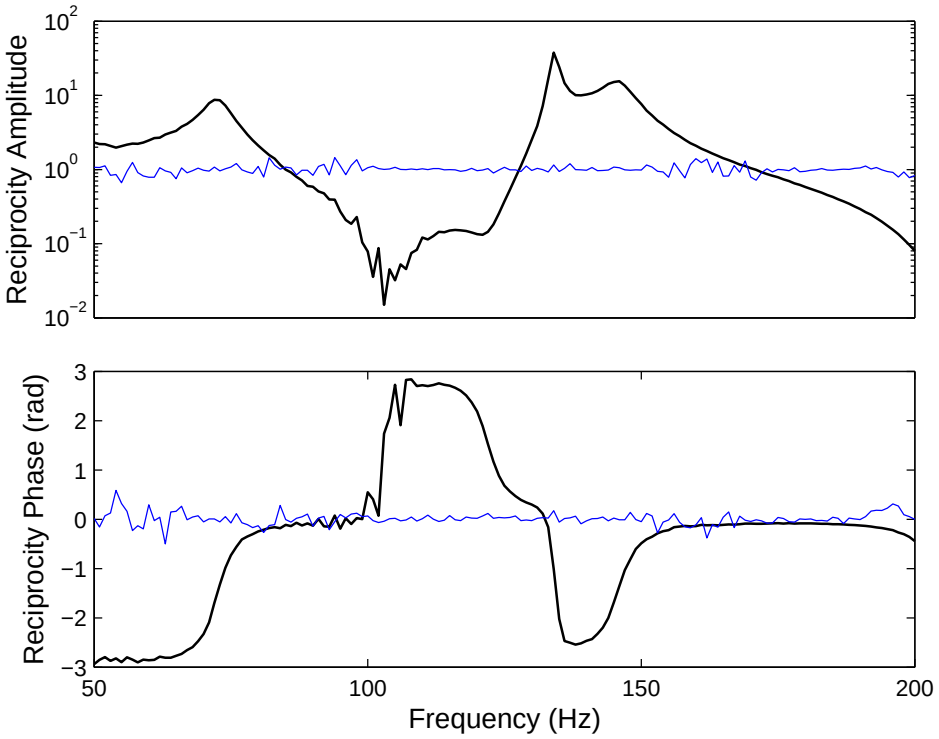

Figure 3.14: Stainless Steel Grids: amplitude and phase of the $\mathbf{T}_{\mathrm{TAC}}$ reciprocity in the frequency domain for $Q_H = 0\,W$ - Two-Load Method with TAC Inversion (bold lines) and Two-Load Method (thin lines).

The *noise* is theoretically taken into account by adding a random amplitude $A_n F_r$ and a random phase $P_n F_r$ to the amplitude and phase of the theoretical transfer function $\widetilde{H}$, where A_n and P_n are arbitrary amplitude and phase of the *noise* level, respectively, and where F_r is a random function whose values are uniformly distributed in an interval constrained between -1 and 1.The choice of a uniform distribution is found to be better than a Gaussian one since it avoids unrealistic values, which may be present whenever the aleatory numerical generation is not constrained. The noisy transfer function is then calculated as below for each frequency i individually, with the random function F_r^i being required accordingly,

$$\widetilde{H}^i_{noise} = |\widetilde{H}^i|(1 + A_n F_r^i) e^{j(\varphi(\widetilde{H}^i) + P_n F_r^i)}. \tag{3.50}$$

Concerning the *bias*, the same disturbance is uniformly applied to the whole spectra. The biased transfer function is then obtained as below,

$$\widetilde{H}_{bias} = |\widetilde{H}|(1 + A_b)e^{j(\varphi(\widetilde{H})+P_b)}, \tag{3.51}$$

where A_b and P_b are the respective amplitude and phase of the *bias* level. Both A_b and P_b are either added or subtracted, thus developing four combinations of *bias*.

The following values are used along the entire sensitivity analysis: $A_n = 0.1$, $P_n = 0.03\pi$ rad, $A_b = 0.1$ and $P_b = 0.03\pi$ rad. They are chosen compromisingly to comparative intents, as previously.

The four curves corresponding to the four combinations of *bias* are plotted as solid curves in all graphs of sensitivity analysis. Concerning the *noise* presentation, however, five curves are plotted per graph with the intent of a clear illustration. They differ by their aleatory nature and are presented as dotted lines. These graphic results are shown in the next eight figures, where both two-load methods can be compared for the Ceramic Catalyst and for the Stainless Steel Grids. Figs. 3.15 and 3.16 give the amplitudes and phases of $\mathbf{T}_{\mathrm{TAC}}$ coefficients when estimated with classical Two-Load Method, while Figs. 3.17 and 3.18 are the corresponding results for the Two-Load Method with TAC Inversion. Likewise, Figs. 3.19 to 3.22 treat the Stainless Steel grids case.

From Figs. 3.15 to 3.18, it is clear that the Two-Load Method overcomes the Two-Load Method with TAC Inversion when applied to a stack-like material. Either amplitude or phase of both *noise* and *bias* achieve a very symmetrical behavior with respect to the theory, and they also enclose quite well the experimental curves, which on its turn fits closely along the theoretical curves.

In the case of the pile of Stainless Steel Grids, as shown in Figs. 3.19 and 3.20, the experimental results obtained with the two-load method without inversion, despite of being poor, are closer to the theoretical curves than the *bias* and the *noise* ones. That suggests a quality of measurements good enough to minimize the effects of both sensitivities; however, as the sensitivity to *noise* is specially high, the experimental curves still result noisy, even though much less than the theoretical *noise* curves. In principle, that could be just a matter of setting up other values for A_n and P_n, but those parameters are chosen the same for all cases, as mentioned before, to standardize all comparisons.

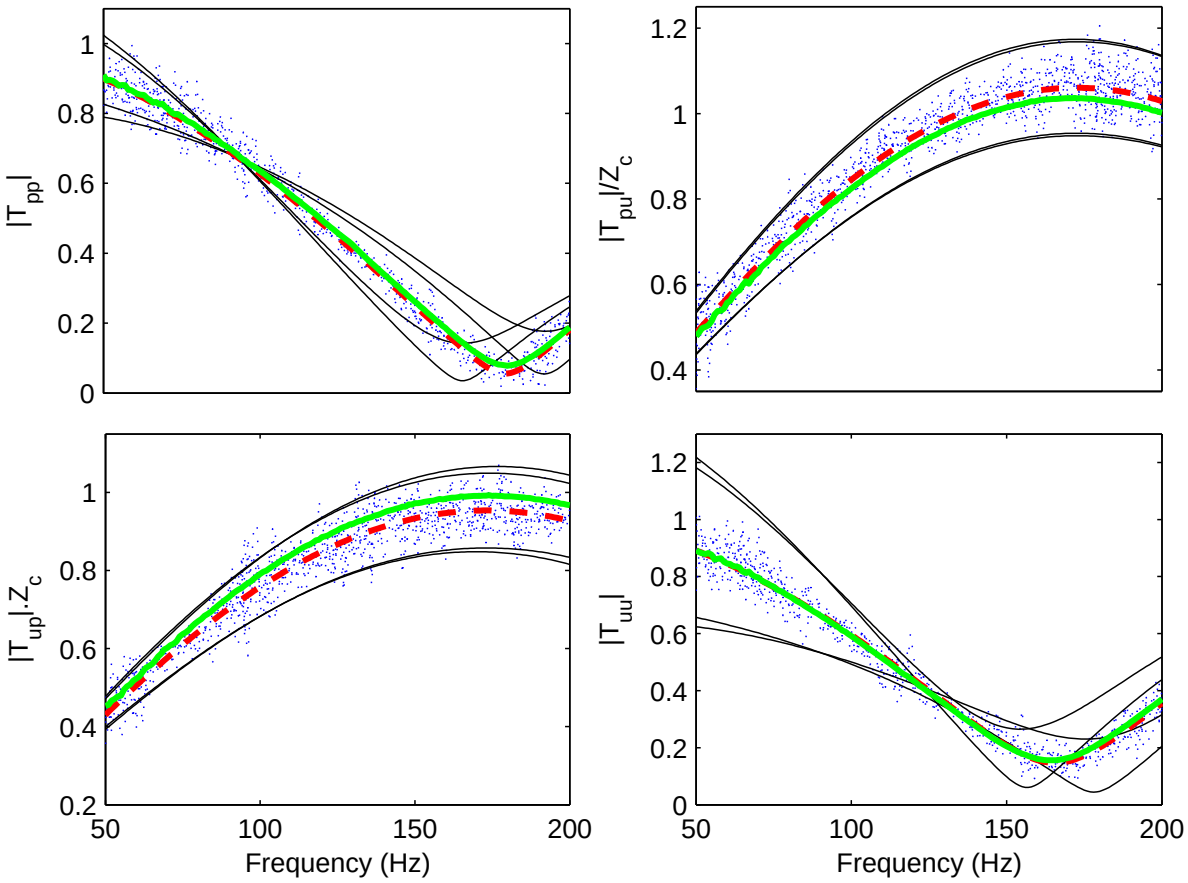

Figure 3.15: Ceramic Catalyst: amplitude of the four $\mathcal{T}$ coefficients in the frequency domain for $Q_H = 0\,W$ in bold lines for the measurements (solid) and theory (dashed) with the respective theoretical *bias* (four thin solid lines per graph) and *noise* (five dotted lines per graph). - Two-Load Method.

Figs. 3.21 and 3.22 reveal a high sensitivity to *bias* of the Two-Load Method with TAC Inversion, which is in accordance with the reciprocity results. A highlighted resonance peak at around $134\,Hz$ appears in both experimental and biased curves. However, despite already having input high levels for A_b and P_b, the experimental peak is still much higher than the biased one (by a factor of 10). That incites for seeing how coherent the curves are for the previous approach, i.e. the two-load method without inversion. About the noisy curves, they are closer to the theoretical reference than the biased ones, as predicted in the reciprocity results. Furthermore, they reveal a little higher sensitivity in the region between $50\,Hz$ to $70\,Hz$, what is indeed shown in the experimental curves.

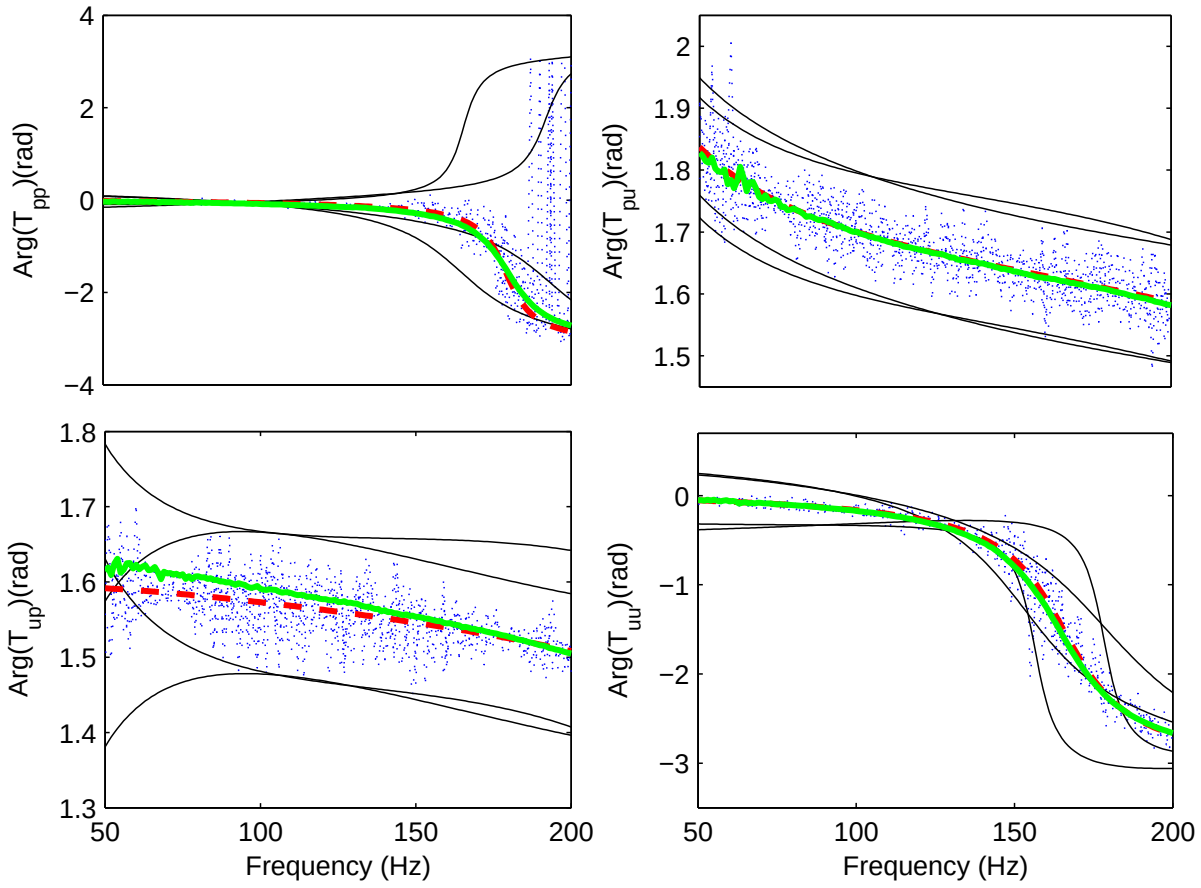

Figure 3.16: Ceramic Catalyst: phase of the four $\mathcal{T}$ coefficients in the frequency domain for $Q_H = 0\,W$ in bold lines for the measurements (solid) and theory (dashed) with the respective theoretical *bias* (four thin solid lines per graph) and *noise* (five dotted lines per graph). - Two-Load Method.

This scenario implies to distrust the biased experimental curves from the Two-Load Method with TAC Inversion not only because of their evident low quality, but also because of a possible error intrinsic to the experimental procedures, since such intense effect does not occur for the Two-Load Method without inversion. One plausible explanation for that is supported by a critical experimental contrast between those methods. The second approach is much more risky than the first one since it requires the actual physical inversion of the TAC, what certainly adds errors in the measurements by the unavoidable variations on positioning. If this issue is solved by a more precise coupling in the TAC connections, the Two-Load Method with TAC Inversion could potentially be better than the Two-Load Method, as its sensitivity is much smaller to *noise* along the whole spectra of analysis. That may be advantageous enough to overcome the higher sensitivity to *bias*, since this one is restricted to a much smaller frequency interval.

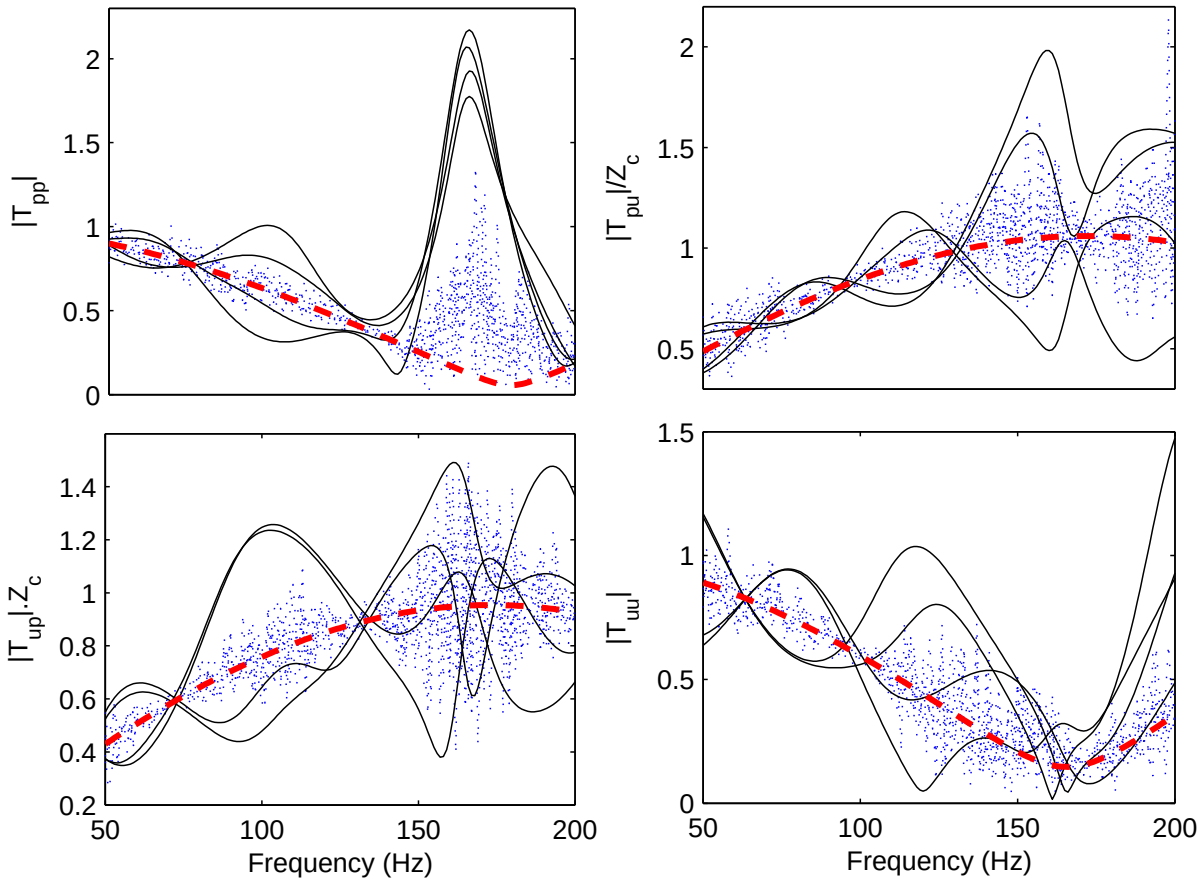

Figure 3.17: Ceramic Catalyst: amplitude of the four $\mathcal{T}$ coefficients in the frequency domain for $Q_H = 0\,W$ in bold lines for the theory (dashed) with the respective theoretical *bias* (four thin solid lines per graph) and *noise* (five dotted lines per graph). - Two-Load Method with TAC Inversion.

In conclusion, the Two-Load Method is indeed much more sensitive to *noise* than the Two-Load Method with TAC Inversion for this kind of material, i.e. a regenerator. Regarding the *bias* curves, both methods show similar behavior, in the same level of disturbance.

Alternatively, another possibility would be to use a two-source method instead of a two-load method. The two-source method basically consists of using an anechoic termination as a load, and proceeding with two measurements with TAC inversion. However, we did not choose to investigate the method, notably because it might have the same drawbacks as the two former methods, which are intrinsic to multiple microphones methods.

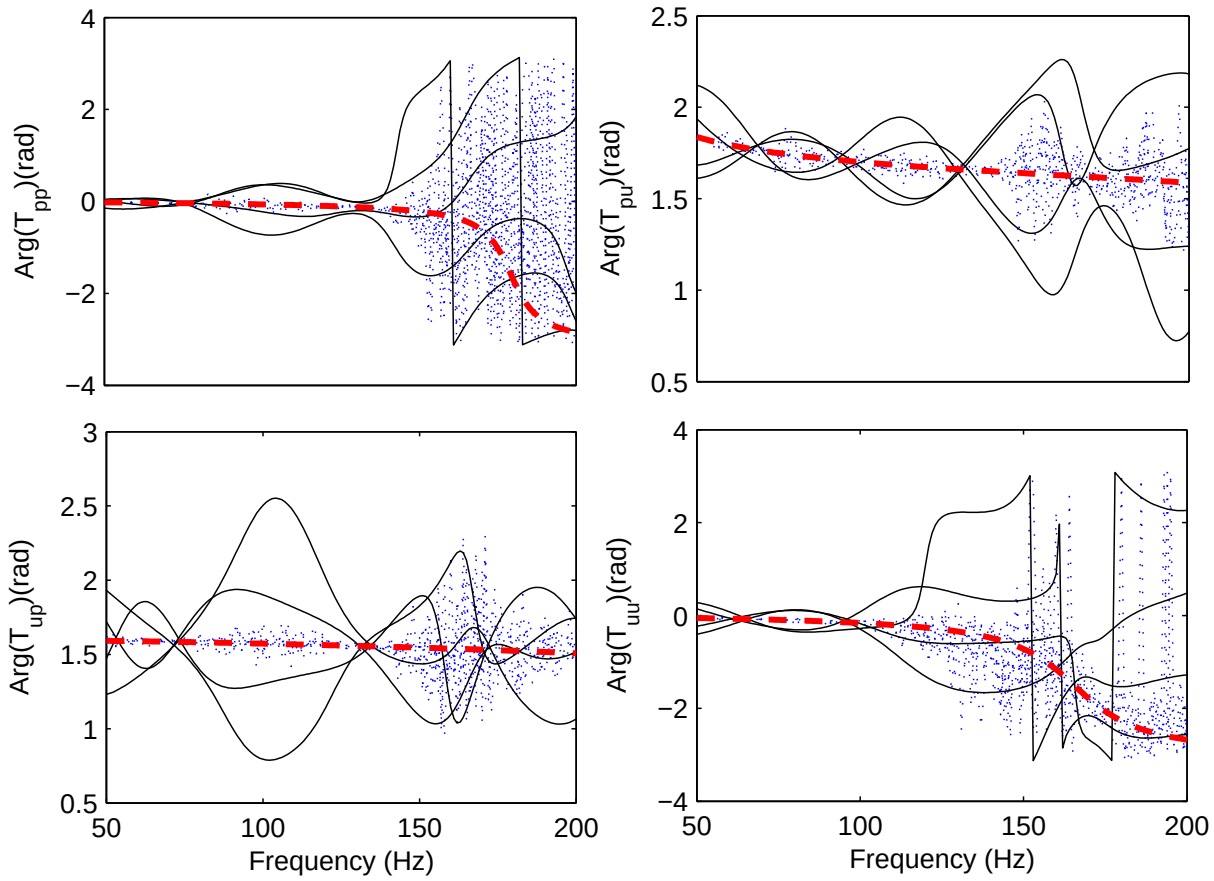

Figure 3.18: Ceramic Catalyst: phase of the four $\mathcal{T}$ coefficients in the frequency domain for $Q_H = 0\,W$ in bold lines for the theory (dashed) with the respective theoretical *bias* (four thin solid lines per graph) and *noise* (five dotted lines per graph). - Two-Load Method with TAC Inversion.

At this point, the search for a third approach is justified since the regenerator-based TAC is not plentifully modeled nor characterized, by far. The Impedance Method is presented in the following Section 3.6.

3.6 Third approach: the Impedance Method

Aiming to solve the problem of characterizing the TAC filled with a material exhibiting a low porosity, as the Stainless Steel Grids, an alternative method is here developed.

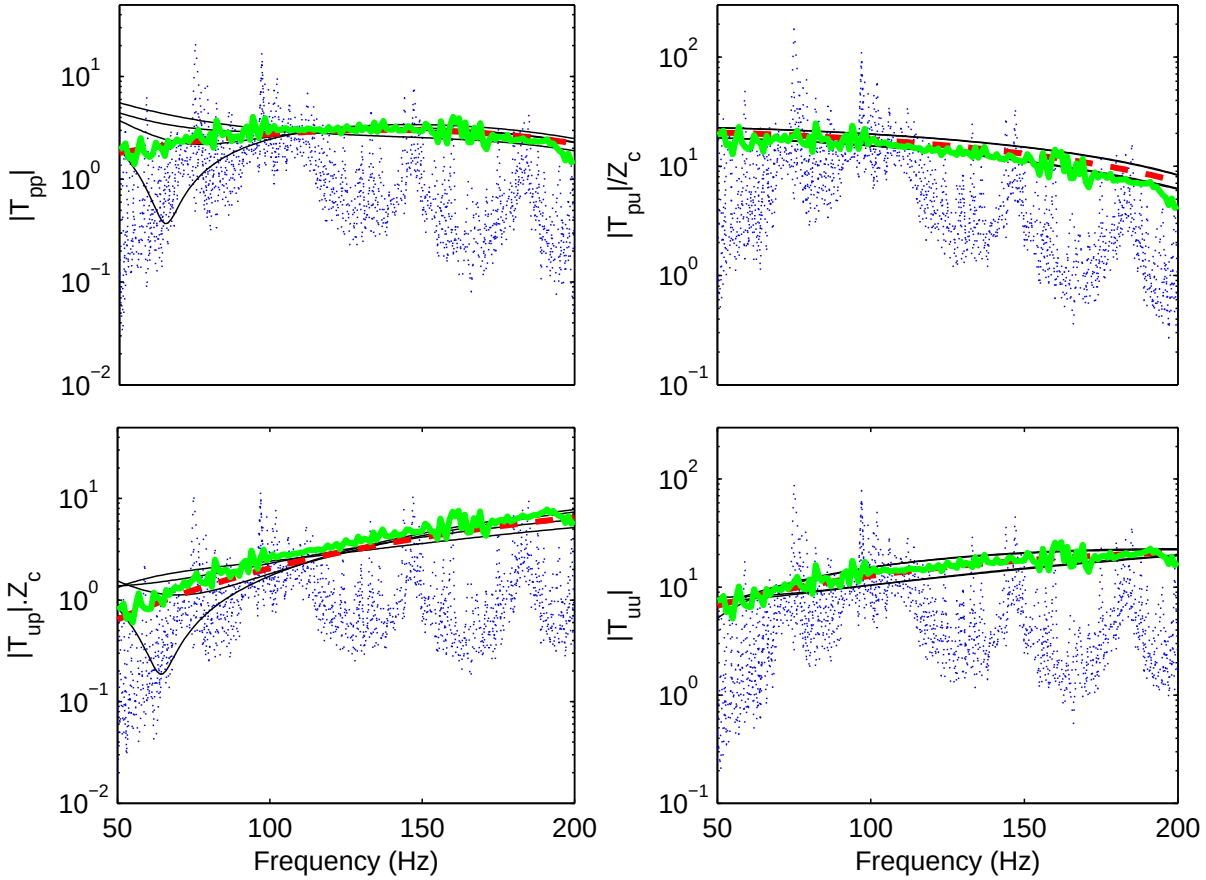

Figure 3.19: Stainless Steel Grids: amplitude of the four $\mathcal{T}$ coefficients in the frequency domain for $Q_H = 0\,W$ in bold lines for the measurements (solid) and theory (dashed), with the respective theoretical *bias* (four thin solid lines per graph) and *noise* (five dotted lines per graph). - Two-Load Method.

The Impedance Method consists of obtaining the $\mathbf{T}_{\mathrm{TAC}}$ coefficients from the measurement of the impedance matrix $\mathbf{Z}_{\mathrm{TAC}}$ (Bannwart *et al.*, 2012, 2013). All measurements are made by means of a specific device called the Acoustic Impedance Sensor (AIS) (Le Roux, 2012) - shown in Figs. 3.23 and 3.26 - coupled to the TAC under test (Figs. 3.24 and C.1). This alternative method is more direct than either previous approaches since there is no need to account for plane wave propagation in some ducts surrounding the TAC, and there are no limitations in the frequency range of analysis relative to the distance between microphones (Boden, 1986).

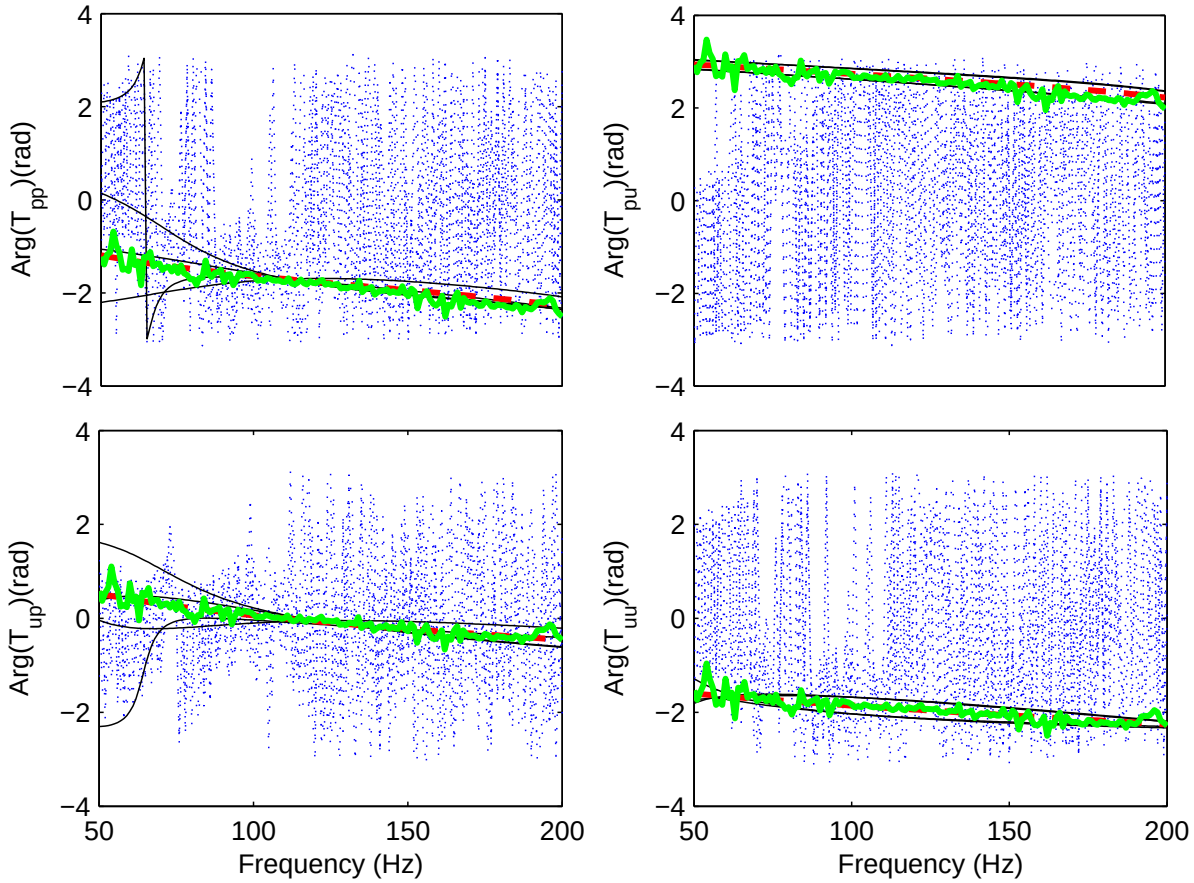

Figure 3.20: Stainless Steel Grids: phase of the four $\mathcal{T}$ coefficients in the frequency domain for $Q_H = 0\,W$ in bold lines for the measurements (solid) and theory (dashed), with the respective theoretical *bias* (four thin solid lines per graph) and *noise* (five dotted lines per graph). - Two-Load Method.

3.6.1 Principle of the method

The impedance matrix of the TAC is defined as

$$\begin{pmatrix} \widetilde{p}_l \\ \widetilde{p}_r \end{pmatrix} = \begin{pmatrix} \mathcal{Z}_{11} & \mathcal{Z}_{12} \\ \mathcal{Z}_{21} & \mathcal{Z}_{22} \end{pmatrix} \times \begin{pmatrix} \widetilde{u}_l \\ \widetilde{u}_r \end{pmatrix} = \mathbf{Z_{TAC}} \times \begin{pmatrix} \widetilde{u}_l \\ \widetilde{u}_r \end{pmatrix}, \tag{3.52}$$

which is in accordance with Fig. 3.1.

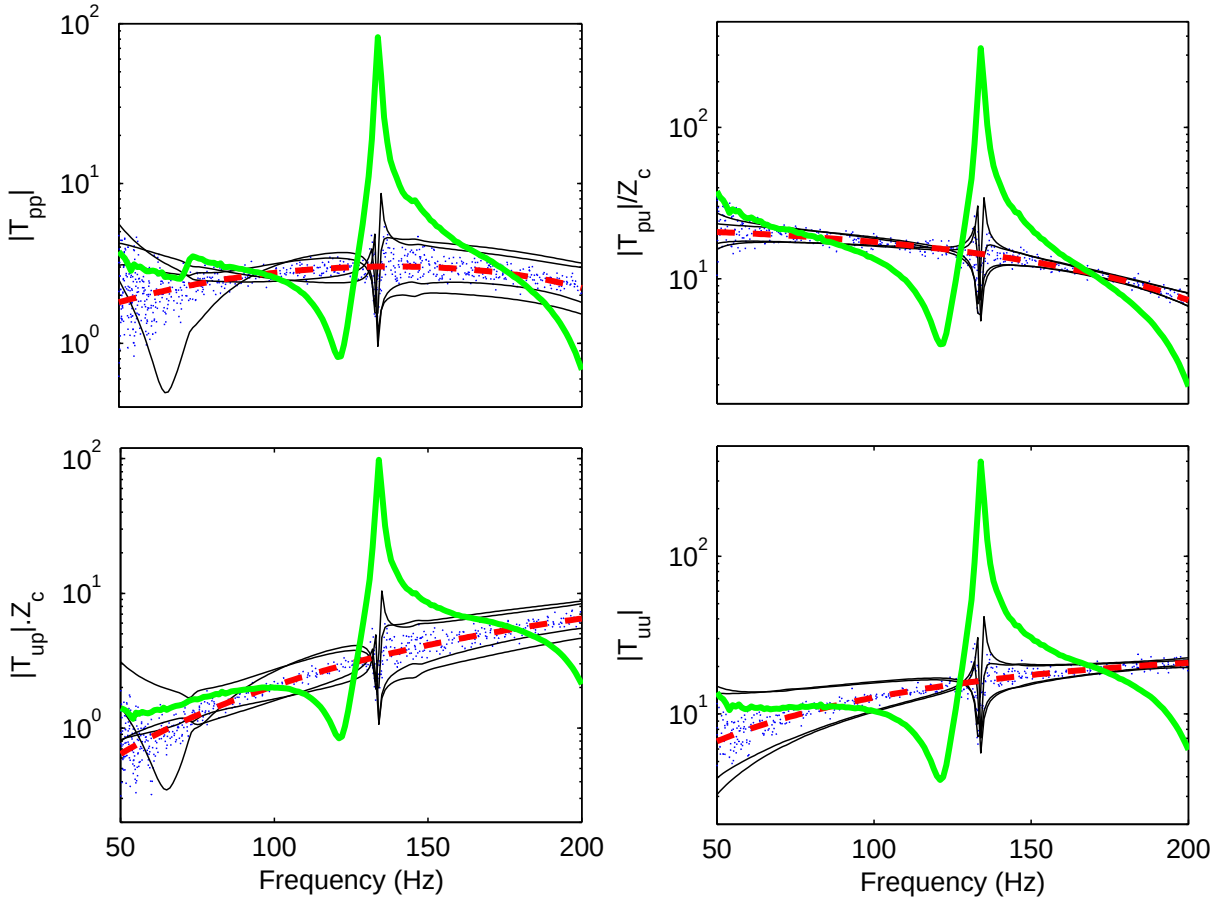

Figure 3.21: Stainless Steel Grids: amplitude of the four $\mathcal{T}$ coefficients in the frequency domain for $Q_H = 0\,W$ in bold lines for the measurements (solid) and theory (dashed), with the respective theoretical *bias* (four thin solid lines per graph) and *noise* (five dotted lines per graph). - Two-Load Method with TAC Inversion.

The $\mathbf{T}_{\mathrm{TAC}}$ coefficients, defined in Eq. (3.1), are calculated from the two-port equations that relate them to the $\mathbf{Z}_{\mathrm{TAC}}$ coefficients, as below:

$$\mathcal{T}_{pp} = \frac{\mathcal{Z}_{22}}{\mathcal{Z}_{12}}, \tag{3.53}$$

$$\mathcal{T}_{pu} = \frac{\mathcal{Z}_{12}\mathcal{Z}_{21} - \mathcal{Z}_{22}\mathcal{Z}_{11}}{\mathcal{Z}_{12}}, \tag{3.54}$$

$$\mathcal{T}_{up} = \frac{1}{\mathcal{Z}_{12}}, \tag{3.55}$$

$$\mathcal{T}_{uu} = \frac{-\mathcal{Z}_{11}}{\mathcal{Z}_{12}}. \tag{3.56}$$

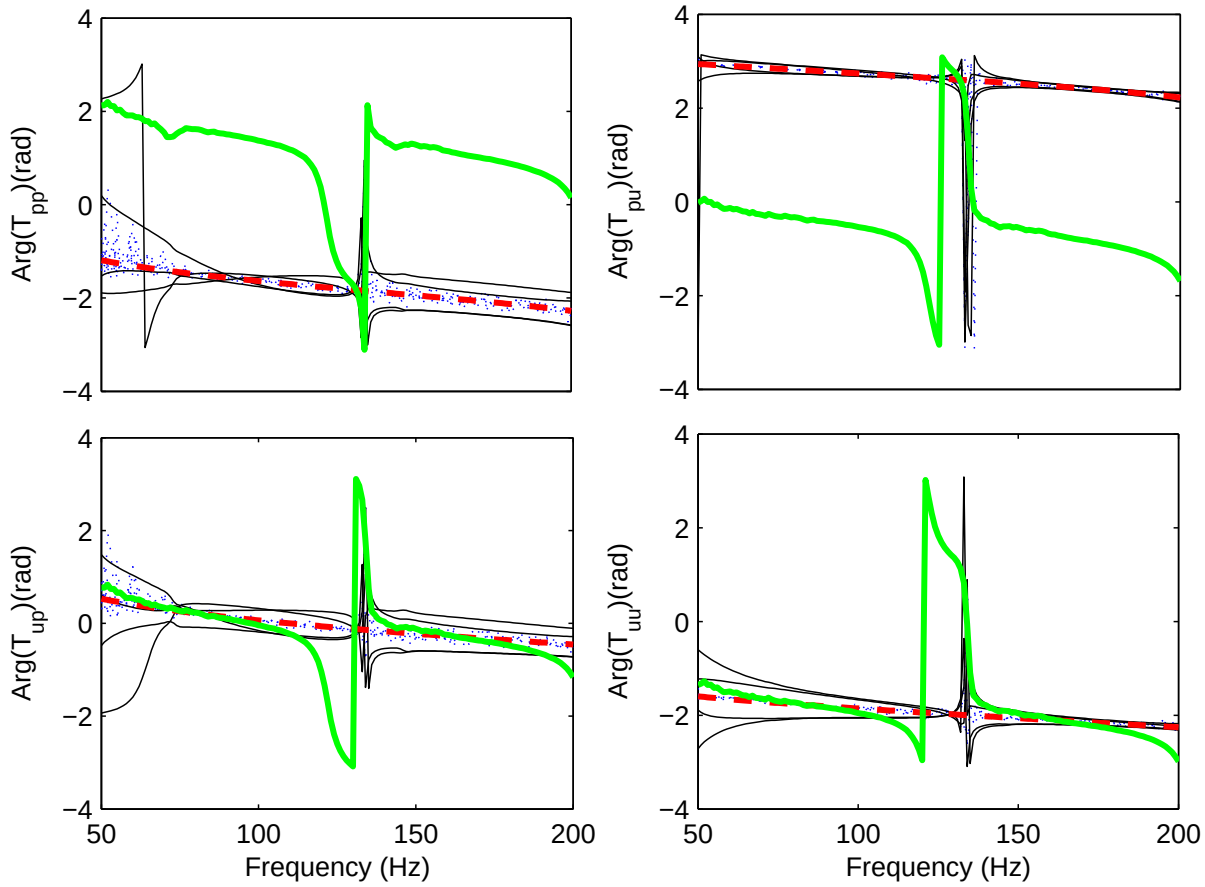

Figure 3.22: Stainless Steel Grids: phase of the four $\mathcal{T}$ coefficients in the frequency domain for $Q_H = 0\,W$ in bold lines for the measurements (solid) and theory (dashed), with the respective theoretical *bias* (four thin solid lines per graph) and *noise* (five dotted lines per graph). - Two-Load Method with TAC Inversion.

The $\mathbf{Z}_{\mathrm{TAC}}$ coefficients are obtained from two sets of measurements, since the TAC is asymmetrical (see *Framework solution for the two-port system*, in Section 3.2). That means that Eq. (3.52) provides two equations and four unknowns, and thus it requires two different setup arrangements to fulfill the 2×2 deterministic system, just as in the previous approaches. Unlike those approaches, however, the Impedance Method does not require two different acoustic loads; instead, the only difference between the first and the second measurement is the TAC orientation, which is inverted for the second measurement.

In the first measurement, the AIS is attached to the *left* side of the TAC, which is referred to as the position x_l aside of the porous material (see Figs. 3.24). In the second measurement, the AIS is placed at the opposite side, referred to as the *right* position x_r.

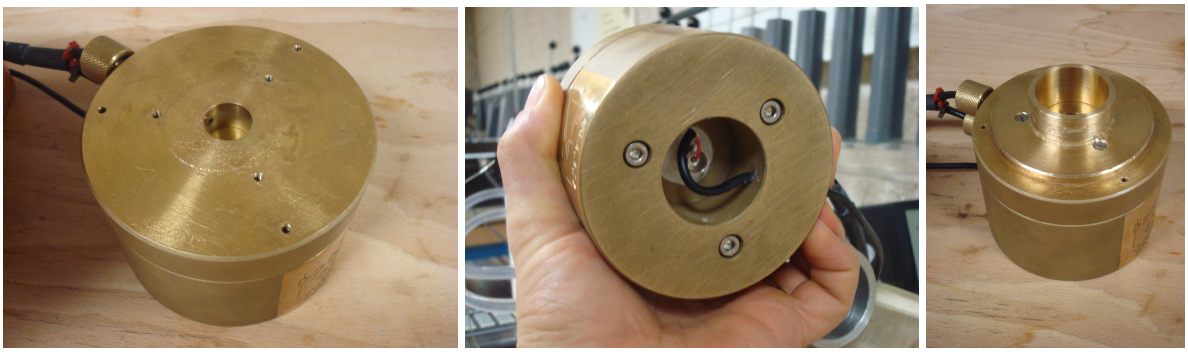

Figure 3.23: Front and back views of the AIS, and the AIS with the Adaptive Part.

For the first measurement one have:

$$\begin{pmatrix} \widetilde{p}_l^{1st} \\ \widetilde{p}_r^{1st} \end{pmatrix} = \begin{pmatrix} \mathcal{Z}_{11} & \mathcal{Z}_{12} \\ \mathcal{Z}_{21} & \mathcal{Z}_{22} \end{pmatrix} \times \begin{pmatrix} \widetilde{u}_l^{1st} \\ \widetilde{u}_r^{1st} \end{pmatrix}. \tag{3.57}$$

However, a rigid wall at $\mathbf{x_r}$ ensures the approximation $\widetilde{u}_r^{1st} \approx 0$, leading to the determination of the first column of $\mathbf{Z}_{\mathrm{TAC}}$:

$$\mathcal{Z}_{11} = \frac{\widetilde{p}_l^{1st}}{\widetilde{u}_l^{1st}}, \tag{3.58}$$

$$\mathcal{Z}_{21} = \frac{\widetilde{p}_r^{1st}}{\widetilde{u}_l^{1st}}. \tag{3.59}$$

For the second measurement it can be written

$$\begin{pmatrix} \widetilde{p}_l^{2nd} \\ \widetilde{p}_r^{2nd} \end{pmatrix} = \begin{pmatrix} \mathcal{Z}_{11} & \mathcal{Z}_{12} \\ \mathcal{Z}_{21} & \mathcal{Z}_{22} \end{pmatrix} \times \begin{pmatrix} \widetilde{u}_l^{2nd} \\ \widetilde{u}_r^{2nd} \end{pmatrix}. \tag{3.60}$$

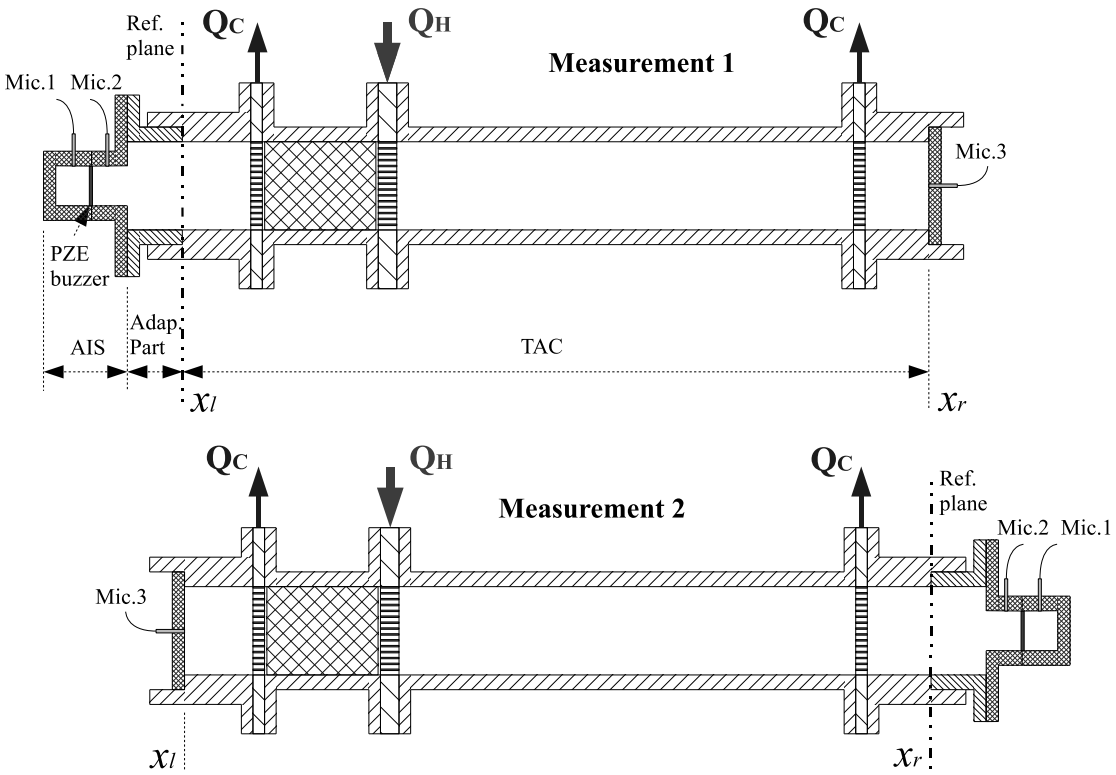

Figure 3.24: Sketch of the AIS attached to the TAC for both measurements.

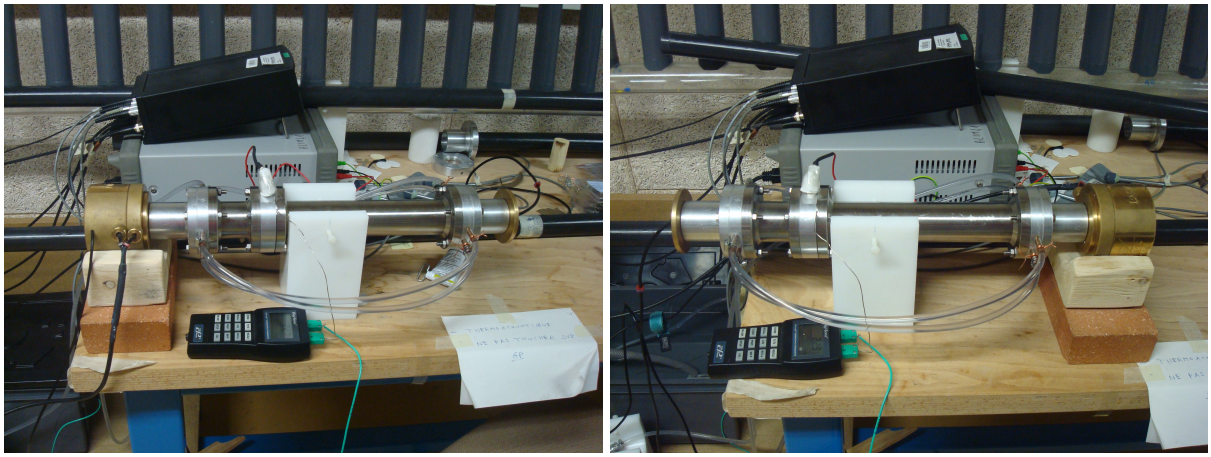

Figure 3.25: AIS attached to the TAC for both measurements.

In the case of the second measurement the rigid wall is set at x_r, and the approximation $\widetilde{u}_l^{2nd} \approx 0$ can be made. Doing so allows finding the remaining coefficients of the second column of $\mathbf{Z}_{\mathrm{TAC}}$:

$$\mathcal{Z}_{12} = \frac{\widetilde{p}_l^{2nd}}{\widetilde{u}_r^{2nd}}, \tag{3.61}$$

$$\mathcal{Z}_{22} = \frac{\widetilde{p}_r^{2nd}}{\widetilde{u}_r^{2nd}}. \tag{3.62}$$

Equations (3.58), (3.59), (3.61), and (3.62) demonstrate that $\mathbf{Z}_{\mathrm{TAC}}$ may be also written as below:

$$\mathbf{Z}_{\mathrm{TAC}} = \begin{pmatrix} \mathcal{Z}_{11} & \mathcal{Z}_{12} \\ \mathcal{Z}_{21} & \mathcal{Z}_{22} \end{pmatrix} = \begin{pmatrix} \mathcal{Z}_{inp}^{1st} & \mathcal{Z}_{T}^{2nd} \\ \mathcal{Z}_{T}^{1st} & \mathcal{Z}_{inp}^{2nd} \end{pmatrix}, \tag{3.63}$$

where $\mathcal{Z}_{inp}^{1st}$ and $\mathcal{Z}_{inp}^{2nd}$ are the *input* impedances at the TAC entry for the first and second measurements, whereas $\mathcal{Z}_{T}^{1st}$ and $\mathcal{Z}_{T}^{2nd}$ are the transfer impedances of the TAC, respective for to each measurement as well.

The Acoustic Impedance Sensor - AIS

A schematic drawing and photographs of the experimental apparatus used for the determination of the impedance matrix of a thermoacoustic core are shown in Figs. 3.24 and 3.23. The AIS itself consists of a piezoelectric buzzer loaded by a small cavity on its rear face and radiating towards a short duct on its front face, as shown in detail in Fig. 3.26. Two microphones (labeled Mic.1 and Mic. 2) are flush-mounted along the wall at both sides of the piezoelectric buzzer. The front cavity of the impedance sensor is coupled to one end of the TAC under test. The other end of the TAC is closed by a rigid wall. Mic.1 measures the pressure $p_1(t)$ inside the rear cavity, while Mic.2 measures the pressure $p_2(t)$ in the front duct. A third microphone (labeled Mic.3), flush-mounted in the center of the closing rigid wall, measures the pressure $p_3(t)$ at the end of the TAC. At low frequencies, below the first resonance of the rear cavity, the pressure is uniform in the cavity and $p_1(t)$ is proportional to the volume velocity $u(t)$ produced

by the buzzer. Then, from the measurement of pressures $p_1(t)$ and $p_2(t)$, and taking into account the acoustic propagation along the front duct, the first measurement configuration (AIS coupled to the left side of the TAC) leads to the calculation of pressure $\widetilde{p}_l$ and volume velocity $\widetilde{u}_l$ at the reference plane located at $x = x_l$, while the second configuration (AIS coupled to the right side of the TAC) leads to the calculation of pressure $\widetilde{p}_r$ and velocity $\widetilde{u}_r$ at the reference plane, this time located at $x = x_r$. Those measurements lead to the estimation of the *input* acoustic impedances $\mathcal{Z}_{inp}^{1st}$ (or $\mathcal{Z}_{11}$) and $\mathcal{Z}_{inp}^{2nd}$ (or $\mathcal{Z}_{22}$), according to Eqs. 3.58 and 3.62 respectively. The *transfer* impedances $\mathcal{Z}_{T}^{1st}$ (or $\mathcal{Z}_{21}$) and $\mathcal{Z}_{T}^{2nd}$ (or $\mathcal{Z}_{12}$) are obtained from measurements of $p_3(t) = p(x_r, t)$ and $p_3(t) = p(x_l, t)$ respectively, in accordance Eqs. 3.59 and 3.61.

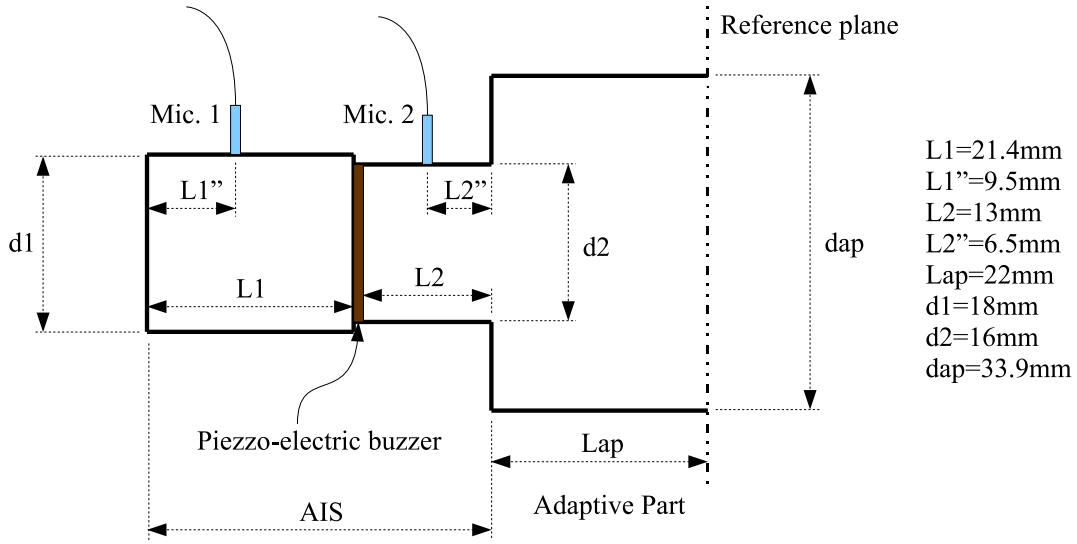

Figure 3.26: Sketch of the Acoustic Impedance Sensor and the Adaptive Part.

In order to not be restricted to very low frequencies and gain precision, more refined impedance expressions account for the microphone positions relative to the reference plane, the microphone sensitivity differences, and all geometrical dimensions concerning the AIS ducts (see Fig. 3.26). The Z-matrix coefficients $\mathcal{Z}_{inp}$ and $\mathcal{Z}_T$ for both first and second set of measurements are generally expressed as follows, as if there were no need for an Adaptive Part to connect the TAC (see Fig. 3.24), nor any relevant waveguide discontinuity. These equations (Macaluso, 2011; Le Roux, 2012) take as reference plane the position just at the exit of the AIS, with $L_{ap} = 0$. To distinguish those generalized impedances from the actual impedances with a real Adaptive Part ($L_{ap} > 0$), they are here assigned as $\mathcal{Z}'_{inp}$ (Eq. (3.64)) and $\mathcal{Z}'_T$ (Eq. (3.65)).

$$\mathcal{Z}'_{inp} = \frac{(\widetilde{H}_{21}/K) - \beta}{1 - (\delta \widetilde{H}_{21}/K)}, \tag{3.64}$$

$$\mathcal{Z}'_{T} = \frac{\widetilde{H}_{31}\left(1 + \delta \mathcal{Z}'_{inp}\right)}{\delta K_T}. \tag{3.65}$$

where the terms

$$\widetilde{H}_{ij} = \frac{\widetilde{p}_i \widetilde{s}_i}{\widetilde{p}_j \widetilde{s}_j} \tag{3.66}$$

are the transfer functions that relate the sound pressure measurements, and $\widetilde{s}_i$ refers to the sensitivity of Mic."i". The terms β and δ are developed from cylindrical waveguide solutions, while K and K_T are related to the calibration of the device (Macaluso, 2011; Le Roux, 2012).

Their corresponding expressions are given in the below:

$$\beta = j Z_{c2} \tan(k L_2^{"}), \tag{3.67}$$

$$\delta = j \tan(k L_2)/Z_{c2}, \tag{3.68}$$

$$K = -j \frac{1}{Z_{c1}} \frac{\widetilde{s}_2}{\widetilde{s}_1} \frac{\sin(k L_1)\cos(k L_2^{"})}{\cos(k L_1^{"})\cos(k L_2)}, \tag{3.69}$$

$$K_T = -\frac{Z_{c2}}{Z_{c1}} \frac{\widetilde{s}_3}{\widetilde{s}_1} \frac{\sin(k L_1)}{\sin(k L_2)\cos(k L_1^{"})}, \tag{3.70}$$

where the dimensions L_1, L_2, $L_1^{"}$ and $L_2^{"}$ provide the cavities lengths and microphones positions, according to Fig. 3.26; the characteristic impedances $Z_{c1} = \frac{\rho c}{S_1}$ and $Z_{c2} = \frac{\rho c}{S_2}$ correspond to the back and front cavities, with their respective cross sections $S_1 = \pi d_1^2/4$ and

$S_2 = \pi d_2^2/4$; the wavenumber $k = 2\pi f/c$ does not account for losses in such small environments, with frequency f in Hz and speed of sound $c \approx 344\,m/s$ at $22\,°C$; and the sensitivities $\widetilde{s}_1$, $\widetilde{s}_2$ and $\widetilde{s}_3$ correspond to the three microphones.

The calibration process is, at first, to remove the TAC and close the acoustic impedance sensor by the rigid plate that supports the microphone 3 (see Fig. mic3). The transfer functions $\widetilde{H}_{21}$ and $\widetilde{H}_{31}$ are then measured and here labeled with the subscript "cal". As a consequence of such a configuration, the impedance at the reference plane is the same as the transfer impedance to the microphone 3 due to the fact that the position is coincident. Assuming $1/\mathcal{Z}_{11,cal} = 1/\mathcal{Z}_{21,cal} \approx 0$ leads to $K = \delta\widetilde{H}_{21,cal}$ and $K_T = \widetilde{H}_{31,cal}$ (Macaluso, 2011). Therefore, as a final result of the calibration, the parameters K and K_T are obtained from the measurements of $\widetilde{H}_{21,cal}$ and $\widetilde{H}_{31,cal}$, and both ratios of sensitivity $\widetilde{s}_2/\widetilde{s}_1$ and $\widetilde{s}_3/\widetilde{s}_1$ are implicitly taken into account. The substitution of K and K_T into Eqs. (3.64) and (3.65) gives

$$\mathcal{Z}'_{inp} = \frac{1}{\delta}\frac{(\widetilde{H}_{21}/\widetilde{H}_{21,cal}) - \delta\beta}{1 - (\widetilde{H}_{21}/\widetilde{H}_{21,cal})}, \tag{3.71}$$

$$\mathcal{Z}'_T = \frac{\widetilde{H}_{31}\left(1 + \delta\mathcal{Z}'_{inp}\right)}{\delta\widetilde{H}_{31,cal}}. \tag{3.72}$$

Consideration of the waveguide discontinuity

The AIS used in this work delivers the acoustic excitation to the TAC under an important geometrical discontinuity. That comes from the sudden diameter variation between the AIS exit and the Adaptive Part, which is from $16\,mm$ to $33.9\,mm$ in an angle of 90 degrees (see Figs. 3.26 and 3.24). The resulting effect is an additional impedance that is here taken into account to improve the measurements accuracy. This impedance is labeled $\mathcal{Z}_{dis}$, and it is subtracted from the first hand measured *input* impedances by the AIS, so that to obtain the corrected $\mathbf{Z}_{\mathrm{TAC}}$ coefficients, which, for instance, do not account for the Adaptive Part yet.

$\mathcal{Z}_{dis}$ is calculated according to the following algorithm (Kergomard, 1987):

• R_{min} is the minimal value between r_2/r_{ap} and r_{ap}/r_2, where r_2 is the AIS front cavity radius and r_{ap} is the Adaptive Part radius;

• If $R_{min} \leqslant 0.55$

then $k_{cor} = 0.82(1 - 1.35R_{min} + 0.31R_{min}^3)$, with k_{cor} being the corrected wavenumber;

◦ else $k_{cor} = \frac{4}{\pi}R_{min1}^2[0.5035 - 0.492log(R_{min1}) - 0.376R_{min1}^2 - 0.852R_{min1}^2 log(R_{min1})]$, where $R_{min1} = 1 - R_{min}$;

• If $r_2 \leqslant r_{ap}$

then $l_{cor} = k_{cor}r_{ap}/R_{min}$, where l_{cor} is the equivalent length;

◦ else $l_{cor} = k_{cor}r_{ap}$;

• Concluding, $\mathcal{Z}_{dis}$ results in

$$\mathcal{Z}_{dis} = \frac{jk_0 l_{cor}}{S_{ap}\rho c}, \tag{3.73}$$

where k_0 is the wavenumber without losses, $S_{ap} = \pi r_{ap}^2$, and ρ is the average gas density.

Applying $\mathcal{Z}_{dis}$ into Eqs. (3.71) and (3.72),

$$\mathcal{Z}'_{inp,dis} = \frac{1}{\delta}\frac{(\widetilde{H}_{21}/\widetilde{H}_{21,cal}) - \delta\beta}{1 - (\widetilde{H}_{21}/\widetilde{H}_{21,cal})} - \mathcal{Z}_{dis}, \tag{3.74}$$

$$\mathcal{Z}'_{T,dis} = \frac{\widetilde{H}_{31}\left(1 + \delta\mathcal{Z}'_{inp,dis}\right)}{\delta\widetilde{H}_{31,cal}}. \tag{3.75}$$

Nevertheless, an Adaptive Part must be provided to connect the AIS to the specific system under analysis, which is the TAC in this study. The Adaptive Part is specifically designed for that, and consists in a short waveguide section of $22\,mm$ length and same diameter as the TAC ends. Therefore, its acoustical effects are not negligible, reminding that the TAC length is only $460\,mm$.

Consideration of the Adaptive Part

In order to take into account the length of the Adaptive Part, which is $L_{ap} = 22mm$, the reference plane is established in between this part and the TAC, as shown in Figs. 3.23, 3.24 and 3.26. That requires changing the reference plane from the AIS exit to the TAC input, which may be at the position x_r or x_l, depending on whether the TAC is inverted or not, respectively. The resulting expressions are:

$$\mathcal{Z}_{inp} = \frac{\cos(k_w L_{ap})\mathcal{Z}'_{inp,dis} + jZ_{cc}\sin(k_w L_{ap})}{\frac{j}{Z_{cc}}\sin(k_w L_{ap})\mathcal{Z}'_{inp,dis} + \cos(k_w L_{ap})}, \tag{3.76}$$

$$\mathcal{Z}_T = \frac{\mathcal{Z}'_{T,dis}}{\frac{j}{Z_{cc}}\sin(k_w L_{ap})\mathcal{Z}'_{inp,dis} + \cos(k_w L_{ap})}. \tag{3.77}$$

Final equations for the $\mathrm{Z_{TAC}}$ and the $\mathrm{T_{TAC}}$ coefficients

Substituting Eqs. (3.74) and (3.75) into Eqs. (3.76) and (3.77), and also rearranging the resulting equations to make explicit the first and second measurements, each $\mathbf{Z}_{\mathrm{TAC}}$ coefficient is described as follows:

$$\mathcal{Z}_{11} = \mathcal{Z}_{inp}^{1st} = \frac{\widetilde{p}_l^{1st}}{\widetilde{u}_l^{1st}} = \frac{\cos(k_w L_{ap})\left[\frac{1}{\delta}\frac{(\widetilde{H}_{21}^{1st}/\widetilde{H}_{21,cal}) - \delta\beta}{1-(\widetilde{H}_{21}^{1st}/\widetilde{H}_{21,cal})} - \mathcal{Z}_{dis}\right] + jZ_{cc}\sin(k_w L_{ap})}{\frac{j}{Z_{cc}}\sin(k_w L_{ap})\left[\frac{1}{\delta}\frac{(\widetilde{H}_{21}^{1st}/\widetilde{H}_{21,cal}) - \delta\beta}{1-(\widetilde{H}_{21}^{1st}/\widetilde{H}_{21,cal})} - \mathcal{Z}_{dis}\right] + \cos(k_w L_{ap})}, \tag{3.78}$$

$$\mathcal{Z}_{12} = \mathcal{Z}_T^{2nd} = \frac{\widetilde{p}_l^{2nd}}{\widetilde{u}_r^{2nd}} = \frac{\frac{\widetilde{H}_{31}^{2nd}}{\delta\widetilde{H}_{31,cal}}\left(1+\delta\left[\frac{1}{\delta}\frac{(\widetilde{H}_{21}^{2nd}/\widetilde{H}_{21,cal}) - \delta\beta}{1-(\widetilde{H}_{21}^{2nd}/\widetilde{H}_{21,cal})} - \mathcal{Z}_{dis}\right]\right)}{\frac{j}{Z_{cc}}\sin(k_w L_{ap})\left[\frac{1}{\delta}\frac{(\widetilde{H}_{21}^{2nd}/\widetilde{H}_{21,cal}) - \delta\beta}{1-(\widetilde{H}_{21}^{2nd}/\widetilde{H}_{21,cal})} - \mathcal{Z}_{dis}\right] + \cos(k_w L_{ap})}, \tag{3.79}$$

$$\mathcal{Z}_{21} = \mathcal{Z}_T^{1st} = \frac{\widetilde{p}_r^{1st}}{\widetilde{u}_l^{1st}} = \frac{\dfrac{\widetilde{H}_{31}^{1st}}{\delta \widetilde{H}_{31,cal}} \left(1 + \delta \left[\dfrac{1}{\delta} \dfrac{(\widetilde{H}_{21}^{1st} / \widetilde{H}_{21,cal}) - \delta\beta}{1 - (\widetilde{H}_{21}^{1st} / \widetilde{H}_{21,cal})} - \mathcal{Z}_{dis} \right] \right)}{\dfrac{j}{Z_{cc}} \sin(k_w L_{ap}) \left[\dfrac{1}{\delta} \dfrac{(\widetilde{H}_{21}^{1st} / \widetilde{H}_{21,cal}) - \delta\beta}{1 - (\widetilde{H}_{21}^{1st} / \widetilde{H}_{21,cal})} - \mathcal{Z}_{dis} \right] + \cos(k_w L_{ap})}, \tag{3.80}$$

$$\mathcal{Z}_{22} = \mathcal{Z}_{inp}^{2nd} = \frac{\widetilde{p}_r^{2nd}}{\widetilde{u}_r^{2nd}} = \frac{\cos(k_w L_{ap}) \left[\dfrac{1}{\delta} \dfrac{(\widetilde{H}_{21}^{2nd} / \widetilde{H}_{21,cal}) - \delta\beta}{1 - (\widetilde{H}_{21}^{2nd} / \widetilde{H}_{21,cal})} - \mathcal{Z}_{dis} \right] + j Z_{cc} \sin(k_w L_{ap})}{\dfrac{j}{Z_{cc}} \sin(k_w L_{ap}) \left[\dfrac{1}{\delta} \dfrac{(\widetilde{H}_{21}^{2nd} / \widetilde{H}_{21,cal}) - \delta\beta}{1 - (\widetilde{H}_{21}^{2nd} / \widetilde{H}_{21,cal})} - \mathcal{Z}_{dis} \right] + \cos(k_w L_{ap})} \tag{3.81}$$

Finally, the substitution of the $\mathbf{Z}_{\mathrm{TAC}}$ coefficients into Eqs. (3.53) to (3.56) leads to the determination of $\mathbf{T}_{\mathrm{TAC}}$.

3.6.2 Sensitivity analysis for the Impedance Method

Before starting with the actual measurements, a sensitivity analysis for the Impedance Method is put forward. That way, if not promising, this third attempt would be dismissed and another solution would be researched. Just like the previous approaches, the same procedures are here applied, except that, instead of adding *noise* and *bias* into the theoretical transfer functions, those disturbances are inserted into the theoretical impedances. Thus, Eqs. (3.50) and (3.51) turn into the equivalent ones below:

$$\mathcal{Z}_{noise}^i = |\mathcal{Z}^i|(1 + A_n F_r^i) e^{j(\varphi(\mathcal{Z}^i) + P_n F_r^i)}, \tag{3.82}$$

$$\mathcal{Z}_{bias} = |\mathcal{Z}|(1 + A_b) e^{j(\varphi(\mathcal{Z}) + P_b)}, \tag{3.83}$$

with A_n, A_b, P_n and P_b being setup at the same levels as for the previous two approaches.

The results are explored in the next four figures from 3.27 to 3.30, handling the Stainless Steel Grids and the Ceramic Catalyst as well. The frequency range chosen for this sensitivity analysis is the same as for the previous approaches, from 50 to 200 Hz, despite of the fact that the actually measured frequency range is much wider, from 30 to 500 Hz. That way, performance comparisons can be made under uniform basis.

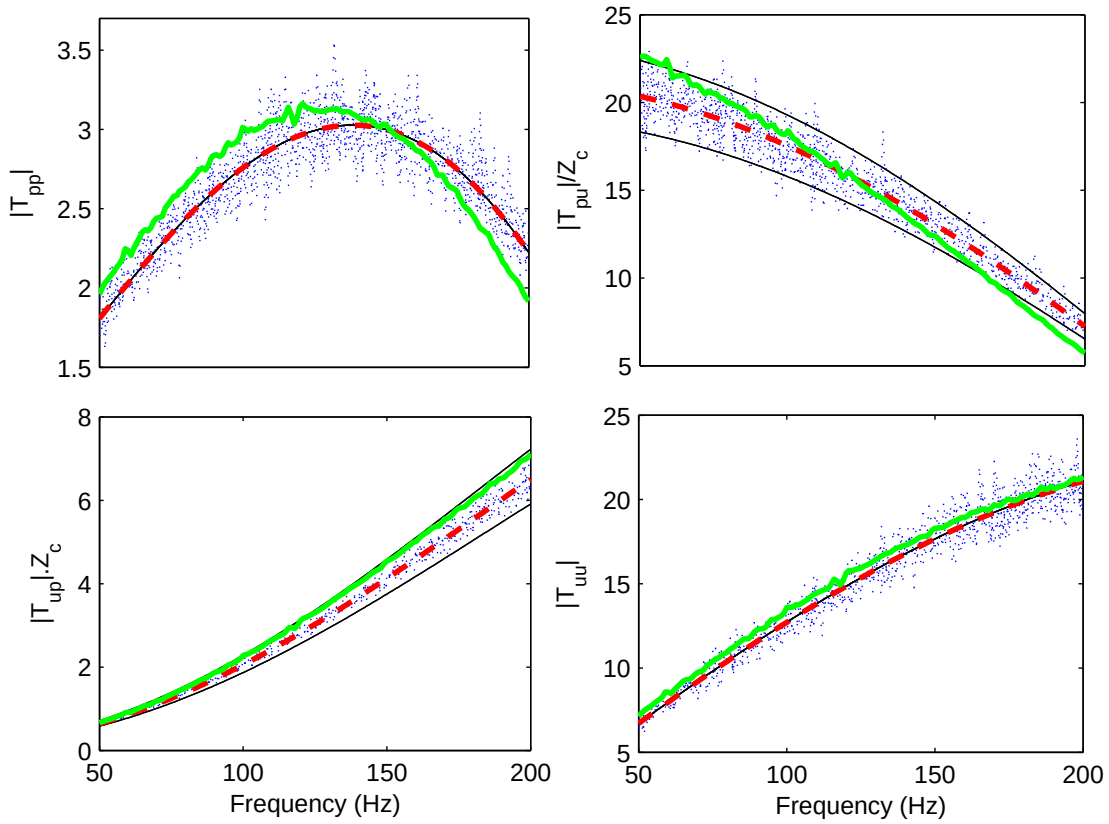

Figure 3.27: Stainless Steel Grids: amplitude of the four $\mathcal{T}$ coefficients in the frequency domain for $Q_H = 0\,W$ in bold lines for the measurements (solid) and theory (dashed), with the respective theoretical *bias* (four thin solid lines per graph) and *noise* (five dotted lines per graph). - Impedance Method.

Figures 3.27 and 3.28 present a smaller sensitivity to *noise* and *bias* for the Stainless Steel Grids in comparison with the previous two-load approaches. That encourages to proceed with actual measurements, which are beforehand presented in these figures by practical purposes, as a matter of fact. The experimental curves behave in good agreement to the semi-theoretical ones, and they are also coherently within the sensitivity constraints. Indeed, the reciprocity parameters $\mathbf{rc} = 1.004 + 0.009i$ and $\sigma_{\mathbf{rc}} = 0.008 + 0.007i$ contribute to verify such agreement. Therefore, at least for a regenerator-like material so far, the Impedance Method is surely proved to be performing. To continue with this method evaluation, a stack-like material - namely the Ceramic Catalyst - is investigated in the following.

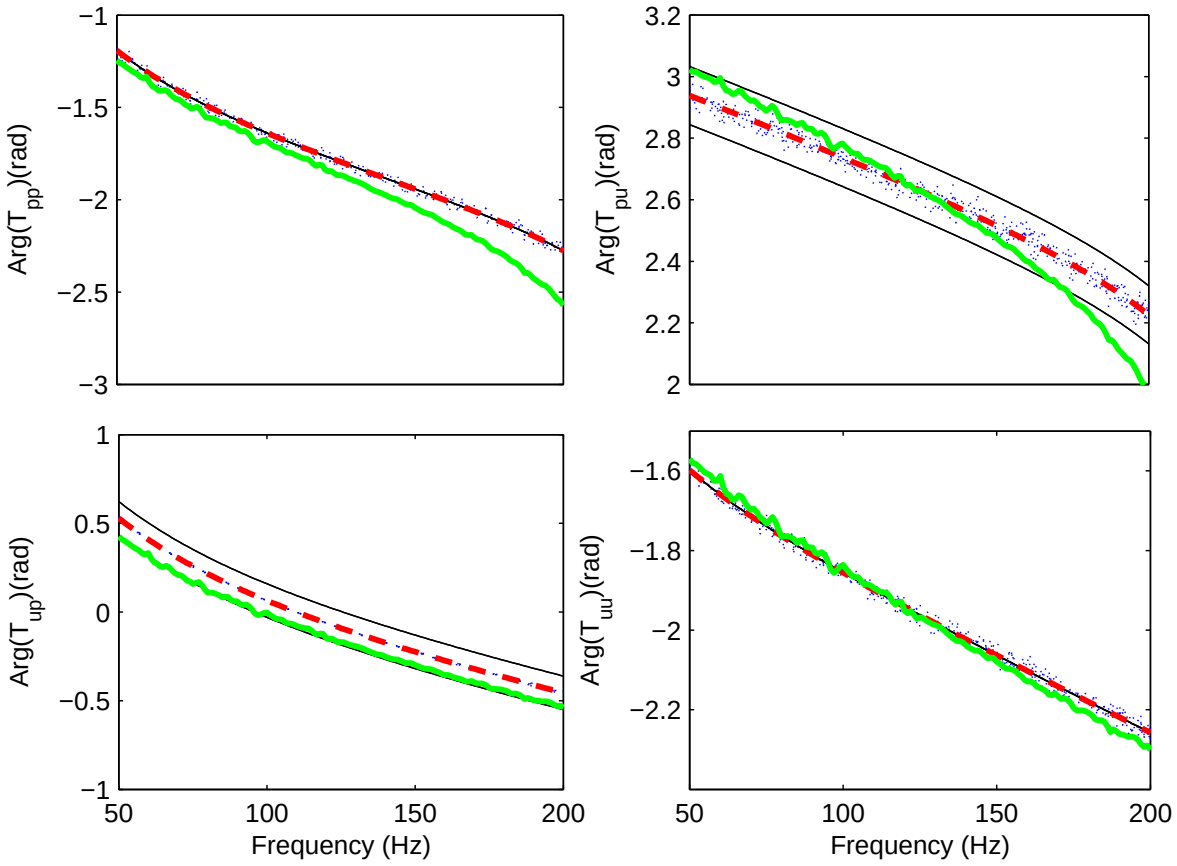

Figure 3.28: Stainless Steel Grids: phase of the four $\mathcal{T}$ coefficients in the frequency domain for $Q_H = 0\,W$ in bold lines for the measurements (solid) and theory (dashed), with the respective theoretical *bias* (four thin solid lines per graph) and *noise* (five dotted lines per graph). - Impedance Method.

Finally, as the conclusive part of the sensitivity analysis, Figs. 3.29 and 3.30 reveal that the Impedance Method is also promising for stack-like materials. The sensitivity predictions for *noise* and *bias* are even better than for the Two-Load Method, as it may be clearly seen. To support this, the experimental curves for the Ceramic Catalyst (beforehand presented) behave in good agreement with the purely theoretical ones. For this material, are recorded the best reciprocity parameters within the 50 to $200\,Hz$ range in this investigation: $\mathbf{rc} = 1.002 - 0.001i$ and $\sigma_{\mathbf{rc}} = 0.001 + 0.002i$ (see Table 3.2).

To conclude the sensitivity analysis for the Impedance Method and also embracing Section 3.5, the Impedance Method is the best method among the three methods tested, as it is the least sensitive to *noise* and *bias*, and as it covers both stack-like and regenerator-like materials. Relying on these results, the Impedance Method is used for subsequent works. In particular, other materials can be tested as stack/regenerator, such as NiCr Foam and RVC Foam.

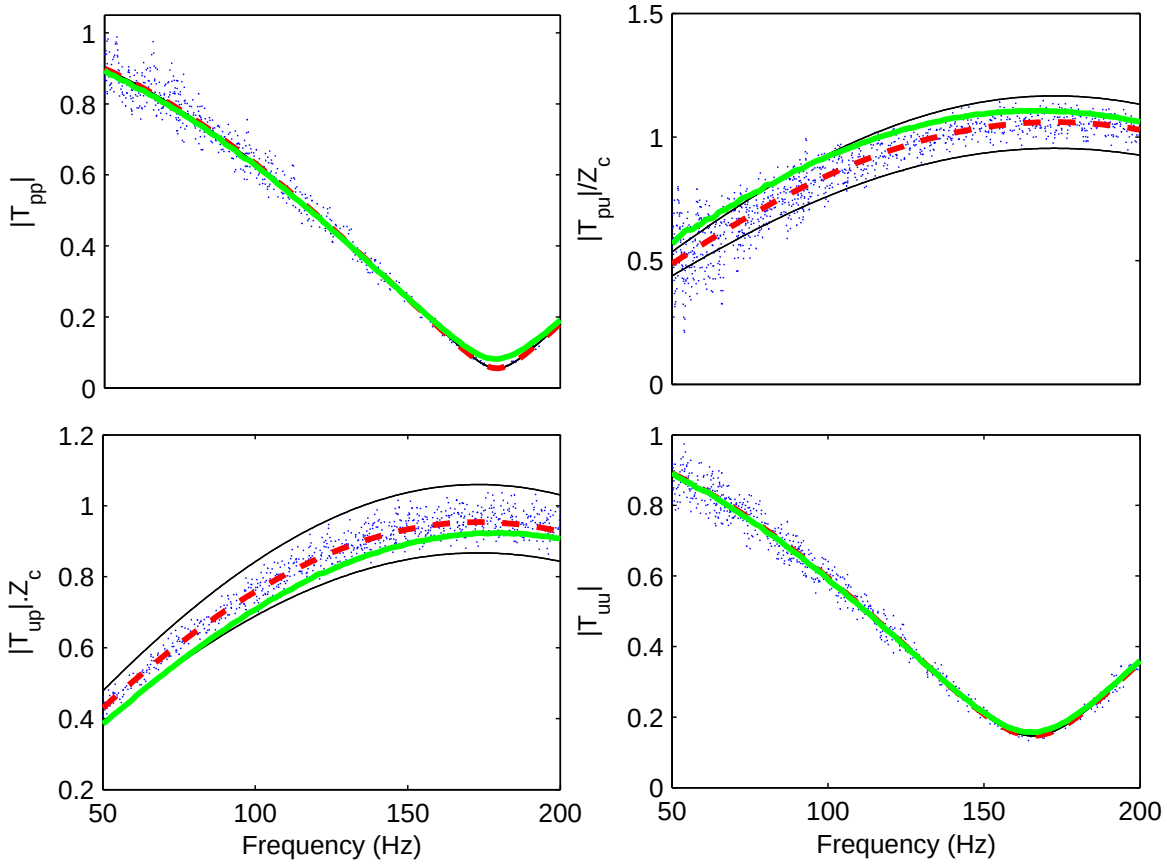

Figure 3.29: Ceramic Catalyst: amplitude of the four $\mathcal{T}$ coefficients in the frequency domain for $Q_H = 0\,W$ in bold lines for the measurements (solid) and theory (dashed), with the respective theoretical *bias* (four thin solid lines per graph) and *noise* (five dotted lines per graph). - Impedance Method.

3.6.3 Experimental setup and procedures

The experimental procedure for the measurement of the impedance matrix $\mathbf{Z}_{\mathrm{TAC}}$ is described below. Each sample is heated by means of a heat power supply Q_H increasing from 0 up to $81\,W$ by steps of $9\,W$. The measurements are made for each heat condition for the first configuration (AIS coupled to the left side of the TAC, see Fig. 3.24, "Measurement 1"). Afterwards, the heat power supply is turned off. The TAC is then naturally cooled and it reaches the ambient temperature homogeneously after a few hours. Subsequently, the impedance sensor is inverted (see Fig. 3.24, "Measurement 2") and the same sequence of measurements is applied, following the same rising heat supplies and keeping the same time intervals between them, in order to obtain a thermal field inside the TAC as similar as possible to the one obtained in the previous set of measurements. Nevertheless, this procedure may be sensitive to ambient

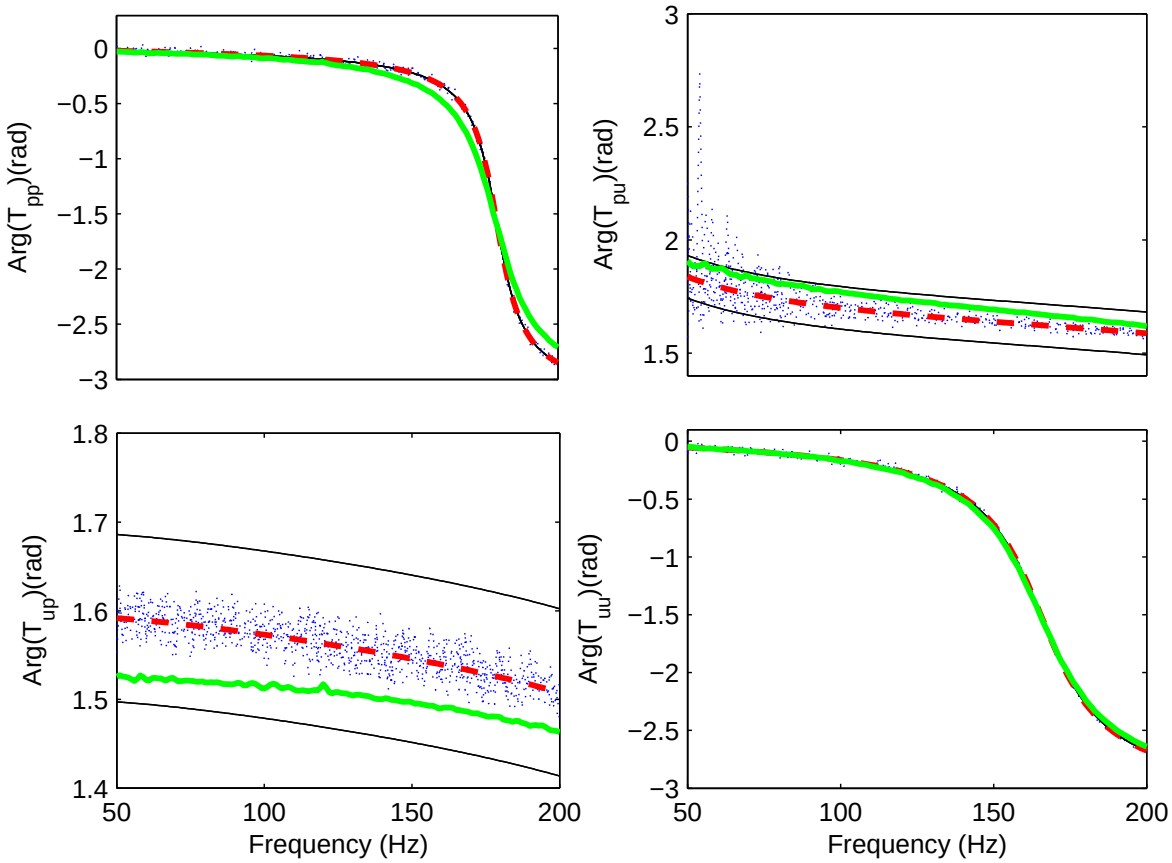

Figure 3.30: Ceramic Catalyst: phase of the four $\mathcal{T}$ coefficients in the frequency domain for $Q_H = 0\,W$ in bold lines for the measurements (solid) and theory (dashed), with the respective theoretical *bias* (four thin solid lines per graph) and *noise* (five dotted lines per graph). - Impedance Method.

temperature variations, or even pressure variations, as the total duration of both sequences of measurements takes several hours. But proceeding this way leads to the best results. As with the previous approaches, all transient thermal guidelines stated in Appendix A are here respected as well. As explained before, the acoustic impedance sensor allows measurements in a much wider frequency range than the Two-Load Method does. Hence, it is chosen to investigate the problem within the interval between 30 to $500\,Hz$, by steps of $1\,Hz$. This allows investigation of a wide range of operating frequencies for different engines configurations. Those results are displayed in the following (Subsection 3.6.4) and in also Appendix D.

3.6.4 Results

In this section, results are given for TAC made of a pile of Stainless Steel Grids, a Ceramic Catalyst, a NiCr Foam (Fig. 3.31) and a RVC Foam (Fig. 3.32). Table 3.2 reports $\mathbf{rc}$ and $\sigma_{\mathbf{rc}}$ for all four materials in two frequency ranges: from 50 to $200\,Hz$, for comparisons with results of the previous approaches (also included), and from 30 to $500\,Hz$, which is the range actually here covered by the Impedance Method. That way, a clear overview of performances of all three approaches is provided. Columns 1, 2 and 3 correspond to the respective three approaches and refer to the narrower frequency range; they consist of results already discussed in the sensitivity analysis (see Section 3.5 and Subsection 3.6.2). The last column, on the other hand, concerns the Impedance Method for the wider frequency range. The Impedance Method provides the best results in all cases, no matter the material kind or frequency range. When comparing third and fourth columns, one can realize a slight decrease in performance for the wider frequency range - particularly for the $\sigma_{\mathbf{rc}}$ values - that indicates some additional *noise* effects. Indeed, such effects are predictable since the wider frequency range reaches a lower limit, $30\,Hz$; this additional interval from 30 to $49\,Hz$ is more susceptible to external influences like the *noise* from the water pump, for example. However, those $\sigma_{\mathbf{rc}}$ values are still low and the reciprocity is considered verified either way.

		Two-Load	Two-Load (Inv.)	Impedance	Imp.(30-$500\,Hz$)
Ceramic Catalyst	$\mathbf{rc}$	$1.010 + 0.002i$	$-$	$1.002 - 0.001i$	$1.003 + 0.000i$
	$\sigma_{\mathbf{rc}}$	$0.002 + 0.002i$	$-$	$0.001 + 0.002i$	$0.003 + 0.003i$
Stainless Steel Grids	$\mathbf{rc}$	$0.996 + 0.005i$	$0.243 - 1.727i$	$1.004 + 0.009i$	$1.003 + 0.006i$
	$\sigma_{\mathbf{rc}}$	$0.134 + 0.123i$	$3.787 + 4.238i$	$0.008 + 0.007i$	$0.010 + 0.012i$
RVC Foam	$\mathbf{rc}$	$-$	$-$	$1.000 - 0.002i$	$0.999 + 0.002i$
	$\sigma_{\mathbf{rc}}$	$-$	$-$	$0.002 + 0.002i$	$0.004 + 0.004i$
NiCr Foam	$\mathbf{rc}$	$-$	$-$	$1.001 - 0.000i$	$1.001 - 0.002i$
	$\sigma_{\mathbf{rc}}$	$-$	$-$	$0.002 + 0.001i$	$0.002 + 0.002i$

Table 3.2: Average reciprocities and standard deviations in the frequency range from 50 to $200\,Hz$ for all three approaches and also from 30 to $500\,Hz$ for the Impedance Method.

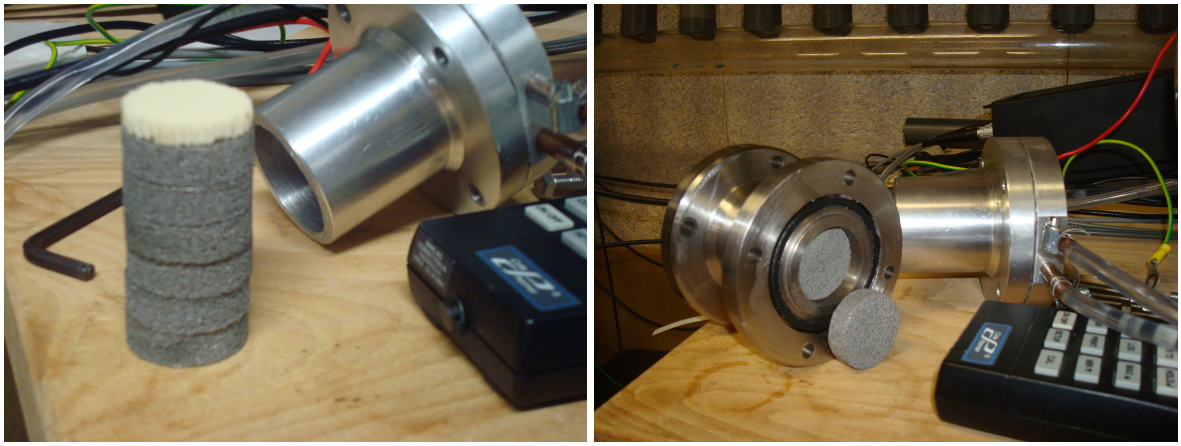

Figure 3.31: Nichrome Foam (six discs), a ceramic washer and the stack/regenerator holder.

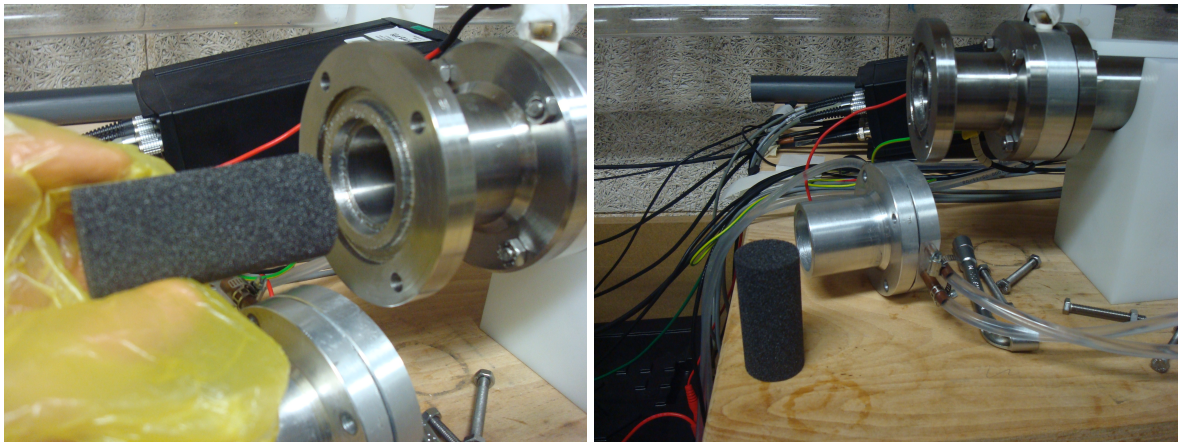

Figure 3.32: Reticulated Vitreous Carbon (RVC) Foam and the open TAC.

The resulting $\mathbf{T}_{\mathrm{TAC}}$ coefficients, deduced from Z_{TAC} measurements, are shown below following the same sequence of Table 3.2, in the frequency range from 30 to $500\,Hz$. Only three heating conditions ($Q_H = 0$, $Q_H = 36\,W$ and $Q = 72\,W$) are shown in this section, for the sake of clarity, just like for the results of the first approach. However, the RVC Foam requires lowering the upper limit of heat input, to avoid its spontaneous combustion, as the whole experimentation is in the presence of atmospheric air. That ended up in lower heating conditions ($Q_H = 0$, $Q_H = 9\,W$ and $Q_H = 18\,W$), according to a specific investigation that led to this finding: measuring the steady state temperature just aside of the HHX, by means of a thermocouple (Fig. 3.33), the temperature reached $\approx 230°C$ for $Q_H = 15\,W$, and $\approx 262°C$ for $Q_H = 18\,W$; hence, a next step of $Q_H = 21\,W$ would have been risky since the temperature limit for the RVC Foam integrity in the presence of oxygen is around $300°C$.

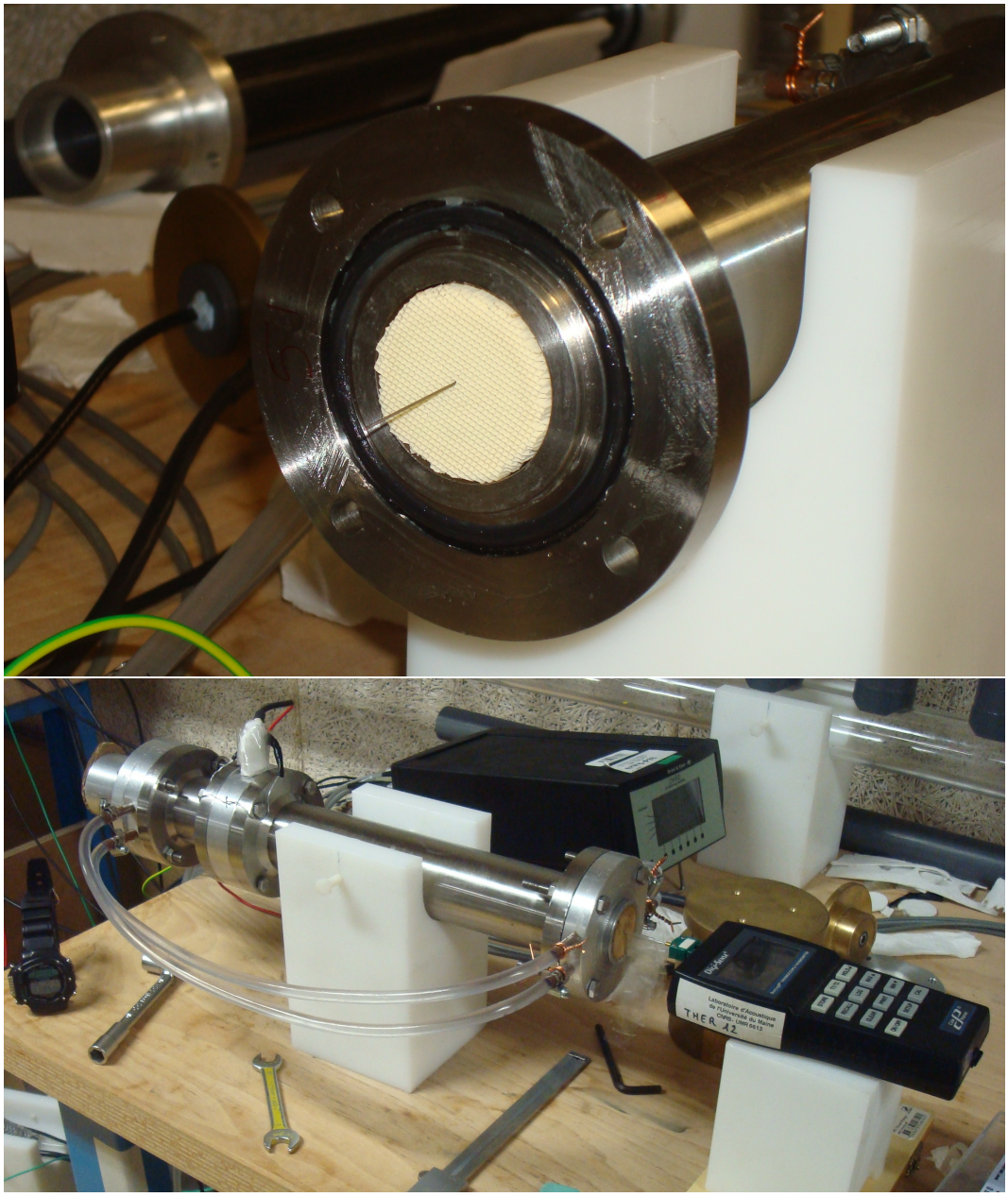

Figure 3.33: Temperature measurements at the right side of the HHX by means of a $35\,cm$ long thermocouple accessing it from the TAC right side; the RVC Foam is within the TAC.

Case of the pile of Stainless Steel Grids

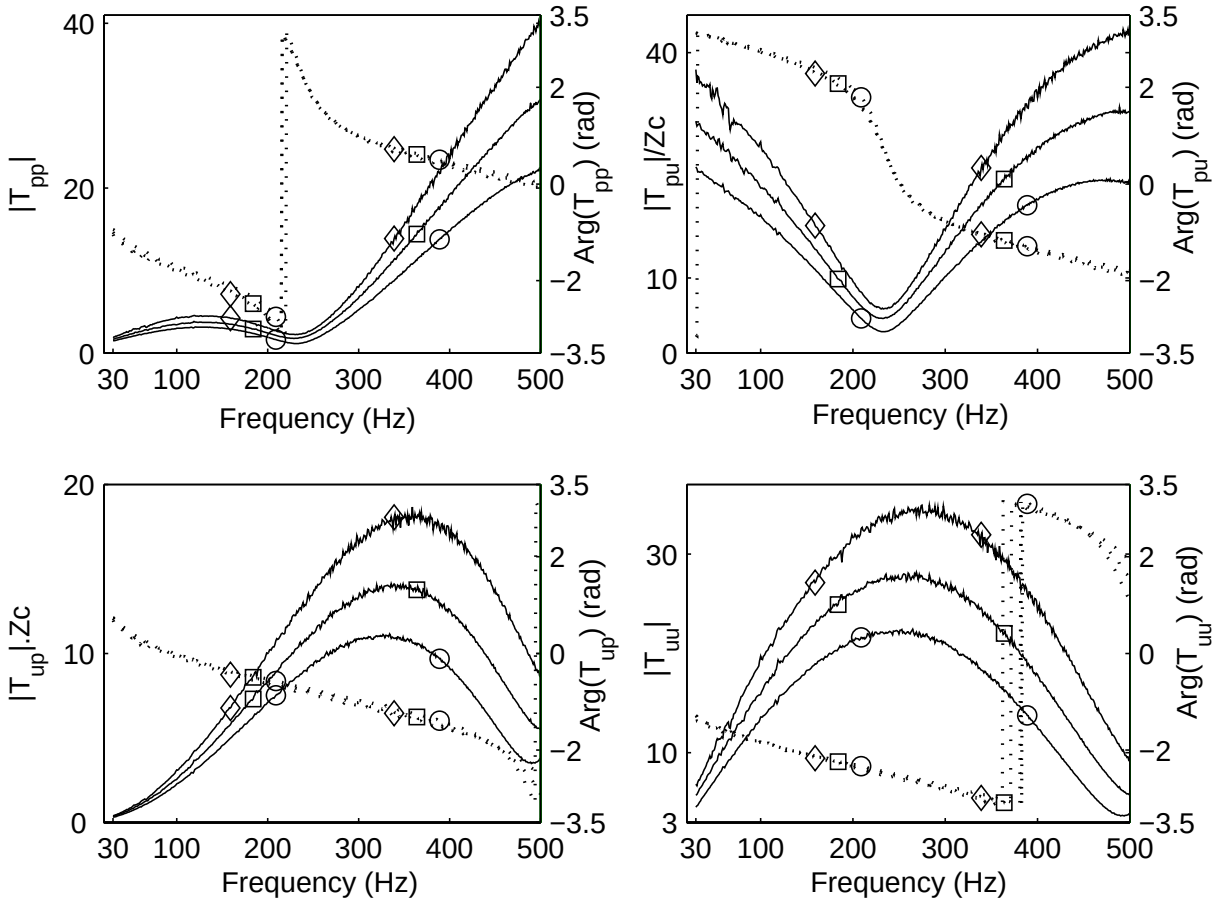

Figure 3.34: Stainless Steel Grids: amplitude (solid line) and phase (dotted line) of the $\mathbf{T}_{\mathrm{TAC}}$ coefficients in the frequency domain for $Q_H = 0\,W(circle)$, $Q_H = 36\,W(square)$ and $Q_H = 72\,W(diamond)$ - Impedance Method.

Case of the Ceramic Catalyst

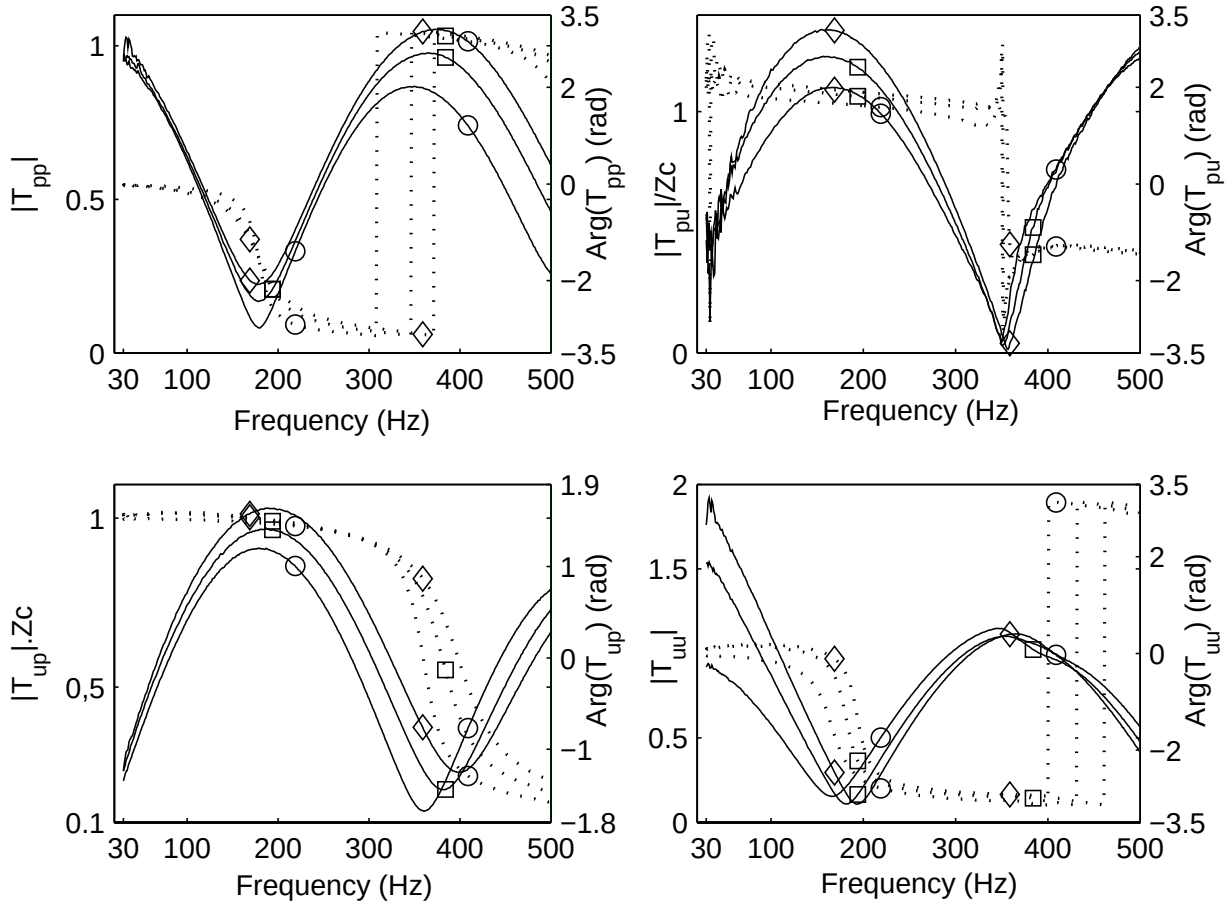

Figure 3.35: Ceramic Catalyst: amplitude (solid line) and phase (dotted line) of the $\mathbf{T}_{\mathrm{TAC}}$ coefficients in the frequency domain for $Q_H = 0\,W(circle)$, $Q_H = 36\,W(square)$ and $Q_H = 72\,W(diamond)$ - Impedance Method.

Case of the NiCr Foam

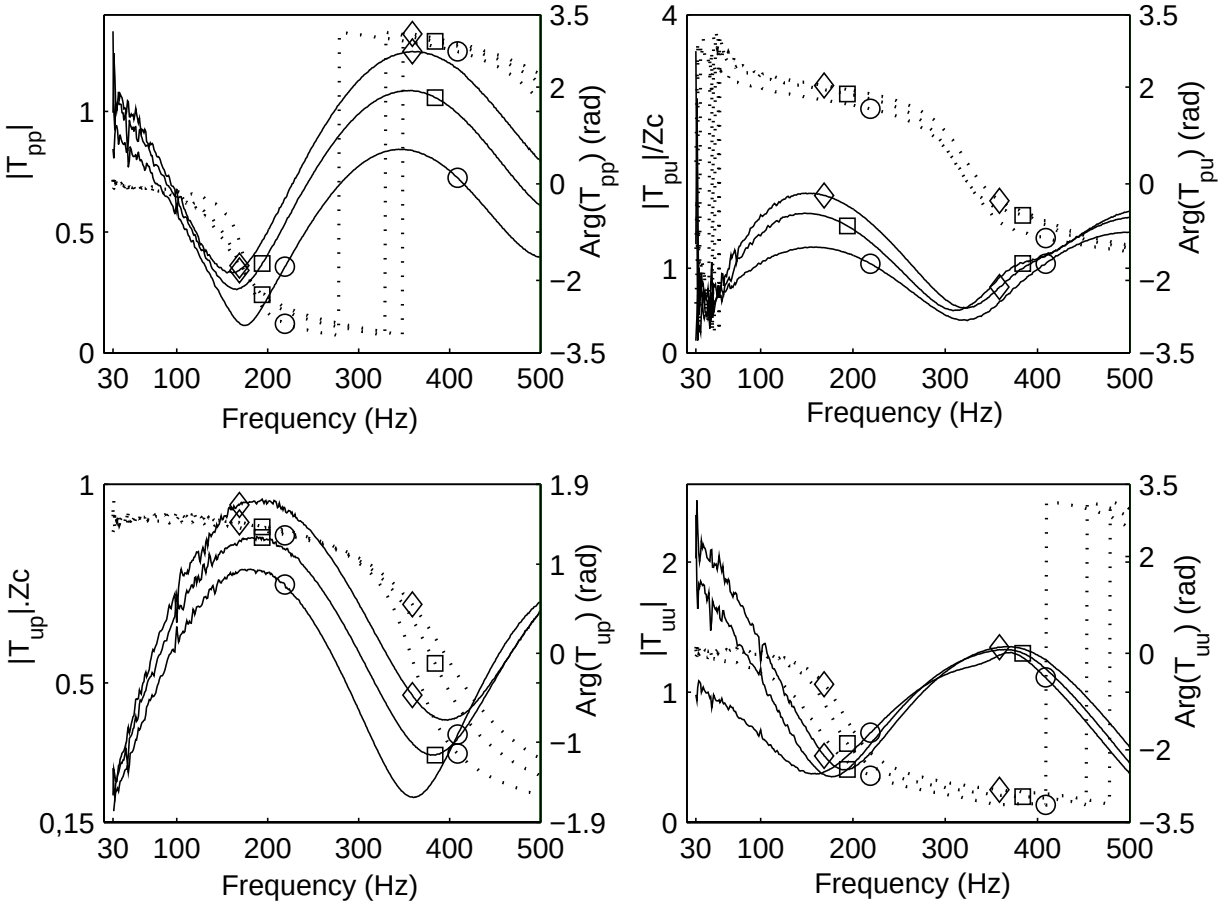

Figure 3.36: Nichrome Foam: amplitude (solid line) and phase (dotted line) of the $\mathbf{T}_{\mathrm{TAC}}$ coefficients in the frequency domain for $Q_H = 0\,W(circle)$, $Q_H = 36\,W(square)$ and $Q_H = 72\,W(diamond)$ - Impedance Method.

Case of the RVC Foam

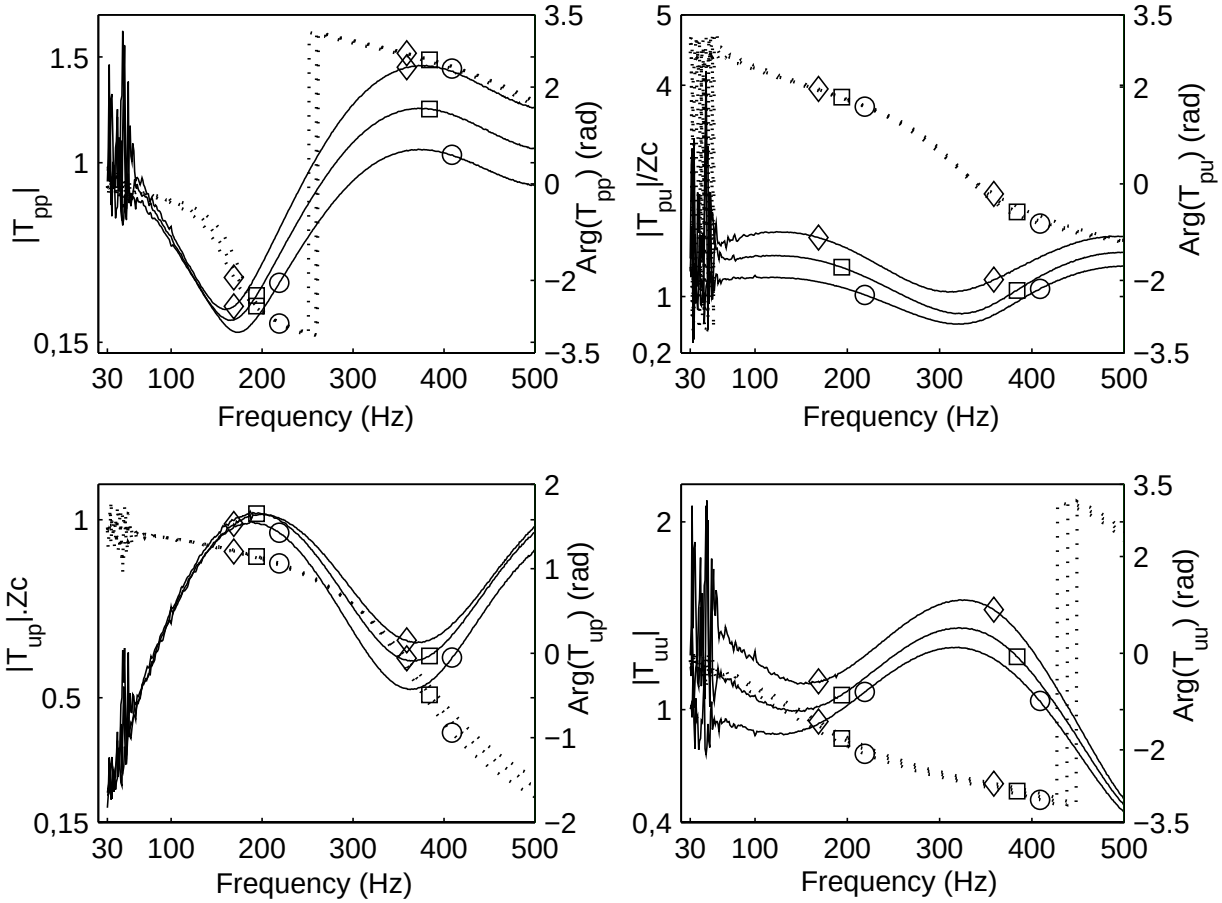

Figure 3.37: RVC Foam: amplitude (solid line) and phase (dotted line) of the $\mathbf{T}_{\mathrm{TAC}}$ coefficients in the frequency domain for $Q_H = 0\,W(circle)$, $Q_H = 9\,W(square)$ and $Q_H = 18\,W(diamond)$ - Impedance Method.

3.6.5 Discussion and comparative analysis with the previous approaches

All curves for $Q_H = 0\,W$ presented in Figs. 3.34, 3.35, 3.36 and 3.37 behave coherently with their corresponding reciprocity parameters, which are presented in Table 3.2. The fact that - for all materials - $\mathbf{rc}$ is close to unity and $\sigma_{\mathbf{rc}}$ is very low gives consistency to the Impedance Method. Either *bias* or *noise* level is low, hence. Such consistency leads to assume that the same quality is achieved for the heated measurements as well, since the same experimental procedures are undertaken, and besides, to consider the thermal effects due to the condition $Q_H > 0$, the transient constraints achieved in Appendix A are here respected as much as for the first approach.

An interesting aspect to note is that $\sigma_{\mathbf{rc}}$ for the Stainless Steel Grids behaves differently than for the other three materials. In fact, it is much bigger, although still small enough to not turn those measurements noisy. That means the $\mathbf{T}_{\mathrm{TAC}}$ coefficients of the Stainless Steel Grids have a higher *noise* level than those of the other materials. Indeed, when visually comparing the curves of Figs. 3.34, 3.35, 3.36 and 3.37, the Stainless Steel Grids case is clearly the most noisy among all four materials, seeming to follow $\sigma_{\mathbf{rc}}$ proportionally. This behavior is also in agreement with the theoretical curves of sensitivity analysis, shown in Figs. 3.27, 3.28, 3.29 and 3.30, where the sensitivity to *noise* is revealed higher for the Stainless Steel Grids than for the Ceramic Catalyst.

Another way to compare those results is to display amplitude and phase of the reciprocity spectrum for the four materials (Fig. 3.38). They behave accordingly both to the comparison above and to the Table 3.2, where the Stainless Steel Grids results are more noisy than the ones for the other materials. However, when comparing those results with the ones obtained by the Two-Load Method (Fig. 3.39) - also for the Stainless Steel Grids - it gets clear once more how advantageous the Impedance Method is. Not only in qualitative aspects, but also because of its easier way to cover a wider frequency range, as is does not depend on fitting waveguide lengths nor microphones positioning to cover specific frequency ranges of interest.

In the case of the Ceramic Catalyst, amplitude and phase of reciprocity are displayed in Fig. 3.40 for both Impedance Method and Two-Load Method. Both also behave coherently to the sensitivity analysis and Table 3.2. Similar low *noise* levels are achieved, whereas the Two-Load Method results are a little more biased for both amplitude and phase, besides the fact that they reach a narrower frequency range.

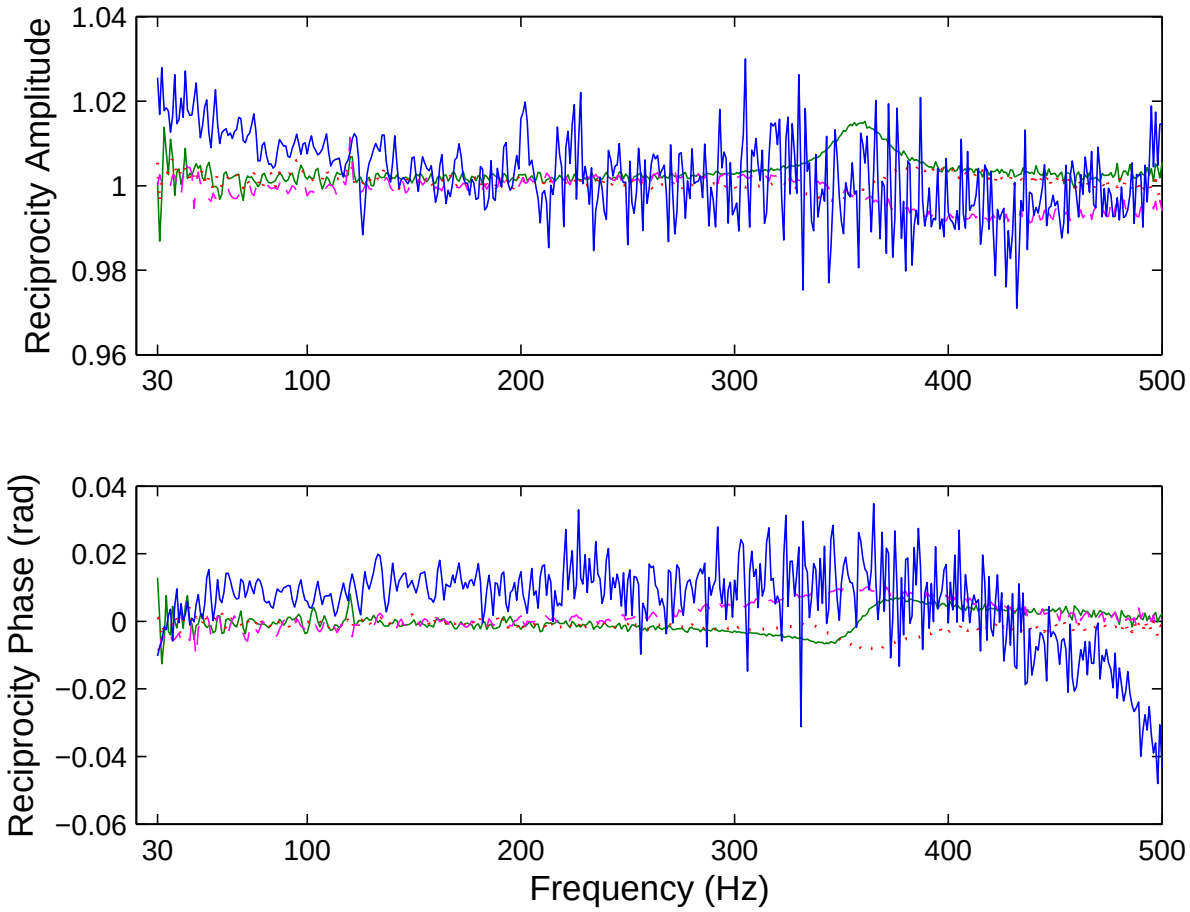

Figure 3.38: Amplitude and phase of the $\mathbf{T}_{\mathrm{TAC}}$ reciprocity in the frequency domain for $Q_H = 0\,W$ for the Stainless Steel Grids (relatively noisy lines), Ceramic Catalyst (continuous thin lines), Nichrome Foam (dotted lines) and RVC Foam (dashed lines) - Impedance Method.

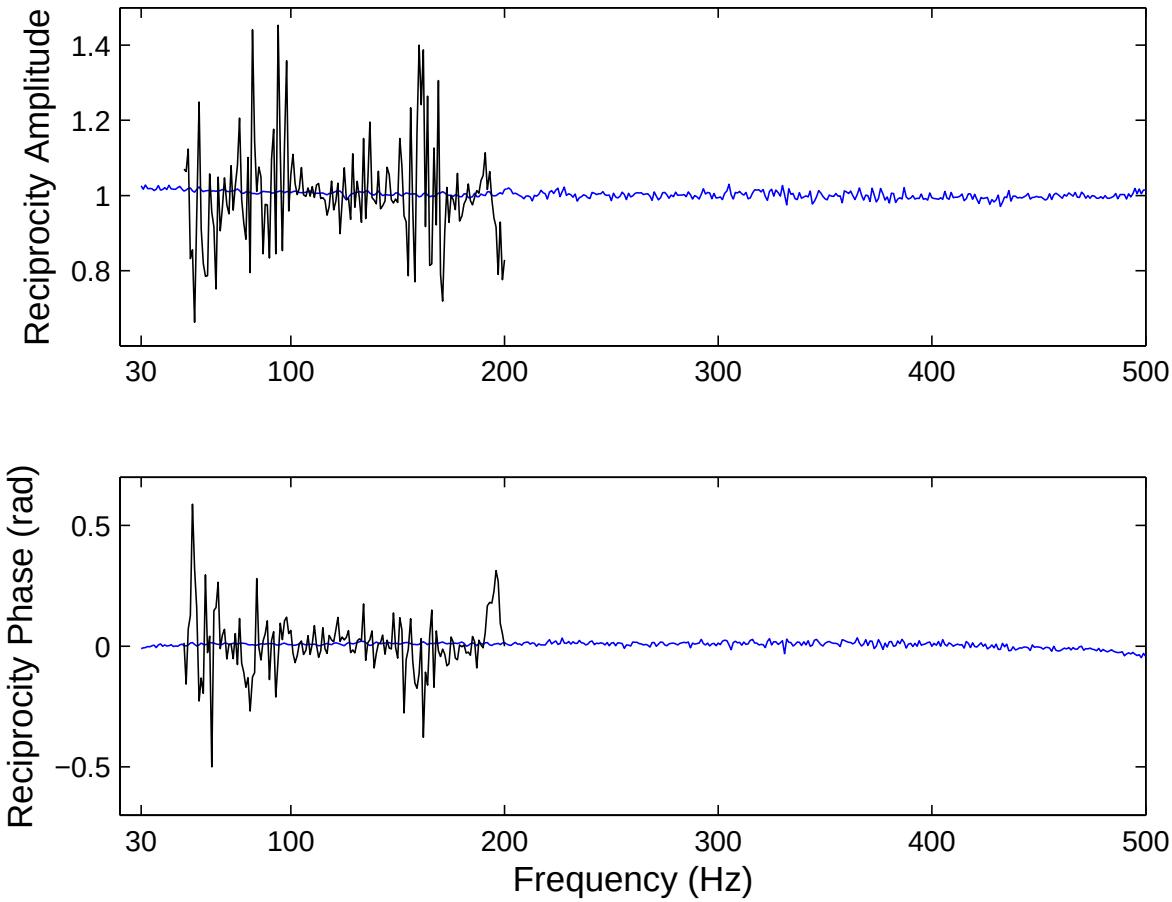

Figure 3.39: Stainless Steel Grids: amplitude and phase of the $\mathbf{T}_{\mathrm{TAC}}$ reciprocity in the frequency domain for $Q_H = 0\,W$ for the Impedance Method and for the Two-Load Method (very noisy lines).

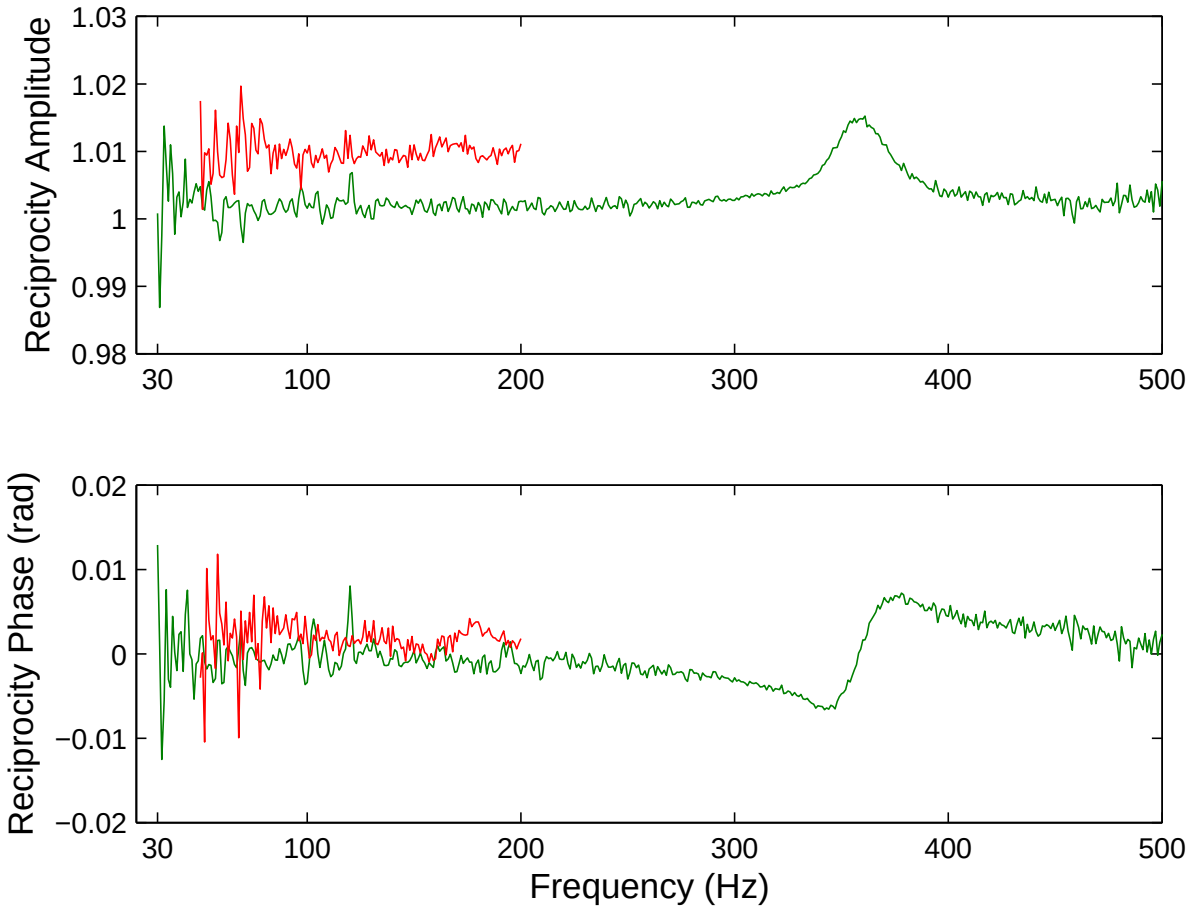

Figure 3.40: Ceramic Catalyst: amplitude and phase of the $\mathbf{T}_{\mathrm{TAC}}$ reciprocity in the frequency domain for $Q_H = 0\,W$ for the Impedance Method and for the Two-Load Method (lines of narrower frequency range).

3.7 Conclusion

The Two-Load Method, either with or without the inversion of the TAC, is not capable of characterization of low porosity materials such as the here tested stacked steel grids - at least for the length of this case-study, which is significantly longer than typical ones used in thermoacoustic systems.

In both cases, a high level of sensitivity to noise (first case) and to bias (second case) is verified experimentally and also confirmed by a numerical simulation. Such accordance between these approaches validates one each other, in fact.

Thus, an alternative method based on the impedance matrix measurement has been developed, which leads to the T-matrix coefficients of the TAC. This method, called "Impedance Method", lead to good results for both stack and regenerator. The low average value of reciprocity and the corresponding standard deviation for $Q_W = 0$ is an indicator of the measurement quality.

This method has been used to characterize different materials which can be anticipated to behave as "stack" or "regenerator" (respective Ceramic Catalyst and Stainless Steel Grids), or in between "stack" and "regenerator" (NiCr Foam and RVC Foam).

The knowledge of the T-matrix coefficients of the TAC at different heating conditions can now be used to determine both the operating frequency f_{op} and the intrinsic thermoacoustic amplification gain G in a thermoacoustic engine. This application of the Impedance Method is discussed in the next chapter.

4 APLICATION TO THE DESIGN OF THERMOACOUSTIC ENGINES

4.1 Introduction

An experimental method allowing the measurement of the T-matrix coefficients of a TAC at different heating conditions has been presented in the previous chapter. The knowledge of these coefficients can be used to predict both the heat power supply and the operating frequency which correspond to the onset of self-sustained acoustic waves in a thermoacoustic engine equipped with the TAC characterized beforehand, as done by Guedra *et al.* (2011). It is however worth mentioning that such a task requires having made the T-matrix measurements for numerous values of heat power supply Q_H, since the accuracy of the predictions of onset is directly related to the step of heat supply ΔQ between two set of measurements. An alternative but similar approach consists in developing an adequate modeling which would predict both the operating frequency $f_{op.}$ and the intrinsic thermoacoustic amplification gain G associated both to a given heat power Q_H supplied to the TAC and to the respective geometry of each element surrounding this TAC. This chapter presents a general modeling method (Bannwart *et al.*, 2013) based on this alternative approach, which allows calculation of both the operating frequency $f_{op.}$ and the thermoacoustic gain G in a thermoacoustic engine from the measured T-matrix components of a given TAC under a given heat power supply Q_H; this approach also leads hence to the determination of the onset of self-sustained oscillations, whose accuracy depends on the step of heat supply ΔQ as well. An optimization of the geometric parameters of each element surrounding the TAC can be then performed by searching the geometrical configuration leading to a maximum value of the gain G. Thereby, this modeling method allows comparison of the potential performances of the different sample materials characterized in Section 3.6, taking G as the main comparative parameter. This method is applied in the following to the optimization of the performances of a simple standing-wave and a simple closed-loop engine (see Fig. 4.1), but it is also easily applicable to a more complicated engine such as the one of Fig. 1.1. Aiming to achieve the best results possible in this work, all experimental data used in this chapter are the ones obtained from the Impedance Method.

4.2 Theory

Two simple thermoacoustic engines are here considered, and they are depicted in Fig. 4.1. The first one is a standing-wave engine which basically consists of the TAC surrounded by two straight ducts closed by rigid ends. The second one is made of a closed-loop, containing the

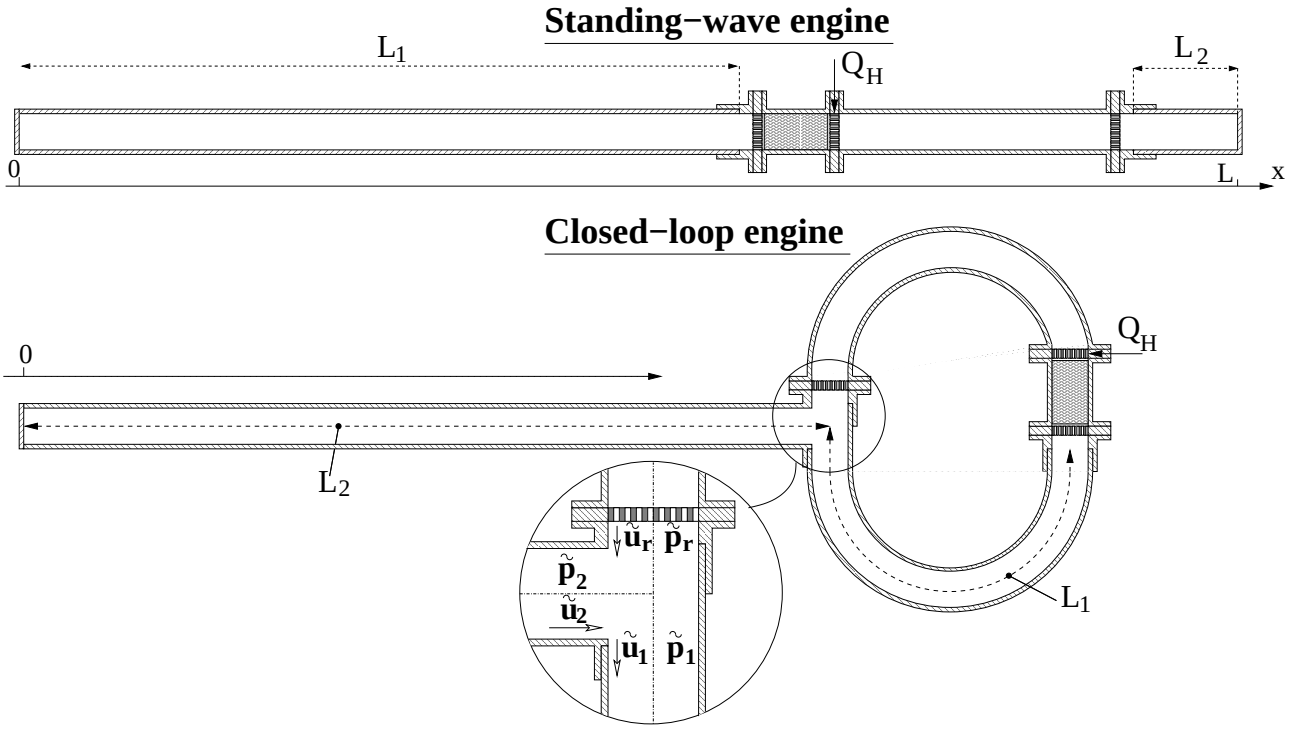

Figure 4.1: Basic configurations for standing-wave and closed-loop engines.

TAC, connected to a straight duct. It is worth noting that in the configuration of the closed-loop engine, it is assumed that the curvature of the waveguide, and especially that of the TAC, has no impact on the propagation of acoustic waves.

4.2.1 Standing-wave engine

First, the standing wave engine of Fig. 4.1 is taken into consideration. Two straight ducts of lengths L_1 and L_2 are connected to the TAC. These ducts have the same inner diameter than the TAC. Assuming the propagation of plane acoustic waves at angular frequency ω, it is possible to relate the acoustic pressure $\tilde{p}_L$ and volume velocity $\tilde{u}_L$ at position $x = L$ to the pressure $\tilde{p}_0$ and volume velocity $\tilde{u}_0$ at position $x = 0$ as follows:

$$\begin{pmatrix} \tilde{p}_L \\ \tilde{u}_L \end{pmatrix} = \mathbf{T_2} \times \mathbf{T_{TAC}} \times \mathbf{T_1} \times \begin{pmatrix} \tilde{p}_0 \\ \tilde{u}_0 \end{pmatrix} = \mathbf{T_{tot}} \times \begin{pmatrix} \tilde{p}_0 \\ \tilde{u}_0 \end{pmatrix}, \tag{4.1}$$

where the T-matrices

$$\mathbf{T_{j_{(j=1,2)}}} = \begin{pmatrix} \cos(kL_j) & iZ_c \sin(kL_j) \\ \frac{i}{Z_c}\sin(kL_j) & \cos(kL_j) \end{pmatrix} \tag{4.2}$$

characterize the lossy propagation of acoustic waves in the ducts of respective lengths L_1 and L_2 and where

$$k = \frac{\omega}{c_0}\left(1 + \frac{f_\nu + (\gamma - 1)f_\kappa}{1 - f_\nu}\right)^{1/2} \tag{4.3}$$

and

$$Z_c = \frac{\rho_0 c_0}{S\left[(1 - f_\nu)(1 + (\gamma - 1)f_\kappa)\right]^{1/2}} \tag{4.4}$$

are the complex wavenumber and the characteristic impedance of the ducts, respectively. In Eqs. (4.3) and (4.4), ρ_0 is the fluid density at room temperature, c_0 is the adiabatic sound speed, γ is the specific heat ratio of the fluid, S is the duct cross-sectional area, and the functions f_κ and f_ν characterize the thermal and viscous coupling between the oscillating fluid and the duct walls (Swift, 2002; Arnott *et al.*, 1991). Then, taking into account that $\tilde{u}_L = 0$ (rigid termination), one gets

$$\begin{pmatrix} \tilde{p}_0 \\ \tilde{u}_0 \end{pmatrix} = T_{tot}^{-1} \times \begin{pmatrix} \tilde{p}_L \\ 0 \end{pmatrix} = \begin{pmatrix} A_{pp} & A_{pu} \\ A_{up} & A_{uu} \end{pmatrix} \times \begin{pmatrix} \tilde{p}_L \\ 0 \end{pmatrix}, \tag{4.5}$$

from which one can write the reflected acoustic impedance at position $x = 0$:

$$Z_0 = \frac{\tilde{p}_0}{\tilde{u}_0} = \frac{A_{pp}}{A_{up}}. \tag{4.6}$$

The knowledge of this reflected acoustic impedance $Z_0 = Z_0(L_1, L_2, Q_H, \omega)$ can be used to determine the resonance frequencies of the complete device. In particular, if the left side of the engine is also terminated by a rigid plug (infinite impedance), then the principle of impedance matching tells that the resonance frequencies correspond to the maxima of $|Z_0|$ (these maxima should tend towards infinity if losses were neglected). As an illustrative example, the modulus of Z_0 and its real part are presented for three levels of heat supply in Fig. 4.2 as a function of the frequency in the particular case when L_1 and L_2 are fixed to $160\,cm$ and $10\,cm$, respectively. The reflected impedance Z_0 is calculated using the experimental transfer matrix $\mathbf{T_{TAC}}$ of the ceramic stack previously determined under different levels of heat power supply.

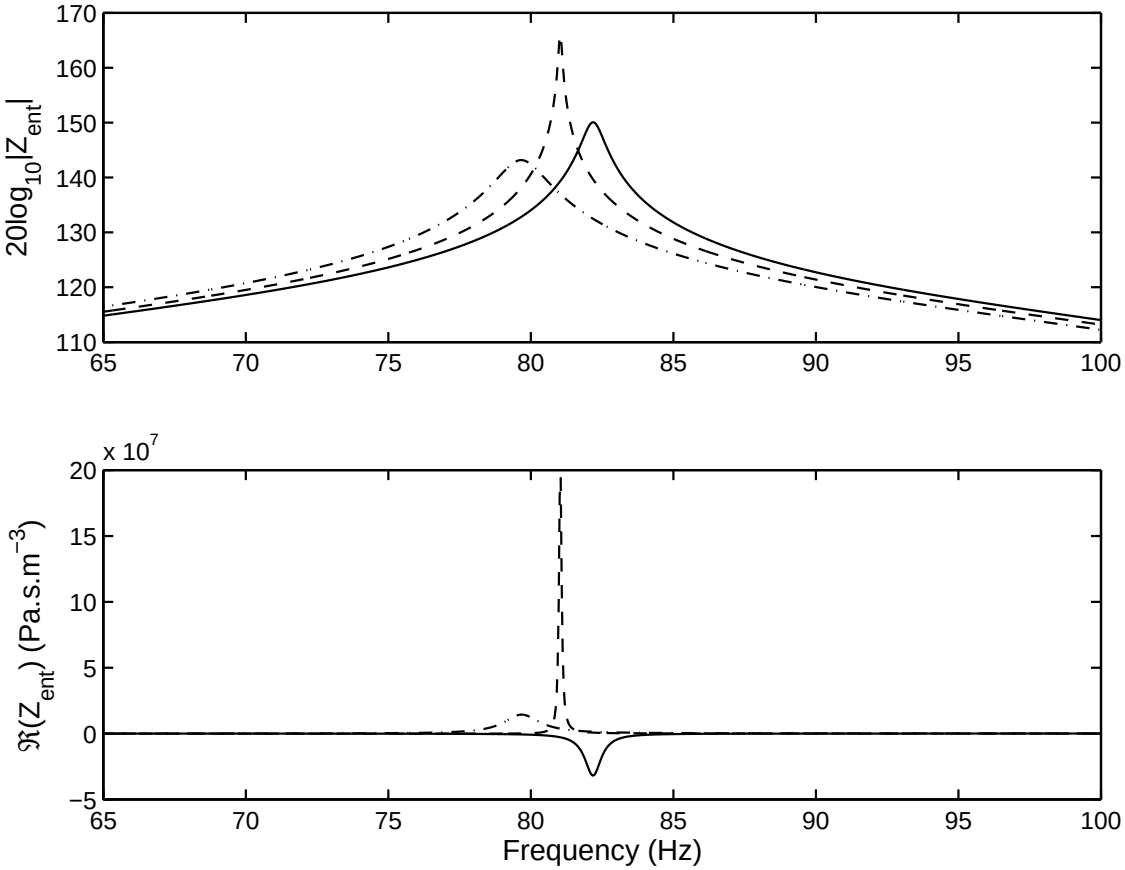

Figure 4.2: Ceramic Catalyst: modulus and real part of the reflected acoustic impedance for $Q_H = 9W$ (dash-dotted line), $Q_H = 18\,W$ (dashed line), and $Q_H = 27\,W$ (solid line).

From the analysis of $|Z_0|$, it appears that the first resonance frequency $f_{op.}$ of the system is around $80\,Hz$, and that it tends to increase with heating. Moreover, the quality factor of the resonance (which is inversely proportional to the width of the resonance peak) increases as Q_H increases from 9 to $18\,W$. This is consistent with our expectations since the quality factor should tend towards infinity as the system approaches the threshold of thermoacoustic instability (Atchley *et al.*, 1992). However, the width of the resonance peak increases as Q_H increases from 18 to $27\,W$, which seems surprising at first sight. Actually, this means that the system is above threshold for $Q_H = 27\,W$ so that the width of the resonance peak is no longer related to the quality factor of the resonance: this quality factor should become negative through onset (Atchley, 1994a), for which the net attenuation of sound becomes negative. Additional insight arises from the analysis of $\Re\,(Z_0)$ at resonant frequency $f_{op.}$, leading to the same conclusions: if $Q_H \leq 18\,W$, the real part of $Z_0(f_{op.})$ is positive which means that work is absorbed by the device, but for $Q_H = 27\,W$ the real part of Z_0 becomes negative which means that work is produced by the system (Hatori *et al.*, 2012). In other words, if $Q_H = 27\,W$ the system is above threshold, and self-sustained acoustic waves should oscillate at frequency $f_{op.}$

(in as much as it is considered that the generation of large amplitude acoustic oscillations does not induce variations of the temperature field inside the TAC with subsequent variations of its transfer matrix).

	Gain G	Operating freq. $f_{op.}$
$Q_H = 9\,W$	-0.14	$79.7\,\text{Hz}$
$Q_H = 18\,W$	0.91	$81.1\,\text{Hz}$
$Q_H = 27\,W$	1.50	$82.1\,\text{Hz}$
$Q_H = 36\,W$	1.82	$83.2\,\text{Hz}$

Table 4.1: Performances for a standing-wave engine equipped with a stack (Ceramic Catalyst) ($L_1 = 160\,cm$ and $L_2 = 10\,cm$).

Once the reflected impedance Z_0 is determined, the resonance frequencies of the device are known. It is then possible to choose a particular working frequency and to calculate a thermoacoustic amplification gain associated to the acoustic mode under consideration. Let's assume that the operating angular frequency $\omega_{op.}$ is fixed to that of the first acoustic mode (which is generally the most unstable mode). Assuming as well that the acoustic pressure $\tilde{p}_0$ at position $x = 0$ is fixed to some arbitrary value P_0, from which one easily gets the corresponding volume velocity $\tilde{u}_0 = P_0/Z_0$, together with the acoustic pressures and volume velocities at positions x_l, x_r and L (which are deduced from $\tilde{u}_0$, $\tilde{p}_0$ and the T-matrices $\mathbf{T_1}$, $\mathbf{T_{TAC}}$, and $\mathbf{T_2}$). Therefore, it is possible to calculate the acoustic power

$$\begin{aligned} \mathbf{W_{loss}} &= \left[\frac{1}{2}\Re\left(\tilde{p}_l\tilde{u}_l^*\right) - \frac{1}{2}\Re\left(\tilde{p}_0\tilde{u}_0^*\right)\right] \\ &+ \left[\frac{1}{2}\Re\left(\tilde{p}_L\tilde{u}_L^*\right) - \frac{1}{2}\Re\left(\tilde{p}_r\tilde{u}_r^*\right)\right] \end{aligned} \tag{4.7}$$

dissipated by viscous and thermal losses into the ducts, where * denotes the conjugate of a complex number, and to calculate the acoustic power

$$\mathbf{W_{TAC}} = \left[\frac{1}{2}\Re\left(\tilde{p}_r\tilde{u}_r^*\right) - \frac{1}{2}\Re\left(\tilde{p}_l\tilde{u}_l^*\right)\right] \tag{4.8}$$

produced within the TAC. The powers W_{loss} and W_{TAC} depend on the unknown parameter P_0, but their ratio does not. Then, a thermoacoustic amplification gain G can be defined as follows:

$$G = \frac{\mathbf{W_{TAC}}}{|\mathbf{W_{loss}}|}. \tag{4.9}$$

This parameter G has the meaning of an energy balance in the system: if $G > 1$, then the acoustic work produced by thermoacoustic effect in the TAC is higher than the losses in the remaining of the device, so that the extra work can be provided to an acoustic load.

The results obtained for the frequency of operation $f_{op.}$ and the corresponding thermoacoustic amplification gain G are reported in Tab. 4.1: the engine under consideration is a standing wave engine equipped with a ceramic catalyst stack, while L_1 and L_2 are fixed to $160\,cm$ and $10\,cm$, respectively. The calculations of G are consistent with the conclusion mentioned above that the heat supply corresponding to onset threshold ($G = 1$) is between 18 and $27\,W$.

4.2.2 Closed-loop engine

The same kind of analysis as the one presented above can be used in the case of a closed-loop engine (see Fig. 4.1) which is the basic geometrical configuration encountered in thermoacoustic Stirling engines that use a regenerator instead of a stack. As in Subsection 4.2.1, the first step consists in determining the reflected impedance Z_0 from the T-matrices $\mathbf{T_{1,2}}$ and $\mathbf{T_{TAC}}$. After a few calculations, one gets

$$Z_0 = \frac{\mathcal{B}_{pp} Z_2 + \mathcal{B}_{pu}}{\mathcal{B}_{up} Z_2 + \mathcal{B}_{uu}}, \tag{4.10}$$

with

$$\begin{pmatrix} \mathcal{B}_{pp} & \mathcal{B}_{pu} \\ \mathcal{B}_{up} & \mathcal{B}_{uu} \end{pmatrix} = T_2^{-1}, \tag{4.11}$$

$$Z_2 = \frac{\tilde{p}_2}{\tilde{u}_2} = \frac{\mathcal{C}_{pu}}{(1-\mathcal{C}_{uu})(1-\mathcal{C}_{pp}) - \mathcal{C}_{pu}\mathcal{C}_{up}}, \tag{4.12}$$

and

$$\begin{pmatrix} \mathcal{C}_{pp} & \mathcal{C}_{pu} \\ \mathcal{C}_{up} & \mathcal{C}_{uu} \end{pmatrix} = T_{TC} \times T_1. \tag{4.13}$$

Therefore, assuming that $\tilde{p}_0 = P_0$ at position $x = 0$, one gets $\tilde{u}_0 = P_0/Z_0$, and

$$\begin{pmatrix} \tilde{p}_2 \\ \tilde{u}_2 \end{pmatrix} = \mathbf{T_2} \times \begin{pmatrix} \tilde{p}_0 \\ \tilde{u}_0 \end{pmatrix}, \tag{4.14}$$

$$\begin{pmatrix} \tilde{p}_1 \\ \tilde{u}_1 \end{pmatrix} = \begin{pmatrix} 1 & 0 \\ 0 & \frac{1-\mathcal{C}_{pp}}{\mathcal{C}_{pu}} \end{pmatrix} \times \begin{pmatrix} \tilde{p}_2 \\ \tilde{u}_2 \end{pmatrix}, \tag{4.15}$$

$$\begin{pmatrix} \tilde{p}_l \\ \tilde{u}_l \end{pmatrix} = \mathbf{T_1} \times \begin{pmatrix} \tilde{p}_1 \\ \tilde{u}_1 \end{pmatrix}, \tag{4.16}$$

$$\begin{pmatrix} \tilde{p}_r \\ \tilde{u}_r \end{pmatrix} = \mathbf{T_{TAC}} \times \begin{pmatrix} \tilde{p}_l \\ \tilde{u}_l \end{pmatrix}. \tag{4.17}$$

From these relations, one obtain the acoustic work produced within the TAC (Eq. (4.8)) and the acoustic work

$$\begin{aligned} \mathbf{W_{loss}} &= \left[\frac{1}{2}\Re\left(\tilde{p}_2\tilde{u}_2^*\right) - \frac{1}{2}\Re\left(\tilde{p}_0\tilde{u}_0^*\right)\right] \\ &+ \left[\frac{1}{2}\Re\left(\tilde{p}_l\tilde{u}_l^*\right) - \frac{1}{2}\Re\left(\tilde{p}_1\tilde{u}_1^*\right)\right] \end{aligned} \tag{4.18}$$

consumed in the remaining of the device, which fulfills the expression for the thermoacoustic amplification gain $G = \mathbf{W_{TAC}}/|\mathbf{W_{loss}}|$, as described in Eq. 4.9.

4.3 Calculation of G and $f_{op.}$ from experimental data

As soon as the experimental transfer matrix of a given thermoacoustic core is measured for various heating conditions, an optimization of the thermoacoustic amplification gain can be done thanks to the theory given in the previous section. This optimization is achieved for a given heat power supply by searching the geometry of the thermoacoustic device which leads to

a maximum value for G. In our case study, this amounts to determining the optimal lengths L_1 and L_2 within their respective arbitrary ranges, which are for instance bounded by the frequency limits, i.e. from 30 to $500\,\text{Hz}$ in our measurements. However, for illustration purposes, it is chosen to show G and $f_{op.}$ for a narrower interval, from 30 to $250\,\text{Hz}$, as the optimal G is still embraced in all cases. This optimization is done for each one of the four thermoacoustic cores made of different materials. Nevertheless, before presenting these results, a comparison is put forward regarding a theoretical transfer matrix in Subsection 4.3.1. In this comparison, it is also shown the advantage of post-treating the experimental data with least squares regression to a polynomial.

4.3.1 Comparison between results from theoretical and experimental data

The validity of the measured $\mathbf{T}_{\text{TAC}}$ by the Impedance Method for both stack-like and regenerator-like porous material has been already proved in Chapter 3. However, in order to illustrate and reverify the accuracy of those experimental data and, reciprocally, the accuracy of the theoretical model for stack-like materials, a comparison between results beyond just the $\mathbf{T}_{\text{TAC}}$ coefficients is here put forward. G and $f_{op.}$ are calculated from data of both origins and compared. The Ceramic Catalyst is the chosen material for that since its geometrical simplicity allows to have a reliable theoretical modeling for its non-heated $\mathbf{T}_{\text{TAC}}$, as discussed in Chapter 2. Therefore, the experimental data are for non-heated $\mathbf{T}_{\text{TAC}}$ as well. As the Ceramic Catalyst is a stack, the most appropriate engine for this study is the standing-wave kind, which is shown in Fig. 4.1.

Figure 4.3 shows the theoretical $f_{op.}$ for the first resonance mode as function of the variable lengths $0.6\,m \leq L_1 \leq 4\,m$ and $0\,m \leq L_2 \leq 0.4\,m$. These intervals are chosen according to the need for a good graphical resolution for the experimental results, which are displayed in the following of these theoretical ones. The number of points per interval are, respectively, 60 and 40, what gives a total of 2400 combinations of engines per analysis. The corresponding G is shown in Fig. 4.4. As these surfaces are calculated from theoretical data, they are smooth.

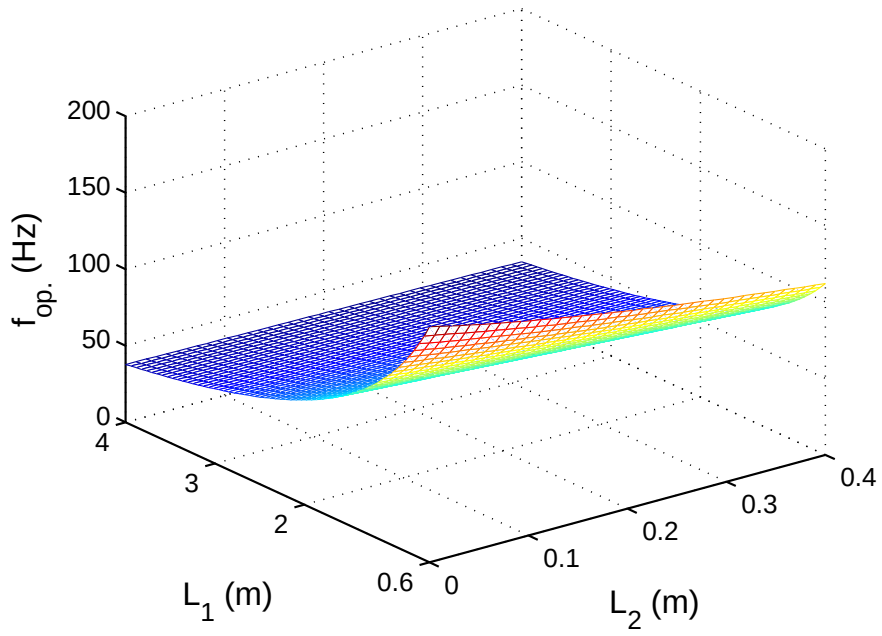

Figure 4.3: Theoretical $f_{op.}$ for standing-wave engines at $Q_H = 0\,W$ for the Ceramic Catalyst.

The corresponding $f_{op.}$ and G from experimental data are very close - but evidently not identical - to previous, as one would expected. For the sake of simplicity, however, only the G surface is here presented (Fig. 4.5). When comparing Figs. 4.4 and 4.5, it is visible some small level of noise in the measured G, which is intrinsic to experimental data and coherent to the results of the sensitivity analysis of Subsection 3.6.2, and to the reciprocity parameters of Tables 3.2 and 4.2. One interesting aspect to note, however, is the non-negligible difference in the optimal G between both the cases. As expected by theory, the maximal G for $Q_H = 0W$ results negative (-0.383), as there is no thermoacoustic production when the temperature gradient along the TAC is zero. That is why this maximal G can reach values close to zero, but still negative. On the other hand, the maximal G from experimental data results positive (0.166). This is due to irregularities in the G surface. Nevertheless, such roughness can be minimized by applying a least squares regression to a polynomial into the measured transfer functions from which the $\mathbf{T}_{\text{TAC}}$ coefficients are calculated. The polynomial regression with the best results in this investigation is of fifth degree, which leads to better and smoother surfaces such as of Fig. 4.6. This polynomial regression (or curve fitting), when applied to the theoretical case does not lead to significant changes, what is interesting with respect to the data quality preservation. Hence, that contributes to the reliability of the already significant improvement in the experimental case (see Table 4.2). Therefore, the polynomial regression of fifth degree is adopted as regular procedure to all following calculations of optimal G or $f_{op.}$.

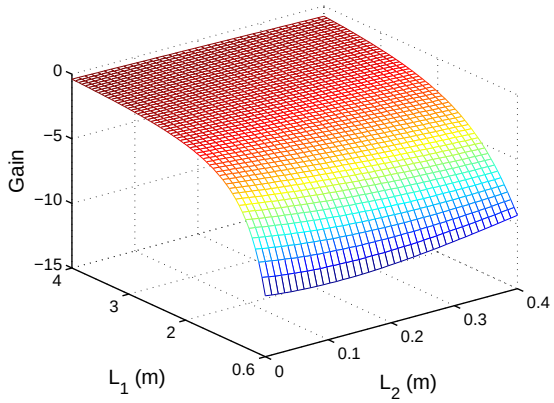

Figure 4.4: Theoretical $Gain$ for standing-wave engines at $Q_H = 0\,W$ for the Ceramic Catalyst.

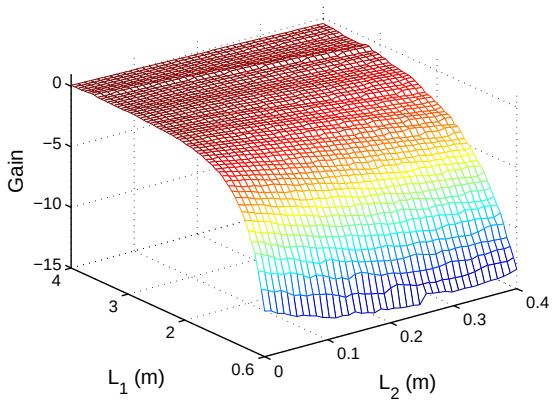

Figure 4.5: $Gain$ for standing-wave engines at $Q_H = 0\,W$ from measured $\mathbf{T}_{\mathrm{TAC}}$ of the Ceramic Catalyst by the Impedance Method.

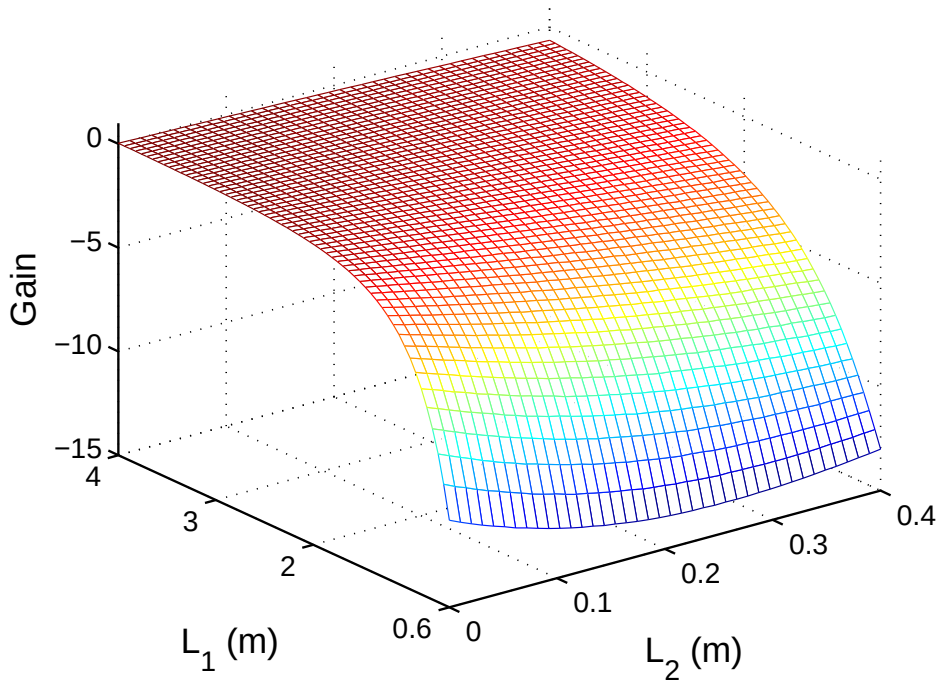

Figure 4.6: $Gain$ for standing-wave engines at $Q_H = 0\,W$ from measured $\mathbf{T}_{\mathrm{TAC}}$ of the Ceramic Catalyst using polynomial regression of fifth degree - Impedance Method.

	Theory	Fitted Theory	Experiment	Fitted Experiment
G	-0.386	-0.383	0.166	0.001
$f_{op.}$(Hz)	38	37.7	42	38.2
$L_1(m)$	4	4	3.60	4
$L_2(m)$	0	0	0	0
$\mathbf{rc}$	$1.000 + 0.000i$	$1.000 + 0.000i$	$1.003 + 0.000i$	$1.002 - 0.001i$
$\sigma_{\mathbf{rc}}$	$0.000 + 0.000i$	$0.000 + 0.000i$	$0.003 + 0.003i$	$0.000 + 0.001i$

Table 4.2: Maximal performances and respective configurations for standing-wave engines at $Q_H = 0\,W$ calculated from theoretical and experimental data, fitted or not with polynomial regression of fifth degree, with their corresponding average reciprocities and average standard deviations in the frequency range from 30 to $500\,Hz$.

4.3.2 Standing-wave engines for $Q_H > 0$

For the standing-wave configuration, optimization results are given in Figs. 4.7 and 4.8 for the case of the Ceramic Catalyst with the maximum value of heat supply $Q_H = 81\,W$. Figure 4.7 shows the evolution of the operating frequency $f_{op.}$, and Fig. 4.8 shows the corresponding thermoacoustic amplification gain G as a function of the variable lengths $0.6\,m \leq L_1 \leq 4\,m$ and $0\,m \leq L_2 \leq 0.4\,m$. For each configuration (in terms of L_1 and L_2), the operating frequency $f_{op.}$ is searched around the first resonance mode (although higher order modes might become more unstable for some values of the lengths L_1 and L_2). To ensure this search, an approximate prediction of the resonant frequency is estimated taking into account the sound speed evolution with the increase in the heating supply Q_H, so that the range of frequency around the resonance can be better adjusted; this procedure is repeated for of each thermal condition. In the case of $Q_H = 81W$, a peak value of $G = 3.31$ is reached with $L_1 = 1.06\,m$ and $L_2 = 0\,m$, at $f_{op.} = 121\,$Hz. It is worth mentioning that the obtained value for the "optimum" length L_2 equals 0, which is equivalent to closing the right side of the TAC by a rigid plug: this result suggests that the length of the Thermal Buffer Tube of the TAC under test is too long (in the sense that if a shorter TBT had been used, a non-zero optimal length L_2 might have been expected).

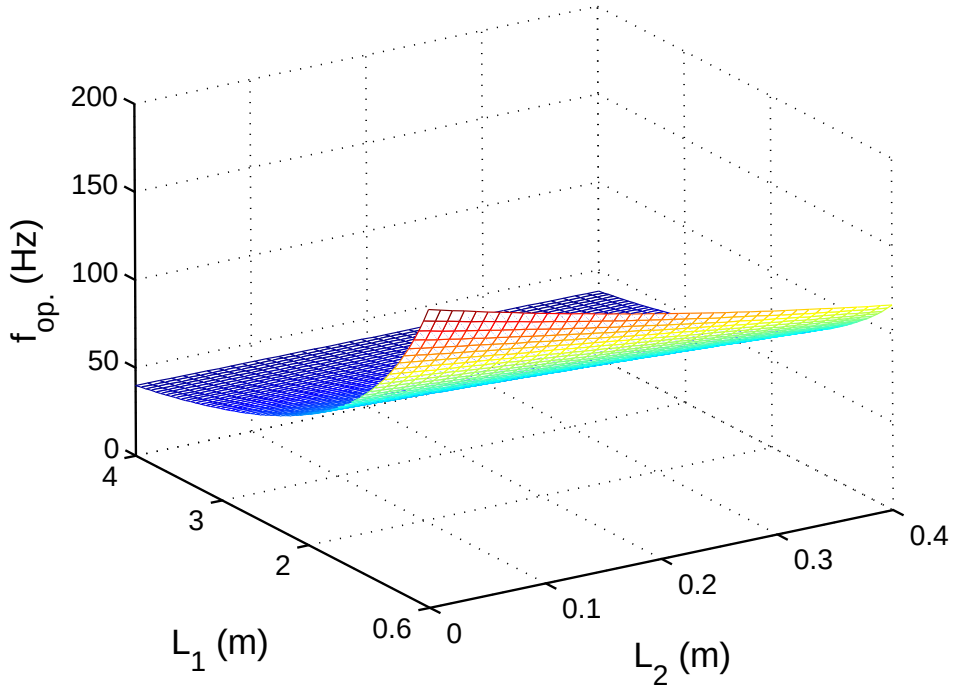

Figure 4.7: $f_{op.}$ for standing-wave engines at $Q_H = 81\,W$ from measured $\mathbf{T}_{\mathrm{TAC}}$ of the Ceramic Catalyst using polynomial regression of fifth degree - Impedance Method.

The same analysis is done for the other three materials, and the results are summarized in Table 4.3. None of them reaches the thermoacoustic outbreak, as their optimal gain are below the unity. In the case of the Nichrome Foam, the maximum G is not so smaller than 1, which is consistent with this material geometrical properties (see Tab. 3.1), closer to the ones of the Ceramic Catalyst; one may expect to reach the onset when slightly increasing Q_H. In the case of the RVC Foam, the results are less promising than the Ceramic Catalyst's case. However, it is worth noting that the maximum heat supply for the RVC Foam is only $18\,W$ due to its temperature limitation in the presence of oxygen (combustion hazard): such a material should be possibly employed as a stack if an inert gas were chosen as the working fluid. At last, as what would be expected, the pile of stainless steel grids is the worst material of all for the standing-wave engine; it has the lowest porosity and smaller average pore radius, which are undesirable aspects for a standing-wave system. These four materials have best performance with $L_2 = 0$. For both RVC Foam and Stainless Steel Grids the $f_{op.}$ results not much higher than 30 Hz, with L_1 at the upper limit of the established constraints, what leads to a less well defined G peak for these general conditions and frequency range.

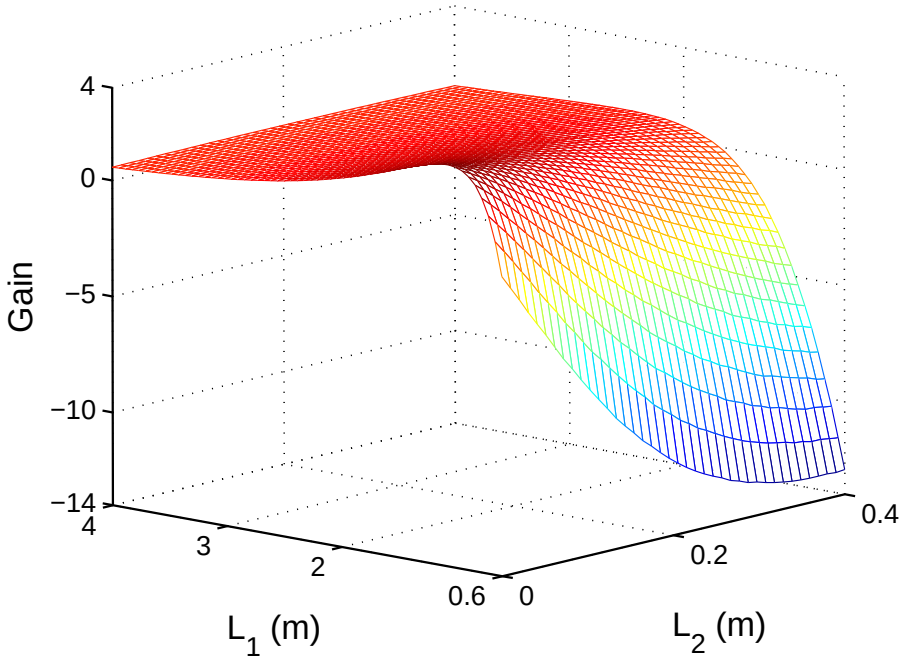

Figure 4.8: $Gain$ for standing-wave engines at $Q_H = 81\,W$ from measured $\mathbf{T}_{\mathrm{TAC}}$ of the Ceramic Catalyst using polynomial regression of fifth degree - Impedance Method.

	G	$f_{op.}$(Hz)	$L_1(m)$	$L_2(m)$
Ceramic Catalyst	3.31	121	1.06	0
Stainless Steel Grids	-0.42	30.2	5.50	0
RVC Foam $(Q_H = 18\,W)$	-0.14	33.7	4.75	0
NiCr Foam	0.84	81.8	1.85	0

Table 4.3: Maximal performances and respective configurations for standing-wave engines at $Q_H = 81\,W$.

4.3.3 Closed-loop engines for $Q_H > 0$

The same kind of comparative analysis is conducted for the closed-loop configuration. The results are summarized in Table 4.4. For this configuration, the pile of Stainless Steel Grids is expected to have the best result. Nevertheless, despite of its favorable properties mentioned before, such material appears in the last performance position. However, when noting the typical lengths of alike materials usually employed as regenerators, which are around few centimeters, it becomes suggestive to consider our $6\,cm$ pile as too long. Indeed, this conclusion would be

in agreement with the strong decay of acoustic pressure level along its axis, as verified during the measurements of its $\mathbf{T_{TAC}}$. Hence, besides low porosity and small average pore radius, this pile also exhibits a length too large, which contributes proportionally to the viscous losses.

Actually, the best performing material here tested is the Nichrome Foam, whose maximum gain reaches 6.88 at 35.2 Hz, with $L_1 = 0.90\,m$ and $L_2 = 3.80\,m$, as illustrated in Figs. 4.9 and 4.10 (note that a contour plot is preferred to a surface area in Fig. 4.11, which shows more clearly the optimum values of L_1 and L_2). From the knowledge of the operating frequency, $f_{op.} = 35.2$ Hz, it is quite direct to estimate the associated thermal boundary layer thickness at room temperature $\delta_\kappa \approx 450\,\mu m$, which is almost as high as the average pore radius ($600\,\mu m$, see Tab. 3.1) of the sample.

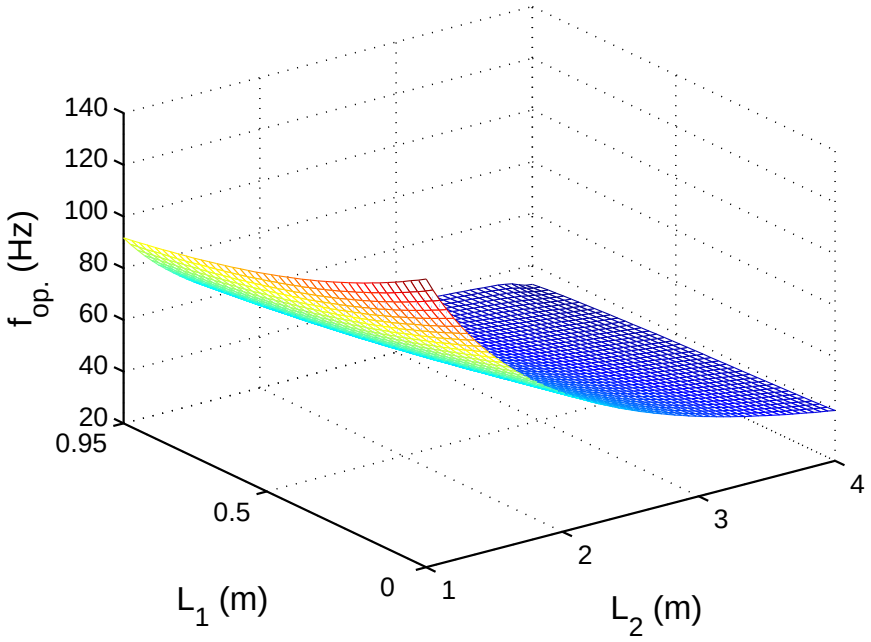

Figure 4.9: $f_{op.}$ for closed-loop engines at $Q_H = 81\,W$ from measured $\mathbf{T}_{\mathrm{TAC}}$ of the Nichrome Foam using polynomial regression of fifth degree - Impedance Method.

The Ceramic Catalyst is the second material that performs above $G = 1$ for this engine, as shown in Tab. 4.4, Fig. 4.12, and Fig. 4.13, the latter being the contour plot of the thermoacoustic gain G as a function of L_1 and L_2. The maximum gain G is 1.47 with a corresponding frequency $f_{op.} = 156$ Hz. In that specific case, the process of optimization leads to an engine which is different from the one obtained with the NiCr Foam. The estimate of the thermal boundary layer thickness at 158 Hz indeed leads to $\delta_\kappa \approx 200\,\mu m$ which is lower than the average pore radius ($530\,\mu m$, calculated from data in Tab. 3.1): the obtained engine is thus much more a closed-loop but stack-based engine rather than a regenerator-based thermoacoustic Stirling engine.

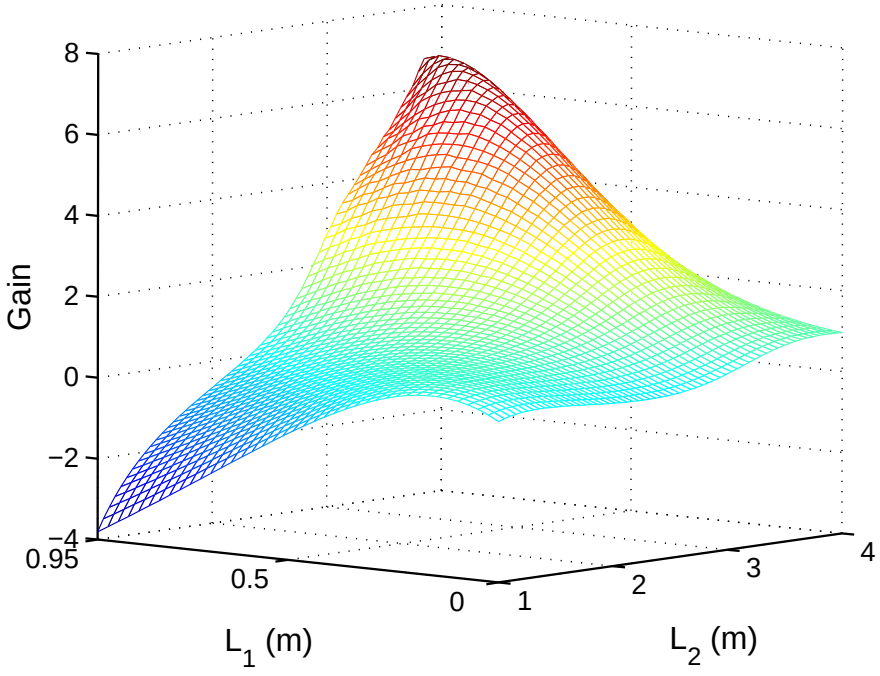

Figure 4.10: *Gain* for closed-loop engines at $Q_H = 81\,W$ from measured $\mathbf{T}_{\mathrm{TAC}}$ of the Nichrome Foam using polynomial regression of fifth degree - Impedance Method.

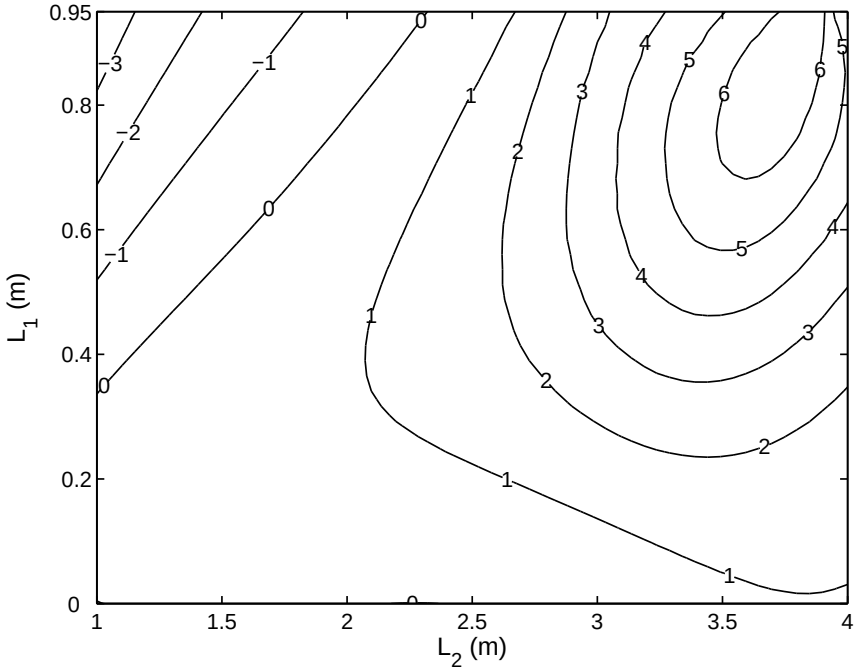

Figure 4.11: *Gain* for closed-loop engines at $Q_H = 81\,W$ from measured $\mathbf{T}_{\mathrm{TAC}}$ of the Nichrome Foam using polynomial regression of fifth degree - Impedance Method.

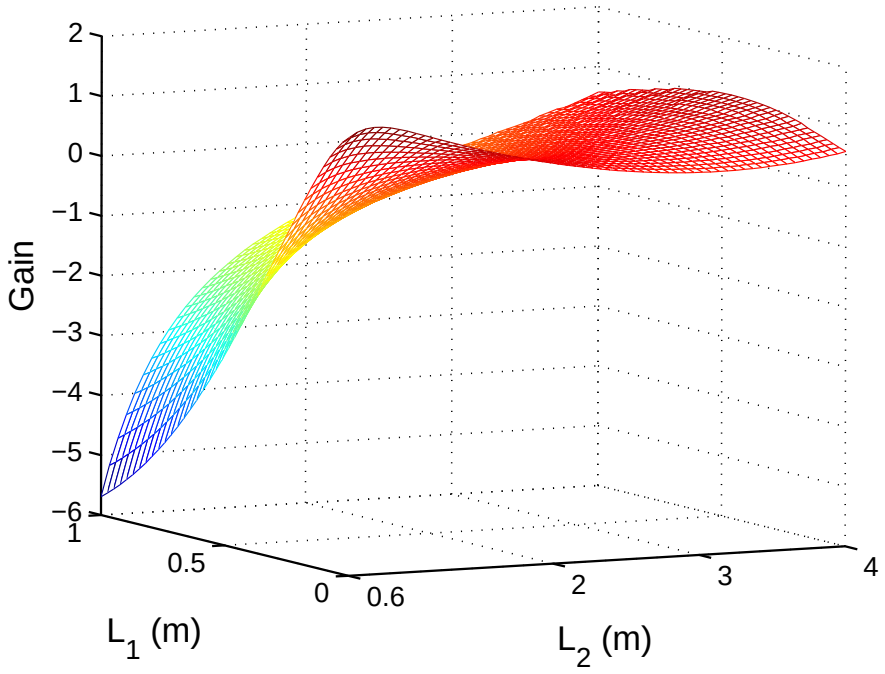

Figure 4.12: $Gain$ for closed-loop engines at $Q_H = 81\,W$ from measured $\mathbf{T}_{\mathrm{TAC}}$ of the Ceramic Catalyst using polynomial regression of fifth degree - Impedance Method.

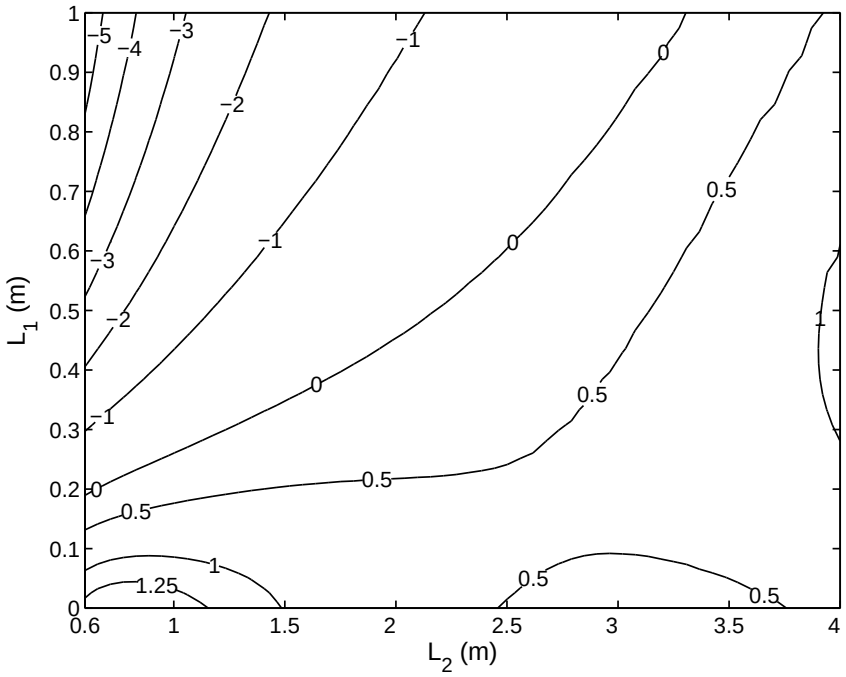

Figure 4.13: $Gain$ for closed-loop engines at $Q_H = 81\,W$ from measured $\mathbf{T}_{\mathrm{TAC}}$ of the Ceramic Catalyst using polynomial regression of fifth degree - Impedance Method.

	G	$f_{op.}$(Hz)	$L_1(m)$	$L_2(m)$
Ceramic Catalyst	1.47	156	0	0.77
Stainless Steel Grids	0.46	55.1	0	2.68
RVC Foam ($Q_H = 18\,W$)	0.87	42.1	0.49	3.24
NiCr Foam	6.88	35.2	0.90	3.80

Table 4.4: Maximal performances and respective configurations for closed-loop engines at $Q_H = 81\,W$.

The RVC Foam does not reach the thermoacoustic outbreak in this engine, but its maximum heat supply $(18\,W)$ is 4.5 times smaller than others maximums $(81\,W)$. Considering that even though with a small Q_H the optimal G reaches 0.87, one may guess that its gain would easily overcome the unity before $(81\,W)$. An experiment in the absence of oxygen could verify the validity of this statement.

5 GENERAL CONCLUSIONS

It has been presented in this work three methods for the transfer matrix measurement of a thermoacoustic core: two of them consisting in applications of a classical two-load acoustic method, and an alternative method here developed based on impedance measurements. Their performances have been evaluated either by sensitivity analysis or by actual measurements involving different porous materials inside this thermoacoustic core. Close agreement has been found between both perspectives, and these three approaches have been extensively analyzed and compared. The third approach, here called Impedance Method, has been proved to be accurate due to its intrinsic low sensitivity to noise and bias, and such accuracy could be verified because of the precision of the acoustic impedance sensor, to the care taken in its calibration, and to the close monitoring over the variation of the temperature distribution. It has been shown that this method, contrarily to the Two-Load Method or the Two-Load Method with TAC Inversion, is accomplishing independently on the material under test, even if dealing with one that resembles a lengthy regenerator.

The T-matrix components of the TAC have been measured for different kinds of materials under different heating conditions, and these data have been used to calculate the associated operating frequency and thermoacoustic amplification gain in both a simple standing-wave engine and a simple closed-loop engine. An optimization process of the engine's operation has been proposed, which consists of maximizing the thermoacoustic amplification gain, and the results obtained also give the opportunity to compare the performances of different materials. The optimization method presented in Sec. 4.3 could be applied to more complicated engines as the one depicted in Fig. 1.1, with many more parameters to adjust (notably the electromechanical parameters of the linear alternator). However, in what concerns the engine performance evaluation, the works presented in this thesis also reveal important features to be improved later on, in future experiments, aiming at more reliable results.

The low predicted performance for the closed-loop engine with the Stainless Steel Grids indicates that this sample may be too long (at least if it shall be used as a regenerator) so that it is difficult to apply a steep temperature gradient along it in order to reach a substantial thermoacoustic amplification, as it would be expected for such material; besides, the proportional viscous dissipation also contributes in this sense. These results are in accordance with the difficulties encountered during the transfer matrix measurements by the Two-Load method due to the strong acoustic pressure decay. These difficulties, for instance, have led to the development

of the alternative method to overcome them. The alternative method has been proved to be capable to evaluate a regenerator for a wide range of lengths (till at least $60\,mm$) with enough accuracy to allow an engine performance prediction. The performance prediction also allows the evaluation of the outreach limits of the TBT length. In the case of the Ceramic Catalyst for the standing-wave engine, for example, the TBT length seems too high, as it is suggested that one would find a better performance for a shorter TBT and a non-zero optimal length L_2.

For practical reasons, air at atmospheric pressure was chosen as the working fluid, despite being inappropriate from the performance concerns (most engines make use of pressurized helium). Therefore, due to this, the predicted onset of thermoacoustic instability $(G > 1)$ was not reached for all kind of materials, and therefore no formal comparative analysis could be achieved.

The results obtained in Section 4.3 have not been confirmed by experiments, notably for the reasons mentioned above but also for practical aspects relative to the difficulty in building the complete engine (for instance, the closed-loop engine equipped with a ceramic catalyst stack is impossible to be built unless bending the TAC). This kind of experimental confirmation has already been carried on by Guedra *et al.* (2011), and it is anticipated that it should also succeed here (at least for the prediction of threshold) since the modeling of Sec. 4.3 is nothing else than the propagation of plane acoustic waves in lossy ducts.

It is worth mentioning that the works presented here are intrinsically limited to the acoustic pressure amplitudes for which the linear approximation can be retained. The measurement method of Section 3.6 could be, in principle, extended to large amplitudes but some nonlinear processes like the generation of acoustic streaming could not be adequately characterized by this way. Actually, the thermoacoustic amplification gain G should be considered cautiously as soon as $G > 1$. The physical meaning of a gain significantly larger than unity (e.g. $G = 6.88$ in Tab. 4.4) is that the heated TAC under consideration has a very high potential of thermoacoustic amplification, but it is clear that as soon as self-sustained oscillations are generated, the associated heat transport by sound (with subsequent variations of the T-matrix components) should be considered.

Now that the so-called Impedance Method has been validated and proved succesful, the present works appeal for several other perspectives. First of all, the existing test-bench could be modified (fitting pieces) to allow the measurements of the T-matrices of the TAC used in other experimental devices at LAUM, and notably two prototypes of thermo-acousto-electric

generators. A first prototype working with air at 5 bars is already available, while a second one (working with Helium at 25 bars) is currently under construction. The obtained data should allow verification that the existing engines are well designed (or not), but it could also be helpful in the theoretical description of the engine (see the following paragraph).

Another issue concerning the use of the experimental transfer matrices of the TAC deals with the development of an adequate modeling of both acoustic propagation and heat transport through the TAC, involving the solving of an inverse problem. More precisely, the objective is to determine unknown parameters using an inverse method so that the theoretical transfer matrix fits the experimental one. The first step is to state the direct problem (notably concerning the simplified description of heat transfer through the TAC). The experimental data obtained under various heating conditions could be used to determine, from the optimization algorithm, some unknown parameters (e.g. axial and transverse thermal diffusivities of the regenerator) involved in the theoretical description of heat transfer within the TAC.

Finally, it would be also interesting to perform the measurements of the T-matrix of the TAC mentioned above as a function of the acoustic power provided by the impedance sensor to the TAC. In particular, measurements could be performed at large amplitude, for which the linear description of thermoacoustic amplification is expected to fail. It is anticipated that both the thermoacoustic heat flux and the viscothermal losses could no longer follow a quadratic dependance with acoustic pressure at large amplitudes. Note that the achievement of this task involves purchasing a new impedance sensor which is able to generate high amplitude sound notably in the low frequency range (under 100 Hz) and this kind of device has been recently developed at the Center of Technological Transfer of the Maine university (CTTM).

REFERENCES

ADEFF, J.A.; HOFLER, T.J.; ATCHLEY, A.A. e MOSS, W.C. **Measurements with reticulated vitreous carbon stacks in thermoacoustic prime movers and refrigerators**. J. Acoust. Soc. Am. **104**(1), 32-38, 1998.

ARNOTT, W.P.; BASS, H.E. e RASPET, R. **General formulation of thermoacoustics for stacks having arbitrary shaped pore cross sections**. J. Acoust. Soc. Am. **90**(6), 3228-3237, 1991.

ATCHLEY, A.A. **Standing wave analysis of a thermoacoustic prime mover below onset of self-oscillation**. J. Acoust. Soc. Am. **92**(5), 2907-2914, 1992.

ATCHLEY, A.A. **Analysis of the initial buildup of oscillations in a thermoacoustic prime-mover**. J. Acoust. Soc. Am. **95**(3), 1661-1664, 1994a.

ATCHLEY, A.A.; BASS, H.E.; HOFLER, T.J. e LIN, H. **Study of a thermoacoustic prime-mover below onset of self-oscillations**. J. Acoust. Soc. Am. **91**(2), 734-743, 1992.

ATCHLEY, A. A.; KUO, F. **Stability curves for a thermoacoustic prime mover**. J. Acoust. Soc. Am. **95**(3), 1401-1404, 1994b.

BACKHAUS, S.; SWIFT, G.W. **A thermoacoustic Stirling heat engine**. Nature **399**, 335-338, 1999.

BACKHAUS, S.; SWIFT, G.W. **A thermoacoustic Stirling heat engine: Detailed Study**. J. Acoust. Soc. Am. **107**(6), 3148-3166, 2000.

BACKHAUS, S.; TWARD, E. e PETACH, M. **Traveling-wave thermoacoustic electric generator**. Appl. Phys. Lett. **85**(6), 1085-1087, 2004.

BAILLIET, H. **Machines thermoacoustiques: études analytiques et expérimentales de couplages et d'effets non linéaires acoustiques**. PhD Thesis, Université du Maine, Le Mans, FRANCE, Octobre, 1998.

BAILLIET, H.; GUSEV, V.; RASPET, R. e HILLER, R.A. **Acoustic streaming in closed thermoacoustic devices**. J. Acoust. Soc. Am. **110**(4), 1808-1821, 2001.

BANNWART, F.C.; PENELET, G.; LOTTON, P. e DALMONT, J.P. **Methods for transfer matrix evaluation applied to thermoacoustics**. Proceedings of the ACOUSTICS 2012, Nantes, France, April 2012.

BANNWART, F.C.; PENELET, G.; LOTTON, P. e DALMONT, J.P. **Measurements of the impedance matrix of a thermoacoustic core: applications to the design of thermoacoustic engines**. J. Acoust. Soc. Am. **133**(5), 2650-2660, 2013.

BANNWART, F. C.; ARRUDA, J.R.F. **Construction of a demonstrative apparatus for the thermoacoustic refrigeration effect**. Proceedings of the XIII Int. Symposium on Dynamic Problems of Mechanics (DINAME 2009), Angra dos Reis, RJ, Brazil, March 2009.

BAO, R.; CHEN, G.; TANG, K.; CAO, W. e JIN, T. **Thermoacoustically driven pulse tube refrigeration below 80K by introducing an acoustic pressure amplifier**. Applied Physics Letters **89**, 211915, 2006.

BASTYR, K. J. ; KEOLIAN, R.M. **High-frequency thermoacoustic-Stirling heat engine demonstration device**. ARLO, **4**(2), 37-40, 2003.

BESNOIN, E.; KNIO, O.M. **Numerical study of thermoacoustic heat exchangers**. ACTA Acustica united with Acustica, Vol. **90**, 2004.

BIWA, T.; UEDA, Y.; YAZAKI, T. e ETAY, J. **Work flow measurements in a thermoacoustic engine**. Cryogenics **41**(5-6), 305-310, 2001.

BODEN, H.; ABÖM, M. **Influence of errors on the two-microphone method for measuring acoustic properties in ducts**. J. Acoust. Soc. Am. **79**(2), 541-549, 1986.

CARTER, R.L.; WHITE, M. e STEELE, A.M. **internal document of the Atomics International Division of North America Aviation Inc.**, 1962.

CEPERLEY, P. **A pistonless Stirling engine - The traveling wave heat engine**. J. Acoust. Soc. Am. **66**(5), 1508-1513, 1979.

CEPERLEY, P.H. **Gain and efficiency of a short traveling wave heat engine**. J. Acoust. Soc. Am. **77**(3), 1239-1244, 1985.

CHEN, G. B.; JIN, T. **Experimental investigation on the onset and damping behavior of the oscillation in a thermoacoustic prime mover**. Cryogenics **39**(10), 843-846, 1999.

DALMONT, J.P. **Acoustic impedance measurement, Part I: A review**. J. Sound. Vib. **243**(3), 427-439, 2001a.

DALMONT, J.P. **Acoustic impedance measurement, Part II: A new calibration method**. J. Sound. Vib. **243**(3), 441-459, 2001b.

DE BLOK, K. **Novel 4-stage traveling wave thermoacoustic power generator**. Proceedings of ASME 2010 3rd Joint US-European FEDSM2010-ICNMM2010, Montreal, Canada, August 2010.

GARDNER, D.L. **A cascade thermoacoustic engine**. J. Acoust. Soc. Am. **114**, 1905-1919, 2003.

GARRETT, S.L. **Resource Letter: TA1: thermoacoustic engines and refrigerators**. Am. J. Phys. **72**, 11, 2004.

GUEDRA, M.; PENELET, G. **On the use of complex frequency for the description of thermoacoustic engines**. Acust. Acta Acust. **98**(2), 232-241, 2012a.

GUEDRA, M. **Etudes semi-analytiques des conditions de déclenchement et de saturation des auto-oscillations dans de moteurs thermoacoustiques de géometries diverses**. PhD Thesis, Université du Maine, Le Mans, FRANCE, Novembre, 2012b.

GUEDRA, M.; PENELET, G.; LOTTON, P. e DALMONT, J.P. **Theoretical prediction of the onset of thermoacoustic instability from the experimental transfer matrix of a thermoacoustic core**. J. Acoust. Soc. Am., **130**(1), 145-152, 2011.

GUSEV, V.; BAILLET, H.; LOTTON, P. e BRUNEAU, M. **Asymptotic theory of nonlinear acoustic waves in a thermoacoustic prime mover**. Acust. Acta Acust. **86**, 25-38, 2000.

HAMILTON, M.F.; ILINSKII, Y.A. e ZABOLOTSKAYA, E.A. **Nonlinear two-dimensional model for thermoacoustic engines**. J. Acoust. Soc. Am. **111**(5), 2076-2086, 2002.

HAO, H.G.; JU, Y.L.; BEHERA, U. e KASTHURIRENGAN, S. **Influence of working fluid on the performance of a standing-wave thermoacoustic prime mover**. Cryogenics **51**(9), 559-561, 2011.

HATORI, H.; BIWA, T. e YAZAKI, T. **How to build a loaded thermoacoustic engine**. J. Appl. Phys. **111**, 074905, 2012.

HIGGINS, B. **Nicholson's**. J1, 130, 1802.

JOB, S. **Etudes théoriques et expérimentales d'un générateur thermoacoustic annulaire à ondes progressives**. PhD Thesis, Université du Maine, Le Mans, FRANCE, Octobre, 2001.

KARPOV, S.; PROSPERETTI, A. **A nonlinear model of thermoacoustic devices**. J. Acoust. Soc. Am. **112**(4), 1431-1444, 2002.

KERGOMARD, J.; GARCIA, A. **Simple discontinuities in acoustic waveguides at low frequencies: critical analysis and formulae**. J. Sound. Vib. **114**(3), 465-479, 1987.

LE ROUX, J. C.; DALMONT, J.P. **A new impedance sensor for industrial applications**. *Acoustics 2012*, Nantes, France (April 23-27, 2012), 2012.

MACALUSO, C. A.; DALMONT, J.P. **Trumpet with near-perfect harmonicity: Design and acoustic results**. J. Acoust. Soc. Am. **129**(1), 404-414, 2011.

MECHEL, F.P. ***Formulas of Acoustics***. Springer, 2008.

MERKLI, P.; THOMANN, H. **Thermoacoustic effects in a resonance tube**. J. Fluid. Mech., **70**, 1975.

MUNJAL, M. L.; DOIGE, A.G. **Theory of a two source-location method for direct experimental evaluation of the four-pole parameters of an aeroacoustic element**. J. Sound Vib. **141**(2), 323-333, 1990.

MUNJAL, M.L. ***Acoustics of ducts and mufflers with application to exhaust and ventilation system design***. Wiley-interscience, New York, 352 pages, 1987.

PENELET, G. **Etude expérimentale et théorique des processus non linéaires de saturation dans un réfrigérateur d'ondes thermoacoustique annulaire**. PhD Thesis, Université du Maine, Le Mans, FRANCE, Novembre, 2004.

PENELET, G.; GAVIOT, E.; GUSEV, V.; LOTTON, P. e BRUNEAU, M. **Experimental investigation of transient non linear phenomena in an annular thermoacoustic prime-mover: observation of doublethreshold effect**. Cryogenics, **42**, 527-532, 2002.

PENELET, G.; GUSEV, V.; LOTTON, P. e BRUNEAU, M. **Experimental and theoretical study of processes leading to steady-state sound in annular thermoacoustic engines**. Phys. Rev. E *72*(1), 016625, 2005a.

PENELET, G.; JOB, S.; GUSEV, V.; LOTTON, P. e BRUNEAU, M. **Dependence of sound amplification on temperature distribution in annular thermoacoustic engines**. Acust. Acta Acust. **91**(3), 567-577, 2005b.

PETCULESCU, A.; WILEN, L.A. **Lumped-element technique for the measurement of complex density**. J. Acoust. Soc. Am. **110**(4), 1950-1957, 2001.

PETCULESCU, G.; WILEN, L.A. **Thermoacoustics in a single pore with an applied temperature gradient**. J. Acoust. Soc. Am. **106**(2), 688-694, 1999.

RIJKE, P.L. **Notiz über eine neue Art, die in einer beiden Enden offenen Röhre enthaltene Luft in Schwingungen zu veretzen**. Ann. Phys. (Leipzig) **107**, 339, 1859.

ROH, H.; RASPET, R. e BASS, H.E. **Parallel capilary-tube-based extension of thermoacoustic theory for random porous media**. J. Acoust. Soc. Am. **121**(3), 1413-1422, 2007.

ROH, H.S. **Measurement and calculation of acoustic propagation constants in arrays of small air-filled rectangular tubes**. J. Acoust. Soc. Am. **89**(6), 2617-2624, 1991.

ROTT, N. **Damped and thermally driven acoustic oscillations in wide and narrow tubes**. Zeitschrift für Angewandte Mathematik und Physik **20**, 230-243, 1969.

ROTT, N. **Damped and thermally driven acoustic oscillations. Part II: stability limit for Helium.** Zeitschrift für Angewandte Mathematik und Physik **24**, 54-72, 1973.

ROTT, N. **Thermoacoustics**. Adv. Appl. Mech. **20**, 135-175, 1980.

SONDHAUSS, C. **Über die schallswingungen der luft in erhitzen glasrohren und gedeckten pfeifen von ungleicher weite**. Ann. Phys. **79**, 1-34, 1850.

STRUTT, J.W. ***The theory of sound (Lord Rayleigh)***. Dover, Melville, 2nd edition, 1945.

SWIFT, G.W. **Thermoacoustic engines**. J. Acoust. Soc. Am. **84** (4), 1145-1179, 1988.

SWIFT, G.W. **Analysis and performance of a large thermoacoustic engine**. J. Acoust. Soc. Am. **92**(3), 1551-1563, 1992.

SWIFT, G.W. **Thermoacoustic engines and refrigerators**. Physics Today, American Institute of Physics, July 1995.

SWIFT, G.W. ***Thermoacoustics - A unifying perspective for some engines and refrigerators***. Acoust. Soc. Am., Melville, NY, 300 pp, 2002.

SWIFT, G. W.; KEOLIAN, R.M. **Thermoacoustics in pin-array stacks**. J. Acoust. Soc. Am. **94**(2), 941-943, 1993.

SWIFT, G. W.; KEOLIAN, R.M. **Dynamic measurements of the thermal dissipation function of reticulated vitreous carbon**. J. Acoust. Soc. Am. **109**(1), 179-184, 2001.

TIJANI, M.E.H. **Loudspeaker-driven thermo-acoustic refrigeration**. PhD Thesis, Technische Universiteit Eindhoven, 2001.

TU, Q.; LI, Q.; WU, F. e GUO, F.Z. **Network model approach for calculating oscillating frequency of thermoacoustic prime mover**. Cryogenics **43**(6), 351-357, 2003.

UEDA, Y.; KATO, C. **Stability analysis of thermally induced spontaneous gas oscillations in straight and looped tubes**. J. Acoust. Soc. Am. **124**(2), 851-858, 2008.

WARD, W. C.; SWIFT, G.W. **Design environment for low-amplitude thermoacoustic engines**. J. Acoust. Soc. Am. **95**(6), 3671-3672, 1994.

WARD, W.C.; SWIFT, G.W. e CLARK, J.P. **Interactive analysis, design, and teaching for thermoacoustics using Delta EC**. J. Acoust. Soc. Am. **123**(5), 3546-3546, 2008.

WHEATLEY, J.; HOFLER, T.; SWIFT, G.W. e MIGLIORI, A. **Understanding some simple phenomena in thermoacoustics with applications to acoustical heat engines**. Am. J. Phys. **53** (2), February 1985.

WILEN, L.A. **Measurements of thermoacoustics functions for single pores**. J. Acoust. Soc. Am. **103**(3), 1406-1412, 1998.

WOLLAN, J.J.; SWIFT, G.W.; BACKHAUS, S. e GARDNER, D.L. **Development of a thermoacoustic natural gas liquifier**. AIChE New Orleans Meeting, New Orleans, 2002.

YAZAKI, T.; IWATA, A.; MAEKAWA, T. e TOMINAGA, A. **Traveling wave thermoacoustic engine in a looped tube**. Phys. Rev. Lett., **81**(15), 3128-3131, 1985.

YAZAKI, T.; TOMINAGA, A. e NARAHARA, Y. **Experiments on thermally driven acoustic oscillations of gaseous Helium**. Journal of low temperature physics **41**(1), 45-60, 1980a.

YAZAKI, T.; TOMINAGA, A. e NARAHARA, Y. **Thermally driven acoustic oscillations: second harmonic**. Physics Letters **79**(5,6), 407-409, 1980b.

YU, Z.B.; LI, Q.; CHEN, X.; GUO, F.Z.; XIE, X.J. e WU, J.H. **Investigation on the oscillation modes in a thermoacoustic Stirling prime mover: mode stability and mode transition**. Cryogenics **43**(12), 687-691, 2003.

YUAN, H.; KARPOV, S. e PROSPERETTI, A. **A simplified model for linear and nonlinear processes in thermoacoustic prime movers. Part 2: Nonlinear oscillations**. J. Acoust. Soc. Am. **102**(6), 3497-3506, 1997.

APÊNDICE A Transient regime investigation

Before proceeding with the $\mathbf{T}_{\mathrm{TAC}}$ measurements, it is necessary to ensure that the steady state regime is satisfactorily approached once new thermal conditions are imposed. That means knowing the characteristic time (τ) for reaching a sufficiently near constant temperature profile along the TAC interior, so that the $\mathbf{T}_{\mathrm{TAC}}$ coefficients are minimally affected by residual thermal transitions. An easy and reliable way to investigate τ is by taking advantage of the experimental setup for the two-load method and to measure the time evolution of the transfer functions $\widetilde{H}_{ij}$ stated in Eqs. 3.17 (or 3.30); by doing so, whenever those thermal conditions are put up with a significant change, the actual acoustical effects can be readily verified not needing to beforehand determine the $\mathbf{T}_{\mathrm{TAC}}$ coefficients.

An arbitrary criterion has to be therefore established to define a tolerable level for the $\widetilde{H}_{ij}$ transitory variations, since the complete thermal stability is never reached due unavoidable influences from the temperature fluctuations of the surrounding ambient, and also due to the external acoustic noise generated by the setup equipments. Hence, the proportions $\widetilde{H}_{ij(after)}/\widetilde{H}_{ij(before)}$ are evaluated till its variations along the frequency domain are within the criterion limits.

It is first assumed by common sense stipulation a tolerance deviation of 2 percent in Amplitude Proportions and of 0.025 rad in the phase differences for the complete frequency spectrum:

$$0.98 \leqslant \frac{|\widetilde{H}_{ij(after)}|}{|\widetilde{H}_{ij(before)}|} \leqslant 1.02, \tag{A.1}$$

$$-\,0.025rad \leqslant \arg(\widetilde{H}_{ij(after)}) - arg(\widetilde{H}_{ij(before)}) \leqslant 0.025rad. \tag{A.2}$$

The transitory thermal influences derive either from an imposed variation on Q_H, or from the thermal interaction with the circulating water inside the AHX - whose temperature is affected by the natural evaporation at the open surface of its reservoir. That justifies a specific and separated investigation regarding the water influence prior to beginning the analysis of the Q_H variation effects.

The preliminary investigation starts with the measurement of $\widetilde{H}_{ij(before)}$ without water circulation. The Ceramic Catalyst 1 (600 CPSI) is placed inside the TAC. However, special cares are taken to ensure as much as possible a uniformity on the temperature distribution throughout the TAC, like having it passed through a long period without any heating at all, to avoid residual warmth from whichever previous experimentation; for this reason, one overnight period is chosen sufficient. Additionally, to prevent from body warmth, even hand-touching on the TAC surfaces is avoided. It is assumed at this point that the ambient air is in a thermal equilibrium with the whole TAC device, homogeneously. In the following, the $\widetilde{H}_{ij(before)}$ measurement is made. Once finished, the water circulation is turned on for $12.5min$ (guessed time period), and, subsequently, the second measurement $\widetilde{H}_{ij(after)}$ is made while the water is kept circulating. Finally, the proportions reported in the statements A.1 and A.2 are put forward, which results in the Figure A.1.

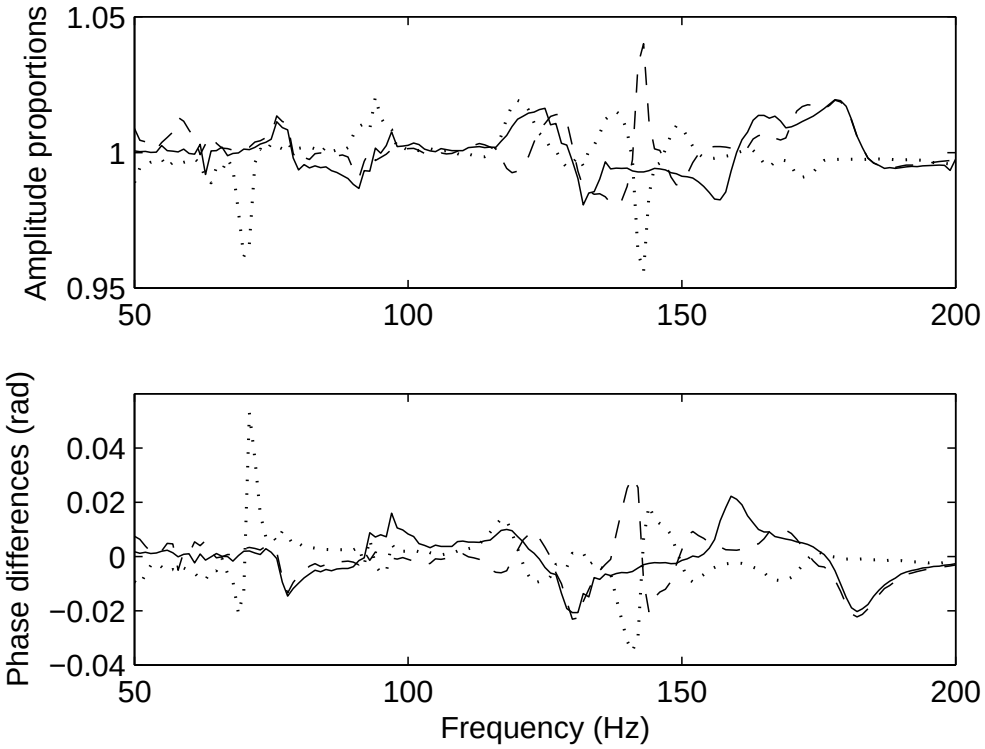

Figure A.1: Amplitude proportions and phase differences between the transfer functions measured before and 12.5 min after turning in the ambient water cooling system for $\widetilde{H}_{21}$ (solid line), $\widetilde{H}_{31}$ (dashed line), and $\widetilde{H}_{43}$ (dotted line).

One may clearly see that the referred inequality is not satisfied, and it indicates a non-negligible warmth effect, peculiarly for $|\widetilde{H}_{21}|$ and $|\widetilde{H}_{31}|$ at around $140Hz$. Such differences are consistent with the fact that, due to the constant presence of the evaporation phenomenon, the water contained in the reservoir is always colder that the ambient air - if there are no longer

thermal remains from any previous heating. Indeed, when actually measuring the temperature in the reservoir and in the ambient air, for this experiment situation, a fluctuating difference between 0.7ºC and 1.8°C is verified, depending on the air humidity. Those facts suggest a considerable significance of the evaporation effect, which must be minimized to then continue the transitory analysis taking into account the Q_H variation effect. In order to do so, before starting with any heating supply, the TAC temperature distribution is stabilized in time with respect to both ambient air and circulating water by means of a robust procedure, which is to turn on the water circulation since the day before. Moreover, to keep this evaporative effect also minimized for the succeeding measurements with heating supply, this procedure is taken as part of the intrinsic preparations from this point forward, independently on the method for the TAC characterization.

To continue with the transitory regime investigation, the case of the effects due to an imposed Q_H variation is put forward. As previously noted, the inequalities A.1 and A.2 are used as the quality parameters. Once the evaporation effects are stabilized, different arbitrary values for Q_H are set, for which the transfer function proportions $\widetilde{H}_{ij(after)}/\widetilde{H}_{ij(before)}$ are measured a predefined time interval of $5min$. The Q_H values are chosen to be representative for the heating situations to be imposed during the $\mathbf{T}_{\mathrm{TAC}}$ measurements, namely $29.3W$, $32.3W$ and $35.3W$. After 12 measurements at $Q_H = 29.3W$, the inequalities A.1 and A.2 are well satisfied; indeed, a nearly steady-state regime is achieved since the third measurement, i.e., after $15min$. Therefore, as it could have been predicted, at the 12^{th} measurement the system shows an almost complete thermal stabilization. For this last measurement is attributed $\widetilde{H}_{ij(before)}$. Then, the heating input is changed to $Q_H = 32.3W$; after $5min$, it is obtained $\widetilde{H}_{ij(after)}$. The calculation of the corresponding proportions gives the results shown in Figure A.2. In this case, there are deviation peaks over 10 percent, what puts in evidence a very important effect, even though it having had $5min$ already passed.

The same procedures are repeated for the following measurements, trying to best capture the $\widetilde{H}_{ij}$ time evolution. From $10min$ forward the time increment is diminished from $5min$ to $1min$, what allowed a more refined evaluation for several time interval combinations. That led to the results presented in Figure A.3, which shows the $\widetilde{H}_{ij(after)}/\widetilde{H}_{ij(before)}$ behavior within an interval between 13 and $18min$, counted since the Q_H transition. For both amplitude proportions and phase differences the deviation peaks are within the stipulated limit established in the inequalities A.1 and A.2. That also reveals what may be called a characteristic time "τ", which is therefore approximately $13min$.

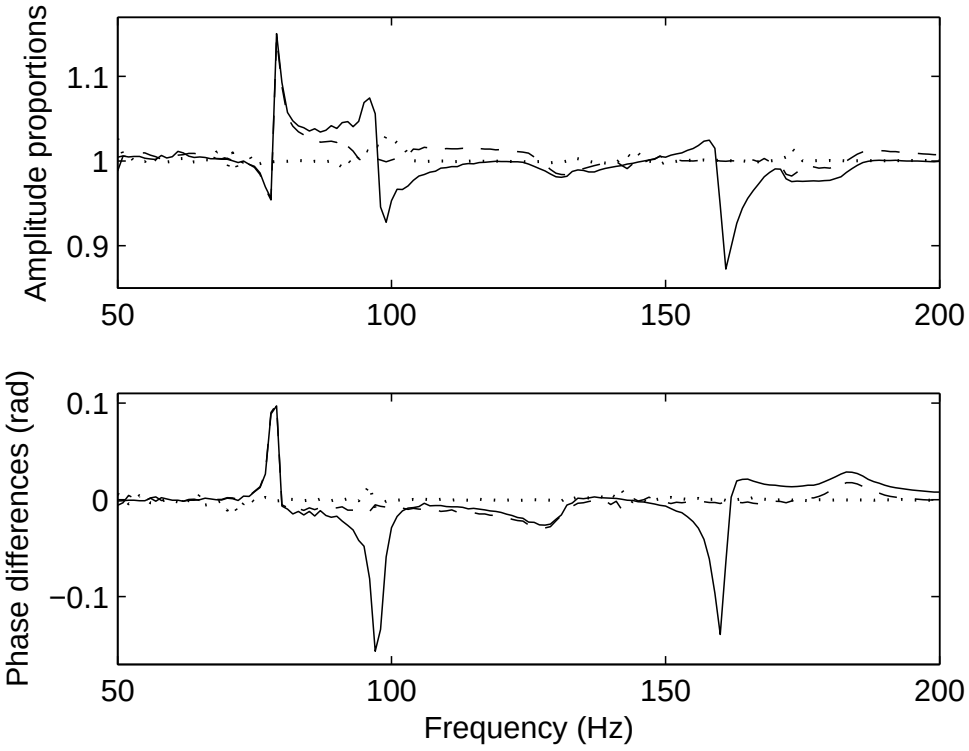

Figure A.2: Amplitude proportions and phase differences between the transfer functions measured just before and $5min$ after the transition of heating input from $Q_H = 29.3W$ to $Q_H = 32.3W$ for $\widetilde{H}_{21}$ (solid line), $\widetilde{H}_{31}$ (dashed line), and $\widetilde{H}_{43}$ (dotted line).

In conclusion, this transitory regime investigation assures that the evaporation effects are suppressed if the water circulation is turned on at the overnight before the experiments, and it also indicates that a time delay of $13min$ is sufficient to minimize the transient effects of the Q_H variation. However, the latter is supported on the constraints A.1 and A.2, which are stipulated by a common sense guessing to start an iterative process, hopefully a well-done trial. Indeed, when obtaining the $\mathbf{T}_{\mathrm{TAC}}$ coefficients later on, the transitory investigation is validated and, consequently, those constraints are proved to be well guessed. Although these results are obtained only for the Ceramic Catalyst 1 circumstance by means of the Two-Load method setup, it is assumed that they can be equally considered for the other materials as well, for all TAC characterization approaches treated here.

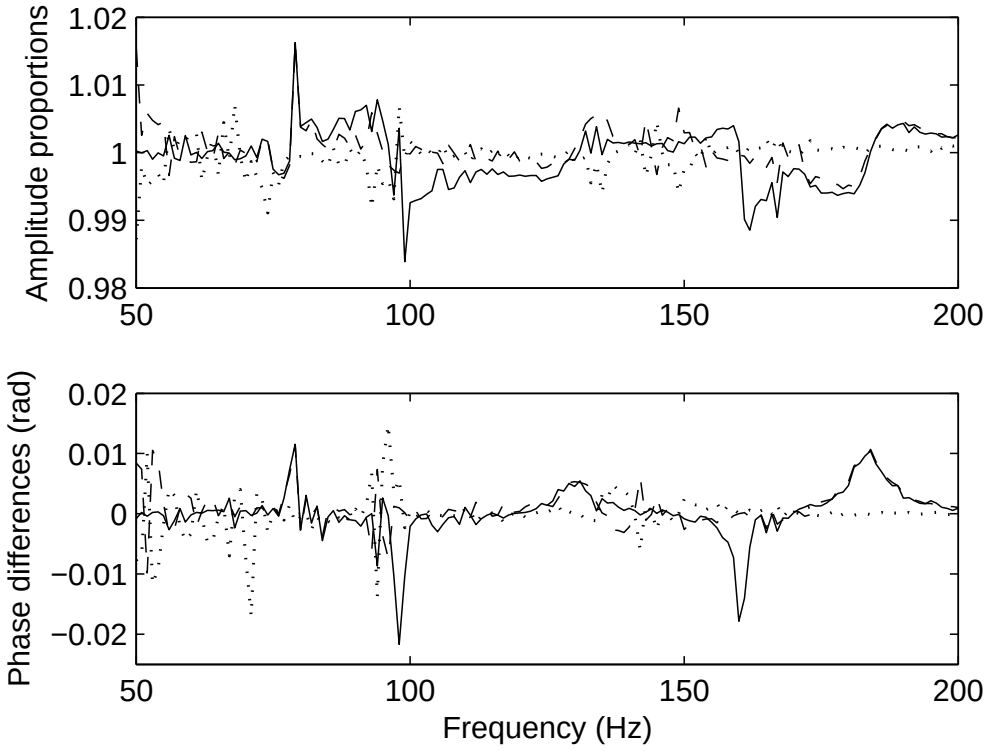

Figure A.3: Amplitude proportions and phase differences between the transfer functions measured 13 and $18min$ both after the transition of heating input from $Q_H = 29.3W$ to $Q_H = 32.3W$ for $\widetilde{H}_{21}$ (solid line), $\widetilde{H}_{31}$ (dashed line), and $\widetilde{H}_{43}$ (dotted line).

APÊNDICE B Calibration for the Two-Load Method

It is a necessary precaution to carry out all standard procedures so as to pursuing the lesser significant error propagation. This case-study is not an exception. On the contrary: in this method the indirectness of the $\mathbf{T}_{\mathrm{TAC}}$ measurement is very important, what may compel the errors impact to devalue or even invalidate the whole experimentation. Thereby, the calibration is put into practice with close attention to employing well suited and clean equipment, and avoiding, as much as possible, sound leakage by means of vacuum grease spreading in all joints and connections.

The four microphones are subjected to both absolute and relative calibration. In the first instance, it is proved that there are important differences between manufacturer's values and the actual measured ones just before the experimentation.

As a matter of fact, the absolute calibration is a priori unnecessary since the measured acoustic pressures are considered at once in the transfer functions reported in Eq. 3.17 (or Eq. 3.30), in which the proportions intrinsically dismiss the need for knowing the microphone sensitivities. That said, a solely relative calibration would be sufficient to go on then with the actual transfer function measurements, not requiring so the absolute one. Notwithstanding, in order to prevent eventual major measurement distortions, and also because it is simple to be effectuated, an absolute calibration is justified in this work.

Subsequently, the relative calibration is proceeded. The microphones are flush mounted one pair at a time at both sides of a chamber device, small enough to ensure their exposure to the same acoustic pressure for the frequency range of interest. Three pairs of microphone combinations are chosen, in accordance with the transfer function arranges stated in Equations 3.17, namely micros 1-2, 1-3, and 3-4. The schematic of the calibration device is shown in Fig. B.1.

These measurements are associated in the expressions in the following, which are actually transfer functions.

$$\widetilde{C}_{21} = \frac{\widetilde{p}_{2cal}}{\widetilde{p}_{1cal}}, \widetilde{C}_{31} = \frac{\widetilde{p}_{3cal}}{\widetilde{p}_{1cal}}, \widetilde{C}_{43} = \frac{\widetilde{p}_{4cal}}{\widetilde{p}_{3cal}}. \tag{B.1}$$

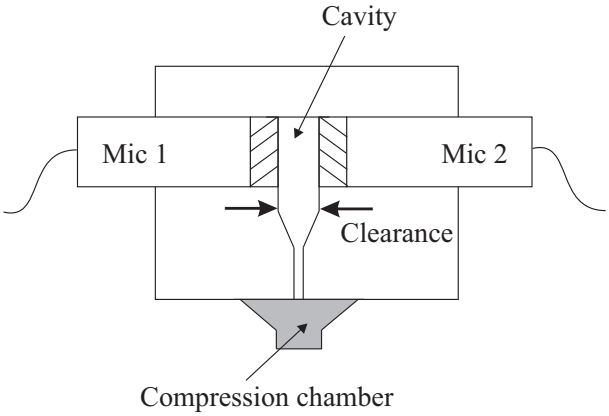

Figure B.1: Detail of the calibration device showing the two micros and the small cavity as the coupling volume submitted to uniform acoustic pressures provided by the compression chamber.

Knowing that the actual acoustic pressure is the same for each pair of microphones, one can conclude that any deviation from the unity in the relations of Eq. B.1 is due to the differences of sensitivity. If these ratios divide the corresponding transfer functions 3.17, then those differences have their effects canceled. The resulting transfer functions become calibrated, as following.

$$\widetilde{H}_{21cal} = \frac{\widetilde{H}_{21}}{\widetilde{C}_{21}}, \widetilde{H}_{31cal} = \frac{\widetilde{H}_{31}}{\widetilde{C}_{31}}, \widetilde{H}_{43cal} = \frac{\widetilde{H}_{43}}{\widetilde{C}_{43}}. \tag{B.2}$$

The frequency range and its incremental step must be the same as the ones employed for the actual $\mathbf{T}_{\mathrm{TAC}}$ measurement, to keep the exact vectorial matching and hence to achieve the calibrating correction for each specific frequency. That means an acoustic field also ranging from 50 to $200Hz$ and paced with a constant increment of $1Hz$. A signal generator is directly connected to a loudspeaker, which in this small chamber case works as a compressor, to produce that acoustic field. Also because of the chamber small size, the use of a signal amplifier is dismissed, as the required acoustic power input is proportionally small.

The results in Figure B.2 illustrates how important the calibration is. Although not impressive, in the order of 1 percent, the deviations may be clearly seen in the amplitude ratios and in the phase differences as well; they also indicate that their behaviors are not abnormal and there are no malfunctions in the whole instrumentation. All transfer functions considered in this approach are calibrated as in B.2.

It is very important to note that, in order to simplify the notation for the transfer functions, the $\widetilde{H}_{ijcal}$ terms have no longer the subscript *cal* from this point on. Thus, the sole description $\widetilde{H}_{ij}$ is presumed to indicate a previous calibration, implicitly, when substituting them into Eqs. 3.26 to 3.29, to finally obtain the $\mathbf{T}_{\mathrm{TAC}}$ coefficients.

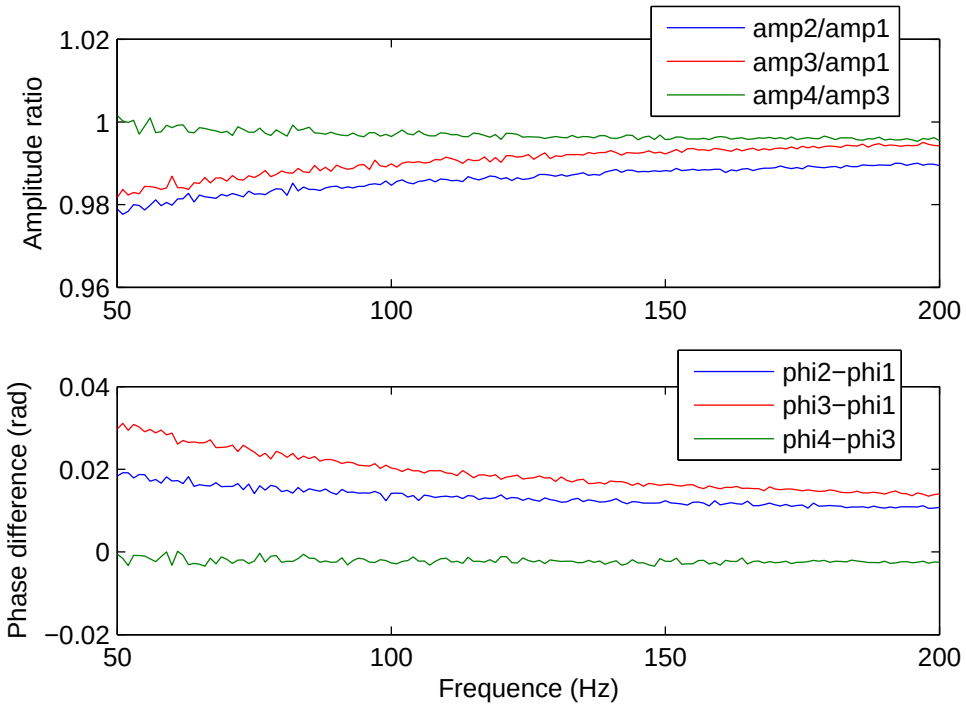

Figure B.2: Calibrating corrections expressed as the spectra of amplitude ratio and phase difference between acoustic pressures as stated in equations B.1.

APÊNDICE C Calibration for the Impedance Method

The calibration is conducted simply by placing the third microphone at the entrance of the AIS (Fig. C.1), and taking impedance measurements just as explained in Chapter 3. That way, the calibrating transfer functions are obtained, to be later on applied into the Z-matrix equations.

Figure C.1: Detail of the third microphone head and its attachment to the AIS for calibration.

APÊNDICE D Results for all heating conditions

This appendix shows the best results for all heating conditions for all measured materials, according to each method, obtained in this work. Heated measurements were done only for the first and third approaches.

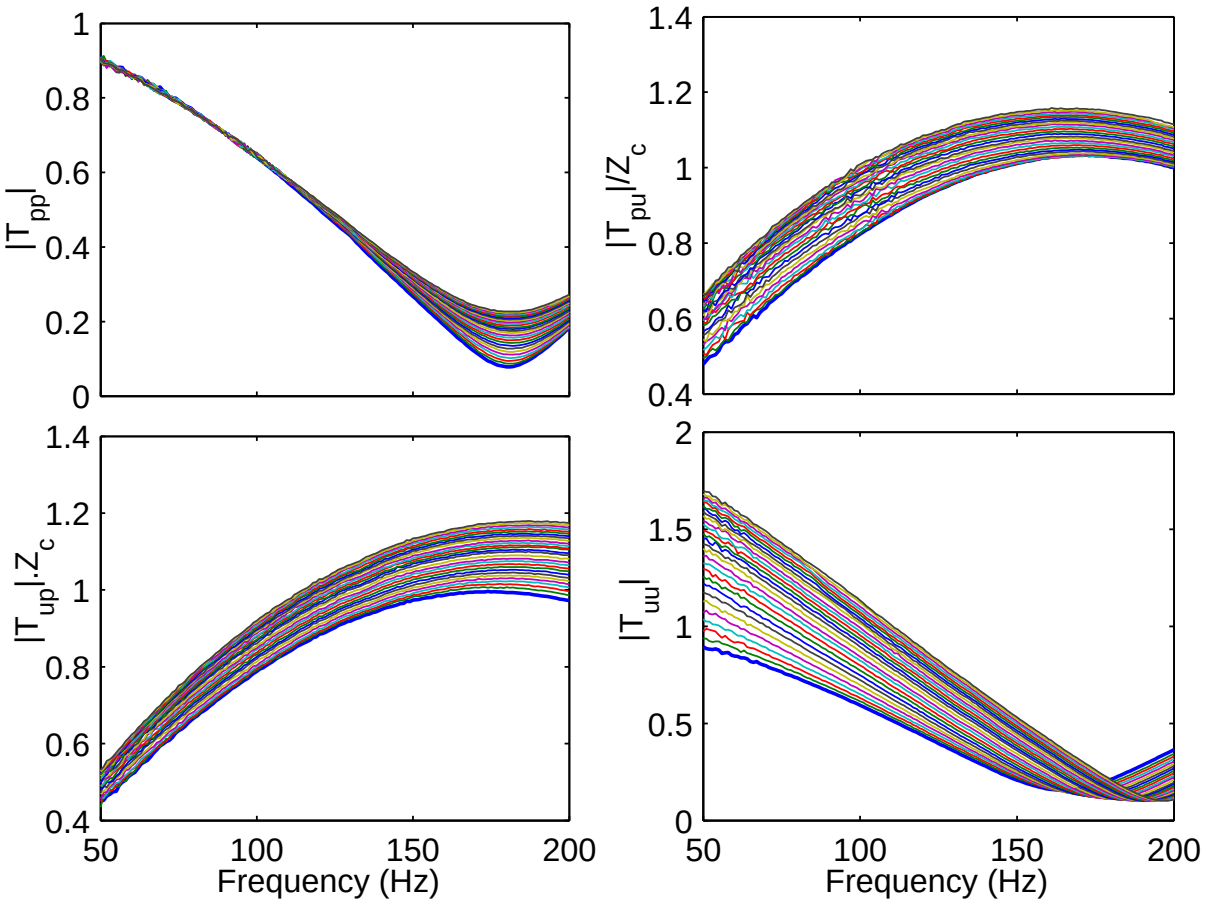

Figure D.1: Ceramic Catalyst 600 CPSI: amplitude of the four $\mathcal{T}$ coefficients in the frequency domain for Q_H ranging from $0W$ to $81W$, by a constant increment of $3W$. The bold graph line corresponds to $Q_H = 0W$. - Two-Load Method.

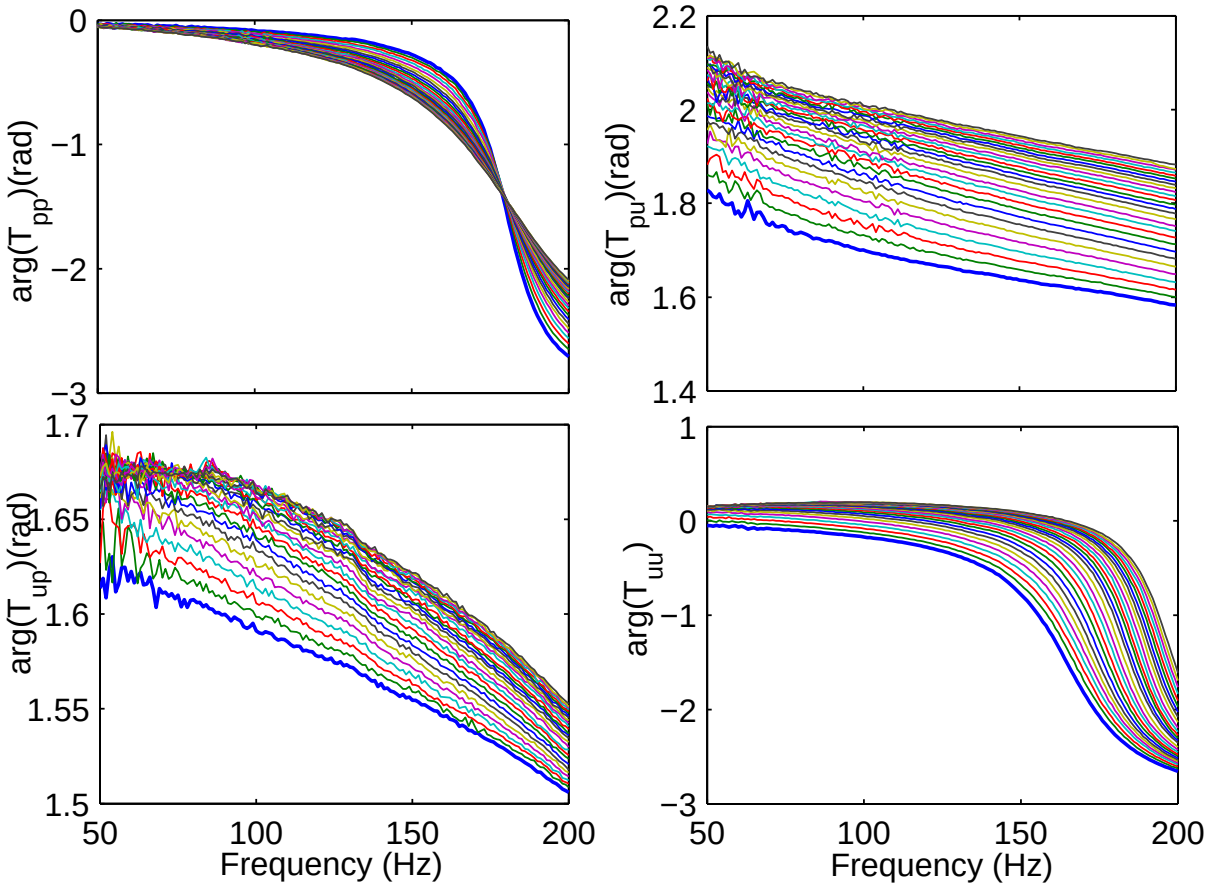

Figure D.2: Ceramic Catalyst 600 CPSI: phase of the four $\mathcal{T}$ coefficients in the frequency domain for Q_H ranging from $0W$ to $81W$, by a constant increment of $3W$. The bold graph line corresponds to $Q_H = 0W$. - Two-Load Method.

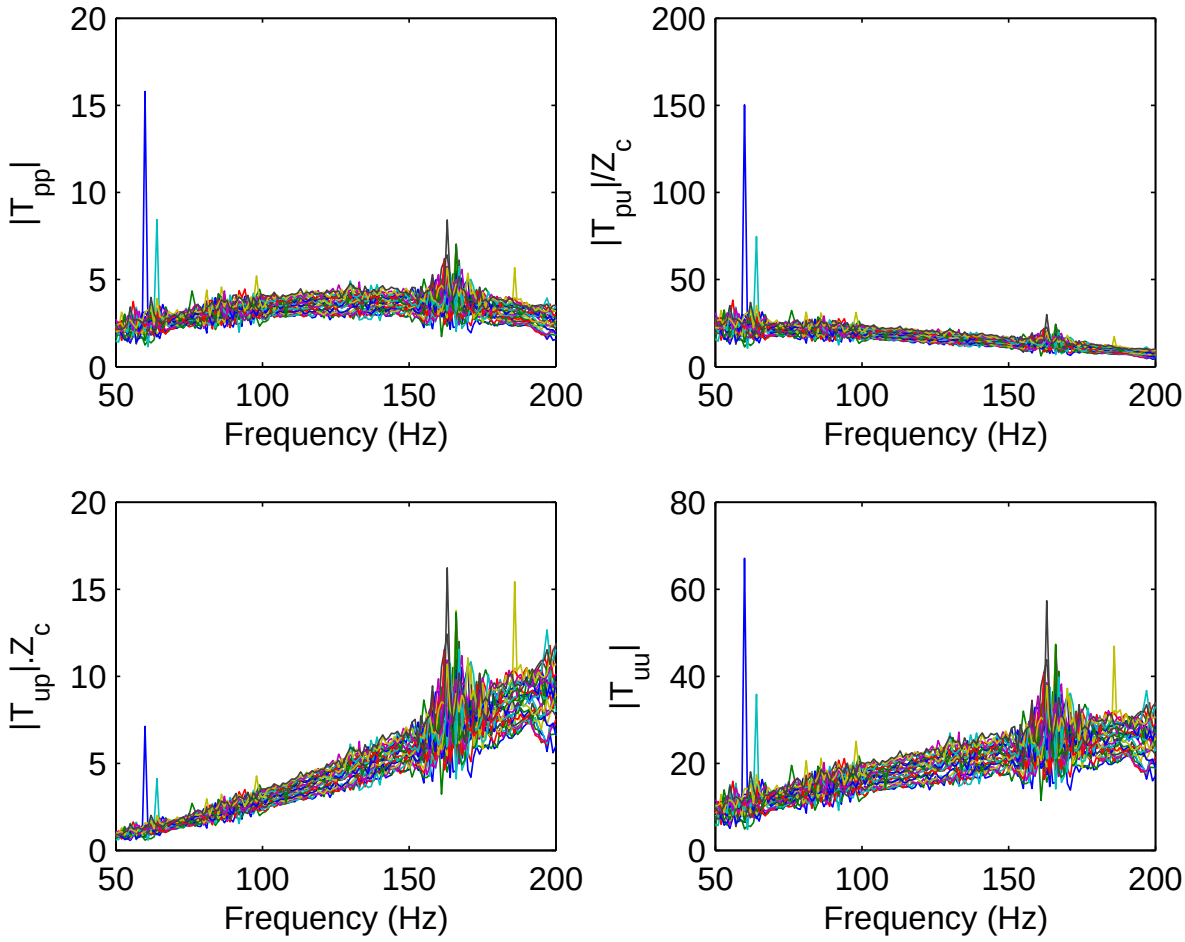

Figure D.3: Stainless Steel Grids: amplitude of the four $\mathcal{T}$ coefficients in the frequency domain for Q_H ranging from $0W$ to $81W$, by a constant increment of $3W$. - Two-Load Method.

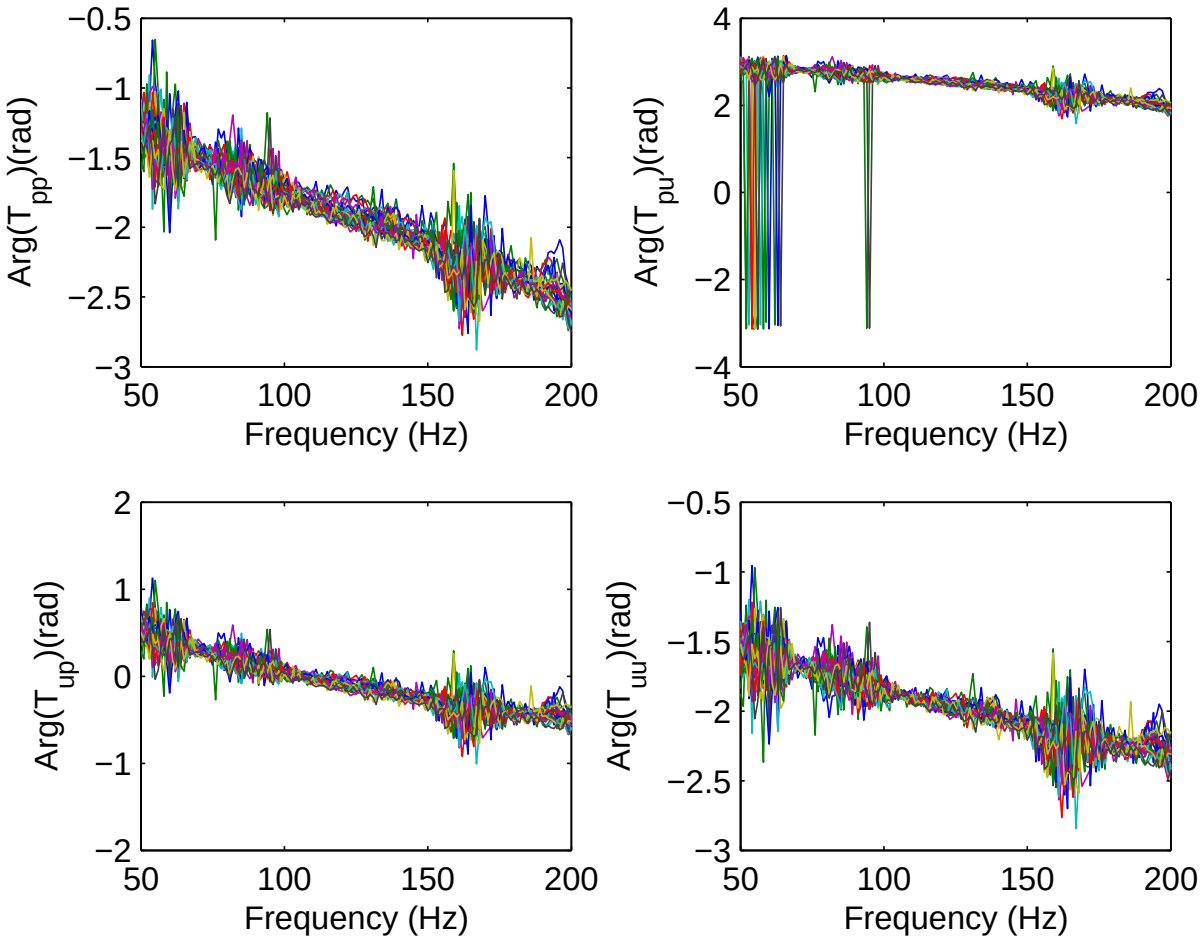

Figure D.4: Stainless Steel Grids: phase of the four $\mathcal{T}$ coefficients in the frequency domain for Q_H ranging from $0W$ to $81W$, by a constant increment of $3W$. - Two-Load Method.

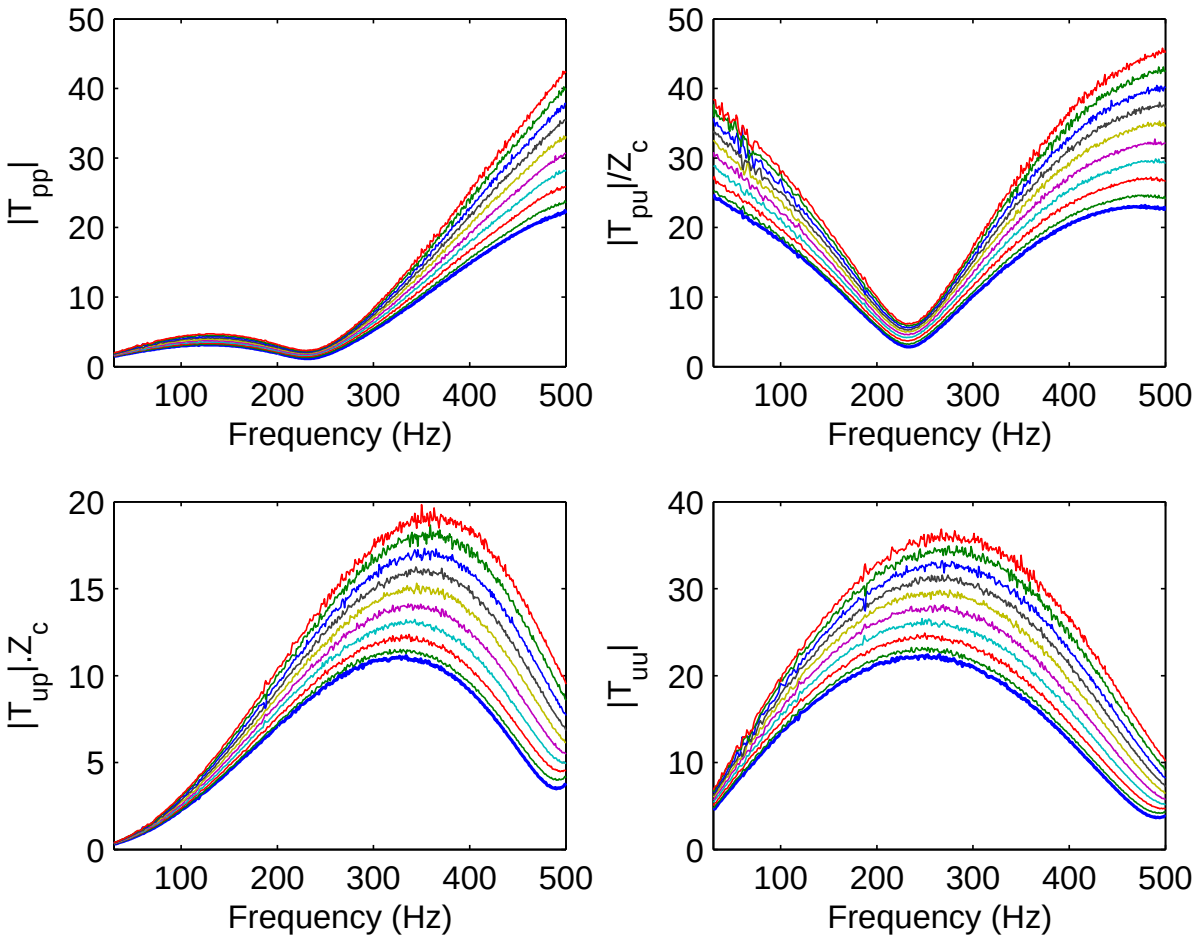

Figure D.5: Stainless Steel Grids: amplitude of the four $\mathcal{T}$ coefficients in the frequency domain for Q_H ranging from $0W$ to $81W$, by a constant increment of $9W$. The bold graph line corresponds to $Q_H = 0W$. - Impedance Method.

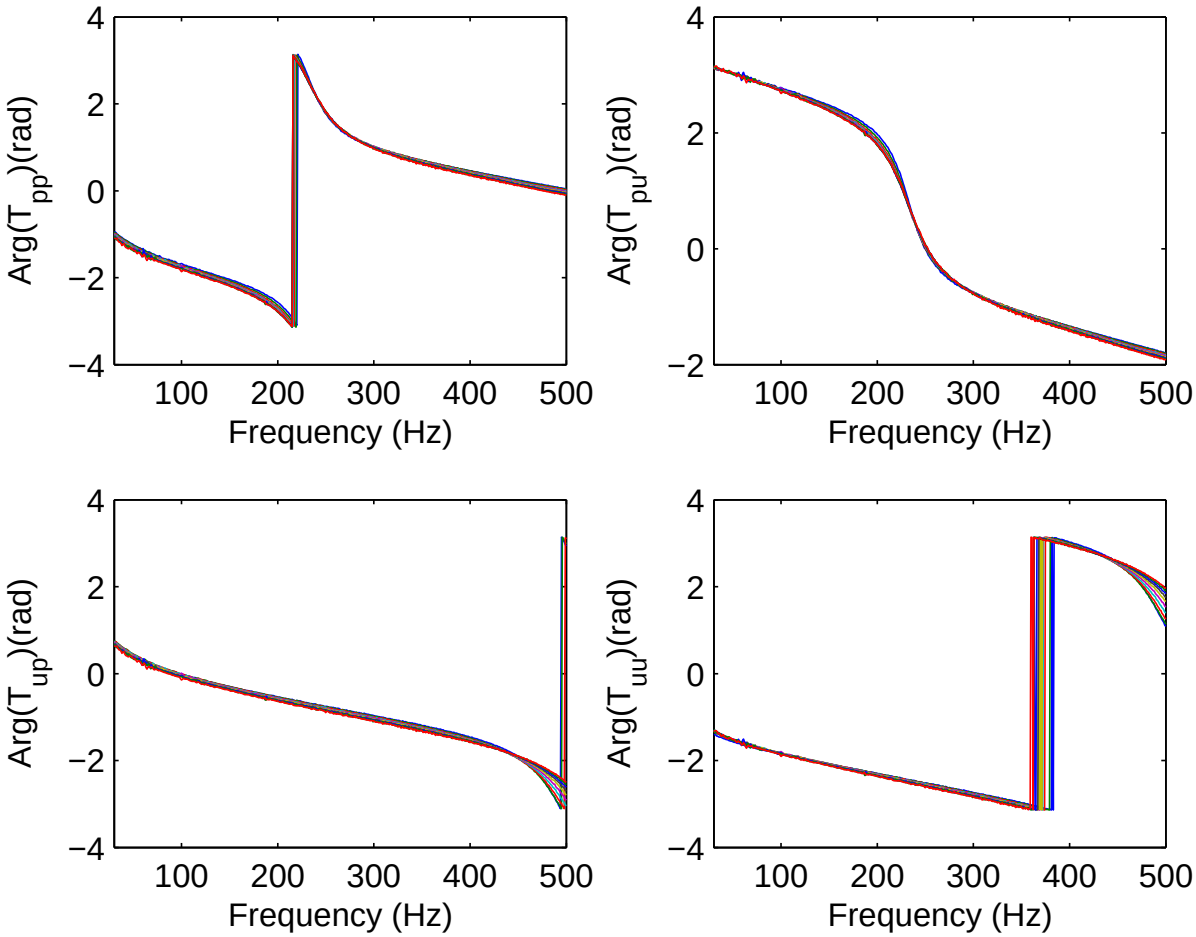

Figure D.6: Stainless Steel Grids: phase of the four $\mathcal{T}$ coefficients in the frequency domain for Q_H ranging from $0W$ to $81W$, by a constant increment of $9W$. The bold graph line corresponds to $Q_H = 0W$. - Impedance Method.

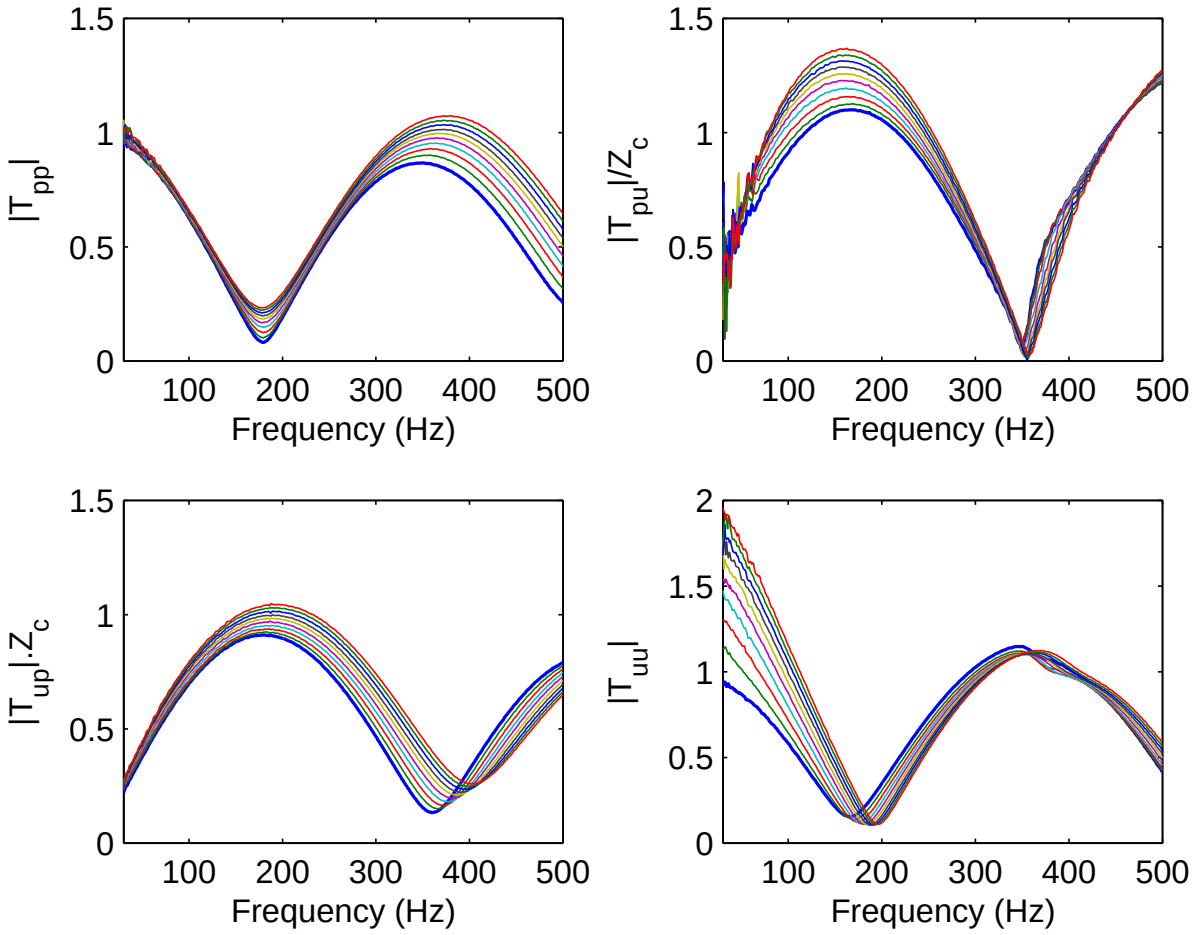

Figure D.7: Ceramic Catalyst 600 CPSI: amplitude of the four $\mathcal{T}$ coefficients in the frequency domain for Q_H ranging from $0W$ to $81W$, by a constant increment of $9W$. The bold graph line corresponds to $Q_H = 0W$. - Impedance Method.

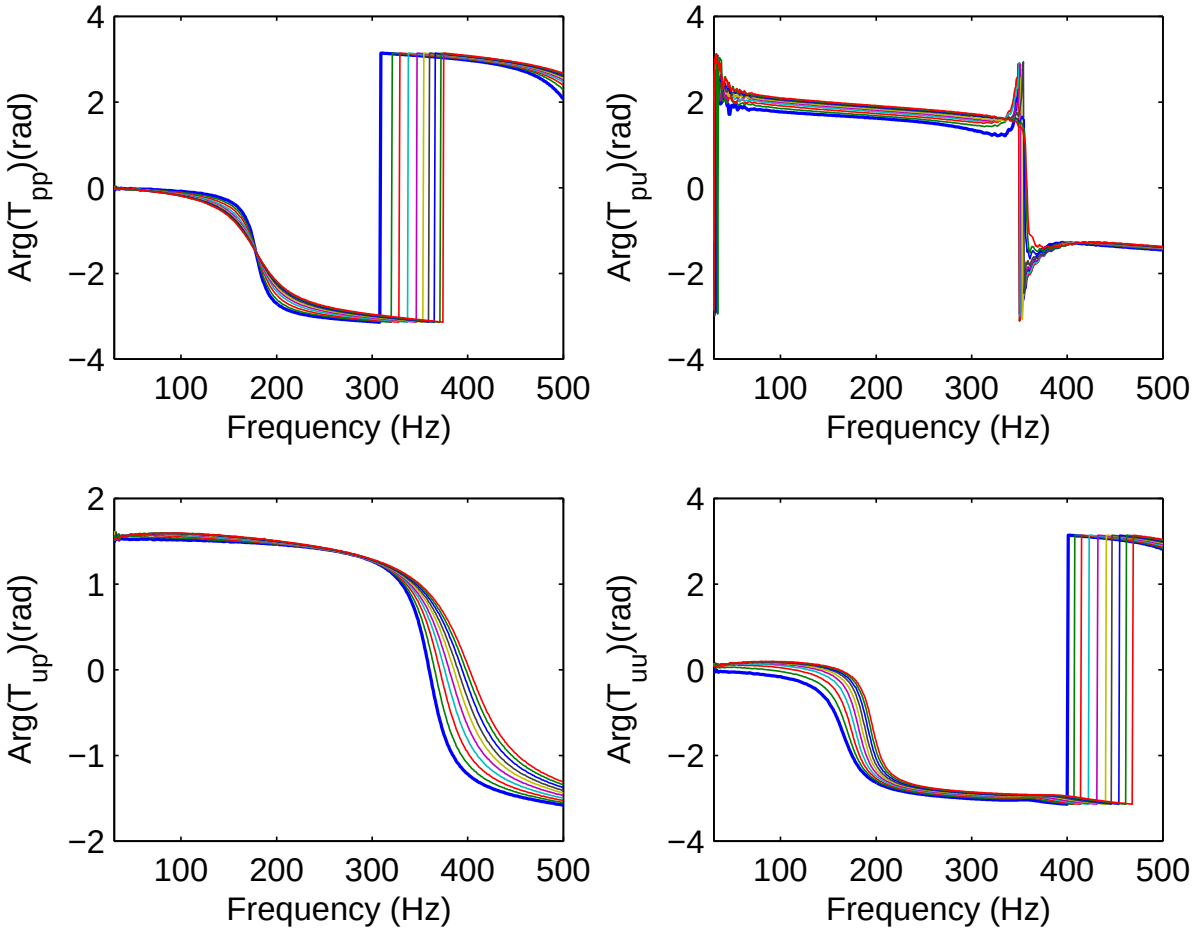

Figure D.8: Ceramic Catalyst 600 CPSI: phase of the four $\mathcal{T}$ coefficients in the frequency domain for Q_H ranging from $0W$ to $81W$, by a constant increment of $9W$. The bold graph line corresponds to $Q_H = 0W$. - Impedance Method.

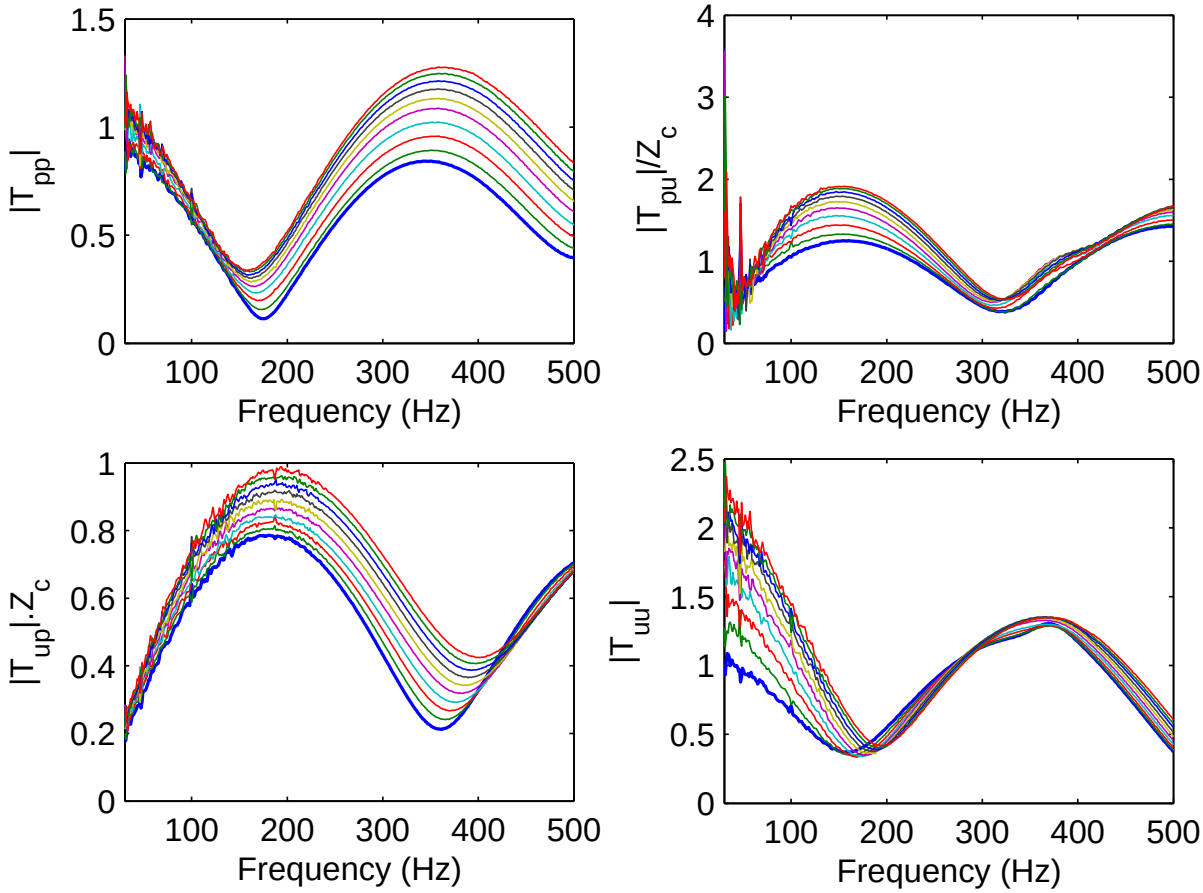

Figure D.9: NiCr Foam: amplitude of the four $\mathcal{T}$ coefficients in the frequency domain for Q_H ranging from $0W$ to $81W$, by a constant increment of $9W$. The bold graph line corresponds to $Q_H = 0W$. - Impedance Method.

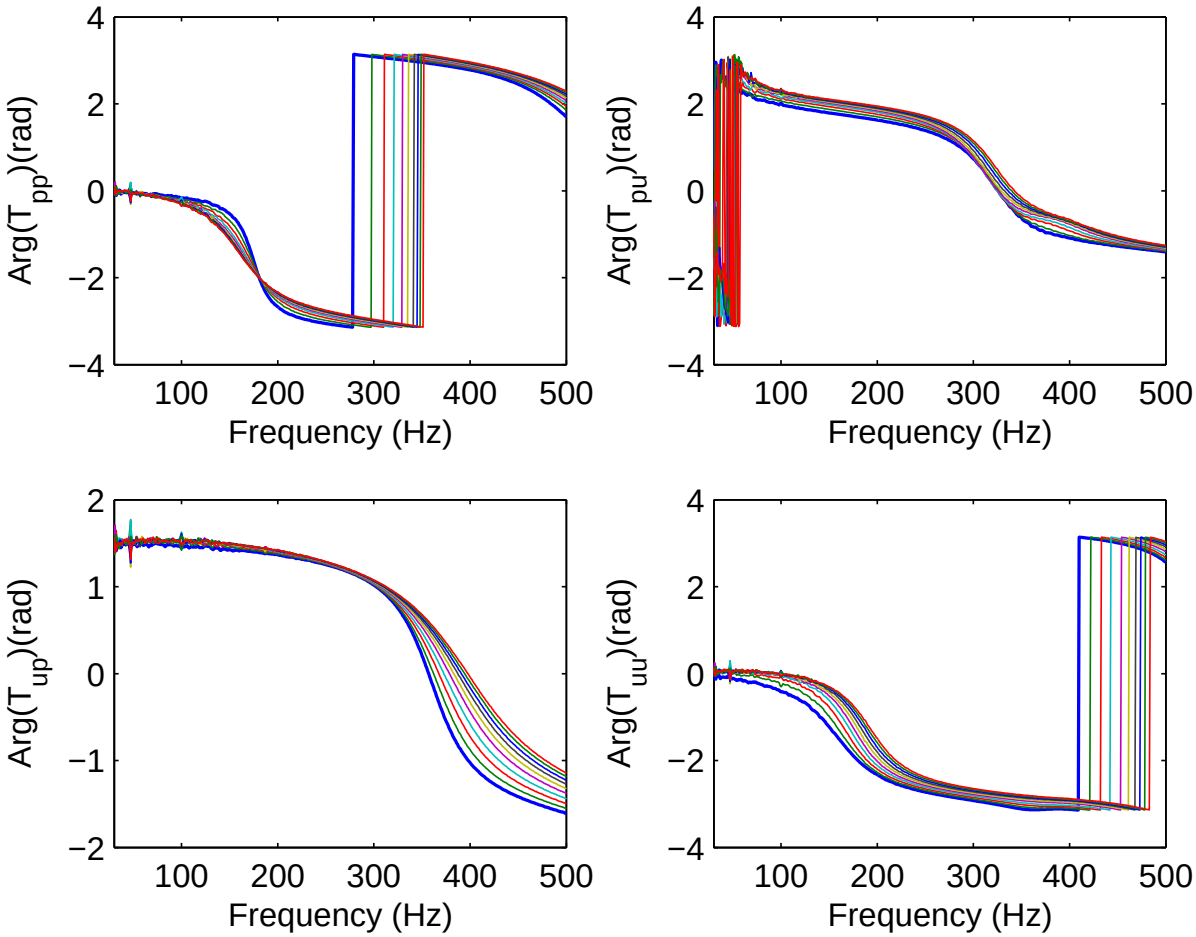

Figure D.10: NiCr Foam: phase of the four $\mathcal{T}$ coefficients in the frequency domain for Q_H ranging from $0W$ to $81W$, by a constant increment of $9W$. The bold graph line corresponds to $Q_H = 0W$. - Impedance Method.

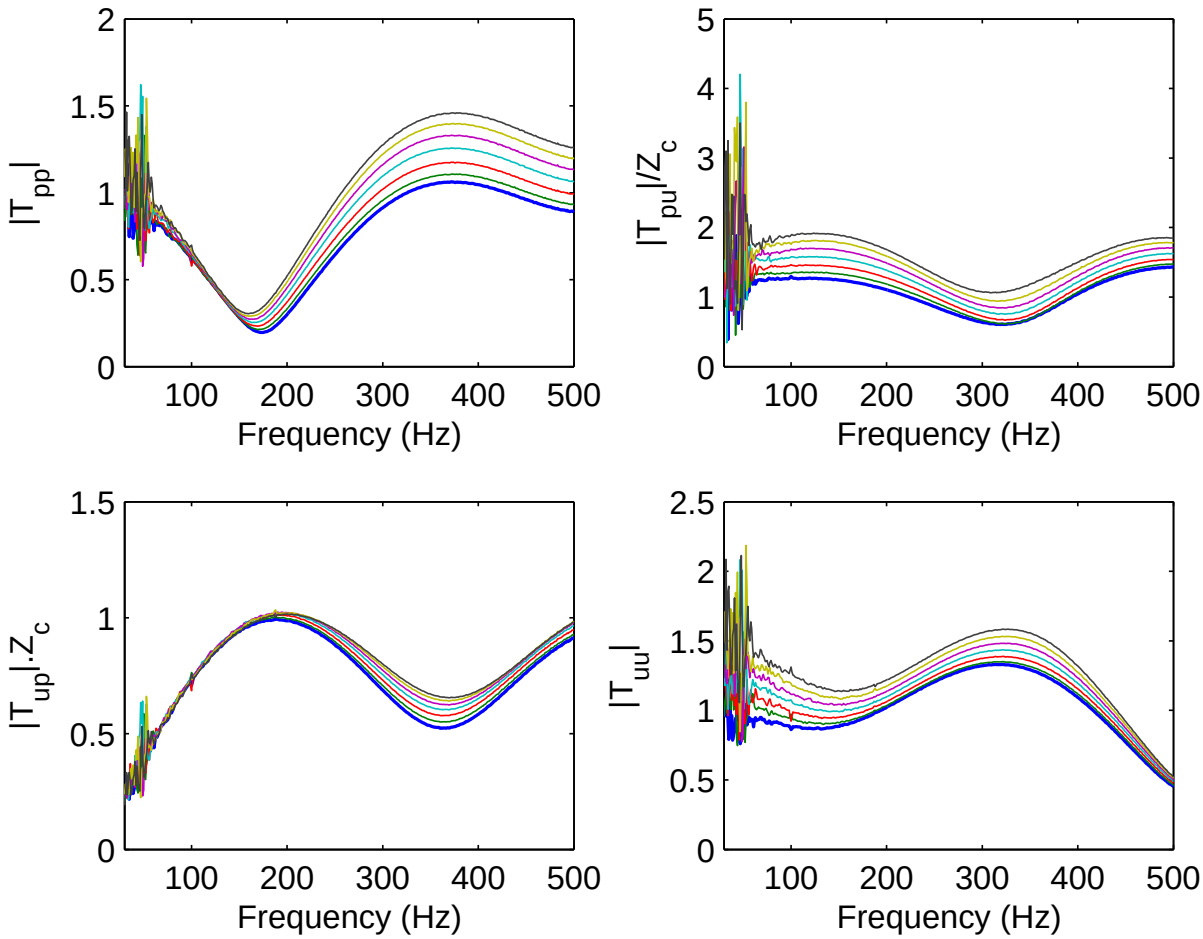

Figure D.11: RVC Foam: amplitude of the four $\mathcal{T}$ coefficients in the frequency domain for Q_H ranging from $0W$ to $18W$, by a constant increment of $3W$. The bold graph line corresponds to $Q_H = 0W$. - Impedance Method.

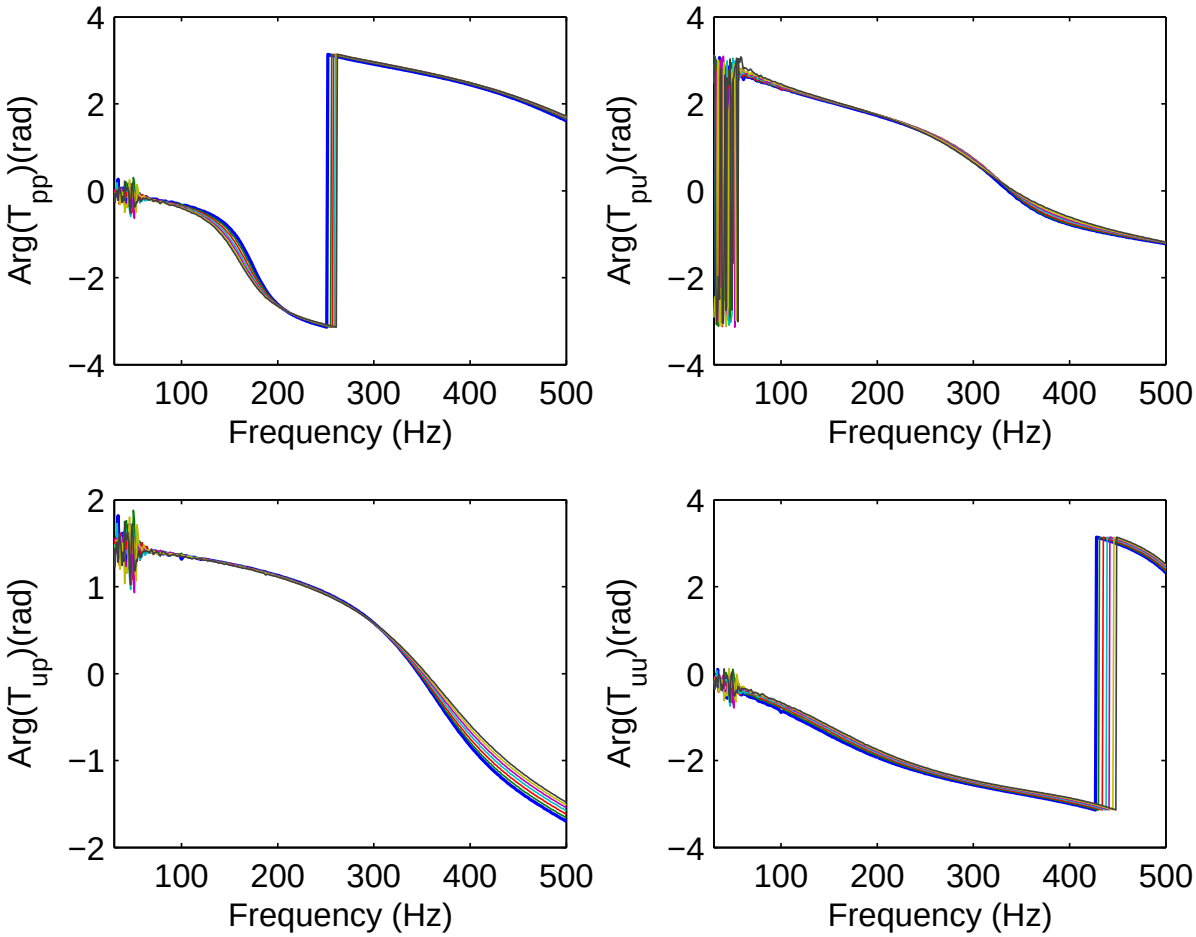

Figure D.12: RVC Foam: phase of the four $\mathcal{T}$ coefficients in the frequency domain for Q_H ranging from $0W$ to $18W$, by a constant increment of $3W$. The bold graph line corresponds to $Q_H = 0W$. - Impedance Method.

APÊNDICE E Thermal effects on reciprocity

An interesting thermal effect has been noticed during the investigation of the NiCr Foam. When measuring this material, in the case by the Impedance Method, not respecting the necessary time delay for a proper thermal stabilization, a strong *bias* was achieved, as shown in Fig. E.1. The reciprocity parameters resulted in $\sigma_{\mathbf{rc}} = 0.9361 - 0.0270i$ and $\sigma_{\mathbf{rc}} = 0.0324 + 0.0335i$. Such measurement was done, although non-recommended, aiming to test how important possible residual thermal effects could have been. For comparison, in the same figure are also shown the best reciprocity results obtained for the NiCr Foam, whose parameters are presented in Table 3.2.

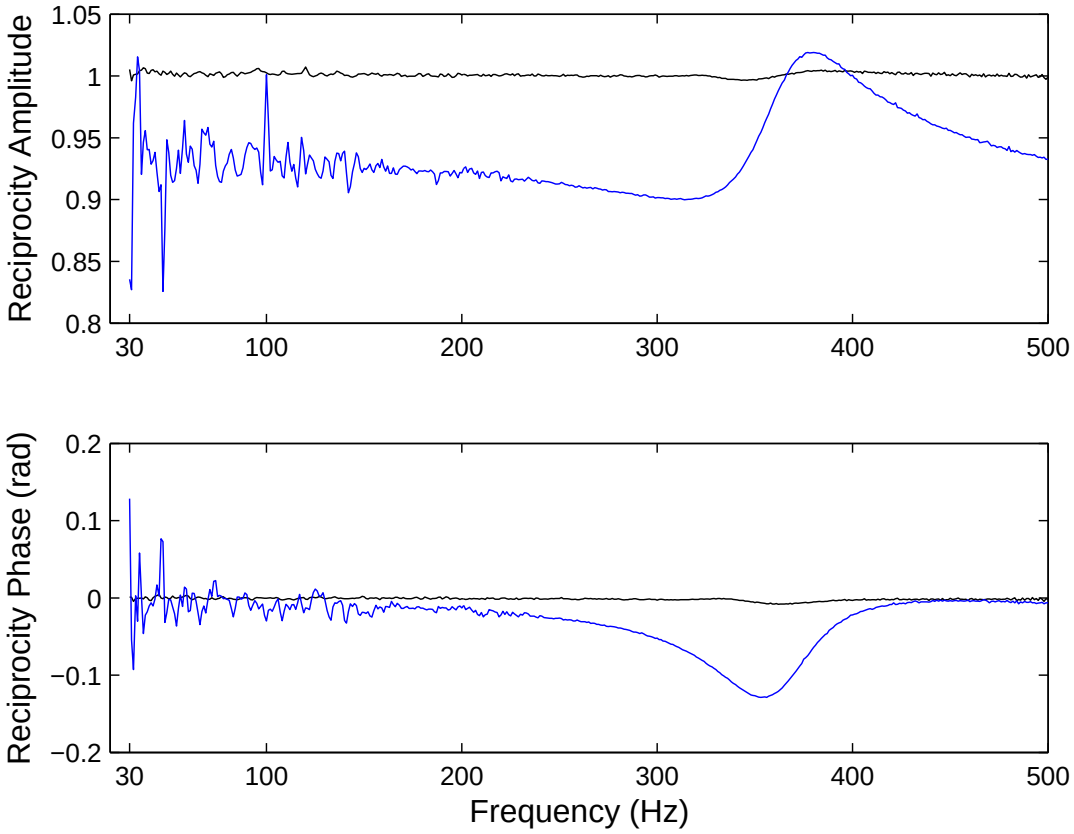

Figure E.1: NiCr Foam: amplitude and phase of the $\mathbf{T}_{\mathrm{TAC}}$ reciprocity in the frequency domain for $Q_H = 0\,W$ for the Impedance Method before (biased and noisy line) and after a better thermal stabilization.